

Arbeitsbericht NAB 16-16

FEBEX-DP Metal Corrosion and Iron-Bentonite Interaction Studies

October 2017

P. Wersin & F. Kober (eds.)

**National Cooperative
for the Disposal of
Radioactive Waste**

Hardstrasse 73
P.O. Box 280
5430 Wettingen
Switzerland
Tel. +41 56 437 11 11
www.nagra.ch

Arbeitsbericht NAB 16-16

FEBEX-DP **Metal Corrosion and Iron-Bentonite** **Interaction Studies**

October 2017

P. Wersin¹ & F. Kober² (eds.)

¹ University of Bern, Switzerland
² Nagra

KEYWORDS

Iron, copper, titanium, corrosion, iron-bentonite interaction

**National Cooperative
for the Disposal of
Radioactive Waste**

Hardstrasse 73
P.O. Box 280
5430 Wettingen
Switzerland
Tel. +41 56 437 11 11
www.nagra.ch

Nagra Arbeitsberichte ("Working Reports") present the results of work in progress that have not necessarily been subject to a comprehensive review. They are intended to provide rapid dissemination of current information.

"Copyright © 2017 by Nagra, Wettingen (Switzerland) / All rights reserved.

All parts of this work are protected by copyright. Any utilisation outwith the remit of the copyright law is unlawful and liable to prosecution. This applies in particular to translations, storage and processing in electronic systems and programs, microfilms, reproductions, etc."

Authors

F. Kober, N. Giroud

Nagra, Wettingen, Switzerland

M. Uyama, T. Hitomi, S. Hayagane, N. Kadota, H. Saito, S. Okamoto, K. Aoshima, M. Osawa

Obayashi, Tokyo, Japan

J. Hadi¹, J.M. Grenèche², P. Wersin¹

¹ University of Bern, Bern, Switzerland; ² Université du Mans, Le Mans, France

D. Svensson, C. Lundgren

SKB, Äspo Hard Rock Laboratory, Sweden

S. Kaufhold, R. Dohrmann, K. Ufer

BGR, Hannover, Germany

E. Torres, M.J. Turrero, L. Sánchez, A. Garralón, P. Gómez, R. Campos

CIEMAT, Madrid, Spain

M. Leal Olloqui, T.B. Scott

University of Bristol, Bristol, United Kingdom

V. Madina

Tecnalia, Donostia-San Sebastián, Spain

Abstract

The FEBEX in-situ experiment was a full scale in-situ heating test with two steel heaters surrounded by bentonite blocks in crystalline rock at the Grimsel Test Site. Saturation of the clay occurred via natural inflow of groundwater from the rock. The heat output was regulated to 100 °C at the heater surface. Operations started in 1996, dismantling of the 1st heater section was carried out in 2002 and the remaining section was replugged. The 2nd heater section was dismantled in 2015 and since then an extensive investigation programme has been conducted (termed FEBEX-DP). A significant part of this programme has been focussed on corrosion of iron and other metals as well as interactions between iron and the FEBEX bentonite.

This report synthesises the corrosion-related work within FEBEX-DP, which includes contributions from BGR, CIEMAT, Nagra, Obayashi, SKB, University of Bern and University of Bristol. The majority of the studied samples included carbon steel based materials, such as the heater, the liner and, to a lesser extent, some sensors. In addition, metal coupons consisting of carbon and stainless steel, copper and titanium materials were analysed. In general, the findings yield a consistent picture. In particular, they have helped to improve the understanding regarding carbon steel corrosion and its impact on the bentonite buffer in a repository-type setting.

From the analysis of the corrosion data it can be deduced that redox conditions were variable, thus passing from oxidizing to reducing in the tunnel. However, oxidizing conditions had the largest imprint on corrosion features, in particular in the central part of the tunnel, i.e. in the zones close to the heater. This is likely explained by continued air movement through the concrete plug, gas/water sampling pipes or cable ducts. Gas monitoring data (documented in NAB 16-13) qualitatively support such prolonged air entry. Variable moisture and oxygen contents led to very heterogeneous corrosion patterns. Extensive corrosion with corrosion layers and surrounding halos in the clay were observed in "wet" zones, whereas "dry" zones often exhibited thinner corrosion layers and less visible effects of iron-bentonite interaction.

Analysis of copper and Cu-Ni alloy coupons placed close to the heater revealed moderate corrosion effects with general corrosion as the main corrosion mode. The total corrosion depth estimated from one sample was ~ 9 µm. For the Cu coupons, in some spots localised corrosion with maximum penetration lengths of 20 – 100 µm was observed. Cu-Ni alloys showed less corrosion than the unalloyed Cu samples. All corrosion features can be explained by aerobic conditions. No effects of anaerobic corrosion could be observed on these surfaces.

Analysis of coupons and one sensor consisting of stainless steel indicated only small corrosion effects. Almost no general corrosion had occurred, but some localised corrosion and, at one location, stress corrosion cracking could be witnessed. For the Titanium coupons, essentially no corrosion features were noted, both for welded and unwelded samples.

The largest dataset was obtained for the corrosion of carbon steel components and their interaction with the surrounding bentonite. General corrosion was found to be the main corrosion mode. The derived corrosion depths of the heater and liner surfaces were about 110 – 190 µm. The predominant identified corrosion products were Fe(III) oxides (mainly goethite, but also hematite, lepidocrocite, maghemite). Chloride accumulation at the heater led to the formation of Cl-bearing Fe(III) oxyhydroxide. Besides Fe(III) oxides, newly formed magnetite and siderite were identified, highlighting that conditions were partially anaerobic. The bentonite clay contacting iron surfaces was enriched in Fe, but the extent of the Fe front into the clay was variable, in the range of 0 – 40 mm, and influenced by the variable moisture conditions. The

main fraction of enriched Fe in the clay consisted of Fe(III) oxides (mainly goethite), manifested by the reddish halo contacting the corrosion layer. The clay adjacent to this Fe(III)-enriched zone was still slightly enriched in Fe, displaying a higher Fe(II)/Fe(III) ratio. This zone, recognisable by the blueish-greenish colour, may extend to thicknesses of up to 200 mm. A phenomenological model was proposed to explain the observed pattern.

Alterations of the clay at the steel contact were minor. Increase of Mg towards the heater was noted, which was however not systematic and appeared not to be related to corrosion but rather to the effect of temperature. The dissolution of some SiO₂ and formation of minor Mg-rich smectite (saponite) close to the heater could be detected. The latter may be partly related to the increase in Mg.

Table of Contents

Authors	I
Abstract	III
Table of Contents	V
List of Tables	VII
List of Figures	IX
1 Introduction	1
1.1 The FEBEX Project	1
1.2 Test configuration during FEBEX I	2
1.3 Dismantling of Heater 1 and test configuration afterwards (FEBEX II)	3
1.4 Concept of the dismantling of Heater 2	4
1.5 Scope of corrosion-related studies in FEBEX-DP	5
1.6 Contents of report	6
2 Sampling	7
2.1 Metal components	8
2.1.1 Heater/liner sampling	8
2.2 Corrosion probe sampling	9
2.3 Sensor sampling	11
2.4 Interface sampling	12
3 Summary of dismantling observations and distribution of water content and density	13
4 Analytical methods and results	15
4.1 Summary of methods/techniques	15
4.2 Corrosion study by Tecnalia	17
4.2.1 Sensors	18
4.2.2 Metal coupons	20
4.2.3 Liner	24
4.2.4 Heater	26
4.2.4 Summary of main findings	27
4.3 Metal corrosion analysis by Obayashi	29
4.3.1 Scope and objective	29
4.3.2 Corrosion study in laboratory	29
4.3.3 Corrosion study of FEBEX-DP sample	41
4.3.4 Discussion and conclusion	49
4.4 Fe-bentonite interface study of Uni Bern	52
4.4.1 Context and goals	52
4.4.2 Materials and methods	53

4.4.3	Results	58
4.4.4	Discussion.....	73
4.5	Fe-bentonite interface study of SKB	81
4.5.1	Introduction	81
4.5.2	Samples	81
4.5.3	Methods	84
4.5.4	Results and conclusions.....	84
4.5.5	Conclusions	87
4.6	Interface study of BGR.....	88
4.6.1	Introduction	88
4.6.2	Materials and methods.....	88
4.6.3	Results	92
4.6.4	Discussion.....	108
4.6.5	Conclusions	109
4.7	Fe-bentonite interface study of Ciemat	110
4.7.1	Introduction	110
4.7.2	Dismantling of the barrier and metal-bentonite interface sampling	110
4.7.3	Methods of analysis	113
4.7.4	Results	117
4.7.5	Summary and discussion	155
4.8	Study of the University of Bristol.....	158
4.8.1	Objectives	158
4.8.2	Materials and analytical methods	158
4.8.3	Results	174
4.8.4	Conclusions	187
5	Discussion	189
5.1	Findings from corrosion studies	189
5.1.1	Carbon steel materials	189
5.1.2	Other metals.....	192
5.2	Findings from iron-bentonite interaction studies.....	193
5.2.1	Behaviour of iron released from carbon steel.....	193
5.2.2	Other findings in the bentonite	195
5.3	Significance of results in relation to other studies.....	196
5.3.1	Comparison with similar types of in-situ studies	196
5.3.2	Links with geochemical and microbiological studies within FEBEX-DP	197
5.3.3	Comparison with corrosion study of FEBEX I	198
5.4	Implications for repository conditions.....	199
5.5	Open questions/recommendations for future projects	200
6	Conclusions	203
7	References	207

Appendix A: Summary of observations from dismantling (Nagra).....	A-1
Appendix B: Additional Analyses on FEBEX-DP Copper Coupons (TECNALIA).....	B-1
Appendix C: Additional Data from the Study by Uni Bern	C-1
Appendix D: Laboratory Sampling Logs of Samples for interface Studies (CIEMAT).....	D-1

List of Tables

Tab. 1:	Corrosion probe racks with their metal coupon specifics in Section 48.....	9
Tab. 2:	Samples analysed for corrosion and Fe-bentonite interaction by the different teams. Sections, sample type and methods.	16
Tab. 3:	Description of samples analysed by Tecnalia (sample codes according to NAB 16-11).	17
Tab. 4:	Minerals identified in the different FEBEX samples (total raw material and coloured aggregates) using XRD.....	67
Tab. 5:	Set of components used to fit the Mössbauer spectra and their possible attribution.....	69
Tab. 6:	Data relative on Fe redox speciation inferred from ⁵⁷ Fe Mössbauer spectrometry.	72
Tab. 7:	Chemical composition of the references.....	91
Tab. 8:	CEC data of the CEC references.....	91
Tab. 9:	Mineralogical composition of the ABM references.....	91
Tab. 10:	Chemical composition of samples taken from Section 36.....	93
Tab. 11:	Cation exchange data of samples taken from Section 36.	93
Tab. 12:	Mineralogical analysis of selected samples from Section 36.	94
Tab. 13:	Chemical composition of samples taken from Section 42a.	96
Tab. 14:	Mineralogical composition as determined by XRD Rietveld analysis of Section 42a.	97
Tab. 15:	CEC data of the samples taken from Section 42a.....	97
Tab. 16:	Chemical composition of samples taken from Section 54.....	99
Tab. 17:	CEC data of the samples taken from Section 54.	99
Tab. 18:	Mineralogical composition as determined by XRD Rietveld refinement.....	100
Tab. 19:	Chemical composition of the samples taken directly from the surface of the metal (liner).	105
Tab. 20:	Mineralogical composition as determined by Rietveld analysis. 0 means < 1 mass% but present.	106

Tab. 21:	CEC data of the E-samples taken directly from the metal surface.	108
Tab. 22:	Bentonite samples studied by CIEMAT for the characterisation of the metal/bentonite interface.	112
Tab. 23:	Position and temperature of the metal/bentonite interfaces studied by CIEMAT for the characterisation of the metal/bentonite interface.	113
Tab. 24:	Dry density, water content and saturation degree determined for the samples studied in this work.....	118
Tab. 25:	Total intruded porosity and pore size distributions measured for bentonite samples collected at the interfaces with metallic elements.....	118
Tab. 26:	Total intruded porosity profiles measured in sample BMD-45-2 and BB-42-5.	121
Tab. 27:	BET- Specific Surface Area values measured in bentonite samples from the FEBEX <i>in-situ</i> test.	122
Tab. 28:	Semi-quantitative XRD analysis performed in the samples studied.....	123
Tab. 29:	EDS analyses of globular Fe oxides shown in Fig. 112 and Fig. 113 (b) and (c).....	131
Tab. 30:	EDS-TEM analysis of the illite particle shown in Fig. 115.....	133
Tab. 31:	EDS -TEM analysis of the maghemite particle shown in Fig. 116.	133
Tab. 32:	EDS analysis of the montmorillonite particle shown in Fig. 118.....	135
Tab. 33:	EDS analysis of the chlorite particle shown in Fig. 119.....	136
Tab. 34:	EDS analysis of the aragonite particle shown in Fig. 120.	137
Tab. 35:	EDS analysis corresponding to Mg-rich phase shown in Fig. 121.....	137
Tab. 36:	Cation exchange capacity (CEC) determined with Cu-triethylenetetramine in samples corresponding to the metal/bentonite interfaces.	140
Tab. 37:	CEC profiles along the studied samples.	140
Tab. 38:	Distribution of exchangeable cations in the studied samples (cmol(+)/kg).....	143
Tab. 39:	Exchangeable Fe measured after its displacement by CsNO ₃ 0.5N method.	144
Tab. 40:	Distribution profiles of exchangeable cations along the studied samples.	144
Tab. 41:	Soluble cations determined in aqueous extracts (S:L 1:4).....	146
Tab. 42:	Soluble anions determined in aqueous extracts (S:L 1:4).....	147
Tab. 43:	Distribution profiles of soluble cations along the studied samples.....	149
Tab. 44:	Distribution profiles of soluble anions along the studied samples.	150
Tab. 45:	Extracted Fe from amorphous Fe oxides in the studied metal/bentonite interfaces according to the Dithionite-Citrate-Bicarbonate (CBD) method.	152
Tab. 46:	Citrate-extractable Fe in the studied metal/bentonite interfaces using a solution of citric acid 0.3N as extractant.	153
Tab. 47:	Total Fe content measured in the bentonite samples studied by Total Reflection X-Ray Fluorescence Spectroscopy (TR-XRF).....	154

Tab. 48:	Distribution of total Fe content measured in the studied samples (wt%): in the exchange complex, sorption sites and precipitated as amorphous iron oxides.....	155
Tab. 49:	Parameters extensometer samples (Hadi 2016).....	159
Tab. 50:	BM-B-41-1 sample data collection.....	168
Tab. 51:	List of samples studied by the University of Bristol.	168
Tab. 52:	Main and accessory minerals in the FEBEX-DP samples.	177
Tab. 53:	Properties metallic coupon sample, M-S-48-1 (Hadi & Wersin 2015).	178
Tab. 54:	Dimensions and weight coupons belonging to the Rack 1A.	180
Tab. 55:	Semi-quantitative analyses of Coupons 1A1-1A5 from Fig. 27 – 31.....	185
Tab. 56:	Fe phases identified on carbon steel surfaces and in Fe/clay interface zone.	190
Tab. 57:	Calculated amounts of O ₂ and Fe in a 1 m long section comprising the heater and the liner (see text).....	192

List of Figures

Fig. 1:	Overall layout of FEBEX " <i>in-situ</i> " test (left) and "mock-up" test (right).	1
Fig. 2:	General layout of the FEBEX " <i>in-situ</i> " test (FEBEX I configuration).....	2
Fig. 3:	Status of the FEBEX " <i>In-situ</i> " test after the partial dismantling (FEBEX II configuration).	4
Fig. 4:	Extensometer type SH-SD1-01 surrounded by bentonite close to the steel liner (upper left) after dismantling of Heater 1 (from Madina & Azkarate 2004).....	6
Fig. 5:	Sampling layout (from Garcia-Siñeriz et al. 2016, NAB 16-11).....	7
Fig. 6:	Cut of the heater at the AITEMIN workshops (left) and a piece of a liner cut onsite from dismantling Section 45 (right).....	9
Fig. 7:	Host block with the racks 1A (left) and 2A (right).....	10
Fig. 8:	Left: A single Ti coupon of Rack 3A surfacing from the host block upon digging (yellow arrow). Two single Teflon screws can also be observed (red arrow). Right: A single Ti coupon of Rack 3A surfacing out the hole of the liner (yellow arrow).	10
Fig. 9:	Rack 4A (copper coupons, left) and retrieved pieces from block 3A (titanium coupons, right).....	11
Fig. 10:	Location of corrosion and Fe/clay interface samples.	12
Fig. 11:	Water content distribution in a vertical longitudinal section (radii A-D).	14
Fig. 12:	Dry density distribution in a vertical longitudinal section (radii A-D).....	14
Fig. 13:	Degree of saturation distribution in a vertical longitudinal section (radii A-D) (inexact values because of solid specific weight and water density uncertainties).	14

Fig. 14:	Upper: Photo of sensor SHSD2-01 and surrounding bentonite. Lower left: Detail of sensor end close to the liner. Lower right: Detail of sensor end close to the rock.	19
Fig. 15:	XRD pattern of corrosion products on surface of nut (upper right) located close to the liner.	20
Fig. 16:	Photographs of Rack A2 (left) and three faces of coupon 2A2.	21
Fig. 17:	Raman spectrum from corrosion products located on a pit of sample 2A2.	21
Fig. 18:	Photographs showing Cu alloy coupon (ref. 4A2) and details of the corroded surface.	22
Fig. 19:	Optical micrograph of section of copper alloy ref. 4A1.	23
Fig. 20:	Example of pit analyses at 0 mm depth from coupon 4A1.	24
Fig. 21:	Liner sample ML45-2, external surface; right: close-up view.	25
Fig. 22:	XRD pattern of sample ML45-2 (see marked rectangles in photo upper right), showing the presence of magnetite, hematite and siderite.	25
Fig. 23:	Heater after transport to AITEMIN facility. Close-up photos showing corrosion features (right).	26
Fig. 24:	XRD pattern of sample MH-02-F9C (see Madina 2016 for details).	27
Fig. 25:	Detail of B-B51-8 sample.	29
Fig. 26:	Detail of accelerated corrosion lab-test method.	30
Fig. 27:	Initial conditions of liner and heater in FEBEX experiment (Enresa 1998).	30
Fig. 28:	Image of a white X-ray measurement.	31
Fig. 29:	Corrosion situation observed by non-destructive CT 3D image.	31
Fig. 30:	Remaining voxel number of carbon steel wire after accelerated corrosion test, small diamonds are actual measurements.	32
Fig. 31:	Cut image of sample after non-destructive CT-XRD.	32
Fig. 32:	SEM-EDX image of anode-side metal corrosion (3 and 7 days).	33
Fig. 33:	Raman spectroscopy result of metal corrosion (3 days).	34
Fig. 34:	Raman spectroscopy results of metal corrosion (7 days sample).	35
Fig. 35:	Image of corrosion mechanism (3 and 7 days).	36
Fig. 36:	XRD analysis point and non-destructive XRD result.	37
Fig. 37:	Observation area conducted by ToF-SIMS.	38
Fig. 38:	Elemental map 3 days after electro-chemical test conducted by ToF-SIMS.	39
Fig. 39:	Elemental map 7 days after electro-chemical test conducted by ToF-SIMS.	40
Fig. 40:	Line graph result of ToF-SIMS for 3 and 7 days.	41
Fig. 41:	Sampling point of M-S-35-1.	41
Fig. 42:	Sample description of M-S-35-1.	42
Fig. 43:	Sample preparation of M-S-35-1.	42
Fig. 44:	Sampling point of BM-C-35-1.	43

Fig. 45:	Sample description of BM-C-35-1.	43
Fig. 46:	Sample preparation of BM-C-35-1.	44
Fig. 47:	Result of electron microscope for sample M-S-35-1.	44
Fig. 48:	Visualisation of corrosion mechanism for sample M-S-35-1.	45
Fig. 49:	Analysis point for sample BM-C-35-1.	45
Fig. 50:	SEM image of sample BM-C-35-1.	46
Fig. 51:	EDX surface analysis image of sample BM-C-35-1.	46
Fig. 52:	Distribution image of metal corrosion products.	47
Fig. 53:	Analysis points of Raman spectroscopy.	48
Fig. 54:	Results of Raman spectroscopy.	49
Fig. 55:	Proposed corrosion mechanism in the engineered barrier.	50
Fig. 56:	Cross-section image of Kunigel-V1 and carbon metal after corrosion test.	51
Fig. 57:	Picture at top of the fissurometer box after partial removal of bentonite layer 45 in FEBEX-DP project.	51
Fig. 58:	Sampling of corrosion features observed in FEBEX DP experiments, here located at the interface between the liner and the bentonite blocks of the layer 62.	52
Fig. 59:	(Left) 6 contiguous polished surfaces of a cross section of block BM-B-41-1 and (right) one polished section of block BM-B-41-2.	53
Fig. 60:	Powder sampling steps in the anaerobic chamber, (upper) original contact with the steel liner prior (a) and after (b) scrapping off the preserved contact area, (bottom) progression of the slicing of the block.	54
Fig. 61:	Schematic of the method for producing large-scale elemental mappings and chemical profiles.	55
Fig. 62:	(left) 2 polished block from block BM-B-41-1 and (right) colour aggregates that were collected in the raw material and powdered.	57
Fig. 63:	"Al-normalized" chemical profiles of major elements Si, Fe and Mg in block BM-B-41-1 from Section 62.	59
Fig. 64:	"Al-normalized" chemical profiles of minor elements Ca, Na, K and S in block BM-B-41-1 from Section 62.	60
Fig. 65:	"Al-normalized" chemical profiles of major elements Si, Mg and Fe in block BM-B-41-1 (long profile, ~ 220 mm) and block BM-B-41-2 (short profile, ~ 40 mm) from Section 62.	61
Fig. 66:	SEM pictures of some ferruginous minerals found in the FEBEX matrix. Letters indicate spots where Raman spectroscopy was performed (spectra shown below).	62
Fig. 67:	Raman spectra collected at spots indicated in Fig. 66 (others can be found in Fig. 4, Appendix C).	63
Fig. 68:	(Upper) SEM pictures collected close to the interface between the FEBEX bentonite block and the steel liner.	64
Fig. 69:	Raman spectra collected at spots indicated in Fig. 64.	65

Fig. 70:	Diffraction patterns of the various coloured aggregates isolated from FEBEX raw bentonite and the bulk raw material.....	66
Fig. 71:	Diffraction patterns of a series of powdered samples from block BM-B-41-1 (domed) and of the raw material (undomed).	68
Fig. 72:	Room temperature and 77K Mössbauer spectra of the raw FEBEX material and samples G30 and B20 from block BM-B-41-1.	70
Fig. 73:	Room temperature and 77K Mössbauer spectra of the raw FEBEX material and a series of 2 samples from block BM-B-41-1.	71
Fig. 74:	Chemical profile of Fe perpendicular to the interface (here normalized by the Al atomic proportions) in block BM-B-41-1.	74
Fig. 75:	Coloured corrosion halos observed around various steel components retrieved upon dismantling of the FEBEX-DP experiment.	77
Fig. 76:	Proposed Fe diffusion mechanism at the Fe-bentonite interface.	79
Fig. 77:	The received sample BM-S-42-4.	82
Fig. 78:	The bentonite-iron contact zone in the received sample BM-2-42-4.	83
Fig. 79:	X-ray diffraction pattern of samples from the following distances from the iron surface in the BM-2-42-4 sample (from above): 50 – 70, 25 – 50, 10 – 25, 0 – 10, 0 – 1 mm.	85
Fig. 80:	X-ray fluorescence data (in wt%) of Fe ₂ O ₃ , MgO, CaO and Na ₂ O as a function of the distance from the corroding iron (mm).	85
Fig. 81:	X-ray fluorescence data (in wt%) of SO ₃ and Cl as a function of the distance from the corroding iron (mm).	86
Fig. 82:	Cation exchange capacity of the bentonite as a function of the distance from the corroding iron (mm).	87
Fig. 83:	Sample location and sampling of FEBEX Section 36.	92
Fig. 84:	STA mass spectrometer curves of two samples taken from Section 36.	94
Fig. 85:	IR spectra of two samples taken from Section 36 (compared with the reference material).	95
Fig. 86:	Sample location and sampling of FEBEX Section 42a.	96
Fig. 87:	Sample location and sampling of FEBEX Section 54.	98
Fig. 88:	XRD powder pattern of selected samples of Section 54 (samples BM-S-54-5B-1N(H) were taken at the same position as BM-S-54-5B-1 from which not enough material was left for XRD Rietveld analysis).	100
Fig. 89:	XRD texture slides of selected samples of Section 54 (black: air dried, red: ethylene glycol treated).	101
Fig. 90:	XRD texture slides, black: REF, red: BM-S-54-1NH.	102
Fig. 91:	STA curves of selected samples taken from Section 54.	102
Fig. 92:	IR spectra of the sample with the largest MgO increase.	103
Fig. 93:	SEM images of the contact surface towards the heater.	104
Fig. 94:	Samples taken directly from or at the liner.	105

Fig. 95:	STA curves of the E-samples taken directly from the metal surface.....	107
Fig. 96:	IR spectra of the E-samples taken directly from the metal surface.	107
Fig. 97:	Position of the bentonite samples studied by CIEMAT in the FEBEX <i>in-situ</i> experiment.	111
Fig. 98:	RH-controlled room for the storage of samples.....	112
Fig. 99:	Pore size distributions measured for samples collected in the vicinity of: A) heater (BMS-54-7) and liner (BMD-45-2 and BMD-52-2); B) cable cap and C) saturated areas (BS-37-1-dummy and BC-47-10-granite).....	120
Fig. 100:	Pore size distributions measured along sample BMD-45-2.....	121
Fig. 101:	X-ray diffraction patterns of oriented aggregates prepared for sample BM-S-54-7: A) air-dried, E) ethylene-glycol solvated and C) heated to 550 °C.....	125
Fig. 102:	X-ray diffraction patterns of oriented aggregates prepared for sample BMD-52-2: A) air-dried, E) ethylene-glycol solvated and C) heated to 550 °C.....	125
Fig. 103:	X-ray diffraction patterns of oriented aggregates prepared for sample BMD-42-5: A) air-dried, E) ethylene glycol solvated and C) heated to 550 °C.....	125
Fig. 104:	X-ray diffraction patterns of oriented aggregates prepared for sample BC-47-10: A) air-dried, E) ethylene-glycol solvated and C) heated to 550 °C.....	126
Fig. 105:	X-ray diffraction patterns of air-dried oriented aggregates for samples: BMS-54-7, BMD-52-2, BB-42-5 and BC-47-10.....	126
Fig. 106:	X-ray diffraction patterns of oriented aggregates glycolated with ethylene-glycol.	127
Fig. 107:	XRD patterns of oriented aggregates heated to 550 °C.....	127
Fig. 108	(Left) Back-scattered cross-section SEM micrograph of the heater/bentonite interface in sample BM-S-54-7, (right) EDS line profile analysis corresponding to Fe (%wt.).	128
Fig. 109:	EDS line profile analysis corresponding to Fe (left) and Mg (right) performed in the heater/bentonite interface in sample BM-S-54-7.	128
Fig. 110:	SEM micrograph of the iron oxide layer found in sample B-B-42-5 (bentonite in contact with the front lid of the heater) and in sample BM-S-54-7 (bentonite in contact with the back lid of the heater).	129
Fig. 111:	(Left) Egg-like structure found in the oxide layer of sample BM-D-45-2; (right) EDS analysis of the outer shell.....	130
Fig. 112:	Precipitation of carbonates (calcite, siderite or ankerite) in sample BM-D-45-2 (liner).	130
Fig. 113:	Micrometric globular iron oxides found in samples in contact with the cable cap: (a) and (b) BM-C-42-1 and the liner (c) B-B-42-5 and (d) M-L-45-3.	131
Fig. 114:	Cross-section SEM micrograph of the fissurometer/bentonite interface in sample B-C-47-10, (right) EDS line profile analysis corresponding to Fe (%wt.).	132
Fig. 115:	(Left) Transmission electron micrograph of a clay particle in sample B-C-47-10, (right) Ring SAED pattern from an illite domain.....	132

Fig. 116:	(Left) Transmission electron micrograph of an iron oxide particle found in sample B-C-47-10, (right) Spot SAED pattern assigned to maghemite.	133
Fig. 117:	(Left) TEM micrograph of a Fe oxide particle found in sample B-C-47-10, (right) corresponding SAED pattern assigned to Ferrihydrite.	134
Fig. 118:	(Left) Transmission electron micrograph of a clay particle sampled at the contact with the heater, (right) Ring SAED pattern from the montmorillonite particle.	134
Fig. 119:	(Left) Transmission electron micrograph of a chlorite particle in sample BM-S-54-7, (right) corresponding ring SAED pattern.	135
Fig. 120:	(Left) Transmission electron micrograph of an aragonite particle in sample BM-S-54-7, (right) Spot SAED pattern from the aragonite particle (see also Tab. 34).	136
Fig. 121:	Transmission Electron micrograph and SAED pattern of a Mg-chabazite crystal found in sample BM-S-54-7, at the contact between bentonite and the heater.	137
Fig. 122:	FTIR spectra in the 950 – 750 cm ⁻¹ region corresponding to heater/bentonite and liner/bentonite interfaces.	138
Fig. 123:	FTIR spectra in the 950 – 750 cm ⁻¹ region for saturated bentonite samples.	139
Fig. 124:	FTIR spectra in the 950 – 750 cm ⁻¹ region obtained for the metal/bentonite interfaces in samples: FEBEX natural, BM-S-54-7, BMD-45-2, BMD-52-2 (heater/liner) and B-C-47-10 (fissurometer close to granite).	139
Fig. 125:	Distribution of exchangeable cations as a function of the distance to the heater.	143
Fig. 126:	Distribution of soluble cations as a function of the distance to the heater.	147
Fig. 127:	Distribution of soluble anions as a function of the distance to the heater.	148
Fig. 128:	Bentonite samples embedded in steel Shelby tubes (Hadi 2016).	159
Fig. 129:	Extensometer sample positions (Hadi 2016).	160
Fig. 130:	Position of the sensor SH-SD2-03, slice/layer 24 (NAB 16-11).	161
Fig. 131:	Sampling Section 54, bentonite 24 slice (NAB 16-11).	162
Fig. 132:	Sampling Section 54, bentonite slice 24 Heater No. 2 (NAB 16-11).	163
Fig. 133:	Layout of sampling in Heater No. 2 (NAB 16-11)	163
Fig. 134:	Location of corrosion coupon, M-S-48-1, in sampling Section 48 (Bárcena & García-Siñeriz 2015a).	164
Fig. 135:	M-S-48-1, metallic coupon or corroded probe (Nagra 2016).	165
Fig. 136:	Location of sample BM-B-41-1 (NAB 16-11).	166
Fig. 137:	Sample BM-B-41-1. Detail of the aureoles formed as a consequence of corrosion close to the liner.	167
Fig. 138:	Sample BM-B-41-1.	167
Fig. 139:	External appearance of the samples retrieved in the vicinity of extensometer SH-SD2-03.	175
Fig. 140:	External appearance of sample BM-B-41-1.	175

Fig. 141:	XRD-Patterns of random powder samples of bentonite samples from FEBEX-DP (Sm: Smectite, Total Phy: Total Phyllosilicates, Qz: Quartz, Cc: Calcite).....	176
Fig. 142:	XRD patterns of oriented aggregates bentonite samples from FEBEX-DP. (a) BM-B-41-1, (b) M-S-48-1, (c) S-S-54-15-A, (d) S-S-54-15-B (EG: Ethylene Glycol, AD: Air Dried).....	177
Fig. 143:	XRD patterns of oriented aggregates bentonite samples from FEBEX-DP. (d) S-S-54-15-C, (e) S-S-54-15-D, (f) S-S-54-15-E (EG: Ethylene Glycol, AD: Air-Dried).	178
Fig. 144:	Outline appearance of the corrosion coupon.	179
Fig. 145:	Appearance of the Rack 1A on reception.	179
Fig. 146:	Photographs of corrosion on the coupon 1A1 (base 1).....	180
Fig. 147:	Photographs of corrosion on the coupon 1A2 (base 2).....	181
Fig. 148:	Photographs of corrosion on the coupon 1A3 (EBW).....	181
Fig. 149:	Photographs of corrosion on the coupon 1A4 (PAW).....	182
Fig. 150:	Photographs of corrosion on the coupon 1A5 (MAGW).....	182
Fig. 151:	Micrograph of Coupon 1A1 (base 1) surface, and its corresponding EDX spectrum.....	183
Fig. 152:	Micrograph of Coupon 1A2 (base 2) surface, and its corresponding EDX spectrum.....	183
Fig. 153:	Micrograph of Coupon 1A3 (EBW) surface, and its corresponding EDX spectrum. Cracking is apparent.....	184
Fig. 154:	Micrograph of Coupon 1A4 (PAW) surface, and its corresponding EDX spectrum.....	184
Fig. 155:	Micrograph of Coupon 1A5 (MAGW) surface, and its corresponding EDX spectrum. Cracking is apparent.....	184
Fig. 156:	Optical micrograph of corrosion coupon showing the location from where the Raman spectrum was collected, and Raman surface spectrum.....	185
Fig. 157:	Optical micrograph of corrosion coupon showing the location from where the Raman spectrum was collected, and Raman surface spectrum.....	186
Fig. 158:	Optical micrograph of corrosion coupon showing the location from where the Raman spectrum was collected, and the Raman surface spectrum.....	186
Fig. 159	Schematic view of the different compartment between carbon-based steels and the bentonite clay (not to scale).	189
Fig. 160:	Sketch showing layered structure of the Fe/clay interface area (not to scale).....	193
Fig. 161:	Fe profiles perpendicular to liner in Section 41, in block BM-B-41-1 (EDX and XRF) and BM-B-41-2 (EDX).....	194
Fig. 162:	Evolution of O ₂ (left) and H ₂ (right) based on gas measurements (Fernández & Giroud 2017).	198

1 Introduction

1.1 The FEBEX Project

FEBEX (Full-scale Engineered Barrier Experiment in Crystalline Host Rock) is a research and demonstration project that was initiated by Enresa (Spain).

The aim of the project is to study the behaviour of near-field components in a repository for high-level radioactive waste in granite formations. The main objectives of the project may be grouped in two areas:

- a) Demonstration of the feasibility of constructing the engineered barrier system in a horizontal configuration according to the Spanish concept for deep geological storage (AGP), and analysis of the technical problems to be solved for this type of disposal method
- b) Better understanding of the thermo-hydro-mechanical (THM) and thermo-hydro-geochemical (THG) processes in the near field, and development and validation of the modelling tools required for interpretation and prediction of the evolution of such processes

The project consists of two large-scale tests (see Fig. 1) – "*in situ*" and "mock-up" (the latter is managed by CIEMAT in Spain) –, a series of laboratory tests, and THM and THG modelling tasks.

The full-scale heating test ("*in-situ*" test), to which this document refers, was performed at the Grimsel underground laboratory in Switzerland, also known as Grimsel Test Site (GTS) or Felslabor Grimsel (FLG in German). A complete description of the FEBEX project objectives and test program may be found in the "FEBEX Full-scale Engineered Barriers Experiment in Crystalline Host Rock. PRE-OPERATIONAL STAGE SUMMARY REPORT" (Fuentes-Cantillana et al. 1998).

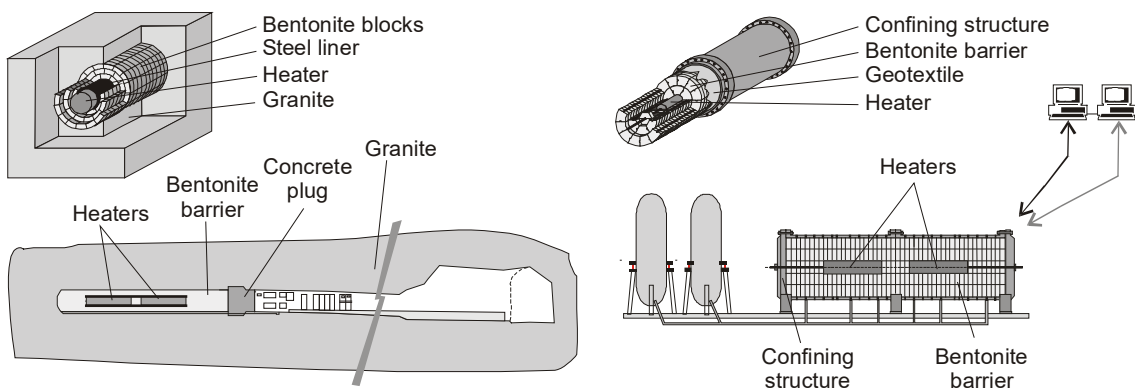


Fig. 1: Overall layout of FEBEX "*in-situ*" test (left) and "mock-up" test (right).

The project started in 1994, and has been supported by the European Commission through consecutive contracts, identified as FEBEX I (contract n° FI4W-CT-95-0006) for the period January 1996 to June 1999, and FEBEX II (contract n° FIKW-CT-2000-00016), from September 2000 to December 2004. Afterwards, NF-PRO took place from January 2005 to December 2007. Finally, in January 2008, the "*in-situ*" test was transferred from Enresa to a consortium composed by SKB (Sweden), POSIVA (Finland), CIEMAT (Spain), Nagra

(Switzerland) and more recently KAERI (South Korea), the FEBEXe Consortium, which supports it currently.

The "*in-situ*" experiment excavation was carried out in 2015 and new partners, interested in taking part in the planned sampling and analysis operations, have been incorporated in the Consortium (now called FEBEX-DP) for that purpose, namely US DOE (USA), OBAYASHI (Japan), RWM (UK), ANDRA (France), BGR (Germany) and SURAO (Check Republic).

1.2 Test configuration during FEBEX I

The installation of the "*in-situ*" test was carried out at the GTS. A horizontal drift with a diameter of 2.28 m was excavated in the Grimsel granodiorite especially for this experiment using a TBM (a tunnel boring machine). Two electrical heaters, of the same size and of a similar weight as the reference canisters, were placed in the axis of the drift. The gap between the heaters and the rock was backfilled with compacted bentonite blocks, up to a length of 17.40 m, this requiring a total 115'716 kg of bentonite. The backfilled area was sealed with a plain concrete plug placed into a recess excavated in the rock and having a length of 2.70 m and a volume of 17.8 m³. Fig. 2 shows the dimensions and layout of the test components schematically.

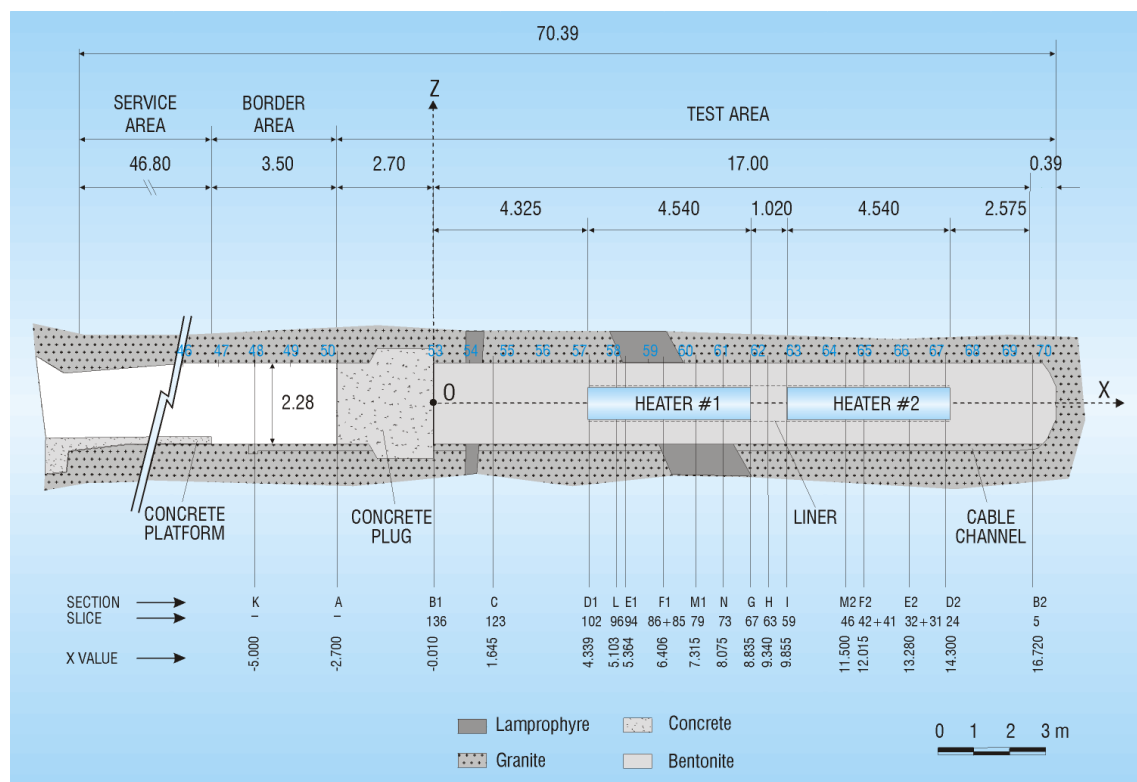


Fig. 2: General layout of the FEBEX "*in-situ*" test (FEBEX I configuration).

A total of 632 instruments were placed in the system along a number of instrumented sections, both in the bentonite buffer and in the host rock, to monitor relevant parameters such as temperature, humidity, total and pore pressure, displacements, ... etc. The instruments were of many different kinds and their characteristics and positions are fully described in the report

titled "FEBEX Full-scale Engineered Barriers Experiment in Crystalline Host Rock. FINAL DESIGN AND INSTALLATION OF THE IN-SITU TEST AT GRIMSEL" (Fuentes-Cantillana & García-Siñeriz 1998).

A Data Acquisition and Control System (DACS) located in the service area of the FEBEX drift collected the data provided by the instruments. This system recorded and stored information from the sensors and also controlled the power applied to the electrical heaters, in order to maintain a constant temperature at the heaters/bentonite interface. The DACS allowed the experiment to be run in an automated mode, with remote supervision from Madrid. Data stored at the local DACS were periodically downloaded in Madrid and used to build the experimental Master Data Base.

The construction of the concrete plug was completed in October 1996, and the heating operation started on 28. February 1997. A constant temperature of 100 °C was maintained at the heaters/bentonite interface, while the bentonite buffer has been slowly hydrating with the water naturally flowing from the rock. A complete report that includes both the installation of the test and the results gathered after two years of operation is given in "FEBEX full-scale engineered barriers experiment for a deep geological repository for high level radioactive waste in crystalline host rock FINAL REPORT" (Fuentes-Cantillana et al. 2000).

1.3 Dismantling of Heater 1 and test configuration afterwards (FEBEX II)

A partial dismantling of the FEBEX "*in-situ*" test was carried out during the summer of 2002, after 5 years of continuous heating. The operation included the demolition of the concrete plug, the removal of the section of the test corresponding to the first heater, and the sealing with a new shotcrete plug. A large number of samples from all types of materials were taken for analysis. A number of instruments were subsequently dismantled, as well as a few new ones installed. Accordingly, system design was adapted, and the physical layout was changed in order to ease the partial dismantling operation.

The buffer and all components were removed up to a distance of 2 metres from Heater 2 to minimise disturbance of the non-dismantled area. A dummy steel cylinder with a length of 1 m was inserted in the void left by Heater 1 in the centre of the buffer. Some new sensors were installed in that one additional metre of bentonite buffer.

Additional sensors were introduced in boreholes drilled in the buffer parallel to the drift. To simplify this operation, the new concrete plug was constructed in two phases: an initial temporary plug measuring just 1 m in length, which was built immediately after dismantling, and a second section to complete the plug length to the 3-m planned in the design of the experiment. Unlike FEBEX I, the new plug was a parallel plug, without a recess excavated in the rock, constructed by shotcreting.

The description of the partial dismantling operation is given in the report titled "Dismantling of the Heater 1 at the FEBEX "*in situ*" test. Description of operations" (Bárcena et al. 2003). The configuration of the test, after completing the partial dismantling operation and construction of the full plug length, is shown in Fig. 3.

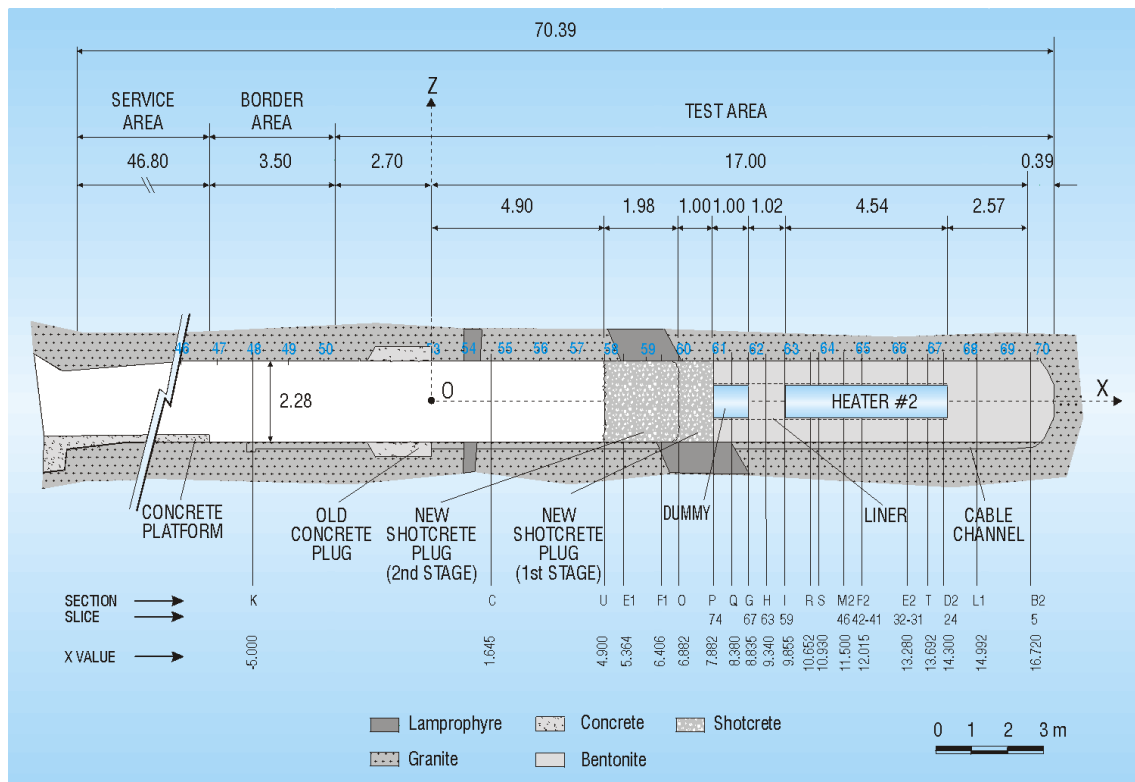


Fig. 3: Status of the FEBEX "In-situ" test after the partial dismantling (FEBEX II configuration).

A more complete report that describes the test from the conception up to two years of operation after the partial dismantling is given in the document titled "FEBEX Full-scale Engineered Barriers Experiment. UPDATED FINAL REPORT 1994 – 2004" (Huertas et al. 2006).

1.4 Concept of the dismantling of Heater 2

The objective of the second dismantling operation, carried out throughout 2015, was to dismantle all the remaining parts of the "in-situ" test, including Heater 2. This operation includes carrying out a complete sampling of the bentonite, rock, relevant interfaces, sensors, metallic components and tracers to allow the analysis of the barriers' condition after 18 years of heating and natural hydration.

Analytical results will be compared with data obtained from the partial dismantling (Huertas et al. 2006); the monitoring data (NAB 16-19) as well as with the results derived from modelling efforts (Lanyon & Gaus 2013). The results are expected to increase the current knowledge and confidence for the FEBEX-DP partners in bentonite performance with a focus on thermo-hydro-mechanical (THM) and thermo-hydro-chemical (THC) processes as well as on corrosion and microbial activity. The reporting of the laboratory analysis and dismantling results is expected to be complete by the end of 2017 with a final integrated report issued in end of 2017/early 2018.

All details about the planned dismantling operation and sampling program are given in the reference documents: "FEBEX-DP (GTS) Full Dismantling Test Plan" (Bárcena and García-

Siñeriz 2015a), "FEBEX-DP (GTS) Full Dismantling Sampling Plan" (Bárcena and García-Siñeriz 2015b) and its update (Rey et al. 2015).

All sample logs of the dismantling operation are documented in AN 15-578 Sample Log Book 34 to 62 FEBEX-DP (Kober 2015).

1.5 Scope of corrosion-related studies in FEBEX-DP

Many high-level waste repository concepts foresee the emplacement of spent fuel and/or vitrified high-level waste encapsulated in iron or copper canisters which are surrounded by compacted bentonite in a deep-seated host rock. The metal and the clay barrier are commonly denoted engineered barrier system (EBS) and are susceptible to deterioration processes. These include corrosion of the canisters and degradation of the clay barrier by heat emanating from decaying waste and by interaction with other components (metals, cement). Moreover, microbial activity may enhance both corrosion and degradation processes in the clay.

The FEBEX experiment offered the unique opportunity to study the corrosion and iron-clay interaction processes in a repository-like setting in detail. The overall objective was to gain an improved understanding of these processes in the light of long-term model predictions regarding repository safety.

The FEBEX experiment contained a variety of different metal components, including the heaters, the dummy, the perforated liner, small metal coupons, and various metal sensors. The largest mass fraction was made of carbon-based steel materials, the main component of heaters, dummy, liner, and many of the sensors. The inevitable corrosion of this iron material consumes molecular oxygen and water generating iron(III) oxide corrosion products (e.g. lepidocrocite, goethite, hematite). This process is enhanced at elevated temperature and dependent on the relative humidity and dissolved salt concentration. Iron corrosion continues to occur once O₂ present in the air-filled gaps and pores of the bentonite has been consumed. During this anaerobic phase hydrogen is produced by the cathode reaction and more reduced iron(III/II) oxides (magnetite, green rust) are formed. Depending on the chemical and microbiological conditions, also other corrosion products, such as siderite and/or iron sulphides may be formed. Corrosion reactions are thus very dependent on the environmental conditions, but, conversely, they also affect the contacting water and gas compositions. Moreover, iron(II) released from corrosion interacts with the surrounding clay and may alter the sealing properties of the bentonite (e.g. Wersin et al. 2007).

Corrosion and corrosion-related interaction processes with FEBEX bentonite were observed after dismantling Heater 1 (Madina & Azkarate 2004, Huertas et al. 2006). A somewhat unexpected observation was the reddish and greenish "halos" around some of the iron components (Fig. 4).



Fig. 4: Extensometer type SH-SD1-01 surrounded by bentonite close to the steel liner (upper left) after dismantling of Heater 1 (from Madina & Azkarate 2004).

The scope of the corrosion-related studies in FEBEX-DP was to build on the preliminary FEBEX I study and to investigate both corrosion and iron-bentonite interaction in more detail. The FEBEX-DP offered an unprecedented opportunity to get better insight into the long-term behaviour of iron corrosion processes in a near-field environment of a nuclear waste repository. Corrosion phenomena of different iron components were studied by Tecnalia, Obayashi and University of Bristol. The research teams of Uni Bern, SKB, BGR, CIEMAT, University of Bristol and Tecnalia investigated the interface area of the iron and the clay in different environments.

1.6 Contents of report

This report documents the findings of the corrosion-related studies. Most of these studies were focused on features and processes at the microscopic scale. However, larger-scale corrosion phenomena occurring at the dm-scale and beyond are also important to address, as was clear from the experience made in FEBEX I. Therefore, a special section (Chapter 3) is dedicated to the observations made during dismantling. In Chapter 4, the individual studies of the different research teams are presented. The overall results are then summarised and discussed in Chapter 5. Therein, the data is also compared with the findings in FEBEX I and the results from microbiological and gas/porewater studies. Some implications for repository conditions are discussed. Finally, the main conclusions from the corrosion-related studies are given in Chapter 6.

2 Sampling

The FEBEX-DP corrosion sampling was set up according to the requirements defined by the general FEBEX-DP Project Plan and the Objective outlined by the COMIC (Corrosion and MICrobiology) group (NAB 16-68), based on experiences from the partial dismantling (Enresa 2006). The major objectives were:

- What is the evolution of the corrosion on the various metals since the first dismantling, with additional time and increased saturation of the buffer?
- To what extent are microorganisms that may accelerate corrosion of canisters in the near-field either by hydrogen/electron scavenging or by production of sulphide and/or gas present in the FEBEX bentonite buffer?

These were approached by a twofold sampling strategy, with

- a) A pre-dismantling scoping definition of certain samples in specific dismantling sections and
- b) A raised awareness that eventual and unexpected corrosion features might occur during the excavation and that should be sampled by on-site decisions

According to the specifics of the various components (heater/liner, corrosion probes, sensors and interfaces) that could be affected by corrosion, a dedicated sampling strategy, procedure and protocol was defined for each section (NAB 15-14, NAB 15-15).

Sampling was designed to optimise visual inspection and various quantitative methods (e.g., SEM, XRD) and metallographic studies. The sampling layout is depicted in Fig. 5.

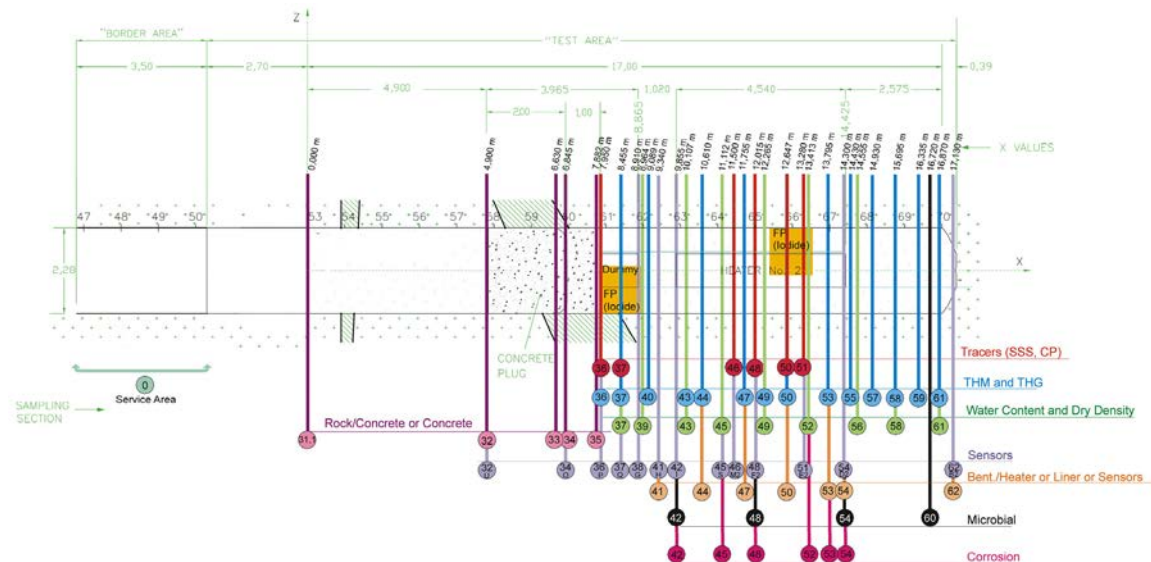


Fig. 5: Sampling layout (from Garcia-Siñeriz et al. 2016, NAB 16-11).

A limited description of the samples labelling code is given below. T-Y are the two initial letters for each sample codification:

T:B: Bentonite

C: Concrete

G: Granite

L: Lamprophyre

M: Metal

S: Sensor

BC: Interface Bentonite-Concrete

BG: Interface Bentonite- Granite

BL: Interface Bentonite- Lamprophyre

BM: Interface Bentonite-Metal

CG: Interface Concrete-Granite

CL: Interface Concrete- Lamprophyre

CM: Interface Concrete-Metal

GM: Interface Granite-Metal

LM: Interface Lamprophyre - Metal

Y:B: Block

C: Core

D: Dice (cube shape)

S: Any shape

For metal samples:

T: Liner

H: Heater

2.1 Metal components

2.1.1 Heater/liner sampling

Originally, for the dummy, the heater and the liner, the necessary metal samples were not planned beforehand nor was it foreseen for them to be cut on site. The idea had been to transport the samples to the designated laboratory or workshop. However, during the dismantling operation it was decided to perform liner and dummy sampling by flame cutting on site based on the experience gathered by the pre-laboratory tests (NAB 16-09); the heater though, was not sampled on site.

Immediate inspection of the liner and the heater on site revealed heater and liner in "dry" conditions with general corrosion features (NAB 16-11). After retrieval of the heater on June 4th, 2015 it was stored outside the FEBEX gallery, protected by a plastic cover, and transported to Spain (AITEMIN premises, Toledo) for further investigations and cutting (Fig. 6) in late

October 2015. Liner pieces were cut in the FEBEX service area from the 1 m-long dismantled liner section by flame cutting in extended pieces (avoiding heat influences), packed and shipped to the individual labs.



Fig. 6: Cut of the heater at the AITEMIN workshops (left) and a piece of a liner cut onsite from dismantling Section 45 (right).

2.2 Corrosion probe sampling

The experiment contained various metal corrosion probes (coupons) assembled in racks and emplaced in prefabricated holes filled with bentonite powder in dismantling Section 48 in bentonite layer 42 (Enresa 1998). The four corrosion probe racks, which were emplaced in two blocks in the vicinity of the liner, contained the following coupons (Tab. 1, Appendix Fig. S48-5):

Tab. 1: Corrosion probe racks with their metal coupon specifics in Section 48.

Suffix ^a: welded coupons (EBW: electron beam welding; PAW: plasma arc welding; MAG: metal active gas (welding); FCAW: flux cored arc welding).

Rack	Material	Type of coupon (and quantity)						Total quantity
1A	Carbon steel TStE355	Base (2)	EBW ^a (1)	PAW ^a (1)	MAG ^a (1)			5
2A	Stainless steel 316L	Base (2)	EBW ^a (1)	FCAW ^a (1)				4
3A	Titanium	TiGr2 (1)	TiGr7 (2)	TiGr12 (2)	Ti2EBW ^a (1)	Ti7EBW ^a (1)	Ti7PAW ^a (1)	8
4A	Copper	Cu 99 % (2)	Cu10Ni (2)	Cu30Ni (1)				5

Focus was given to the position of the block containing the coupon according to the test plan and to maintaining the block's integrity during dismantling. Originally, the idea was to use a sharp knife or a saw in order to extract the block by hand when possible. In case the block status did not allow the use of this method, only the coupon would be sampled by trying to keep the

adhered bentonite to the coupon surface, if any. If possible, at least 50 – 100 g of bentonite was to be sampled.

During dismantling (Fig. 7 to 9), the status of the coupons required an adjustment of the sampling strategy because the corrosion probes were affected by two different types of perturbation. On the one hand some of them were partially affected by the new pipes drilled during the partial dismantling in 2002. This disturbed two and broke one of the installed racks. Specifically Rack 3A (titanium) at the 5 o'clock position was affected by this drilling (Fig. 7, Fig. 8; NAB 15-68). On the other hand, it became clear that some of the coupons had been partially exposed during the time between the retrieval of the heater and the actual dismantling of Section 48 (25 days). Consequently, the coupons were exposed to the galleries' atmosphere due to ventilation through the perforated liner which was open, even though the void of the empty liner in the front was protected by installing a temporary lid and shifting this during progress of the dismantling (NAB 15-11/NAB 15-12).



Fig. 7: Host block with the racks 1A (left) and 2A (right).



Fig. 8: Left: A single Ti coupon of Rack 3A surfacing from the host block upon digging (yellow arrow). Two single Teflon screws can also be observed (red arrow). Right: A single Ti coupon of Rack 3A surfacing out the hole of the liner (yellow arrow).



Fig. 9: Rack 4A (copper coupons, left) and retrieved pieces from block 3A (titanium coupons, right).

2.3 Sensor sampling

If possible, sensor samples were marked in order to position their orientation and rotation. Care was taken to protect the sensor head and the cable ends.

Visual on-site inspection and description of sensors, seals and cables was performed taking note of corrosion fractures or mechanical damages, the potential of a flooded filter, etc. (NAB 15-11/20). The signals and functionality of in-situ sensors were checked before and after removal from the buffer. Samples were further labeled, packed and shipped to AITEMIN workshops for laboratory testing, apart from TDR (time domain reflectometry) sensors which were analysed on site only. TDR revealed no corrosion features apart from sensor WT-M2-09 where the copper electrodes showed corrosion-like stains. It was presumed that water had intruded inside the coating film and affected the TDR trace (NAB 15-21).

Generally, sensors were in better condition visually than the ones gathered during the first dismantling: less corrosion effects or mechanical damage except for the crack meter, which was not correctly sealed against the wall during installation and exhibited heavy localised corrosion (NAB 15-11/16-68). No obvious corrosion by bacteria was found this time, which could be related to a lower degree of voids left around the sensors in this part of the buffer (NAB 15-11).

Many sensors were tested and verified post-mortem in the lab as reported in NAB 15-20 or investigated in terms of corrosion effects (XRD/SEM and metallographic analysis, NAB 15-54) (Section 4.2).

2.4 Interface sampling

Interface samples, i.e., metal samples in contact with the rock, the buffer and the cement, were to be sampled intact, but this turned out not to be feasible in the field. Integrity of the intact contact was either not given initially or the dismantling activities loosened the interface. Only in a few cases, mostly in sections where no sampling had been foreseen, some metal pieces containing some adhered bentonite could be preserved (Sections 4.4, 4.5, 4.6, 4.7).

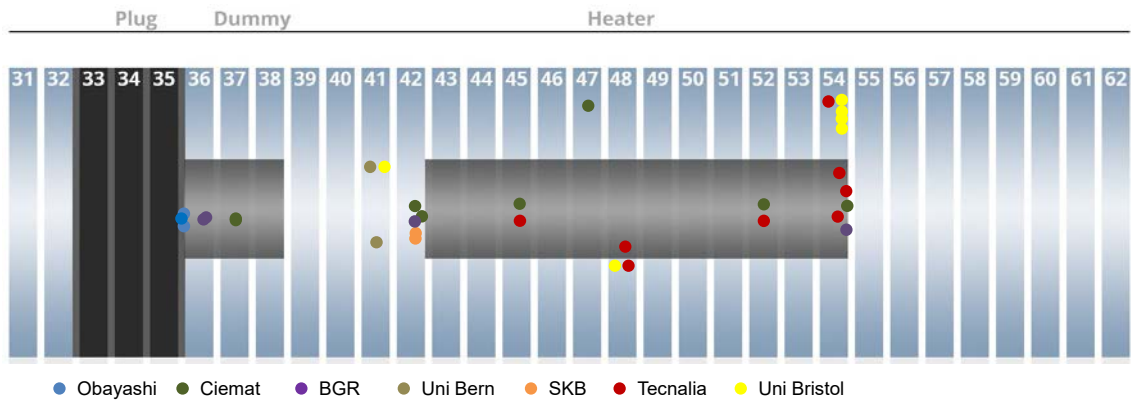


Fig. 10: Location of corrosion and Fe/clay interface samples.

In Fig. 10, the sections and the location of the samples studied by the different teams are displayed. It should be noted that sampling of interfaces was based on visual observations and not on statistics. Hence, the majority of samples was extracted from locations with visible corrosion effects. This aspect is shortly discussed in Section 5.2.

3 Summary of dismantling observations and distribution of water content and density

Selected observations of corrosion features during dismantling are compiled in Appendix A. Therein, a photographic documentation for a number of sections is presented. In the following, a short summary of the observed corrosion features is given.

Dummy Sections (36 – 38)

Various prominent corrosion features (e.g. halos around the liner and sensors) were observed in these sections which experienced a complex history. In particular, these were opened, refilled and re-instrumented in 2002. Samples from the perforated liner with adhered bentonite on the inner side, that had extruded through the holes, were provided to Obayashi and Ciemat. This clay material exhibited a reddish colour hinting at the presence of Fe(III) oxides. A sample at the outer liner-bentonite interface was provided to BGR.

Section 41

In this section, which contained the liner with no heater or dummy inside, an extensive halo exhibiting a black crust on the liner in contact with a reddish and greenish clay was observed in the upper part. This halo was sampled by Uni Bern. In contrast, the lower part, which was also sampled by Uni Bern did not show any corrosion signs around the liner.

Heater sections (42, 44, 46 – 48, 52, 54)

The clay protruding through the liner and adhering to the heater in its front part (Section 42) displayed a yellowish-brownish colour close to the metal contacts, suggesting the presence of Fe(III) oxides. These features were much less pronounced on the back side of the heater. Corrosion features were also observed in the filtered sections of gas pipes and around displacement sensors in the outer part of the tunnel. Corrosion halos were observed around the cable duct in the roof. The dismantled fissurometer located close to the tunnel wall displayed extensive corrosion and a large halo in the surrounding clay. The heater surface in Section 48 exhibited circular corrosion spots with a greening centre surrounded by yellow-brownish aggregates. In the same section, the racks holding the coupons, had been emplaced in a prefabricated hollow of a bentonite block. No visible corrosion features or discolouration of the clay which was powdery and dry, were observed. A displacement sensor which was extracted for corrosion analysis by TecNALIA displayed a prominent corrosion halo at its end close to the tunnel wall.

Water content, dry densities and degree of saturation

These parameters, which were determined for the entire FEBEX II configuration, are presented in detail in Villar et al. (2016). They yield a consistent pattern with lower water contents and higher dry densities in the areas closer to the heater (Fig. 11, Fig. 12). This results in lower saturation degrees (~ 80 %) close to the heater, progressing to full saturation towards the outer parts (Fig. 13).

These boundary conditions are important to keep in mind regarding the corrosion-related processes as further discussed in Chapter 5.

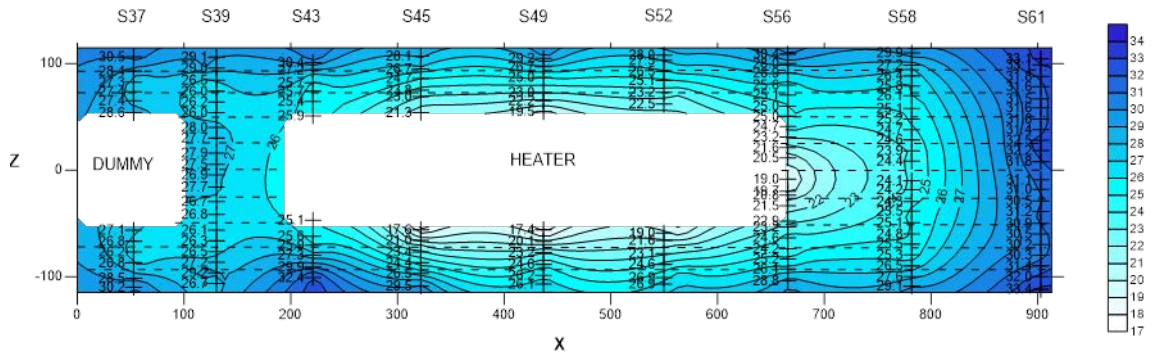


Fig. 11: Water content distribution in a vertical longitudinal section (radii A-D).
(From Villar et al. 2016, NAB 16-12)

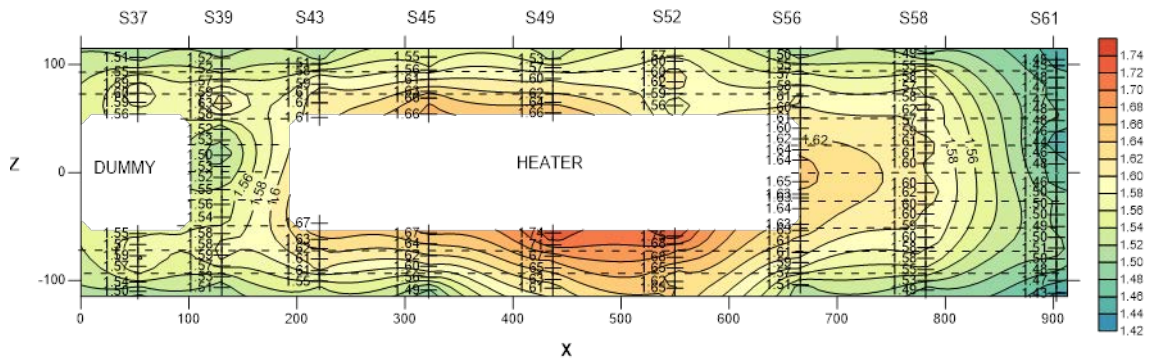


Fig. 12 Dry density distribution in a vertical longitudinal section (radii A-D).
(From Villar et al. 2016, NAB 16-12)

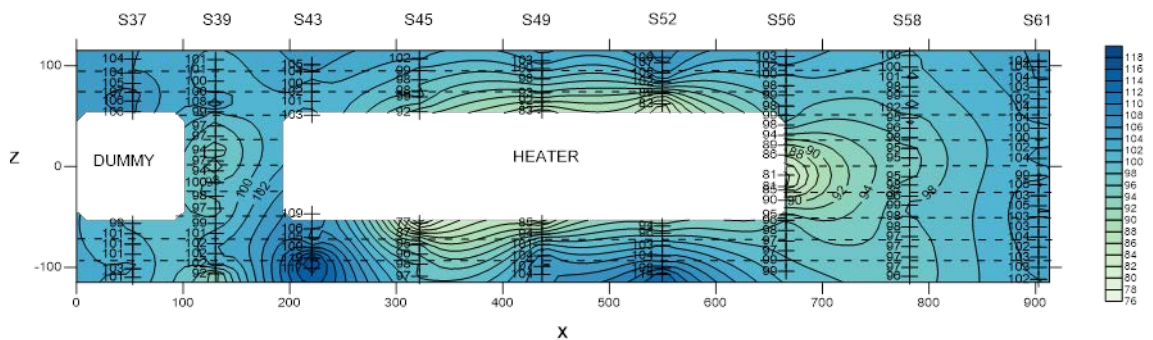


Fig. 13: Degree of saturation distribution in a vertical longitudinal section (radii A-D)
(inexact values because of solid specific weight and water density uncertainties).
(From Villar et al. 2016, NAB 16-12)

4 Analytical methods and results

4.1 Summary of methods/techniques

A variety of different samples was studied by the different research teams. Iron parts with or without the adjacent clay were sampled from the heater, liner, dummy and different sensors. The sample types and their location in the experiment (section) as well as the methods applied are listed in Tab. 2.

The methods used by the different teams for the different purposes are listed below. Besides, all samples were documented photographically.

- Optical microscopy/visual inspection; this method was applied for the corrosion study of Tecnia.
- Scanning Electron Microscopy (SEM) imaging (secondary electron or backscatter electron mode) of the metal surface was performed on metal surfaces by Tecnia, Obayashi and the University of Bristol (UoB). The same method was also used to study the interface of the metal with the clay by Obayashi and Uni Bern. The clay adjacent to the metal was studied by BGR and Ciemat.
- Scanning Electron Microscopy combined with Energy Dispersive X-ray analysis (SEM/EDX); this method was applied to obtain the chemical composition of corrosion products on the metal surface by Tecnia, University of Bristol and Obayashi. The elemental mapping of the clay at the interface was conducted by Ciemat and Uni Bern.
- High resolution Transmission Electron Microscopy (TEM) was applied on clay samples by Ciemat.
- X-Ray Diffractometry (XRD) was performed on corrosion products (Tecnia, University of Bristol) and on powdered clay samples to obtain information about the mineralogical composition (Ciemat, SKB, BGR, Uni Bern).
- X-Ray Fluorescence spectrometry (XRF) was applied on powdered materials including the Fe/clay interface and the adjacent clay material to obtain information about the elemental composition (BGR, SKB and Uni Bern).
- μ -Raman spectroscopy was applied by Obayashi, Uni Bern and Tecnia to identify corrosion products and certain phases of the original material.
- Fourier Transformed Infrared Spectrometry (FTIR) was applied to powdered samples of the metal/clay interface and the clay to obtain mineralogical information (Ciemat, BGR).
- Mössbauer spectrometry was carried out on samples of the metal/clay interface and the adjacent clay by Uni Bern to obtain information on the iron speciation and mineralogy and the Fe(II)/total Fe ratios. Cation Exchange Capacity (CEC) was determined on clay samples as a function of distance from the metal contact by BGR, SKB and Ciemat.
- Simultaneous Thermal Analysis (STA) was applied on clay samples to obtain information on the mineralogical and organic carbon composition by BGR.
- Bulk properties of the clay materials, such as water contents and density were determined by Ciemat and BGR.
- Surface area measurements by the BET method and analysis of pore distribution by mercury injection porosimetry (MIP) on clay samples were conducted by Ciemat.

- Obayashi further conducted an accelerated corrosion test on one sample which was subsequently analysed by Computer-Tomography coupled with x-ray diffraction (CT-XRD) and Time of Flight Secondary Ion Mass Spectrometry (ToF-SIMS).

Tab. 2: Samples analysed for corrosion and Fe-bentonite interaction by the different teams. Sections, sample type and methods.

Organisation	Section studied	Sample type	Methods
Tecnalia	54	Sensors	Visual, SEM/EDX, XRD, optical microsc.
	48	Coupons	Same as sensors, Raman spectrometry
	45, 52	Liner	Same as sensors
	54?	Heater	Same as sensors
Ciemat	42, 54	Clay (interf. Heater)	Bulk properties, SEM, TEM, XRD, FTIR, MIP, BET, wet chemistry on Fe speciation
	45, 52	Clay (interf. Liner)	Same
	37	Clay (betw. Liner and dummy)	Same
	47	Clay (interf. Sensor)	Same
Obayashi	35	Liner-clay interf.	SEM/EDX, μ -Raman, lab corrosion test, CT-XRD, ToF-SIMS
	35	Dummy	SEM/EDX, μ -Raman
BGR	36	Liner-clay interf.	XRF, XRD, FTIR, STA, CEC
	42	Liner-clay interf.	XRF, XRD, CEC
	54	Clay –heater	XRF, XRD, FTIR, STA, CEC, SEM
	E2-E8	Liner (corr. Products)	XRF, XRD, FTIR, STA, CEC
SKB	42	Clay (interf. Metals)	XRD, XRF, CEC
Uni Bern	41	Clay (interf. Liner)	SEM/EDX, Mössbauer, XRF, XRD, μ -Raman

The following Section 4.2 is a summary of the report written by Tecnalia (NAB 16-54). The other Sections 4.3 – 4.8 are individual contributions from the different teams.

4.2 Corrosion study by Tecnia

The corrosion study conducted by Tecnia is documented in detail in NAB 16-54 (Madina 2016). Here, we give a summary of this study focussing on the main findings related to the corrosion of the studied samples. The study on the leachates and microbiological characterisation of bentonite samples is not reported here.

The methods employed included:

- Visual examination of samples to identify corrosion features
- SEM/EDX of the metallic surfaces to determine the microstructure and chemical composition of the sampled sections
- XRD and, in some cases, Raman spectrometry on corrosion products to determine mineralogical composition of corrosion products
- Optical and SEM microscopy to analyse microstructure, morphology and extent of the corrosion-derived damage

An overview of the samples and the corresponding studies conducted is presented in Tab. 3.

Tab. 3: Description of samples analysed by Tecnia (sample codes according to NAB 16-11).

Sample Type	Sample Code	Sample Description/Studies Carried Out
Sensors	SHSD2-01 (S-S-54-14A)	Extensometer-type sensors; active element is protected by austenite alloy tube.
	SHSD2-02 (S-S-54-15A)	1. Visual examination on receipt. Identification of the sections to be studied. Dry cut is used in this first stage.
	SHSD2-03 (S-S-54-15)	2. These sections were studied in two ways: <ul style="list-style-type: none"> • SEM/EDS analysis on dry cut, non-embedded sections. The surface of the sections was examined in detail by scanning electron microscopy (SEM). Corrosion products and/or deposits on the samples were chemically analysed by Energy Dispersive X-ray Spectroscopy (EDX), using a microanalyser coupled to the SEM microscope. • The mineralogy of corrosion products was determined XRD. 3. Metallographic study: Metallographic probes were studied by optical and SEM microscopy in order to analyse the microstructure, morphology and extent of the corrosion-derived damage. 3-5 metallographic probes were prepared for each sensor/extensometer.
Coupons	2A M-S-48-2	Coupons of stainless steel (316L), Ti alloys and Cu alloys.
	3A M-S-48-3	1. Visual examination of the coupons on receipt.
	4A M-S-48-4	2. The analyses were done in the same way as for the sensors.
	BM-S-54-3	

Tab. 3: Cont.

Sample Type	Sample Code	Sample Description/Studies Carried Out
Liner	ML-45-1 ML-45-2 ML-45-3 ML-45-4	Perforated steel tube 970 mm in diameter and 15 mm thick. Visual examination of the 2 sections of the liner on receipt. Identification of the sections to be studied (dry cut).
	ML-52-1 ML-52-2 ML-52-3 ML-52-4	The analyses were done as for the sensors. 1 – 3 metallographic probes were prepared from each quarter of the liner.
Heater	MH-02-F9C MH-01-F3C MH-03-ET	Carbon steel cylinder with welded lids, wall thickness 100 mm. Visual examination of the heater. 3 sections were taken by dry cut (radial), two of them from the front (F): references MH-01-F3C and MH-02-F9C, and the third one from the end (E): (reference MH-03-ET. Where 3C means 3 o'clock position, 9C: 9 o'clock and T = top. The analyses were done as for the sensors. 2 – 3 metallographic probes were prepared from each of three sections.

4.2.1 Sensors

The stainless-steel tube devices surrounding three extensometers located in Section 54 were analysed. Visual inspection revealed similar corrosion features for the three devices. The largest corrosion was observed at end pieces which served for anchoring the sensors to the rock and liner, respectively (Fig. 14). Reddish-brown corrosion products were observed on carbon steel components at these ends, which were not observed in the central parts made of stainless steel. Mechanical damage was observed there but no localised corrosion features could be detected.

From SEM/EDX and XRD analyses the nature of corrosion products in the carbon steel components could be identified. EDX analyses confirmed that the reddish-brown corrosion products are predominantly constituted of Fe and O. A significant amount of sulphur was detected. Magnetite was identified as the main phase in a black oxide layer from a screw close to the rock. Another specimen consists of a nut situated close to the liner; this sample revealed the presence of magnetite and siderite (Fig. 15). It should be noted that XRD cannot identify non-crystalline iron oxyhydroxides, whose presence is probable.



Fig. 14: Upper: Photo of sensor SHSD2-01 and surrounding bentonite. Lower left: Detail of sensor end close to the liner. Lower right: Detail of sensor end close to the rock.

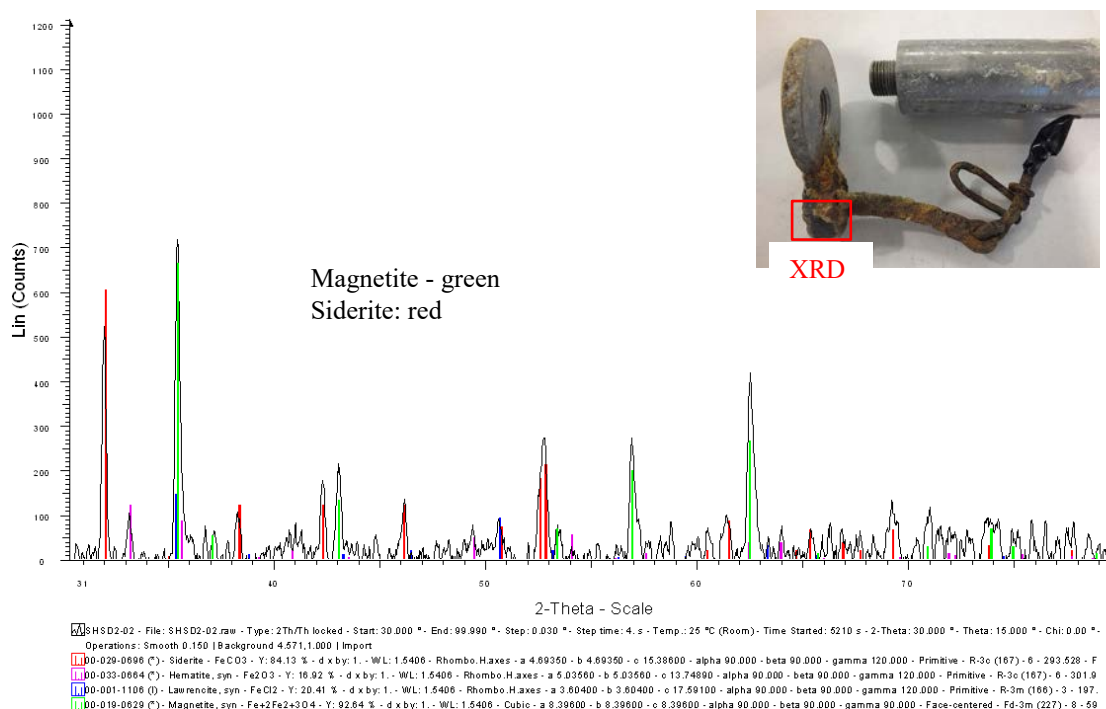


Fig. 15: XRD pattern of corrosion products on surface of nut (upper right) located close to the liner.

Corrosion features were further analysed by optical and scanning electron microscopy. The 316L stainless steel tube did not exhibit any signs of localised or general corrosion. However, corrosion damage was observed for the carbon steel parts, including the screws, nuts and iron welding parts.

4.2.2 Metal coupons

Different metal coupons had been emplaced on Teflon racks and inserted into bentonite blocks close to the heater. As outlined in Chapter 2, some of these racks were damaged during the partial dismantling in 2002. Three racks comprising stainless steel (316L – Rack 2A), titanium alloy (Rack 3A) and copper alloy (Rack 4A) were analysed. Generally speaking, the coupons were exposed to low humidity conditions because they were emplaced close to the heater.

Stainless steel (316L)

These four coupons, which had been placed on the same Teflon rack (Fig. 16), did not exhibit any visual signs of general corrosion. Nevertheless, pitting corrosion is observed in all four coupons and cracking is revealed in 2A2 (Fig. 16, centre). Corrosion products are associated with the pits (brownish-black) and cracks (reddish). From EDX analysis, it can be deduced that the corrosion products are enriched in Fe and O and contain Cr and also Cl. From XRD, no phases could be identified due to the poorly crystalline nature of the corrosion products. Therefore, μ -Raman spectrometry was conducted, but it even then it was difficult to detect mineral phases. Magnetite and hematite were detected in one pit area of sample 2A2 (Fig. 17).

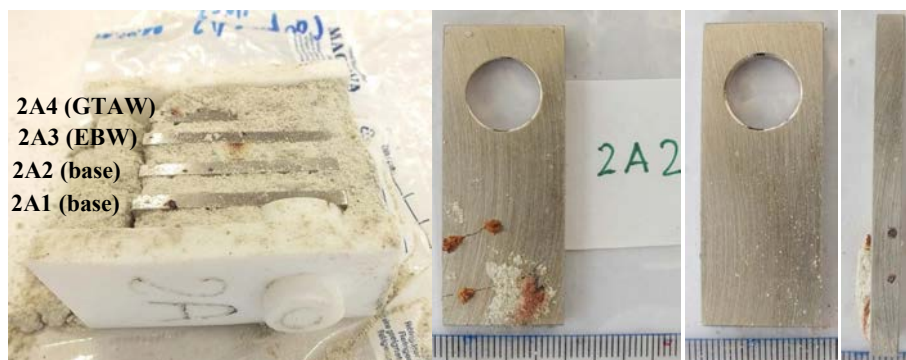


Fig. 16: Photographs of Rack A2 (left) and three faces of coupon 2A2.

The samples 2A1 and 2A2 are base materials, whereas 2A3 and 2A4 are coupons with welded joints.

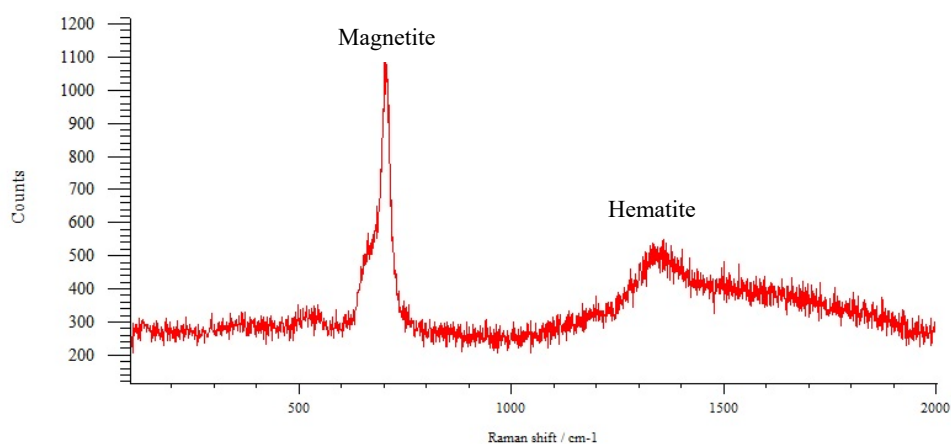


Fig. 17: Raman spectrum from corrosion products located on a pit of sample 2A2.

The cracks studied with optical microscopy exhibited branched morphology and transgranular progression (not shown), which is typical for stress corrosion cracking of stainless steel. In the cracking areas, preferential corrosion of the ferrite bands was observed. The pits are filled with corrosion products. For sample 2A2 a penetration depth of about 300 microns for the pit was estimated. There were no clear differences noted between base and welded samples.

Titanium alloys

As outlined in Chapter 2, the rack with the Ti coupons was partially damaged and two of the coupons were missing. Three of the recovered coupons were bent. From visual inspection, very little or no corrosion could be inferred. Reddish particles (presumably iron oxides) were observed on the surface of almost all coupons. SEM/EDX analysis showed that they consist mainly of Fe and O. No meaningful results on these reddish particles could be obtained from XRD. The origin of these Fe-rich particles is not clear. They may be related to some contamination before or during the in-situ test.

Copper alloys

The five coupons from Rack 4A consist of different Cu alloys: Cu-ETP (two coupons), Cu10Ni (two coupons) and Cu30Ni (one coupon).

The Cu-ETP coupons exhibit both a brownish red colour on the surface and greenish areas mixed with the clay (Fig. 18). Corrosion appears to be generally uniform and only small areas of localised corrosion at the edge of coupons were observed. SEM/EDX analysis revealed that the surface is predominantly of Cu and O. Chloride was detected in all of the corrosion products, but was enriched in the greenish areas. The XRD pattern suggests the presence of cuprite (Cu_2O). Metallographic analysis confirmed the generation of a relatively uniform corrosion layer and the presence of a small localised corrosion area with a maximum depth of about 100 microns. The pit is filled with clay material, but without any copper.

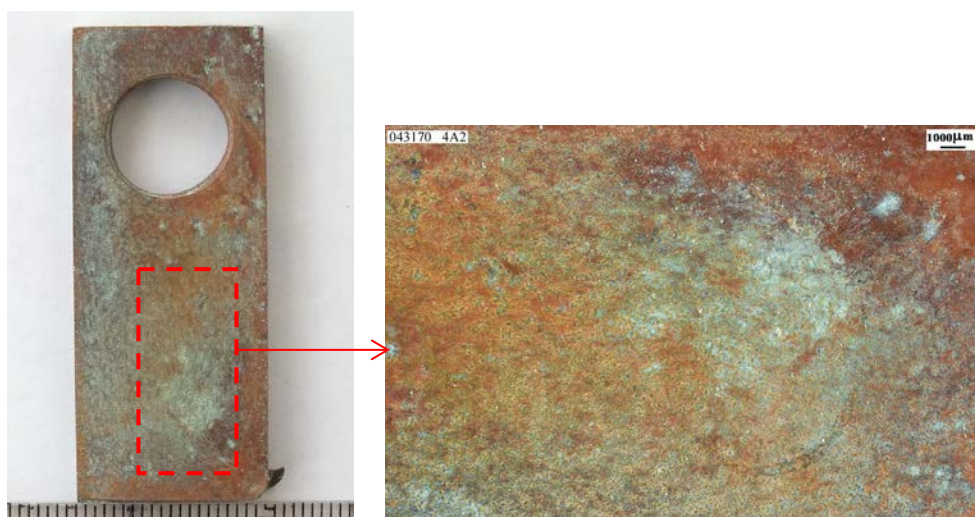


Fig. 18: Photographs showing Cu alloy coupon (ref. 4A2) and details of the corroded surface.

The Cu-Ni type coupons showed a blackish-grey surface with greenish areas admixed with the clay. Also for these samples, general corrosion seems to be dominant mode and no signs of localised corrosion were found. SEM/EDX analysis indicated the presence of a Cu-Ni oxide layer containing variable amounts of Cl. From XRD analysis, no Cu chloride phase could be identified. Cuprite was identified for the Cu10Ni sample, but not for sample Cu30Ni which exhibited less corrosion. Metallographic analysis confirmed the general corrosion mode. A few very small areas of localised corrosion were observed with penetration areas of less than 50 microns.

There were no indications of anaerobic corrosion in any of the Cu and Cu-Ni coupons, such as formation of Cu sulphide phases.

Additional analyses

Further analyses of the Cu-ETP coupons were conducted upon request of SKB. This additional study by Tecnia is presented in Appendix B. The main objective was to analyse the extent of localised corrosion that was observed in one coupon specimen in more detail. A further objective was to estimate the corrosion rate on another specimen based on weight-loss measurements.

Three zones close to the localised corrosion area described above were analysed with regard to pit depth and chemical composition in the pits (Fig. 19). The coupon was embedded in resin and slightly polished. The occurrence of localised corrosion was confirmed and pits with maximum depth in the range of roughly 20 – 60 μm were determined; an example is shown in Fig. 20. The pits were filled with clay material and generally little to no Cu corrosion products were found in the pits. The measurements were repeated on other areas after further polishing and removal of about 5 mm. Very similar observations were made.

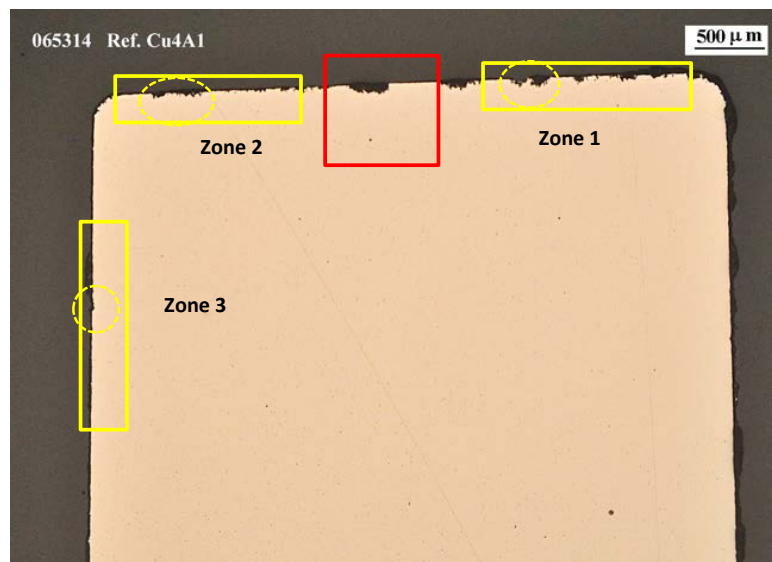


Fig. 19: Optical micrograph of section of copper alloy ref. 4A1.
Zones analysed at 0 mm depth.

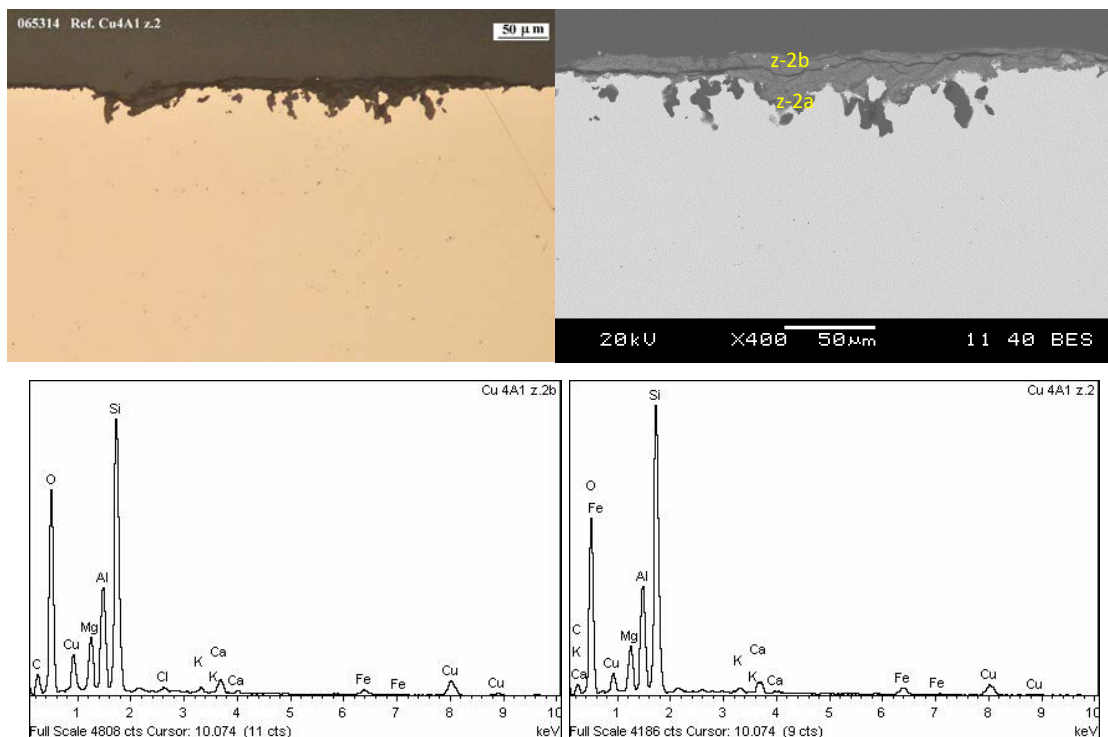


Fig. 20 Example of pit analyses at 0 mm depth from coupon 4A1.

Upper: Optical and backscattered SEM micrographs of the maximum pit depth in Zone 2, and associated EDS spectra. Without metallographic etching. Lower SEM/EDX spectra of Zone z-2b (left) and Zone z-2a (right).

Weight-loss measurements were conducted on another coupon sample (Sample 4A2) by removing the corrosion layer with 10 % sulphuric acid. The total corrosion depth derived was 8.5 µm. Assuming 18 years of corrosion time, the average corrosion rate is thus about 0.5 µm/a.

4.2.3 Liner

Liner samples from Sections 45 and 52 were studied. Visual inspection indicated a fairly compact but non-uniform corrosion layer (Fig. 21) and higher extension of corrosion in areas bordering the holes and in areas of separation between blocks. General corrosion is the main process on both sides of the liner. No visible signs of localised corrosion were found. Corrosion was slightly more extended in the upper sections of the heater (between 9 and 3 o'clock).

SEM/EDX analysis indicated that the reddish corrosion products consist principally of Fe and O. A significant peak of Cl was detected in the EDX spectra. From XRD analysis, magnetite, akageneite (Cl-bearing iron oxyhydroxide) and hematite were identified. Minor siderite was also found (Fig. 22). In one sample (ML45-1) halite was detected. Note that for samples of Section 52 no SEM/EDX and XRD analyses were conducted.



Fig. 21: Liner sample ML45-2, external surface; right: close-up view.

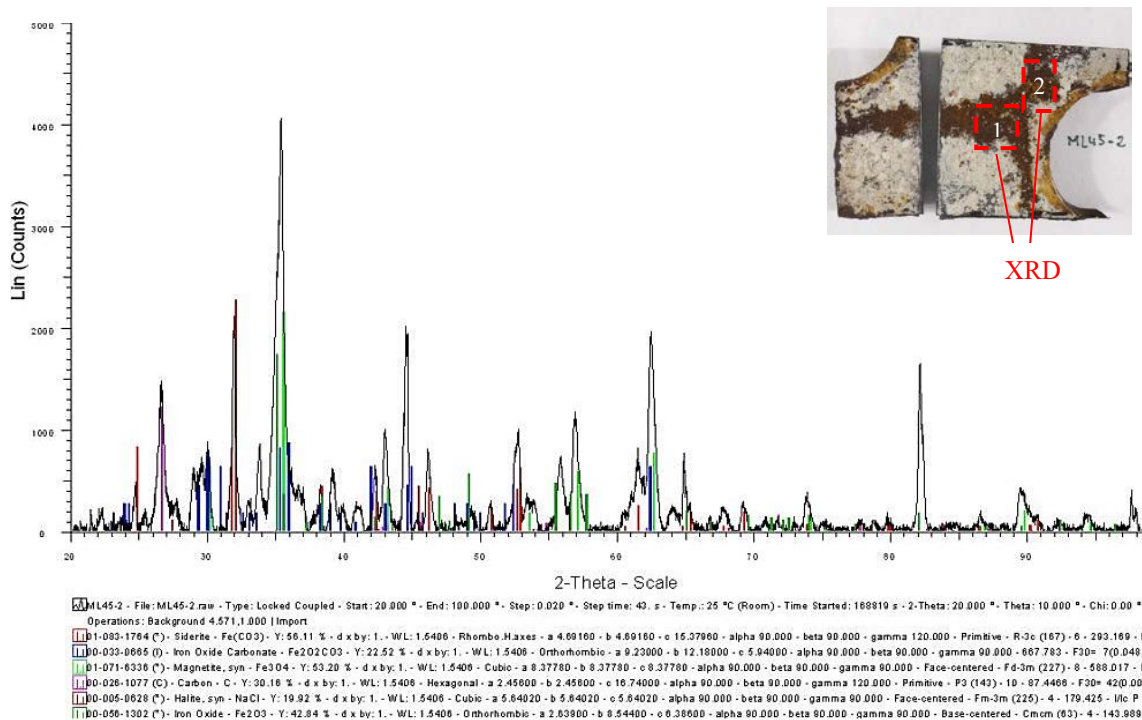


Fig. 22: XRD pattern of sample ML45-2 (see marked rectangles in photo upper right), showing the presence of magnetite, hematite and siderite.

From optical and scanning electron microscopy, a fairly compact, uniform and firmly attached oxide layer for the external surface of maximum thicknesses of 200 – 250 μm was revealed. The internal surface showed the same feature, albeit exhibiting a slightly thinner oxide layer, with a maximum thickness of about 180 μm . No localised corrosion features could be found.

The thickness of the liner was measured on metallic probes. This yielded 14.7 ± 0.15 mm. Assuming an initial thickness of about 15 mm and considering that corrosion occurred on both sides the corrosion depth values are about 150 ± 75 μm . These corrosion depths are in the same range as deduced from the corrosion layer thicknesses, which were 200 – 250 μm on the external surface and up to 180 μm on the internal surface in Section 45. Accounting for the different densities of the corrosion layer and carbon steel (assumed to be 4.2 g/cm³ and 7.69 g/cm³, respectively), corrosion depths are derived as 98 – 137 μm . This is in the same range as deduced from direct measurements of the liner thickness.

A somewhat larger extension of the corrosion layers was observed for Section 52 than for Section 45. The external surface exhibited maximum corrosion external surface layer thicknesses of 300 – 350 μm and about 250 μm for the internal surface layer. Using the same premises as for Section 45, this yields 109 – 191 μm . This is also in a similar range as estimated from direct measurements of the liner thickness.

4.2.4 Heater

The heater was transported from the Grimsel Test Site to the former AITEMIN facility in Toledo (Spain). Samples were extracted there by cutting wedge-shaped pieces with a circular saw on November 24, 2015. It should be noted that the heater had been exposed to the atmosphere under variable temperature and moisture conditions since early June 2105, thus almost for half a year. This may have contributed to the corrosion results summarised below.

Visual examination showed a fairly uniform corrosion layer and no visible localised corrosion or pitting, thus indicating general corrosion as the main corrosion mode. The corrosion layer consisted of reddish brown corrosion products. The front part, which was in direct contact with the clay, exhibited a larger extension of corrosion (Fig. 23). The welded joints of the two-lid cylinder were in good condition.



Fig. 23: Heater after transport to AITEMIN facility. Close-up photos showing corrosion features (right).

The three extracted samples (MH-01, MH-02, MH-03) included sections from the lid, the welded joint and the cylinder. SEM/EDX analysis indicated that corrosion products are essentially composed of Fe and O. Cl and small amounts of S were also detected. XRD analysis carried out on two samples enabled the identification of akaganeite ($\text{Fe}^{3+}\text{O}(\text{OH},\text{Cl})$) as the main iron oxide phase (Fig. 24).

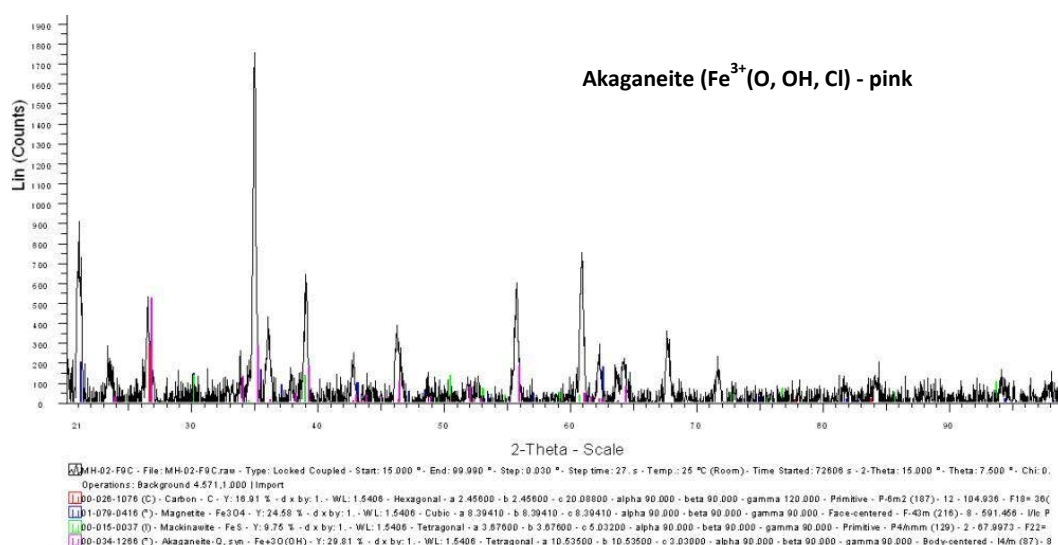


Fig. 24: XRD pattern of sample MH-02-F9C (see Madina 2016 for details).

Optical and scanning electron microscopy confirmed the fairly homogeneous nature of the corrosion layer with a thickness of roughly 200 μm . Some small localised corrosion areas exhibited corrosion layer thicknesses up to 400 μm .

4.2.4 Summary of main findings

Carbon and low-alloyed steel components

The largest corrosion damage is observed on the carbon-steel components at the end pieces of the sensors. A general corrosion mode could be deduced for these components. Hematite and magnetite were identified as iron oxide phases, but non-crystalline iron oxide phases may also be part of the reddish-brownish corrosion products where also siderite could be identified. From the corrosion morphology and the presence of sulphur, microbiologically influenced corrosion (MIC) may have occurred.

The perforated liner exhibited a non-uniform general corrosion mode. No localised corrosion features (e.g. pitting, cracks) were found. The corrosion layers were somewhat thicker on the outer surface exposed to the clay reaching up to 350 μm . For the inner surface, corrosion layer thicknesses were ≤ 200 μm . The corrosion products were found to be mainly iron oxides and siderite. Significant amounts of chloride were found in all analysed samples.

For the heater, a uniform general corrosion mode could be inferred. No localised corrosion was detected. Corrosion was more extensive in the front part which was in direct contact to the clay. There the corrosion layer was up to 400 μm thick, whereas in the other parts it reached about 200 microns. The welded joints displayed good conditions. Iron(III) oxides (akaganeite) are the main corrosion products.

Stainless steel components

For the stainless-steel tubes of the sensors, some mechanical damage was found but no signs of general or localised corrosion were detected.

The 316L coupons exhibited localised corrosion in the form of pitting and in one specimen cracking was detected. In the cracks, chloride was found. This compound is known to favour crevice corrosion cracking (SCC) in this type of stainless steel. Besides chloride, the extent of SCC increases with O₂ content. The presence of corrosion products inside the cracks suggests that cracking occurred during the initially aerobic period of the FEBEX test. However, ingress of O₂ during and after dismantling cannot be entirely excluded from contributing to SCC.

The pits found in the coupons were filled with brown corrosion products forming a cap and consisting of Cl-bearing iron oxides. Magnetite and hematite were identified as crystalline phases in this material. Pit penetration was estimated at about 300 µm, which is not very deep and suggests fairly slow propagation of corrosion damage.

No difference in base (parent) and welded coupon materials was noted.

Titanium coupons

For the titanium coupons, no corrosion phenomena were observed. Thus, no difference between the corrosion behaviour of unwelded and welded samples was noted.

Copper coupons

For the Cu and Cu-Ni alloy coupons, general corrosion was found to be the main corrosion mode. From weight-loss measurements on one Cu coupon, an average corrosion rate of 0.47 µm/a was derived. The Cu-Ni coupons showed less general corrosion and no signs of localised corrosion. Cuprite (Cu₂O) was found as corrosion product in all studied samples.

The Cu coupons revealed some spots of localised corrosion. The pits, analysed on one sample exhibited maximum penetration depths which were generally in the range of 20 – 60 µm. The largest depth reached was about 100 µm. These pits were filled with clay material and little or no Cu-corrosion products.

Redox conditions

The results from the corrosion study revealed that mixed redox conditions occurred in the in-situ test as was also proposed by an earlier investigation (Giroud 2014, NAB 14-55). It appears that the majority of the Fe(III) oxides (hematite, akaganeite, probably also non-crystalline oxyhydroxides) formed during the initial aerobic phase. It cannot be ruled out, however, that aerobic corrosion after dismantling also contributed to the observed corrosion products. The presence of reduced iron phases, such as magnetite and siderite, found in the inner and outer part of the liner, shows the importance of anaerobic corrosion once the oxygen in the tunnel was depleted. It is also worth noting that the Cu coupons revealed no signs of anoxic or microbially-induced corrosion.

4.3 Metal corrosion analysis by Obayashi

4.3.1 Scope and objective

Geological disposal is the most realistic option for high-level radioactive waste disposal (hereafter HLW) in Japan. In considering longterm stability for geological disposal, several types of material as a candidate for an engineered barrier with the host rock are studied. One option is to use a combination of carbon steel and bentonite. Carbon steel shows uniform corrosion in many cases (McCafferty 2010). Therefore, we investigated the longterm corrosion tendency and mineralogical interaction of carbon steel for longterm safety of geological disposal within the FEBEX dismantling project (hereafter FEBEX-DP). For this purpose, an electrochemical method for accelerated corrosion was studied.

4.3.2 Corrosion study in laboratory

Sample preparation

Serrata clay blocks were used as proxy for the engineered barrier system in the FEBEX-DP. We selected a sample for a laboratory experiment to study the corrosion of metal surrounding compacted bentonite extracted from B-B51-8 (Fig. 25). This sample was not much affected by saturation due to the infiltrating porewater at the test site.

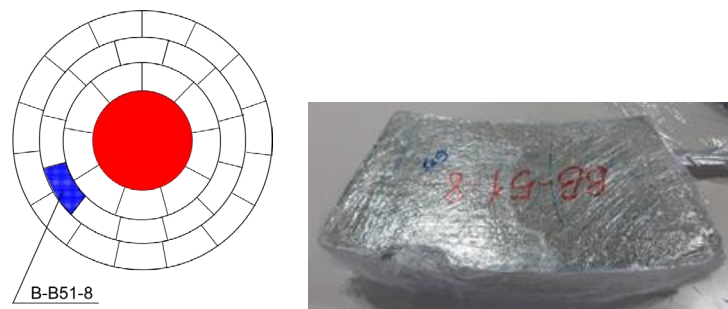


Fig. 25: Detail of B-B51-8 sample.

Accelerated corrosion lab-test method

An electrochemical method was used to achieve accelerated corrosion and allow the investigation and study of the longterm corrosion tendency of carbon steel.

Fig. 26 shows a sample exposed to an accelerated corrosion test. Compacted Serrata bentonite extracted from a B-B51-8 sample and two carbon steel wires, SWRS82A, were put into a ceramic case. These carbon steel wires were not polished beforehand, which means that the oxide scale existed before the corrosion test. These oxide scales are formed on carbon steel when these are exposed to surrounding oxygen.

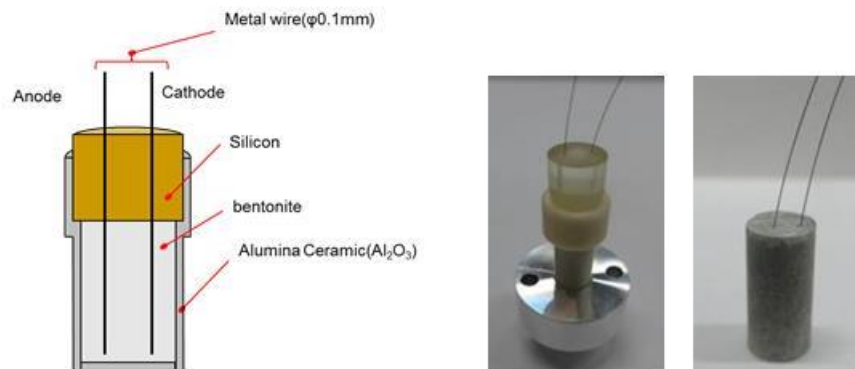


Fig. 26: Detail of accelerated corrosion lab-test method.

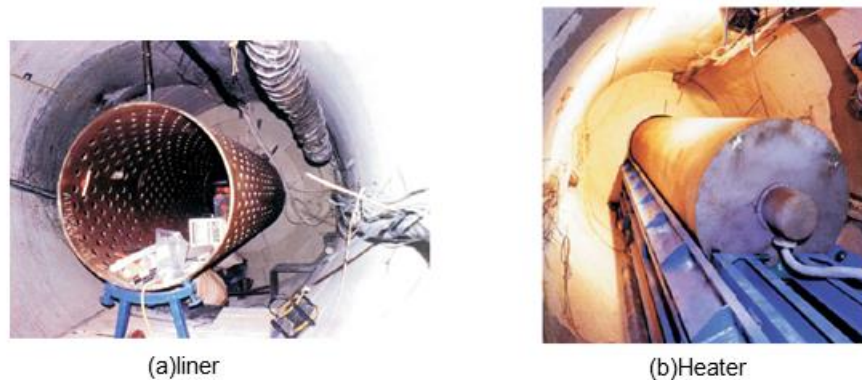


Fig. 27: Initial conditions of liner and heater in FEBEX experiment (Enresa 1998).

The carbon steel wires were set parallel at 2 mm intervals. On one side the steel wire formed a cathode and on the other side an anode. As in the previous test (Uyama et al. 2016), for a current density of 0.1 mA/cm^2 , an appropriate supply current was determined as $2.5 \times 10^{-3} \text{ mA/cm}^2$ ($0.1 \text{ mA/cm}^2 \times 0.025 \text{ cm}^2$), taking into account the stable electron transfer in bentonite and near the surface of the carbon steel. The corrosion test times were set at 3 and 7 days based on a calculation of the total corrosion volume from Faraday's laws of electrolysis.

Fig. 27 illustrates the initial conditions of carbon steel, liner and heater in the FEBEX experiment (Enresa 1998).

Metal corrosion evaluation

To evaluate metal corrosion in bentonite, corrosion rate and total current volume were observed by non-destructive X-ray CT; corrosion products were observed by SEM-EDX and Raman spectroscopy.

1. Result of non-destructive X-ray CT

Non-destructive X-ray CT consisting partly of integrated X-ray CT and X-ray diffraction (hereafter CT-XRD) was conducted by the SPring-8 facility in Hyogo prefecture, Japan (Fig. 28). CT is performed for non-destructive internal observation using an X-ray camera and

XRD is for identifying the material by X-ray diffraction using a SSD camera (Hitomi et al. 2013). Our experimental unit placed in SPring-8 can use white X-ray containing spacious energy spectra.

Firstly, X-rays travel through slit (S1) from the left side in Fig. 28 and irradiate a given sample while an X-ray camera obtains CT image of the sample. Secondly, the internal point for the observation of XRD is decided from this CT image. Finally, a second X-ray beam through slit (S1) is applied to sample on a rotatable stage so diffracted X-ray data is obtained by SSD (solid state detector) at a fixed angle setting ($2\theta = 20$ degree). In our case, the energy dispersion type for XRD was used instead of the angle dispersion type. This method can be conducted continuously without sample change between the test of CT and XRD.

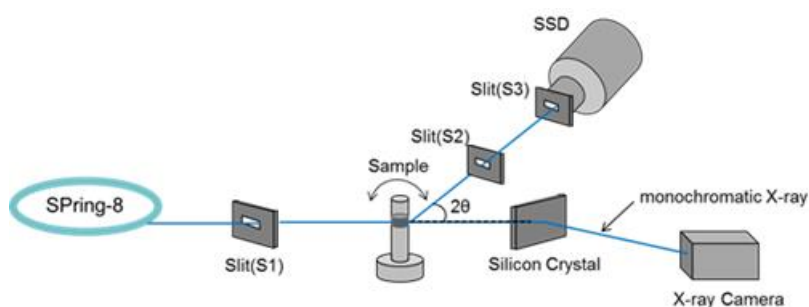


Fig. 28: Image of a white X-ray measurement.

Fig. 29 shows a 3D calculation image of the analysed non-destructive CT for SPring-8. (The result of XRD is given in the following chapter.) The left figure shows the corrosion situation after 3 days and the right one shows the same after 7 days. The tube-like image in Fig. 29 is the remaining uncorroded carbon steel wire on the Serrata clay. The anode side of steel wire was corroded and the volume of corrosion increased gradually as corrosion test time passed. Fig. 30 shows the total number of pixels on the anode side for each corrosion test time. This result roughly lies between the bivalent and trivalent value of the Fe ion reaction of Faraday's law.

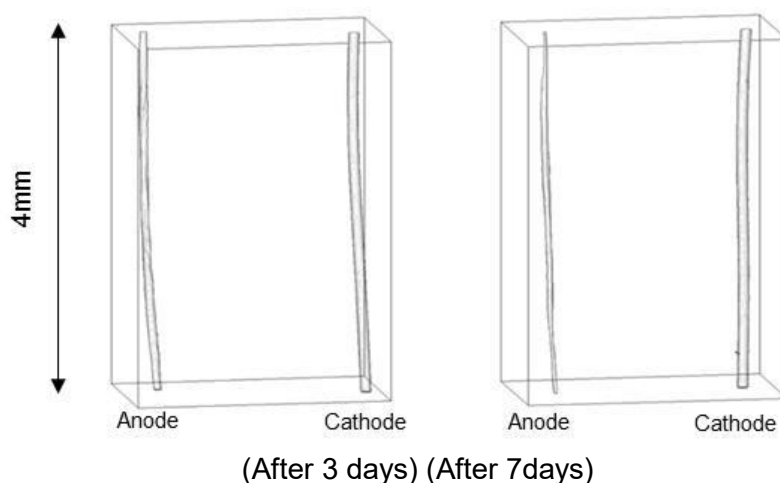


Fig. 29: Corrosion situation observed by non-destructive CT 3D image.

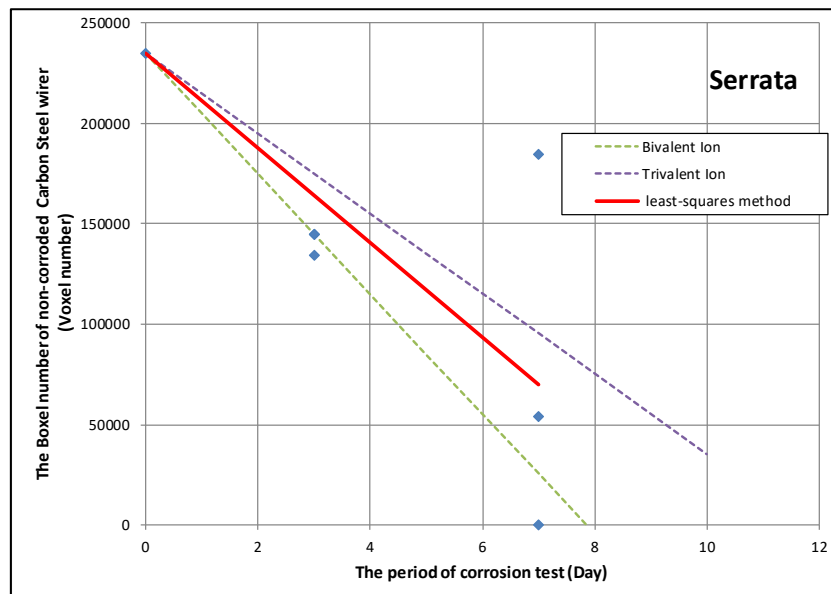


Fig. 30 Remaining voxel number of carbon steel wire after accelerated corrosion test, small diamonds are actual measurements.

2. SEM-EDX image

After the CT-XRD analysis using the SPring-8 facility, each sample was cut with a wire cutter using a dry method for the next analysis (Fig. 31). The SEM image of Fig. 32 displays the anode side. The white area is the non-corroded Fe and the surrounding grey colour is iron oxide. The sample treated for 7 days in the corrosion test was more corroded than the one treated for 3 days. This result is almost the same quantitatively as the CT image result shown in Fig. 29. Therefore, the calculated 3D-CT image is realistic.

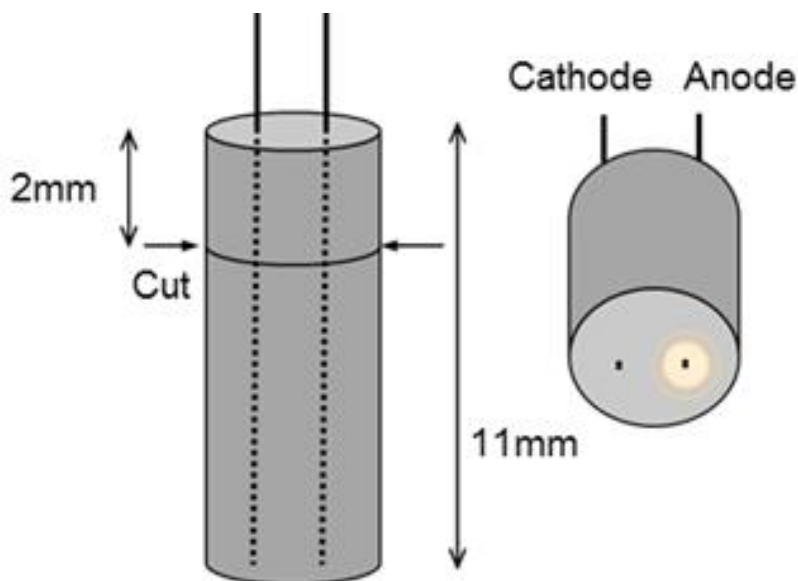


Fig. 31: Cut image of sample after non-destructive CT-XRD.

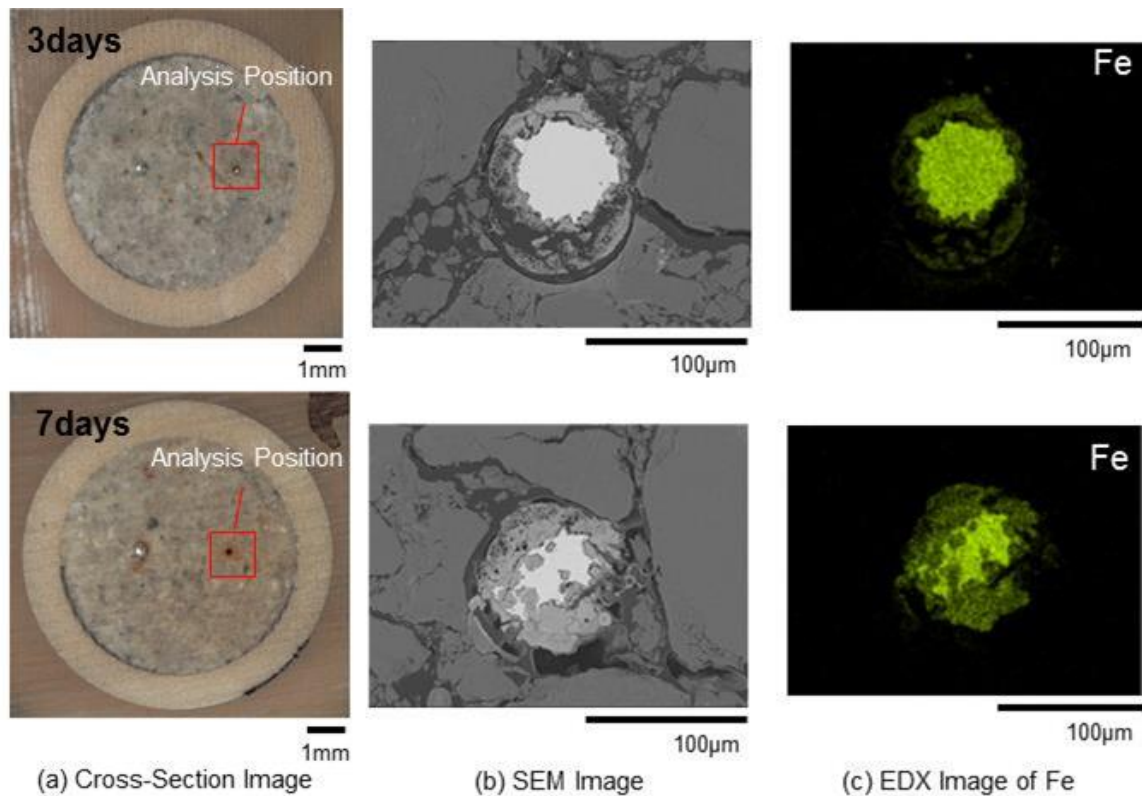


Fig. 32: SEM-EDX image of anode-side metal corrosion (3 and 7 days).

3. Raman spectroscopy

Raman spectroscopy analysis identified corrosion products on the steel wire at the anode side. These samples were prepared after 3 and 7 days of accelerated corrosion testing. The white colour (Fig. 33) represents non-corroded Fe and the grey colour area surrounding the non-corroded Fe represents corrosion products. From the result of Raman spectroscopy, it can be deduced that the corrosion mechanism was the same as in the previous laboratory experiment (Uyama et al. 2016), because corrosion products were found under the initial oxide scale.

The image of corrosion mechanism in this laboratory test is shown in Fig. 35. This corrosion product would expand over the surface oxide scale that existed initially before the corrosion test. This result implies that corrosion products, hematite and goethite, found by Raman spectroscopy were affected at the bentonite side.

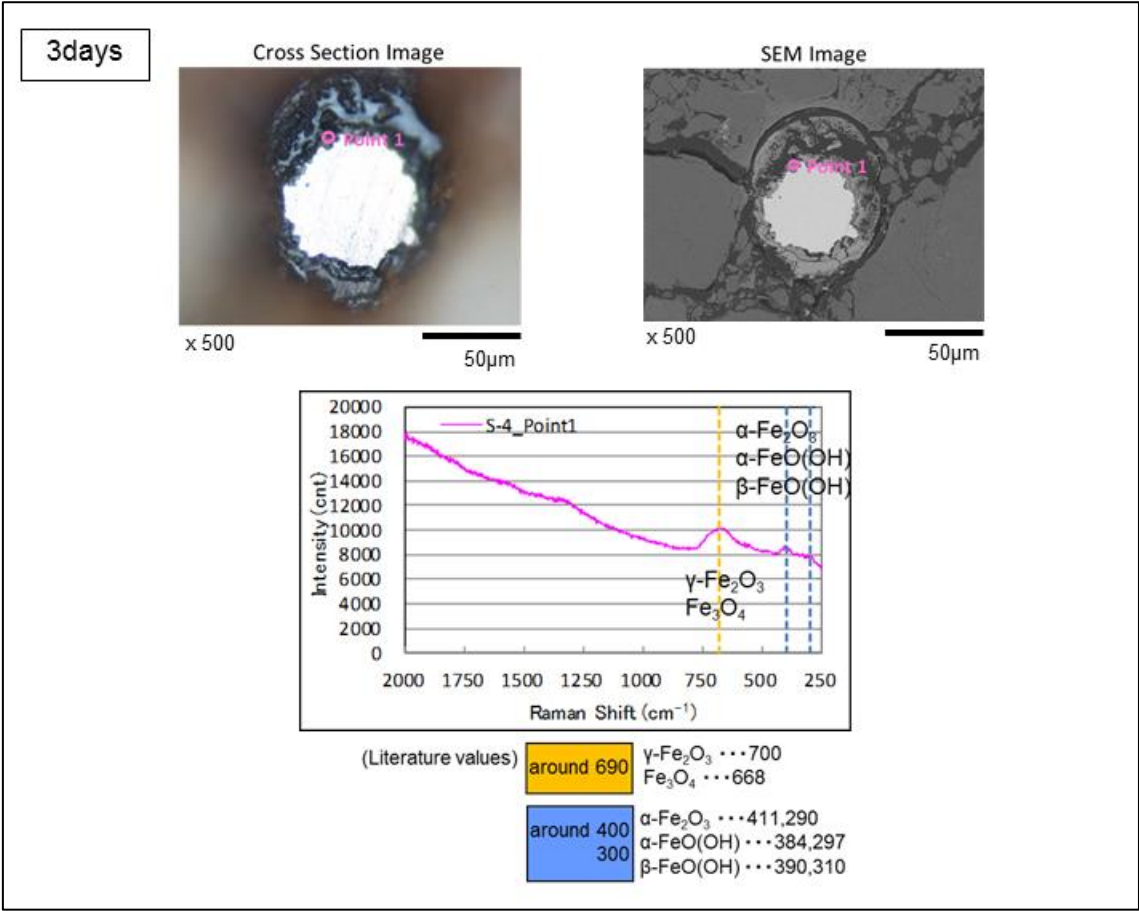


Fig. 33: Raman spectroscopy result of metal corrosion (3 days).

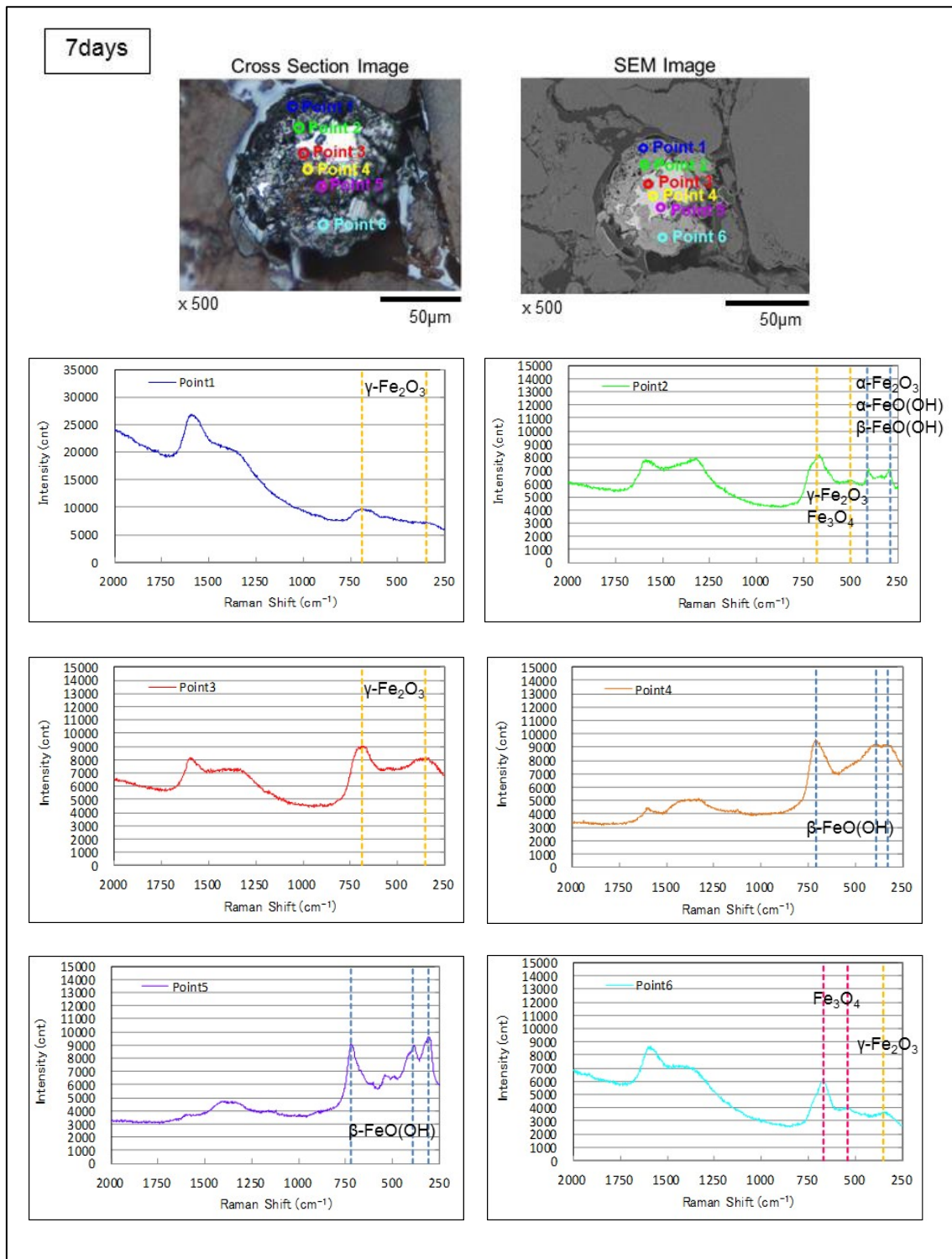


Fig. 34: Raman spectroscopy results of metal corrosion (7 days sample).

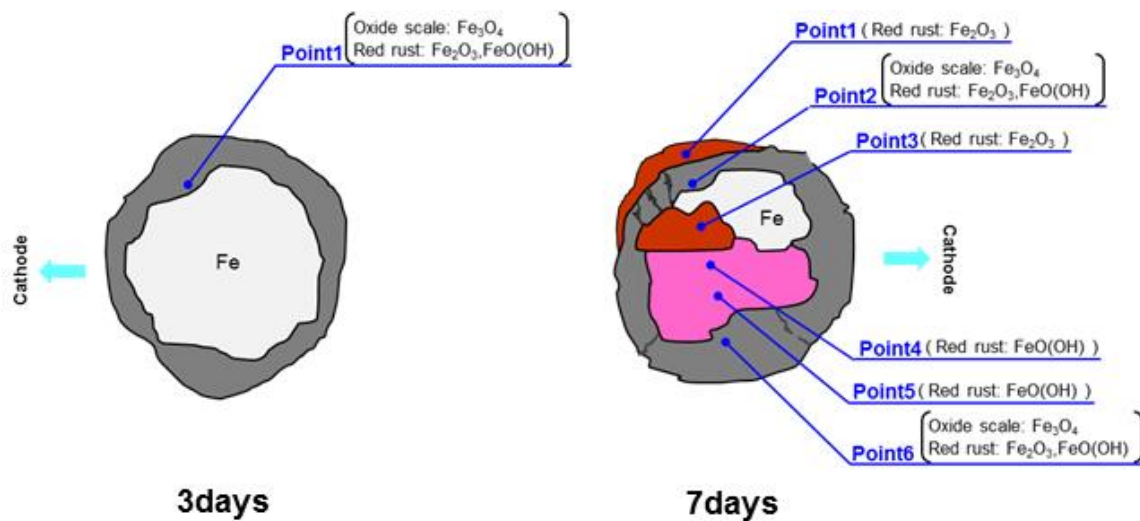


Fig. 35: Image of corrosion mechanism (3 and 7 days).

Diffusion of Fe ion in compacted bentonite

The elemental composition of the Serrata bentonite close to the wire metal contact but beyond the corrosion layer was analysed by the non-destructive XRD and ToF-SIMS methods. The accelerated corrosion test periods were 3 and 7 days.

1. Result of non-destructive XRD

Fig. 36 shows a cross-section image of a sample analysed by CT using the SPring-8 facility. The analysis method does not imply cutting the sample and is affected by oxidation during the sample preparation and analysis work. The positions of the red dots are the XRD analysis points. We compare the state before the corrosion test with that of 7 days after the corrosion test for the same sample and the same distance from the anode side (Fig. 36, Point 4). A hematite peak was found at Point 4 in the 7-day sample after the corrosion test. Corrosion products were probably formed on the bentonite side, where a red dust ring was found surrounding the anode electrode in the cross-section picture (Fig. 34).

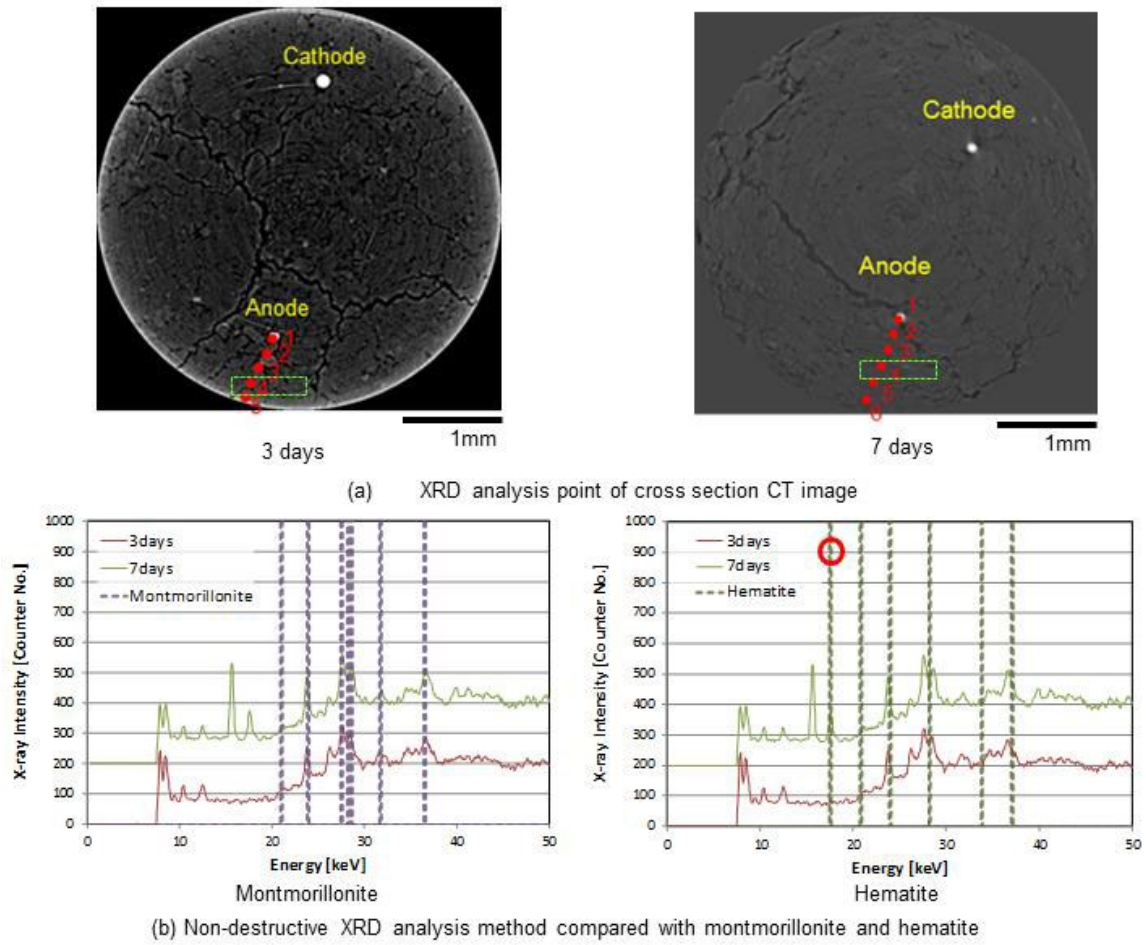


Fig. 36: XRD analysis point and non-destructive XRD result.

2. ToF-SIMS analysis

The ToF-SIMS analysis method, Time of Flight Secondary Ion Mass Spectrometry, is a surface analytical technique that focuses a pulsed beam of primary ions onto a sample surface, producing secondary ions in a sputtering process. The analysis point from anode to cathode determines the position shown in Fig. 37. Spots of analysis were 5 mm square and 4 points were analysed.

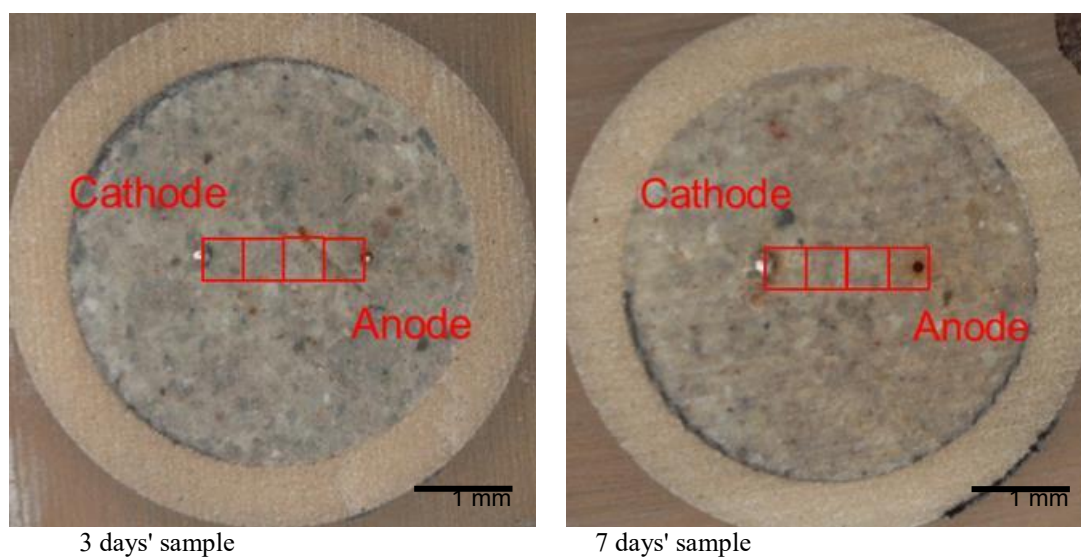


Fig. 37: Observation area conducted by ToF-SIMS.

Fig. 38, Fig. 39 and Fig. 40 show the results of ToF-SIMS data. They include an ion elemental map and a line graph of ion count number at a minimum number of observation spots. The light colour indicates high, and the dark colour indicates low elemental concentrations. The right side is the anode and left side is the cathode.

These ion movements would result from Fe ionization of metal corrosion.

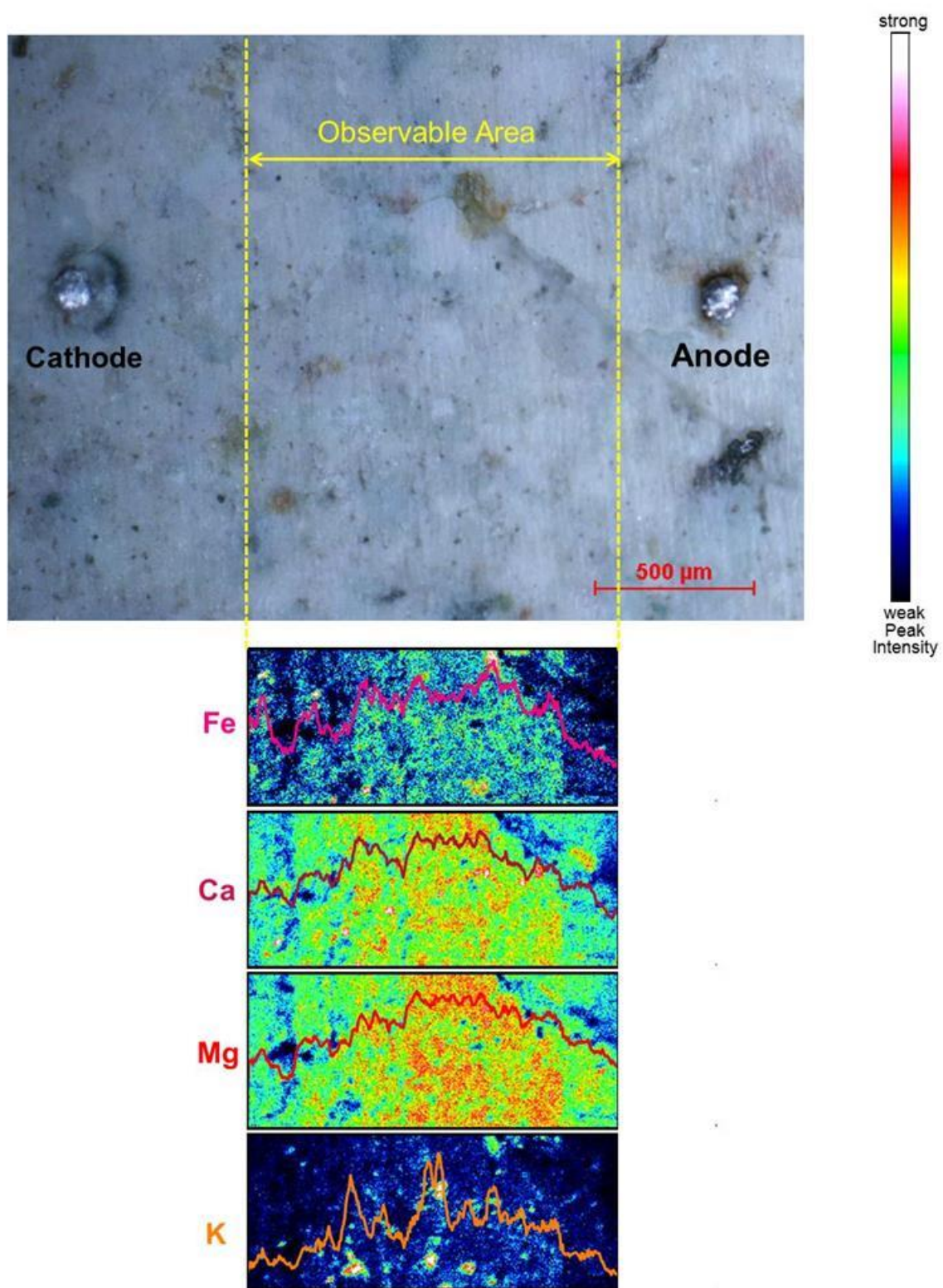


Fig. 38: Elemental map 3 days after electro-chemical test conducted by ToF-SIMS.

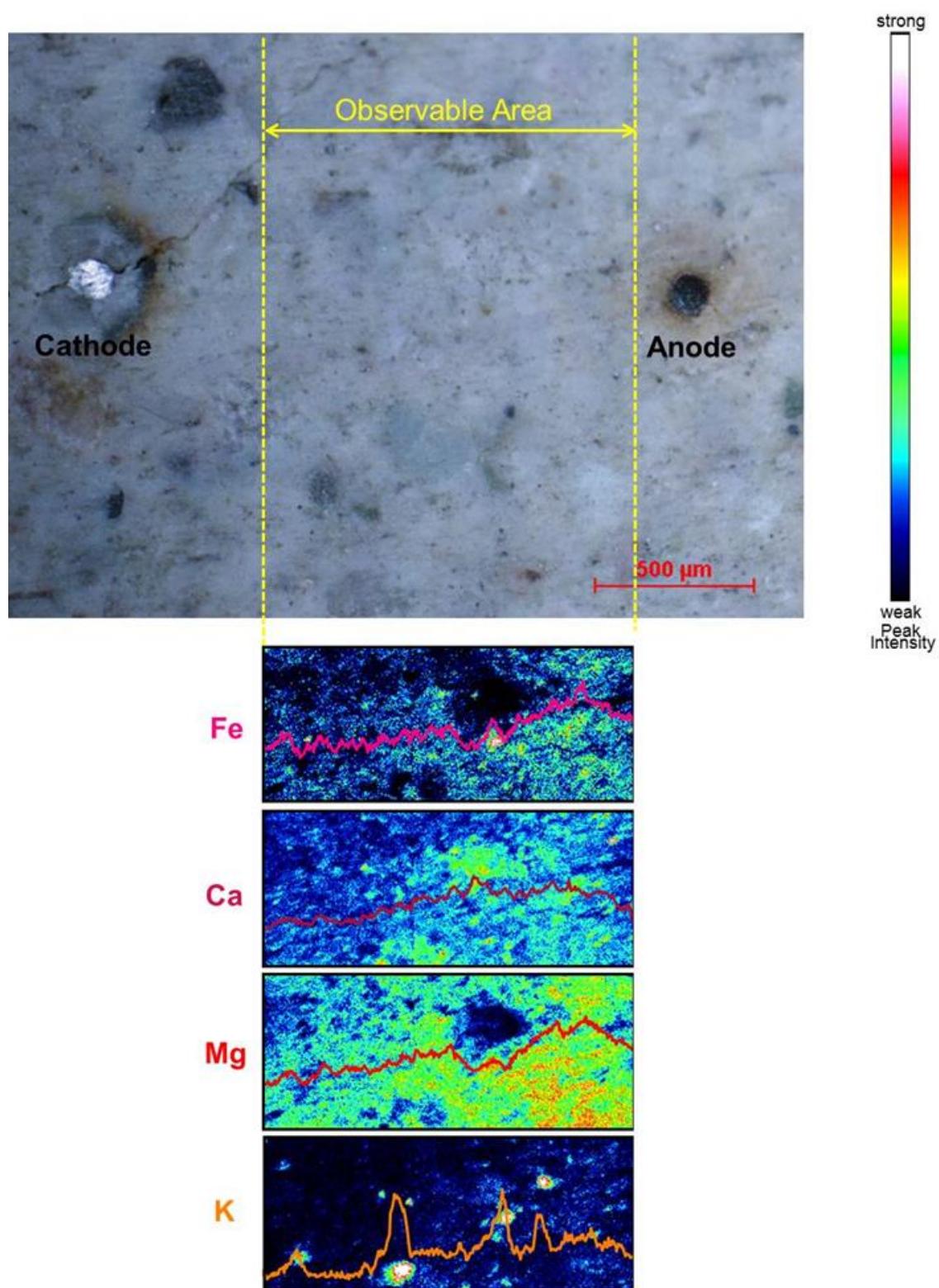


Fig. 39: Elemental map 7 days after electro-chemical test conducted by ToF-SIMS.

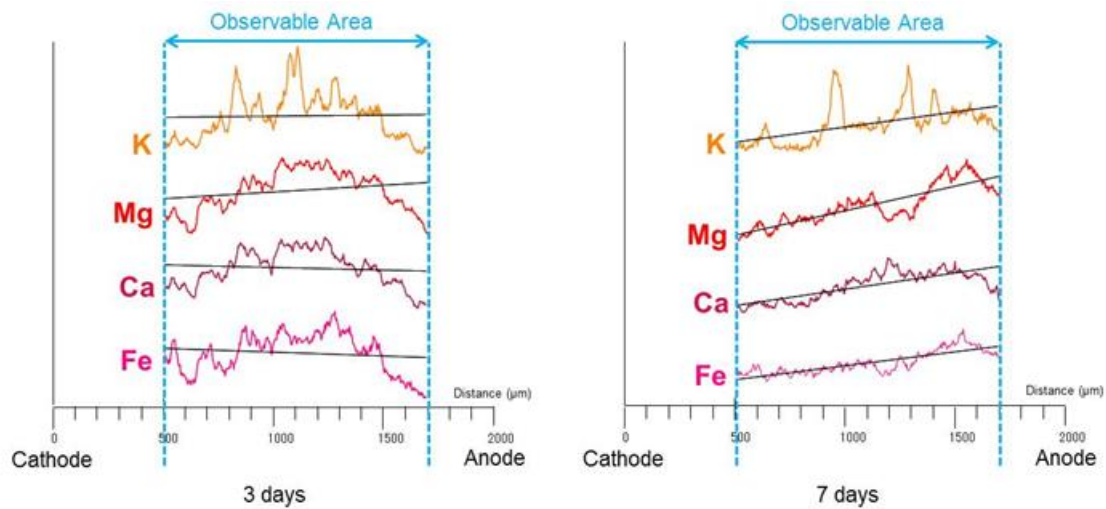


Fig. 40: Line graph result of ToF-SIMS for 3 and 7 days.

4.3.3 Corrosion study of FEBEX-DP sample

Sample preparation

From the samples transported from the GTS according at our request, M-S-35-1 and BM-C-35-1 were selected for analysis. These samples had a relatively intact bentonite/metal interface. The M-S-35-1 sample was the front cover of the dummy metal and the BM-C-35-1 sample was taken from the liner metal/cement interface. The sample details are outlined in the following.

1. M-S-35-1

Fig. 41 shows the sampling location of M-S-35-1. This sample is purely carbon steel of the front cover of the dummy metal. Before cutting, the sample was molded by epoxy resin to prevent removal of the interface corrosion material from the metal plate. After the epoxy resin had solidified (Sankei 010-8140 and 8142), the metal plate was cut by shearing (Fig. 42 and Fig. 43).

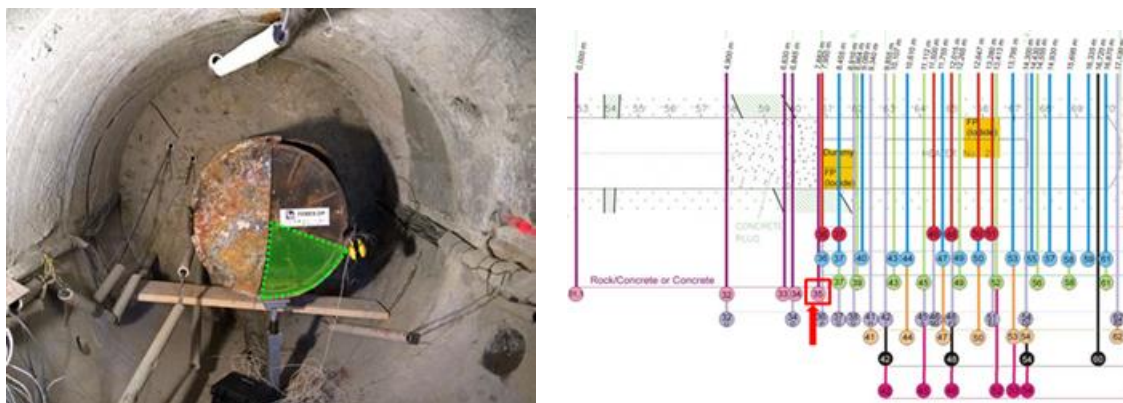


Fig. 41: Sampling point of M-S-35-1.



Fig. 42: Sample description of M-S-35-1.

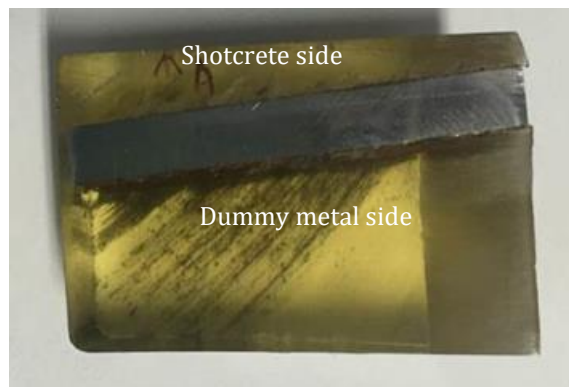


Fig. 43: Sample preparation of M-S-35-1.

2. BM-C-35-1

Fig. 44 shows the sampling point of BM-C-35-1. The sample was a mixture of bentonite and carbon steel of the liner metal/bentonite interface.

It was cut into 10 mm squares with a micro cutter equipped with a diamond cutting blade for dry cutting (Fig. 45 and 46). The resulting samples were molded into epoxy resin and acrylic resin ("Sikadure No.52" and "Acryl-one") to provide firm protection and mechanical stability for further treatment.

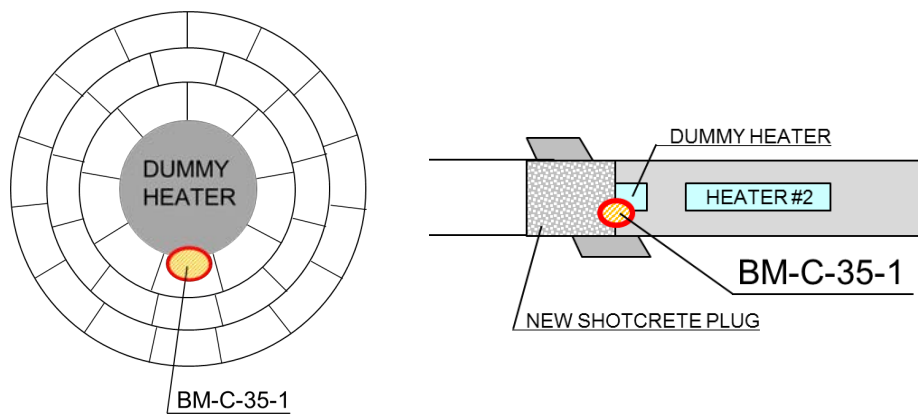


Fig. 44: Sampling point of BM-C-35-1.

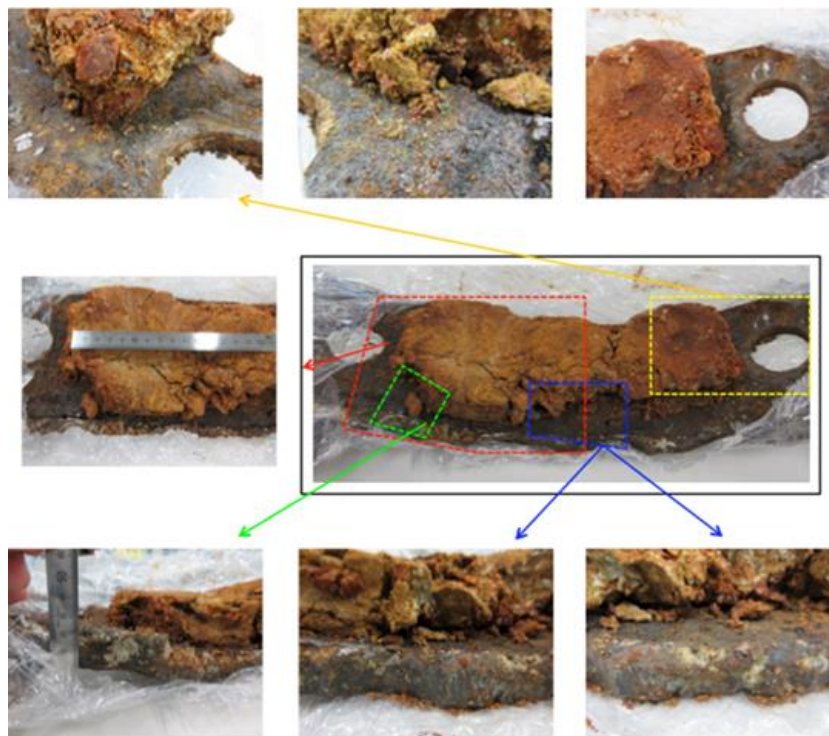


Fig. 45: Sample description of BM-C-35-1.

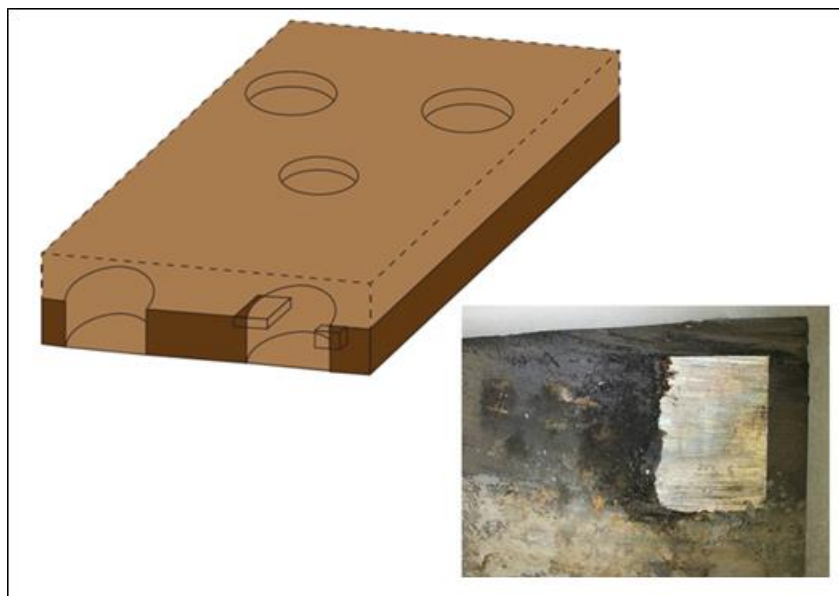


Fig. 46: Sample preparation of BM-C-35-1.

Analysis results

1. M-S-35-1

Because of the difficulty of determining the mechanism of metal corrosion with some materials, the analysis of only metal was first performed with sample M-S-35-1.

Fig. 47 shows a result obtained from cross-section image for sample M-S-35-1. Some red rust was found inside of the oxide scale. This form of corrosion is similar to that of the accelerated corrosion test. Fig. 48 shows a prediction of the corrosion mechanism.

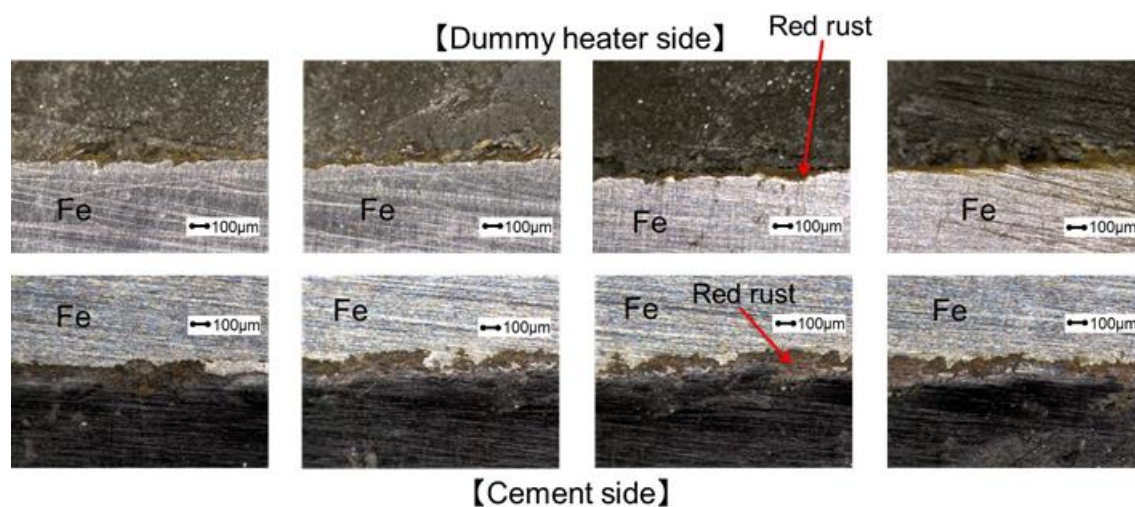


Fig. 47: Result of electron microscope for sample M-S-35-1.

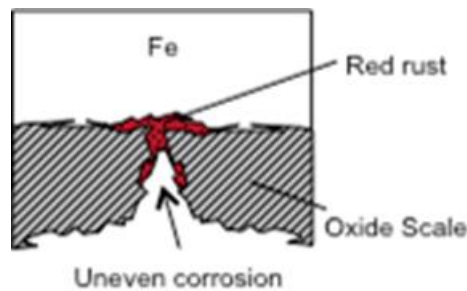


Fig. 48: Visualisation of corrosion mechanism for sample M-S-35-1.

2. BM-C-35-1

a) SEM-EDX

The preparation of the corroded metal with the bentonite contact is shown in Fig. 49.

The SEM image revealed a layer of corrosion products near the bentonite during the *in-situ* experiment (Fig. 50).

The metal side is visible as a white area on the upper side and the grey-colour side is bentonite, which has irregular contact with the corrosion layer on the metal side and shows some layers on the bentonite side.

Fig. 51 shows EDX element maps of the metal liner in contact with bentonite. The light colours represent high, and the dark colours represent low elemental concentration. The upper side, Zone 1, has a high weight % of Fe. In the area inside the fracture, Zone 2, Fe is found but Si and Ca are not. This would be a corrosion zone. Zone 3 below Zone 2 has a mixture of bentonite and Fe. The area of highlighted Fe in Zone 3 would be corrosion products taken from the part of Zone 2 and as a result there is no peak value for Si and Ca in this area. Fig. 52 is the distribution image of metal corrosion products near the interface between metal and bentonite. This result is almost same as the sample of M-S-35-1.

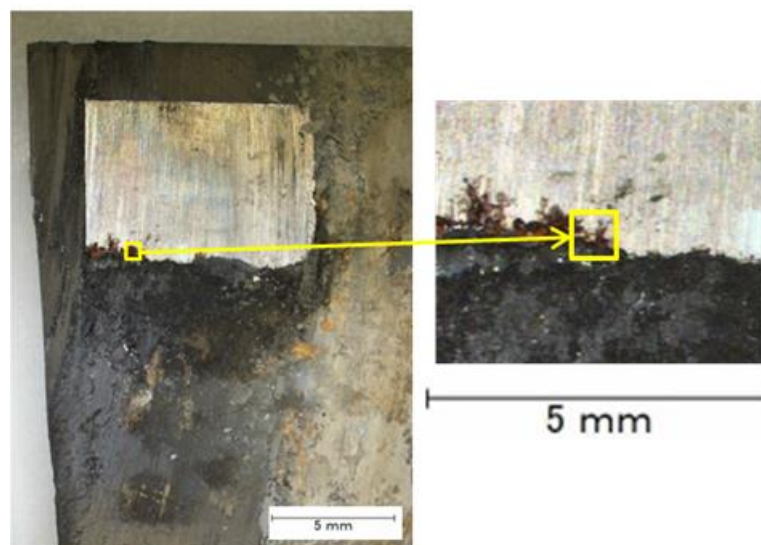


Fig. 49: Analysis point for sample BM-C-35-1.

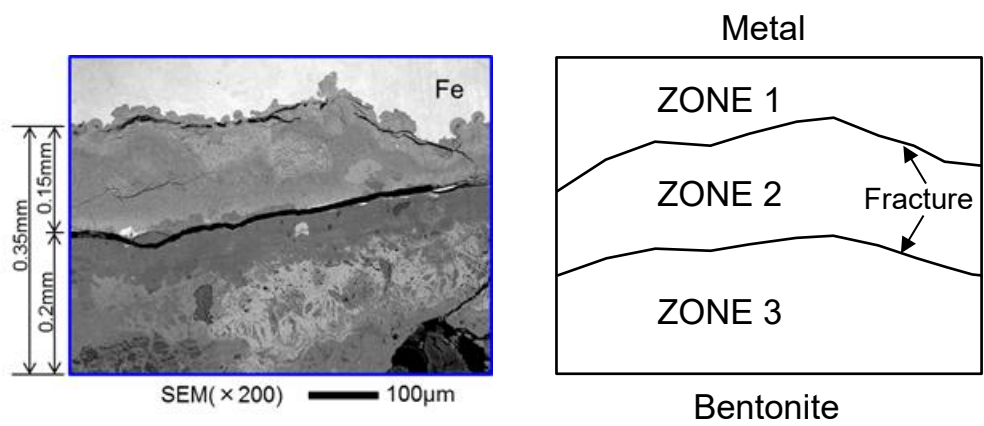


Fig. 50: SEM image of sample BM-C-35-1.

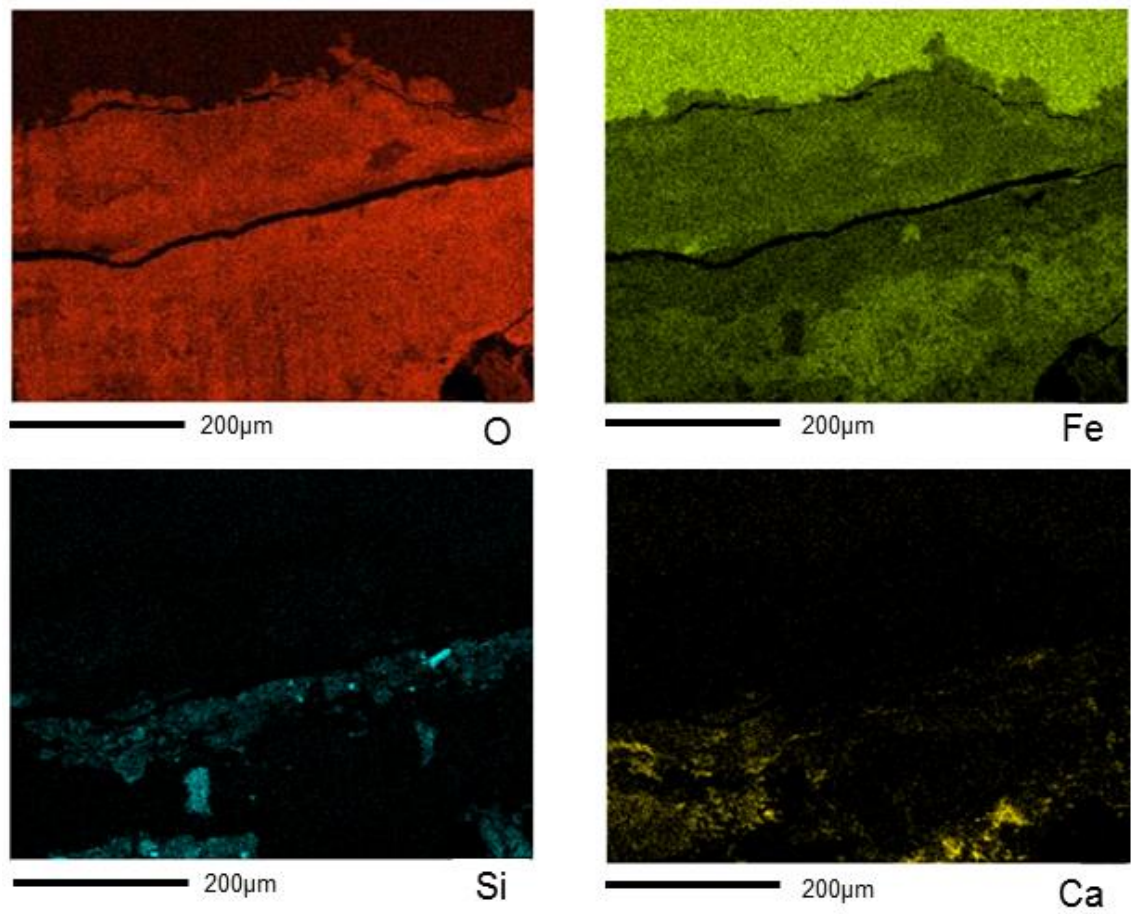


Fig. 51: EDX surface analysis image of sample BM-C-35-1.

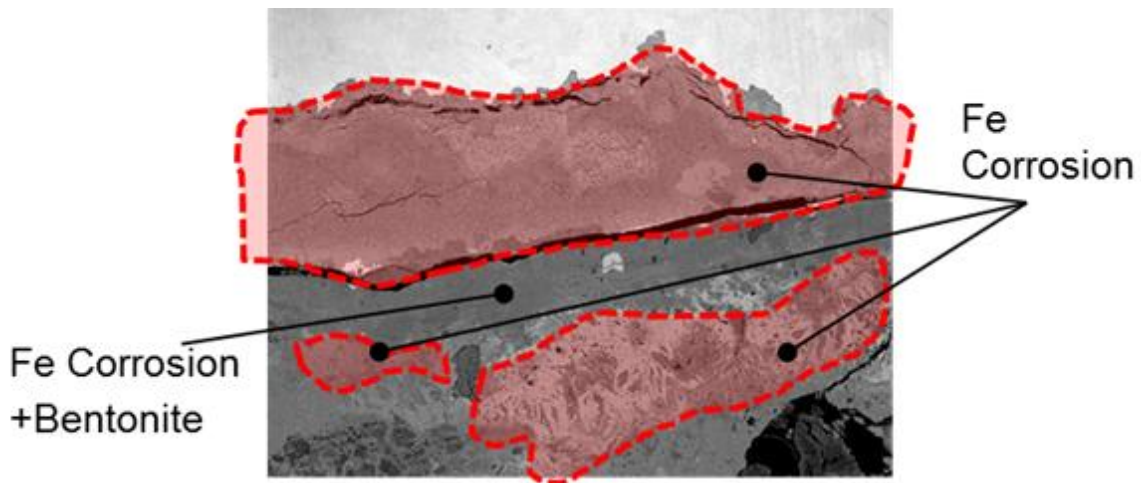


Fig. 52: Distribution image of metal corrosion products.

b) Raman spectroscopy

Raman spectroscopy analysis was performed to identify the corrosion products. Points at different distances from the metal surface were analysed (Fig. 53).

Fig. 54 shows the Raman spectroscopy results. Points 1 and 2 which were within 0.002 mm from the Fe surface were identified as hematite. Point 3 was near the crack at 0.15 mm from the iron source; hematite and siderite are identified there. The peak intensity at Point 3 is weaker than that at Points 1 and 2.

The points further away from the cracks below 0.3 mm from the iron source were found to be mainly goethite at Points 4 and 5. Some hematite was also observed at Point 5. The mean observed goethite transformed from hematite was affected by water from the bentonite. Further away from the iron source below 0.7 mm, the corrosion products were mostly altered from hematite to goethite. Siderite whose formation seems to be favoured by the bentonite was also identified.

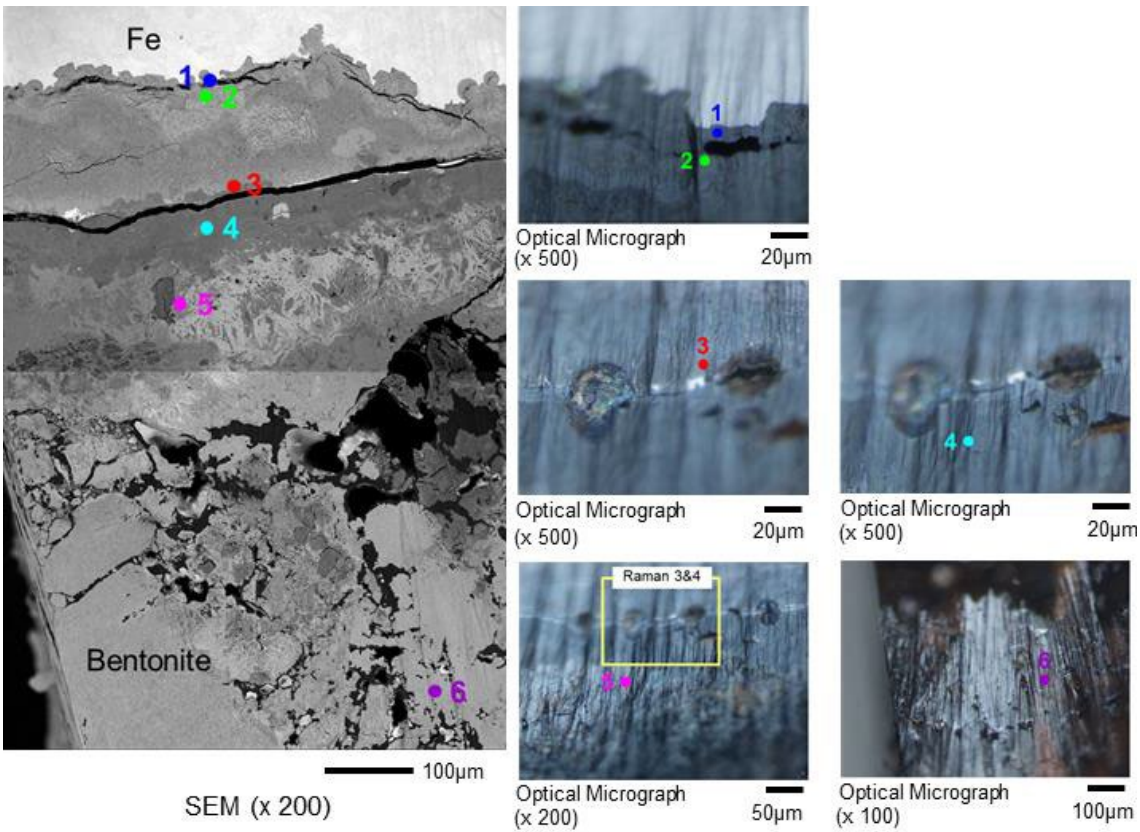


Fig. 53: Analysis points of Raman spectroscopy.

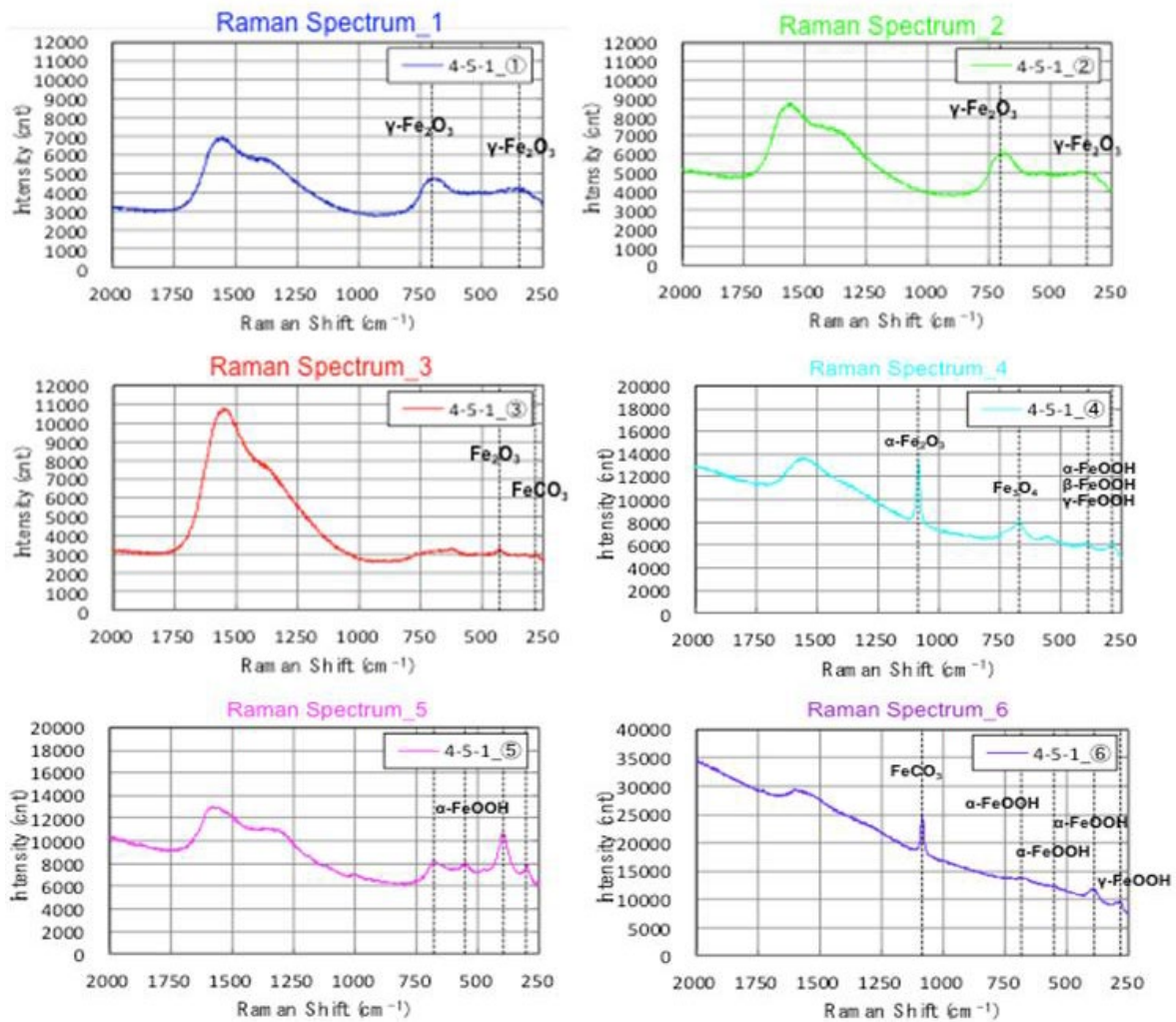


Fig. 54: Results of Raman spectroscopy.

4.3.4 Discussion and conclusion

This section describes the corrosion mechanism of carbon steel exposed to bentonite. We have formulated a hypothesis based on experimental and analysis results as shown in Fig. 55.

In the first stage, the carbon steel corrodes at a low corrosion potential which is controlled by the iron metal and the thin oxide (magnetite) scale. The scale initially has some micro cracks. Next, H_2O and O_2 from the bentonite side penetrate into these cracks and reach the iron interface. The corrosion potential of iron is lower than that of magnetite. Thus, the inner iron layer behaves as an anode instead of the outer magnetite layer. As a result, the internal iron is corroded, and iron oxide as red rust is formed underneath the initial oxide scale. This corrosion phenomenon was also found at the surface of the dummy metal of M-S-35-1.

The difference between trivalent or bivalent iron corrosion products is determined by the presence of the internal oxidation state during the test. Molecular O_2 moved from the inner gap between the bentonite block and the metal of the liner or heater as in the ABM experiment (Wersin et al. 2015). Furthermore, some O_2 in the bentonite pores and porewater was present (NAB 14-55 and NAB 16-13).

For a laboratory experiment (Tsushima et al. 2003) under limited initial oxygen conditions, using carbon steel (SM400B) with a Fe_3O_4 layer extending into bentonite (Kunigel-V1), the corrosion product was a mixture of FeCO_3 and $\text{Fe}_2(\text{OH})_2\text{CO}_3$. The iron in these minerals was in the bivalent form. The metal with Fe_3O_4 of other experiments where no care was taken regarding the surrounding oxygen before the sample setting (Uyama et al. 2016) formed trivalent iron as Fe_2O_3 or FeOOH . In many cases, FeOOH was found near the bentonite because this side contained water.

In the next step, the corrosion occurring under the surface oxide scale as magnetite that existed already at installation, is peeled off because of expansion of inner corrosion of the metal.

After the oxygen surrounding the FEBEX-DP sample was consumed, bivalent iron was formed as FeCO_3 on the bentonite side. This phenomenon looks like the experiment under limited oxygen. Therefore, it is suggested that the same reaction occurred in the BM-C-35-1 sample of FEBEX-DP.

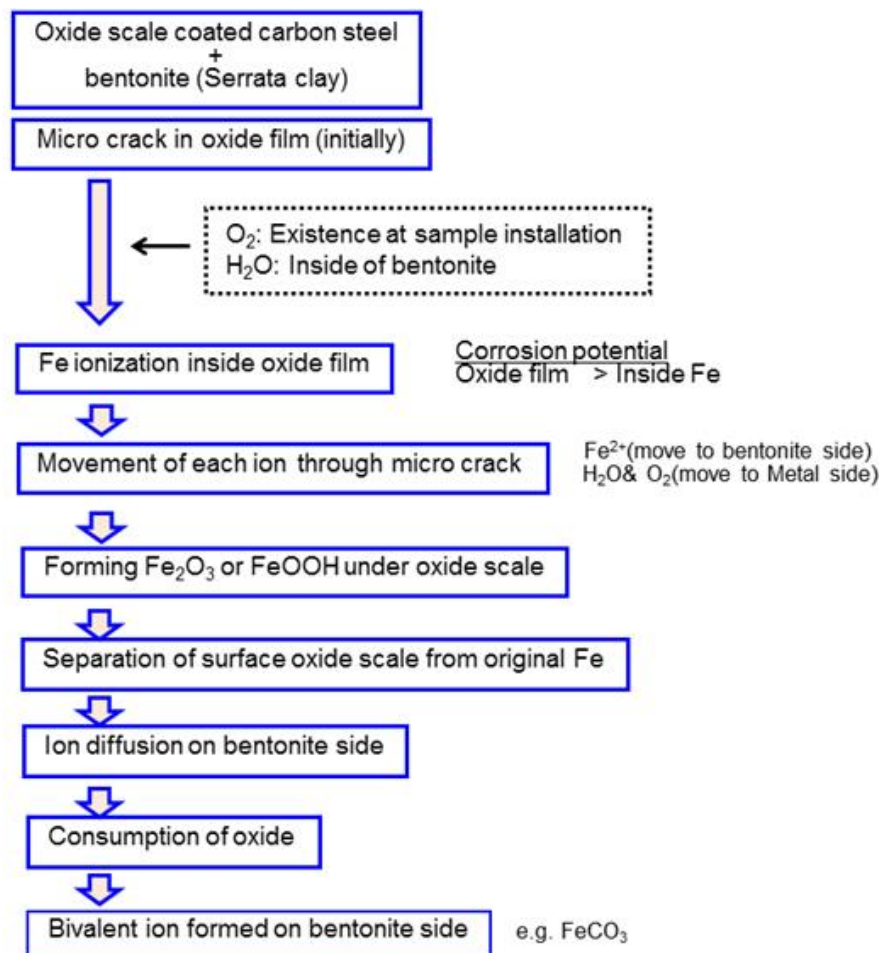


Fig. 55: Proposed corrosion mechanism in the engineered barrier.

Another phenomenon was that iron movement in bentonite was found on the bentonite side like the ToF-SIMS result of BM-C-35-1 and the observed cross section of the sample photo after the accelerated corrosion test.

Ionization of Fe from corrosion affects the surrounding bentonite. Especially, this trend is observed at high ionization tendency on the bentonite side as K, Ca, Mg, Na. There are some iron and other ions of the aggregations on the bentonite side that were confirmed by ToF-SIMS results. Fig. 56 is a cross-section image of Kunigel-V1 and carbon metal after a corrosion test. A reddish rusty ring is clearly found around the carbon steel wire around the anode. Fig. 57 shows a picture that in the frontal part of the fissurometer box after partial removal of the bentonite layer 45. The ring shaped red rust found some distance away from the metal would represent a similar mechanism of Fe ion diffusion. Therefore, the appearance of a red rust layer at the bentonite side would be confirmed in the place that has an iron rich phase. However, this phenomenon is very complex and the process understanding needs to be improved in further studies.

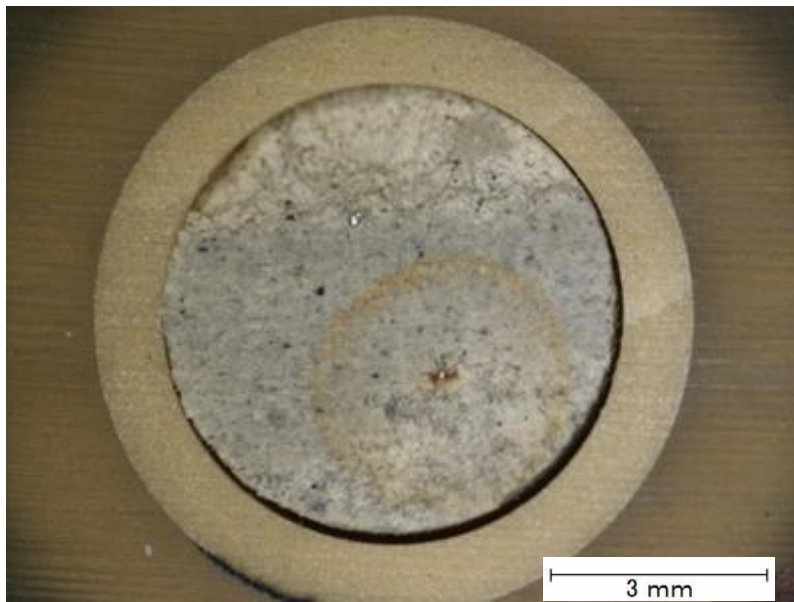


Fig. 56: Cross-section image of Kunigel-V1 and carbon metal after corrosion test.



Fig. 57: Picture at top of the fissurometer box after partial removal of bentonite layer 45 in FEBEX-DP project.

4.4 Fe-bentonite interface study of Uni Bern

4.4.1 Context and goals

The FEBEX experiment consists of an *in-situ* full-scale engineered barrier system (EBS) test for the disposal of high level waste (HLW). It involved a steel liner surrounded by a clay barrier, enclosing two heaters. Heating (100 °C) was started in 1997, and a partial dismantling was performed in 2002. The first heater was then replaced by a dummy cell. The second dismantling was initiated in 2015. Most of the retrieved steel pieces (liner, heater, dummy cell, extensometers, fissurometers, drilling rods, cable ducts) appeared to be more or less corroded. The impact of corrosion could also be observed in some zones of the bentonite surrounding those corroded objects, appearing as concentric and coloured (red, orange, blue) halos (Fig. 58).

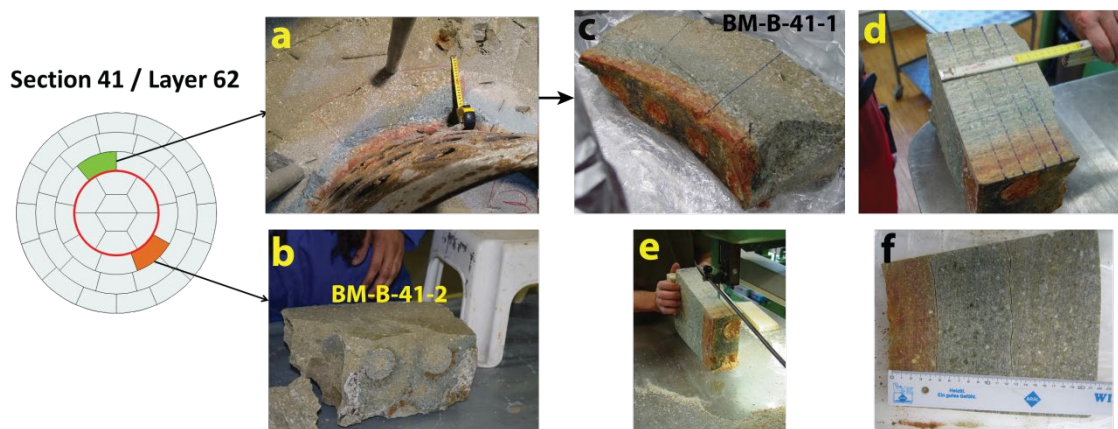


Fig. 58: Sampling of corrosion features observed in FEBEX DP experiments, here located at the interface between the liner and the bentonite blocks of the layer 62.

Pictures c to d detail some steps of subsampling block BM-B-41-1.

Samples from various locations were collected and stored at the institute for Geological Sciences in Bern. The study was mainly focused on a block from the upper part of bentonite layer 62 (Fig. 58a) and aimed at understanding the impact of the extended corrosion of steel on the bentonite block, particularly regarding the diffusion of Fe into the bentonite. Such an investigation is challenging for several reasons. It merges two large and still developing fields of research, i.e. corrosion and clay chemistries. The redox aspects add difficulties as a retrieved sample can undergo post-transformations upon exposure to the ambient atmosphere, further complicating the diagnosis of the *in-situ* Fe-bentonite interactions. It requires specific care in the sample handling, storing and analysis. Thus, dismantling is a critical part as the events occurring during this first step will influence the following steps. Finally, the low amount of clay samples usually retrieved in such Fe-bentonite experiments (at most a few mm thick crust from the interface with steel) also limits the possibilities of investigation. In this study, however, the 20 kg block ($\sim 480 \times 125 \times 220$ mm l*w*h) enabled us to investigate a large amount of material. Moreover, the large block could be retrieved and collected with minimal exposure to the atmosphere (few hours) before being packed in argon purged, evacuated bags.

4.4.2 Materials and methods

The block BM-B-41-1 was first subsampled at the institute, using a band saw (bi-metal M51, Fig. 58c-d). Twenty-millimeter-thick slabs were extracted from the middle part and selected for the present study. All other parts were immediately repacked in purged bags and stored inside a cool room (5 °C). Some of these slabs were sent to SKB (Daniel Svensson) and to the University of Bristol (Macarena Leal Olloqui). The study of these is presented in Sections 4.5 and 4.8, respectively.

Two different sampling routines were further applied:

On the one hand, 6 contiguous blocks (36 – 37 mm long, 20 mm large) were cut and vacuum-embedded in epoxy resin, and further polished (Fig. 59, left). The polished surfaces, forming a profile perpendicular to the interface and crosscutting the entire block were analysed by SEM-EDX to obtain backscatter images and chemical maps, and to establish chemical profiles of the major elements perpendicular to the interface. Raman spectroscopy was also employed to identify some of the numerous accessory phases present in the matrix, focusing on the Fe-bearing species. One polished section was prepared which was obtained from the significantly less impacted block BM-B-46-2 (Fig. 59, right).

On the other hand, one slab was almost entirely powdered in a glovebox (Fig. 60). 5 – 6 mm thick layers parallel to the interface were progressively scraped off the slab (using a ceramic knife), and stored in individual tubes. 30 different samples (~ 20 g) were separated (i.e. up to 18 cm deep in the block). The outermost layer was also powdered. All samples were analysed by XRF. Some of these samples were then selected for more in-depth characterisation (^{57}Fe Mössbauer and XRD).

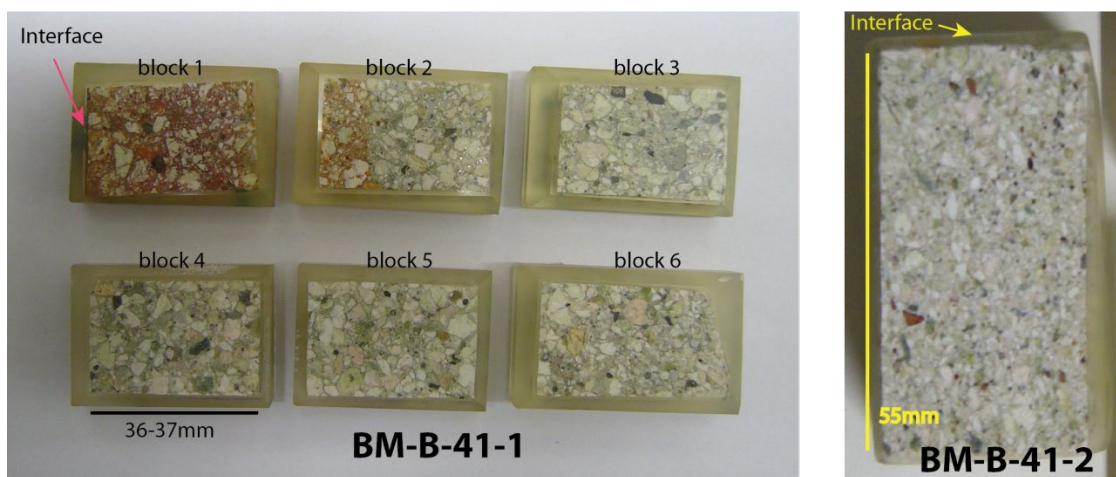


Fig. 59: (Left) 6 contiguous polished surfaces of a cross section of block BM-B-41-1 and (right) one polished section of block BM-B-41-2.

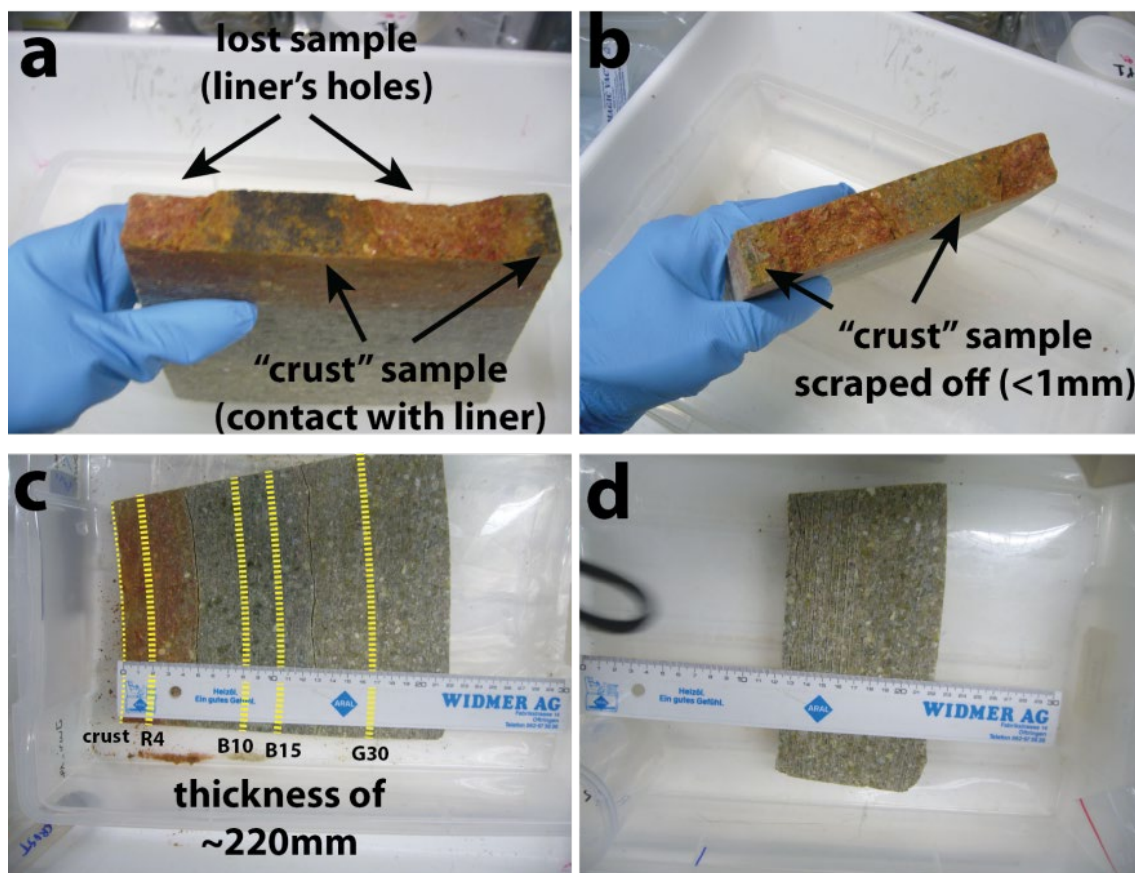


Fig. 60: Powder sampling steps in the anaerobic chamber, (upper) original contact with the steel liner prior (a) and after (b) scrapping off the preserved contact area, (bottom) progression of the slicing of the block.

Dashed yellow lines on picture (c) indicate the location of the samples studied by Mössbauer spectrometry.

Polished blocks

SEM-EDX and chemical profiles

The uncoated sample surface was examined in a SEM (Zeiss EVO-50 XVP) equipped with a EDAX Sapphire light element detector in low-vacuum mode (10 – 20 Pa) with a beam acceleration of 20 kV, a sample current of 500 pA, and a working distance of 8.5 mm. The beam current was adjusted to yield a dead time of 8 – 15 % for EDX analysis (energy dispersive spectroscopy). EDX element maps with a resolution of 256×200 pixels were acquired using a dwell time of $200 \mu\text{s}/\text{pixel}$. Mappings were usually conducted with a magnification of $80\times$, which thus results in pixel size of c.a. 10 mm^2 and maps of c.a. $140 \times 110 \text{ mm}$. Contiguous mappings were collected in series, in order to obtain large scale mosaic-like elemental mappings (Fig. 61). Mapped elements generally included C, O, Na, Mg, Al, Si P, S, Cl, K, Ca, Ti and Fe. The total grid dimension was usually of 26 – 27 sectors along the x-axis and 8 sectors along the y-axis. Given the parameters of analysis (resolution, dwell time), such mappings take 12 hours of acquisition time per block. Output data from the operating software (Smartsem®, ZEISS for the SEM part and Genesis®, AMETEK for the EDX part) were collected and treated with an in-

house Matlab algorithm in order to establish chemical profiles (wt%, at%), large-scale elemental mappings and backscatter images.

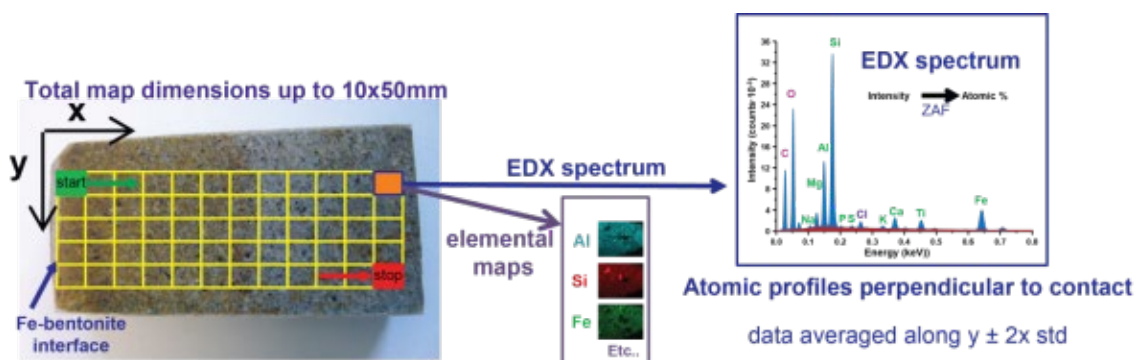


Fig. 61: Schematic of the method for producing large-scale elemental mappings and chemical profiles.

In the present report, the main data obtained from the SEM-EDX survey are presented as "Al-normalized" chemical profiles of the major elements (Si, Fe, Mg, Ca, Na, K, S). Such a diagram represents the atomic ratio of a given element over aluminum as a function of the distance to the interface. Chemical profiles of the major elements as atomic% (including Al) are also displayed in the supplementary materials (Appendix C). The main assumption underlying this "Al-normalization" procedure implies that, amongst the probed elements, aluminum is the least likely to change in terms of amounts and spatial localisation (Ackermann 1980, Luoma 1990). It is the second major element of the bentonite. As it is the least likely element to be dissolved and transported elsewhere and can be thus used as a proxy for tracking the local variations of all the other probed elements relative to the original bentonite. The so-called "Al-normalized" values were computed directly from the ZAF quantification results. For a given element the ratios of the atomic proportions of this element over the aluminum content calculated in each sector (of a given column of the analysis grid) were averaged. The error bars accounts for two times the standard deviation. In the case of Fe, the mapped sectors containing large (0.1 – 1 mm) goethite grains from the original FEBEX matrix were not included into the profile (further detailed below).

Raw EDX data were corrected using individual Standard Element Coefficients (SEC) factors for each element. These factor were determined from the EDX analysis of seven different raw bentonites (not including FEBEX, but of very similar composition) for which references XRF data were also available (Svensson et al. 2011). They are dependent on sample type and on the device. They were determined about a year before, in the framework of the ABM2 investigations (Hadi et al. subm.). Even though the same apparatus is used in the present study, one cannot rule out that some parameter values may have slightly changed since then. The determined SEC facotrs usually range between 0.9 and 1.1 (1.3 for Na), meaning that correction usally accounts at most for $\pm 10\%$ of the measured value. The actual difference between the presented determination and reality can thus be expected to be of the same order of magnitude at most.

A series of further backscatter images and chemical mappings are available from the authors upon request.

μ-Raman spectroscopy

Raman spectroscopy was performed with a Jobin Yvon LabRAMHR800 instrument, consisting of an Olympus BX41 confocal microscope coupled to an 800 mm-focal-length spectrograph. An unattenuated He–Ne laser (20 mW, polarized 500:1) with an excitation wavelength of 632.817 nm (red) was focused on the sample surface and the Raman signal was collected in reflection mode. The sampled volume was a few μm^3 using a 100x objective. Spectra were measured in Raman shift intervals of 150 to 1'400 cm^{-1} (in 5 steps of 250 cm^{-1}). Acquisition time for each step was 2×15 s, i.e. 2.5 minutes in total. Acquisition time was extended for some analysis in the clay matrix. However, only some of these latter measurements were preformed, because fluorescence issues caused an important background in spectra from the clay matrix and the epoxy resin. As for SEM-EDX, analyses were performed on polished surfaces prepared aerobically and thus unprotected during analysis. Raman spectroscopy was therefore performed above all to identify the original accessory Fe phases of the bentonite. The spectra were recorded with Labspec V4.14 software (HORIBA Scientific). Identification of the species was done with the help of the spectra library included in the HORIBA Edition of the KnowItAll®. The spectra presented in this report indicate the name(s) of identified specie(s) and the corresponding reference number(s) in the library, which actually regroup several libraries for organics, minerals and gemstones (such as Minlab v3 or RRUFF (Lafuente et al. 2015)).

Powdered samples

Powdered samples were collected in an anaerobic chamber (Fig. 60). Once the "crust sample" (the actual contact with the liner) was scraped off (< 0.5 mm), 5 – 6 mm thick layers parallel to the interface were progressively isolated with a ceramic knife. Samples were named after the colour of the sampled bentonite and the order of sampling. The names and corresponding distance to the interface are indicated in Fig. 58 and Appendix C, Tab. 1 and 2.

Each sample was first gently crushed down to ~ 5 mm pieces and placed into a glass tube. Several of these tubes were then placed into a plastic pot for the freeze-drying step. This step was carried out outside the anaerobic chamber and care was taken to minimize exposure of the sample to the ambient atmosphere. The pot was placed into the airlock of the anaerobic chamber and a cycle of vacuum followed by rapid depressurization of the chamber was applied in order to vacuum pack the pot. The pot was then dipped into liquid nitrogen for 20 min., and freeze-dried overnight (in a Leybold Heraeus GT2 freeze dryer). The higher vacuum reached in the freeze dryer allowed to reopen the vac-sealed pots. Once dried, the chamber was quickly repressurized to vac-seal the pot again, and to transport it back to the anaerobic chamber. Samples were then further crushed by hand in an agate mortar and stored in glass tubes. A supplementary tube was included with the samples; it contained a few grams of green rust and ferrous hydroxides. This additional tube was intended to act as an oxygen scrubber in case of accidental exposure of the samples upon the freeze-drying step (the powder was placed close to the lid of the pot, while the samples were rather at the bottom). Dramatic colour change of the Fe hydroxides (from black-green or blue to red-brown) would also indicate such an event. A batch of raw FEBEX bentonite was also provided by AITEMIN (as a coarse powder, and also as a block). The coarse powder was further crushed in an automatic tungsten carbide mill and used as a raw material for spectroscopic characterisation and diffraction. A portion of the raw bentonite block was also gently crushed by hand, and various coloured aggregates were separated (Fig. 62). They were further crushed by hand in an agate mortar and analysed by XRD to determine the mineralogical composition.

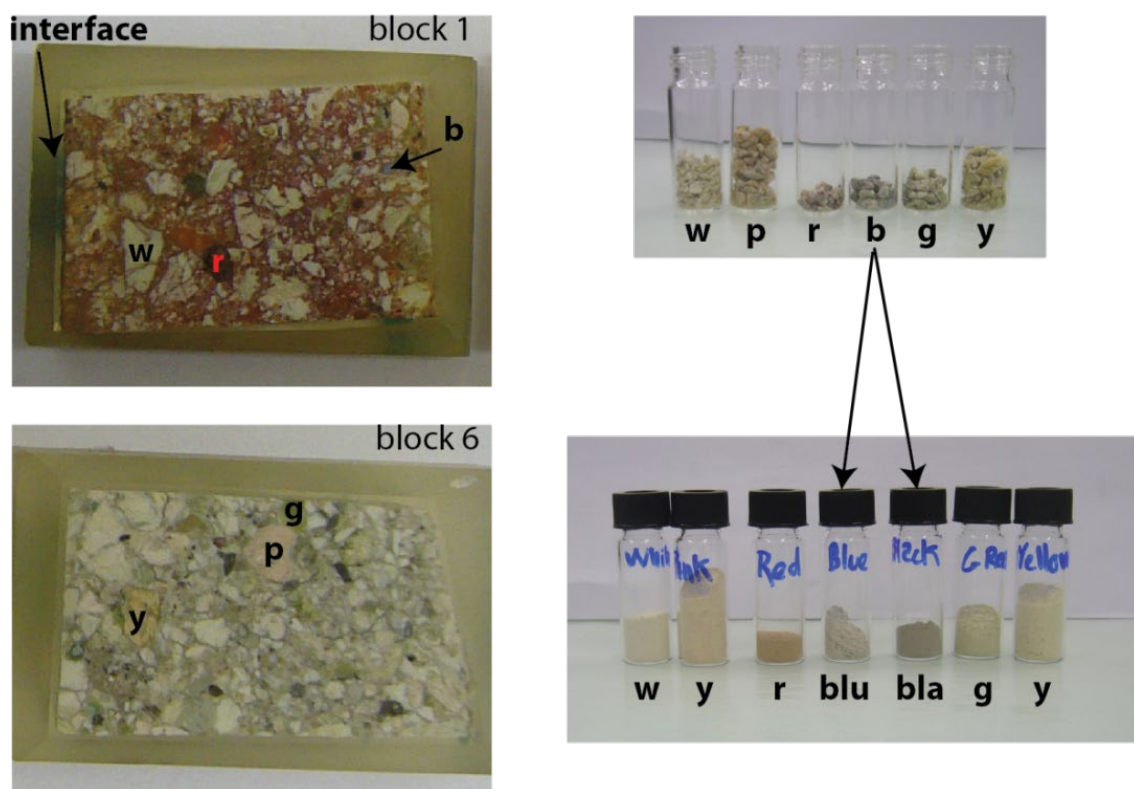


Fig. 62: (left) 2 polished block from block BM-B-41-1 and (right) colour aggregates that were collected in the raw material and powdered.

Letters indicate the colour of the sample (w: white, p: pink, r: red, b and blu: blue, bla:black, g: green, y:yellow).

XRF analyses were conducted at the University of Fribourg, Department of Geosciences. Glass pellets were made by fusing a 1:10 mixture of sample powder and Li-tetraborate at 1150 °C. XRF analyses of major elements were performed on a Philips PW 2400 spectrometer and corrected with the internal Philips software X40 on the basis of a set of international rock standards. Loss on ignition (LOI) was determined by mass difference before and after fusing. The resulting data are displayed in Appendix C.

The Mössbauer spectra were recorded at room temperature (RT, 295 K) and at 77 K using a constant acceleration spectrometer and a ^{57}Co source diffused into an Rh matrix. Velocity calibrations were carried out using a Fe foil at RT. The values of the hyperfine parameters were refined using a least-squared fitting procedure with a discrete number of independent quadrupolar doublets and magnetic sextets composed of Lorentzian lines. The values of isomer shift are reported relative to that of the Fe spectrum obtained at RT. The proportions of each Fe species were established from the relative spectral area, assuming thus the same values of the f-Lamb-Mössbauer factors characteristic of each phase. Further description of the fitting procedure is detailed in the discussion of the data.

XRD analyses of samples from block BM-B-41-1 were conducted using an Anton Paar domed sample holder for air sensitive materials (equipped with a polycarbonate dome). The powdered samples were front-loaded on the sample holder in the anaerobic chamber, the surface was flattened with a glass slide and the dome closed before out of the chamber. Sample were usually measured coarse-grained. The raw bentonites were also analysed without the dome. The

samples were analysed with PANalytical X'Pert PRO X-ray diffractometer, and recorded using Cu K α radiation with a wave length of 1.54 Å at 40 mA and 40 kV. The samples were scanned from 5° to 60° 2 θ angle using a step size of 0.0167 °2 θ and a time of 1'600 s per step, with automated divergence slits. The sample was spun all along the measurement, at a rate of a revolution every 8 seconds. Raw material and coloured fractions isolated from raw material (Fig. 62) were analysed without the dome.

4.4.3 Results

The main results of the SEM-EDX and Raman investigation of polished surfaces are presented in a first part. Data obtained on powder samples are detailed in a second part.

Polished blocks

SEM-EDX investigation allowed establishing a chemical mapping of the major elements (including C, O, Si, Al, Fe, Mg, Ca, Na, K, S, Ti) of a large portion of the polished section (a total surface of 22 cm² on overall for block BM-B-41-1 and 40 cm² for block BM-B-41-2). Backscatter images were also collected on most of the mapped area (but not all due to technical problems with the SEM). These data are not presented in the present report, but are available upon request. This section presents the "Al-normalized" chemical profiles of the major elements perpendicular to the interface and throughout the entire block BM-B-41-1 and some of the notable features relative to Fe originating from the original matrix and from the corrosion of the liner.

Chemical profiles of major elements in block BM-B-41-1

Fig. 63 displays the "Al-normalized" chemical profiles of major elements Si, Mg and Fe while Fig. 64 displays the profiles of less abundant elements Ca, Na K and S, obtained with SEM-EDX and XRF. Reference values inferred from inter-laboratory XRF analysis of the raw material are displayed on the diagram (reference data in NAB 16-68). A "bulk" value is also indicated, it corresponds to the average value measured in the outmost 4 cm of the studied block (by SEM-EDX), assumed to be far away from the interface and thus exempt of perturbations.

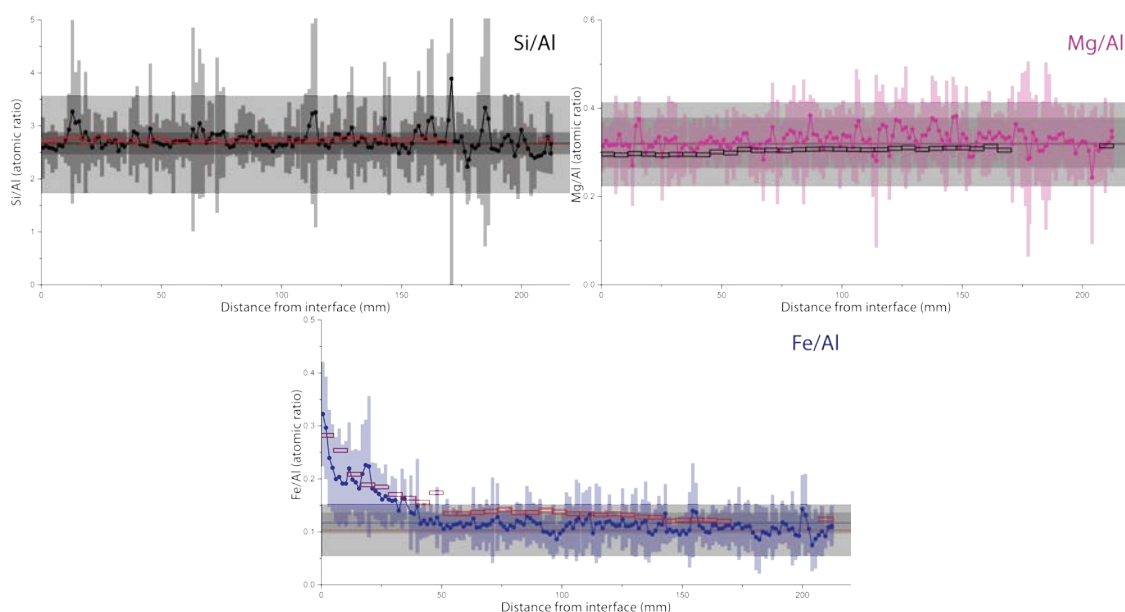


Fig. 63: "Al-normalized" chemical profiles of major elements Si, Fe and Mg in block BM-B-41-1 from Section 62.

Empty rectangles represent XRF values on powdered samples (Appendix C, Tab. 1 and Tab. 2). Horizontal lines of the same colour as the data set represent average reference values measured in raw material, dark grey areas account for 2x the standard deviation on several measurements done in different laboratories (reference data in NAB 16-68). Horizontal lines of contrasting colour represent average "bulk" values in the outermost area of the block (between distance of 180-and 220 mm), light grey areas account for 2x the standard deviation.

Data suggests that there are no net changes in Si/Al throughout the entire profile relative to the original material. Localized peaks in Si content can be ascribed to the presence of large grains of Si richer phases in the heterogeneous bentonite matrix (e.g. quartz, cristobalite, tridymite). EDX and XRF data are very consistent.

In addition, EDX data tends to suggest no net changes in Mg/Al relative to the original material either. However, fluctuations in content are less pronounced at the vicinity of the interface (at distance < 70 mm) than in the rest of the block, where Mg content seems to be slightly increased. XRF data on powdered samples indicate in fact that there is a slight decrease in Mg content when progressing toward the interface.

Dealing with Ca content, EDX data suggest a slight global decrease but this is within the uncertainty of the reference data. Similarly to Mg, fluctuations in content are less pronounced at the vicinity of the interface (at distance < 100 mm) than in the rest of the block. Again, XRF data indicate in fact that there is a slight decrease in Ca content when progressing toward the interface.

With regard to K and S content, data suggest no changes relative to the raw material. A slight decrease is observed with EDX but it remains within the uncertainty of the reference data. The small and constant difference between XRF and EDX data can be ascribed to an underestimated SEC (Standard Element Coefficient) factor for these two elements, and their lower contents close to or below the quantification limit of EDX. The very low content in S (< 0.1 wt%) indicates that the pyrite content in the FEBEX bentonite is also very low (i.e. also < 0.1 wt%).

The S peak visible at a distance of ~ 170 mm is due to the presence of a large gypsum (or anhydrite) grain (from the original FEBEX material).

The drop in Na content toward the heater is more obvious, and is observed throughout the entire profile. As for K and S content, the SEC factor may be slightly underestimated, given the difference between EDX and XRF data.

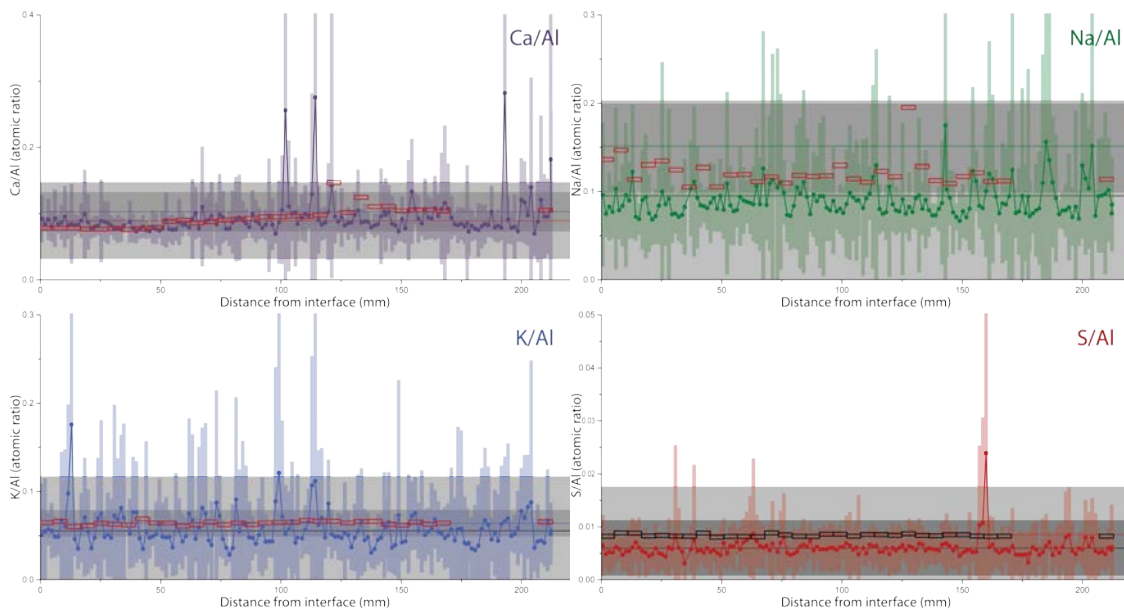


Fig. 64: "Al-normalized" chemical profiles of minor elements Ca, Na, K and S in block BM-B-41-1 from Section 62.

Empty rectangles represents XRF values on powdered samples (Appendix C, Tab. 1 and Tab. 2). Horizontal lines of the same colour as the data set represent average reference values measured in raw material, dark grey areas account for 2x the standard deviation on several measurement done in different laboratories (reference data in NAB 16-68) Horizontal lines of contrasting colour represent average reference values in the outermost area of the block (between distance of 180 and 220 mm), light grey areas account for 2x the standard deviation.

The most obvious changes are observed in the Fe/Al ratio (Fig. 63). Data clearly indicate a progressive increase of Fe content when progressing toward the interface, starting from a distance between 150 and 100 mm from the interface. A very slight decrease in Fe content is observed at greater distance but it falls within the uncertainty of reference data. Thus, data may also suggest no changes in that area.

Comparison between blocks BM-B-41-1 and BM-B-41-2

Fig. 65 displays the chemical profiles for major elements Si, Mg and Fe in the visually significantly less impacted block BM-B-41-2. The data relative to block BM-B-41-2 are also displayed. Chemical profiles of other elements (Mg, Ca, Na, K and S) are displayed in Appendix C, Fig. 3).

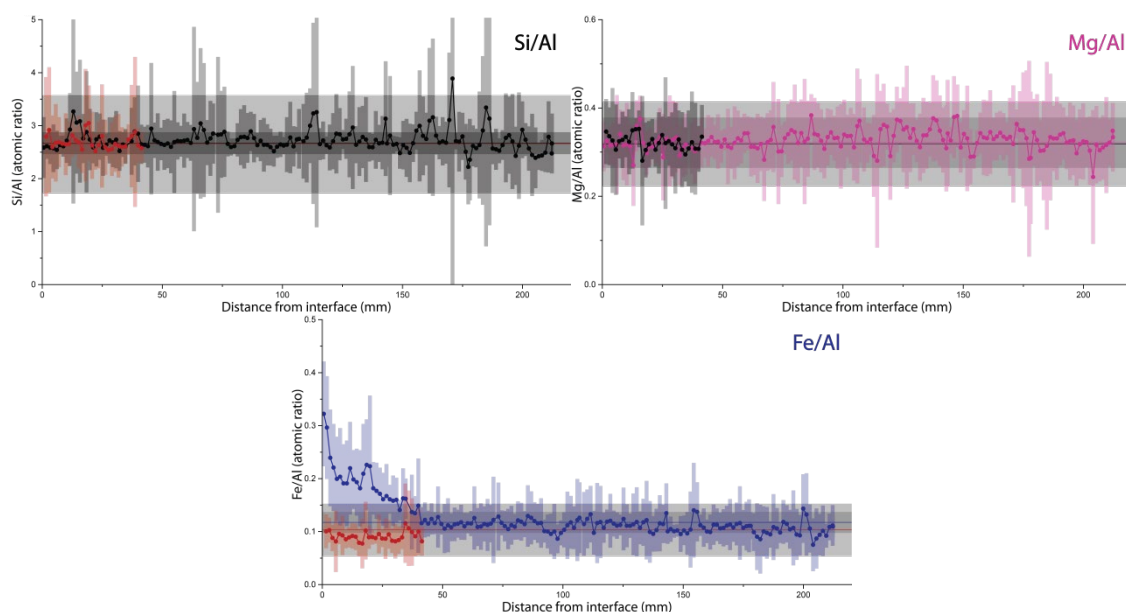


Fig. 65: "Al-normalized" chemical profiles of major elements Si, Mg and Fe in block BM-B-41-1 (long profile, ~ 220 mm) and block BM-B-41-2 (short profile, ~ 40 mm) from Section 62.

Horizontal lines and grey areas represent same data as in Fig. 65 (i.e. reference and bulk values).

Chemical profiles of all the major elements in block BM-B-41-2 show that there is no change at all, relative to the original material. All profiles are flat and consistent with the reference value. A slight downward shift is observed for data with respect to Fe and S, not only regarding reference XRF values, but also regarding the levels measured in the outer portion of block BM-B-41-1, assumed to be the least impacted of the sample. This can be attributed to underestimated SEC factors.

Accessory iron phases in FEBEX bentonite

According to previous characterizations on raw FEBEX material (Villar et al. 2006), most (at least 80 %) of the Fe should be present in clay minerals. Still, a great variety of accessory Fe-bearing species can be found in the matrix. The identification of these species is, however, rare in the literature. A better knowledge of this presence as accessory phases is of importance for establishing a profile of the "background Fe" present in the bentonite and to understand the further changes in Fe content at the vicinity of the interface with the liner.

Raman spectroscopy was primarily attempted to identify the Fe accessory minerals present in the FEBEX material, occurring as μm - to mm -size crystals and easy to spot from microscope images. This method is more difficult to apply for the clay matrix because of high fluorescence of the sample. Mixing with epoxy resin further complicates such analysis. Some analyses were, however, performed at the vicinity of the interface and are presented in the next section. This section is focused on pre-existing Fe-bearing species. Various Fe-rich phases could be observed scattered in the FEBEX matrix. Only a fraction could be easily discriminated and identified by Raman spectroscopy. Fig. 66 displays some examples of phases that could be identified on polished surfaces.

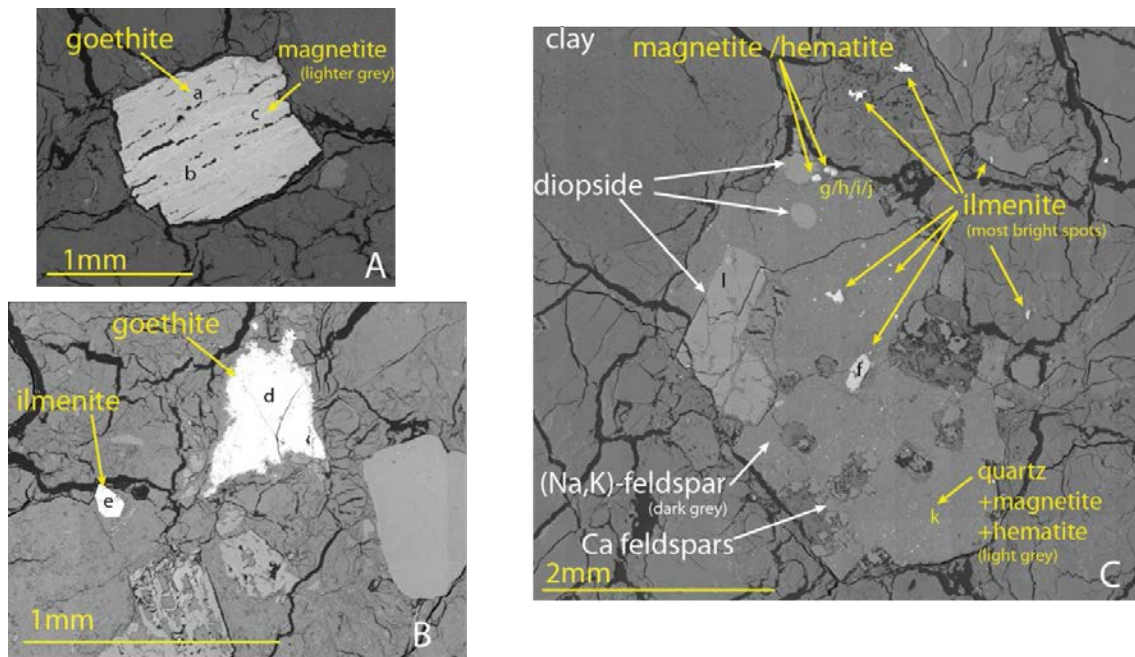


Fig. 66: SEM pictures of some ferruginous minerals found in the FEBEX matrix. Letters indicate spots where Raman spectroscopy was performed (spectra shown below).

The main accessory Fe-bearing phase encountered in the FEBEX bentonite is goethite (Fig. 66A and Fig. 66B). It can be found as very large grains (from μm to more than 1 mm), as illustrated in Fig. 66A & Fig. 66B and Fig. 68A. The mapped sectors where these grains were found were not taken into account when establishing the chemical profile of Fe (Appendix C, Fig. 1). Magnetite can often be found in the core of the larger grains (Fig. 67A and C). The second Fe phase easily identifiable is ilmenite. It is found in smaller (from μm to more than 100 μm) grains.

However, a notable quantity of accessory Fe appears to be sitting in submicronic grains, themselves enclosed in other accessory minerals, which are more difficult to discriminate on chemical mappings and SEM images. An example of such a complex assemblage is displayed in Fig. 66C. Medium (few μm) to large (100 μm) grains of either ilmenite or "hemato-magnetite" can be easily discriminated. This latter denomination refers to grains of Fe oxides presenting a core of magnetite (Fig. 67g) and a shell of low crystalline hematite/magnetite mixture (Fig. 67j). Still, the large grains enclosing those grains identified above are composed of a mixture of Na-K feldspars intermingled with quartz. This latter quartz contains in fact a significant quantity of Fe, occurring as magnetite and various forms of more crystalline hematite (Fig. 67k).

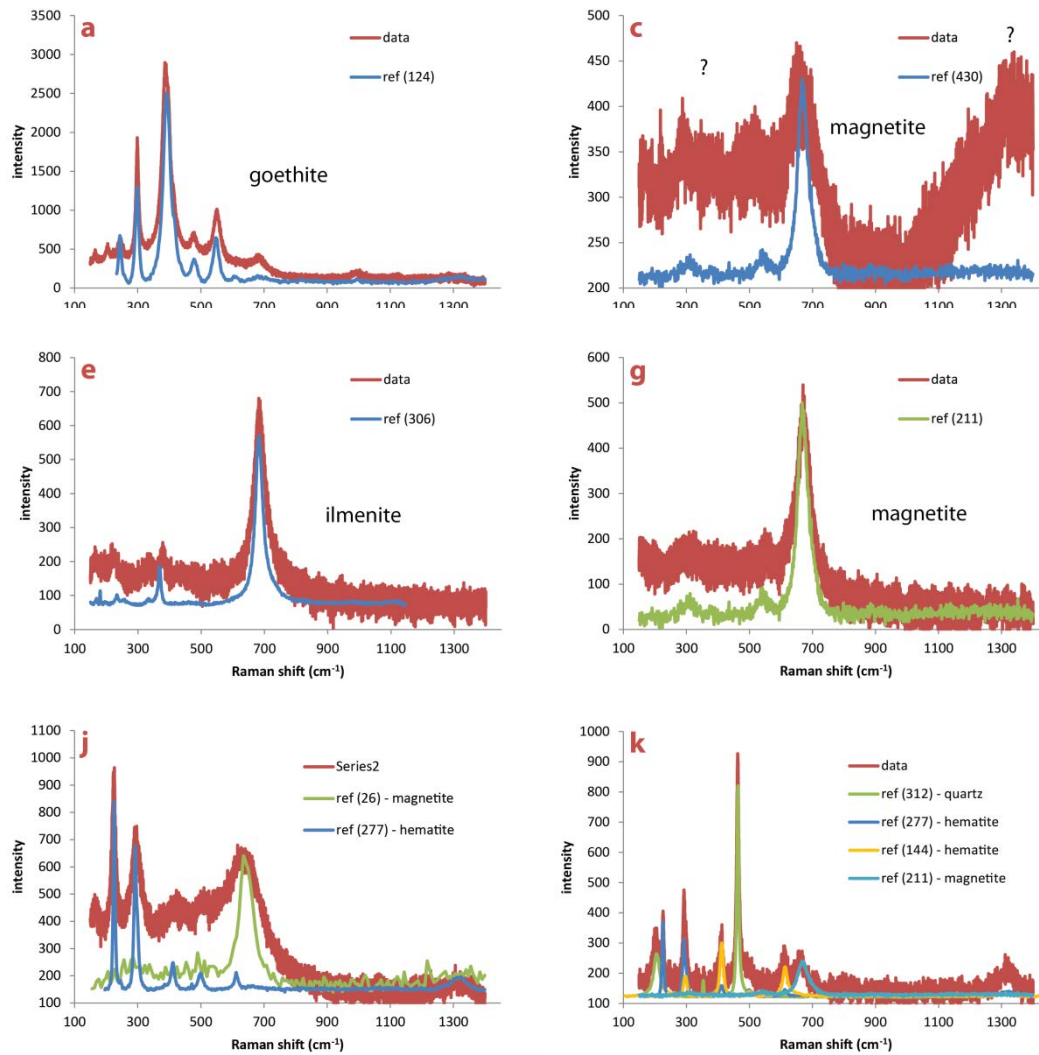


Fig. 67: Raman spectra collected at spots indicated in Fig. 66 (others can be found in Fig. 4, Appendix C).

Fe accumulation at the interface

Fig. 68 displays two backscatter images taken at the vicinity of the interface with the liner (the rim of the block is seen at the left side of each picture).

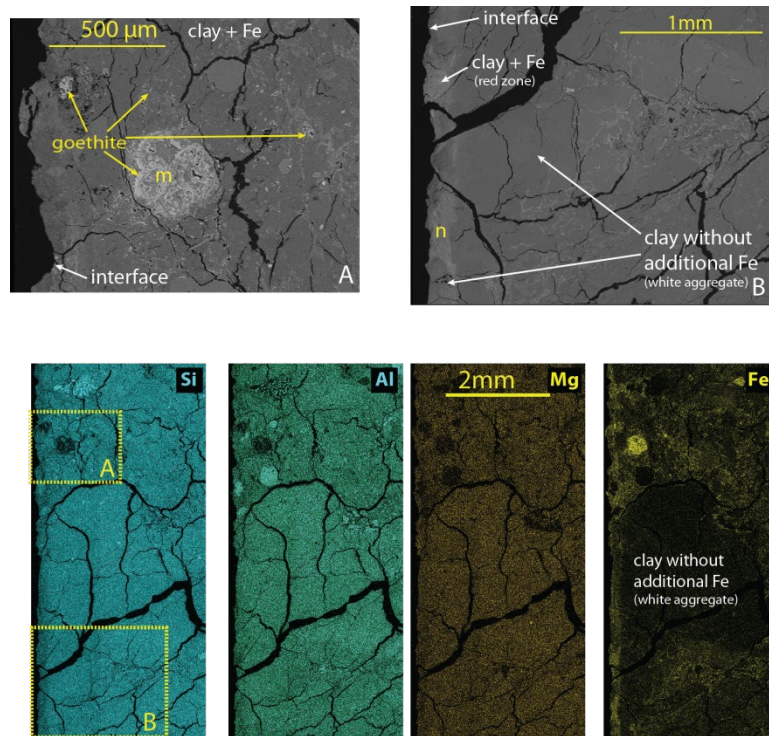


Fig. 68: (Upper) SEM pictures collected close to the interface between the FEBEX bentonite block and the steel liner. Letters indicate spots where Raman spectroscopy was performed (spectra shown below). (bottom) EDX mappings for the major elements in the same area. Positions of the two electronic pictures are indicated on the Si map.

The largest goethite features observed in Fig. 68A can be actually inferred to be part of the original accessory phases (removed when establishing chemical profile of Fe (Appendix C, Fig. 1)). Besides these two large grains, other bright spots (or rather lines) are observed in this area. They are usually only observed in the red zone of the sample, and especially close to the interface. These features indicate the zones where additional Fe (from the corroding liner) tends to be accumulated. The few clear Raman spectra collected in such a zone suggest that the main Fe-bearing species is goethite (Fig. 69n). Fig. 68B also shows that a clear contrast can be observed between the Fe-enriched clayey part of the bentonite and zones where no net Fe accumulation is observed. A clear contrast can be observed with the naked eye where the Fe-enriched clay appears red, while the other zone free of additional Fe appears as white spots (see block 1 of sample BM-B-41-1 in Fig. 59 and in Fig. 60). The strong red colouration of the bentonite can be due to the accumulation of goethite. The white zones are in fact mainly composed of smectite and amorphous silica (further discussed in next section).

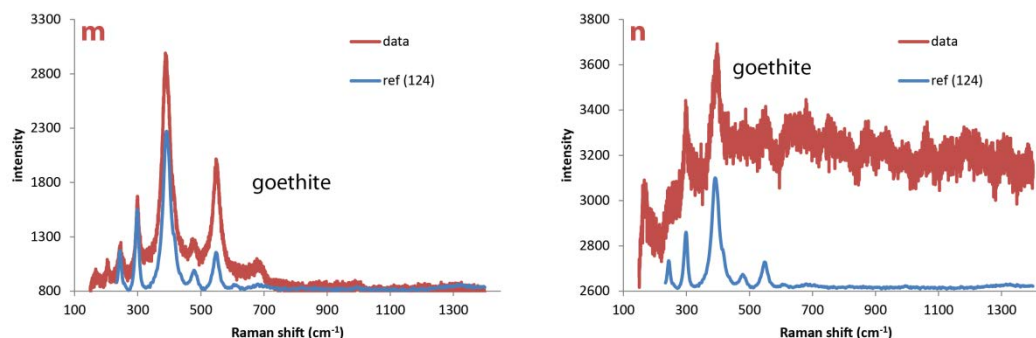


Fig. 69: Raman spectra collected at spots indicated in Fig. 64.

Powdered samples

Two different series of powdered samples have been investigated by XRD: the various coloured aggregates isolated from FEBEX raw material, and the profile sample collected in block BM-B-41-1 retrieved from the FEBEX-DP experiment.

XRD analysis of fractions collected from raw material

Data collected on 7 different coloured aggregates isolated from raw FEBEX bentonite (Fig. 62) are compared in Fig. 70. The diffractogram of raw material is displayed as a comparison. Some notable features are outlined. A list of identified species and their relative contribution (compared to the raw material) are indicated in Tab. 4.

The first aspect to be observed concerns the 001 line (around $6 - 7^\circ 2\theta$), corresponding to the basal reflection of the smectite(s) present in FEBEX bentonite. In standard conditions, i.e. 30 – 50 % RH, 25 °C, sodic montmorillonites display a basal spacing of $\sim 12 \text{ \AA}$ while calcic ones display a basal spacing of $\sim 15 \text{ \AA}$ because of the presence of one supplementary water layer in the interlayer (Ayari et al. 2007, Fernández et al. 2004). Mg exchanged montmorillonites display a slightly smaller (14.7 \AA) basal spacing than when Ca is present. These values are however valid in wet conditions and would be in fact lower in dryer conditions (as the thickness of the water layer decreases).

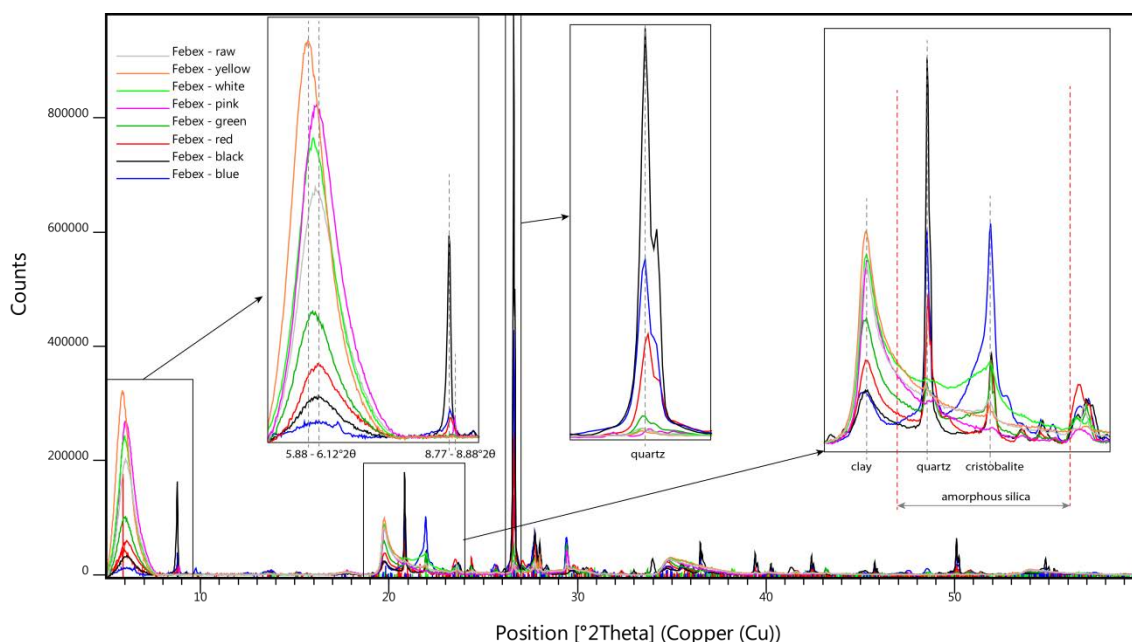


Fig. 70: Diffractograms of the various coloured aggregates isolated from FEBEX raw bentonite and the bulk raw material.

Raw FEBEX bentonite displays an average basal spacing of 14.6 Å. This is consistent with the exchangeable population in the pristine material (Villar et al. 2006), dominated by Ca ($37 - 43 \text{ meq}\cdot\text{g}^{-1}$) and Mg ($31 - 32 \text{ meq}\cdot\text{g}^{-1}$), and containing less Na ($24 - 27 \text{ meq}\cdot\text{g}^{-1}$) and K ($2 - 3 \text{ meq}\cdot\text{g}^{-1}$).

The various coloured aggregates clearly display different mineralogical compositions. Light coloured aggregates are higher in smectite than the bulk raw material (yellow > pink > white), while the dark coloured aggregates are in fact much lower in smectite (green > red > black > blue). A small shift is observed between the positions of the 001 line, accounting for a basal spacing varying between 14.4 Å in dark coloured aggregates to 15.0 Å in light coloured ones. This may account for the slight variation in the composition of the clay interlayer and/or structure. It was previously observed that the majority of the material (> 90 %) consists of illite- smectite mixed layers (10 – 15 % of illite layers) (Villar et al. 2006). No attempt to decipher the presence of interstratification was done in the present work. Present data do show, however, that the main clay mineral is montmorillonite. The lower clay content of dark coloured aggregates correlates well with their higher content in quartz (green < red < blue < black) and cristobalite (red~black << blue). This aspect is also consistent with the fact that these aggregates are notably harder than the light-coloured ones.

Another significant difference is seen regarding the accessory minerals, indicated by the reflection at slightly higher angles ($8.77 - 8.88^\circ 2\theta$). These reflections account for the basal reflection of clay minerals displaying a d-spacing shorter than smectites ($9.9 - 10.1 \text{ Å}$), due to the absence of interlayer water. This is explained by the presence of micas and/or more probably illite, as a better match with reference patterns is often found in the present case. The presence of a notable range of micas (biotite, sericite, muscovite) was noted in previous characterizations of the FEBEX bentonite (Villar et al. 2006). The present results suggest that such phases (mica and/or discrete illite aggregates) are more likely to be found in the dark coloured aggregates (red~blue << black) which are in fact poor in smectites.

The sample made of white aggregates stands out of the sample sets. On the one hand, a higher amount of clay than the bulk raw material is observed, as in the other light coloured samples. On the other hand, it also contains a higher amount of cristobalite than the dark coloured samples. In addition, the higher counts observed in the 20 – 23 °2θ region suggest the presence of amorphous silica.

Tab. 4: Minerals identified in the different FEBEX samples (total raw material and coloured aggregates) using XRD.

Mineral(s)	Sample							
	Raw	Yellow	Pink	White	Green	Red	Black	Blue
mmt/I-S*	+++	++++	++++	++++	++	+	-	--
Illite/mica	-	--	+	-	-	++	+++	++
Quartz	+	+	+	+	++	+++	+++++	+++++
Cristobalite	-	-	-	+	++	+++	+++	++++
Calcite	+	-	++	-	+++	++		+++
Na/K-feldspars	+	-	-	-	+	+	+	+
Na/Ca-feldspars	-	+	-	--	+	++	++	++
Pyroxenes**	-	-	-	-	+	+	+	+
Amorphous Si	--	--	--	++	+	--	--	+

* Montmorillonite and/or interstratified illite-smectite

** Include ideal pyroxene, pigeonite and diopside

Domed XRD analysis of samples from block BM-B-41-1

Data collected on 11 domed powdered samples from block BMB-B-41-1 are compared in Fig. 71. The diffractogram of the undomed raw material is displayed as a reference. It must be emphasized that the raw material was analysed undomed and as received (i.e. in standard conditions). The powdered samples from block BM-B-41-1 were analysed after anaerobic preparation including freeze-drying followed by crushing and storing in notably drier conditions. These were analysed under the dome, thus in slightly drier conditions of analysis compared to the undomed samples.

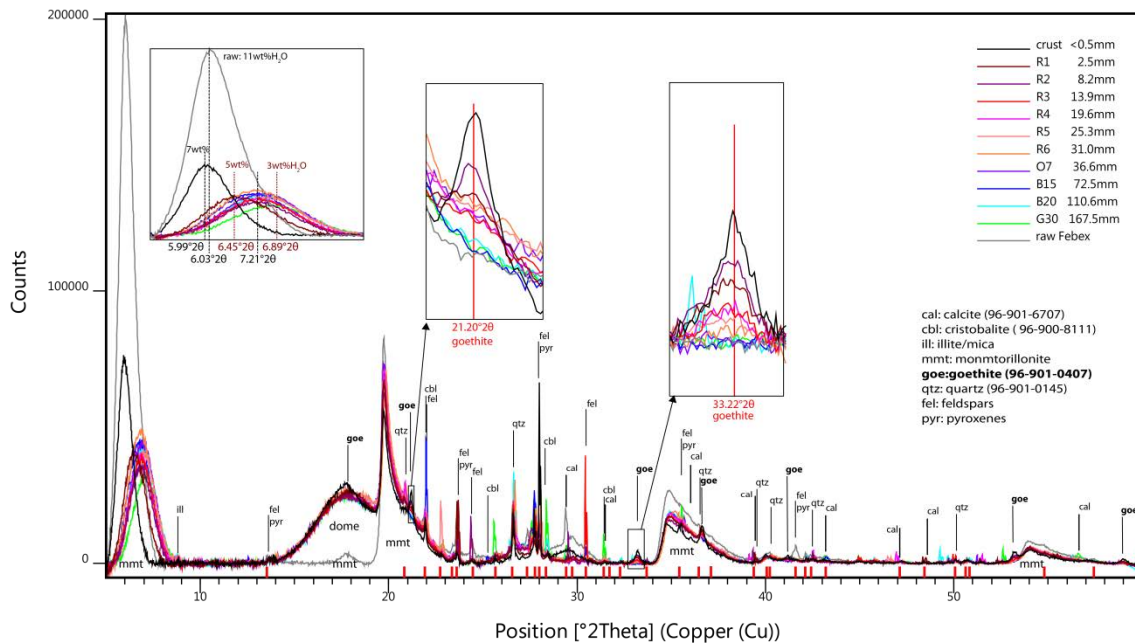


Fig. 71: Diffraction patterns of a series of powdered samples from block BM-B-41-1 (domed) and of the raw material (undomed).

Data collected on the FEBEX-DP samples (excluding the crust) exhibit lower basal spacings than the raw material, ranging from 12.2 (G30) to 13.7 Å (R2); most samples display a similar value of 12.8 Å. The crust sample displays a higher value of 14.8 Å, closer to the original value. The general observed drop in intensity is due to the presence of the dome. This trend is consistent with the slight variation in their water content (Appendix C, Tab. 1 & Tab. 2), ranging from 3 wt% in G30 to 5 wt% in R2, while most of the samples contain ~ 4 wt%. The crust sample contains a slightly higher amount of water (7 wt%). The raw sample was more hydrated (11 wt%). On the one hand, these results suggest that there are no clear differences in basal spacing between the various samples retrieved from FEBEX DP experiment (i.e. same spacing throughout the entire profile). On the other hand, there is a slight general increase of the basal spacing at the end of the experiment (compared to the raw material). This could be for instance induced by a slight exchange of Na for Ca and/or Mg. CEC measurements on samples retrieved in the partial dismantling of FEBEX-DP experiment in 2006 tend to support such an assumption (Villar et al. 2006).

Besides slight changes in basal spacing and features related to the dome (the mount located around 17 – 18° 2θ and the general drop in intensity), a notable number of differences is seen between the different samples above positions of 20° 2θ. More or less strong reflections are randomly observed in the retrieved samples. The majority can in fact be observed in the raw sample as well (indicated by red marks on the X-axis, Fig. 71), with more or less strong intensity, and can thus be ascribed to single reflections from original accessory minerals (due to preferential orientation). Most of these random reflections could be attributed to calcite, cristobalite, quartz, illite, micas, pyroxenes and feldspars.

A group of 7 reflections is not observed in the raw material but only in a group of samples from the red area and from the crust. Their positions correspond to goethite. Indeed, these data show that goethite has been accumulated in the retrieved samples, at distances up to at least 40 mm from the interface. This accumulation progressively decreases with increasing distance from the interface.

⁵⁷Fe Mössbauer spectrometry

Room temperature (300 K) and 77 K Mössbauer spectra of a set of FEBEX-DP samples (including raw material) are displayed in Fig. 72 and Fig. 73, and the corresponding hyperfine parameters are indicated in Appendix C, Tab. 3 & Tab. 4. The Mössbauer spectra consist of the superimposition of quadrupolar and magnetic features. They were fitted with minimal sets of features consisting in quadrupolar doublets and magnetic sextets, whose potential attributions are detailed in Tab. 5.

Tab. 5: Set of components used to fit the Mössbauer spectra and their possible attribution.

Component of the spectra		Possible attribution	Remark
oct-Fe(III)	Doublet	Clay minerals (mainly montmorillonite, but also some illite and or micas)	Present in any sample can decrease in febex-dp samples.
		Hematite	Accessory phase in raw material Only at 300 K
		Small (< 5 nm) grains of goethite	
		Medium (5 – 25 nm) grains of goethite	Only at 300 K
		Green rust	Only in retrieved samples
		Lepidocrocite, sorbed Fe (III), ferrihydrite	Lower probability
oct- Fe(II)	Doublet	Clay minerals (mainly illite and or mica, and probably montmorillonite), ilmenite	Present in any sample Can increase in retrieved samples.
		Siderite/ankerite, sorbed Fe(II), green rust, ferrous hydroxides, chuckanovite, Fe ₂ OH ₃ Cl, amakinite/ferrobrucite	Only in retrieved samples
Hematite	Sextet	Hematite, may also include some goethite (when q.s. < 0.2 mm)	Accessory phase in raw material Only at 77 k
Goethite	Sextet	Large (> 25 nm) grains of goethite	Only at 300 k
		Medium (5 –25 nm) to large (> 25 nm) grains of goethite	Only at 77 K

All observed doublets stand for paramagnetic high-spin octahedral Fe (further referred to as "para-oct-Fe"), but can also include superparamagnetic species at room temperature (e.g. small grains of goethite). The sextet stands for magnetic species (at room temperature only), and also include superparamagnetic species at low temperature.

Data collected on raw material indicate that ~20 % of Fe sits in magnetic (11 – 13 % goethite) and superparamagnetic (<9 % hematite) species. Magnetite may be present, but to a much lower extent (<2 % of total Fe). This is consistent with observations from SEM-EDX and Raman investigations suggesting that the most abundant Fe accessory phases are large grained goethite (i.e. magnetic at 300 K), but that notable amounts of smaller sized hematite grains (thus magnetic only at low temp) are also present. The main pool of Fe (75 %) is octahedral Fe³⁺ and can be ascribed to the main phase of the bentonite, i.e. the smectite. A small portion (5 %) of Fe is present as octahedral Fe²⁺. It can be rather ascribed to secondary clay minerals (illite and or

micas), other silicates (pyroxenes) or ilmenite. Thus, ilmenite would be at best the third most abundant accessory mineral (at most 5 % of total Fe) after goethite and hematite.

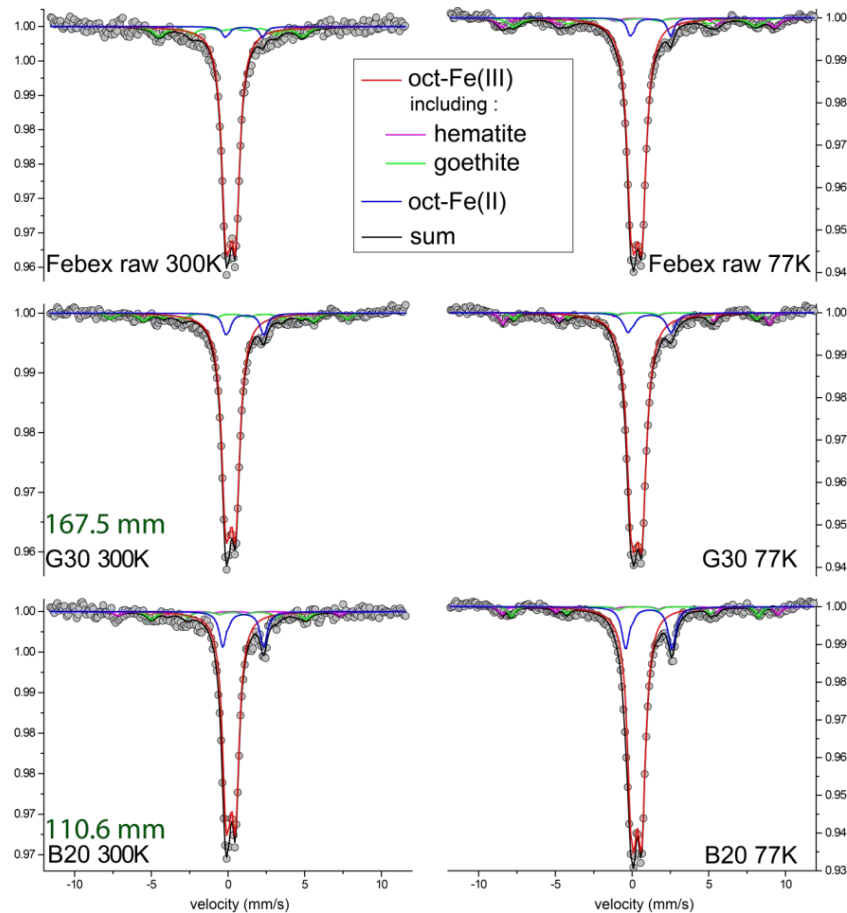


Fig. 72: Room temperature and 77K Mössbauer spectra of the raw FEBEX material and samples G30 and B20 from block BM-B-41-1.

The hyperfine parameters are displayed in Appendix C, Tab. 3 and Tab. 4.

Data collected on sample G30 (167.5 mm from the interface) indicate a lower content in magnetic and superparamagnetic species (at most 12 %), which seems to consist mostly of goethite. Only a small portion can be hematite (< 4 %). In parallel, a slight increase in reduction level of Fe is seen (from 5 to 9 %). Moreover, XRF data suggest a slight increase of the Fe content in this sample (+ 6 %). The possibility that these slight differences between G30 and raw sample are due to natural variations in the FEBEX material, or related to inhomogeneous sampling cannot be ruled out. Still, these differences can also be explained by dilution of pre-existing Fe by additional Fe from the corroding heater. For instance, when excluding magnetic and superparamagnetic species from the counts in both samples, the data in fact account for the presence of an additional 5 % Fe^{2+} and almost no net changes in Fe^{3+} (+ 1 %). This is consistent with a 6 % increase of total Fe.

Data collected on samples B20 (110.6 mm from the interface) and B15 (8.2 mm) are remarkably similar. Compared to the raw material, data indicate a notably lower content in superparamagnetic species (10 %, goethite:hematite ratio is 1:1) and the absence of magnetic

species. The reduction level of Fe is also notably higher (15 – 16 %). XRF data also suggest a slight increase of the Fe content in this sample (+ 12 and + 13 % respectively). In this case, the observed changes in Fe speciation and content (along with the blue colour) are explained by the presence of additional Fe from the corroding heater, resulting in an increase in Fe^{2+} content in the sample. Indeed, when excluding superparamagnetic species from the counts, mass balance calculations of paramagnetic Fe content indicate the presence of 12 % and 11 % (respectively in B20 and B15) additional Fe^{2+} and no net changes in Fe^{3+} (+ 1 % and - 1 % respectively). Such values are consistent with the increase in total Fe content suggested by XRF.

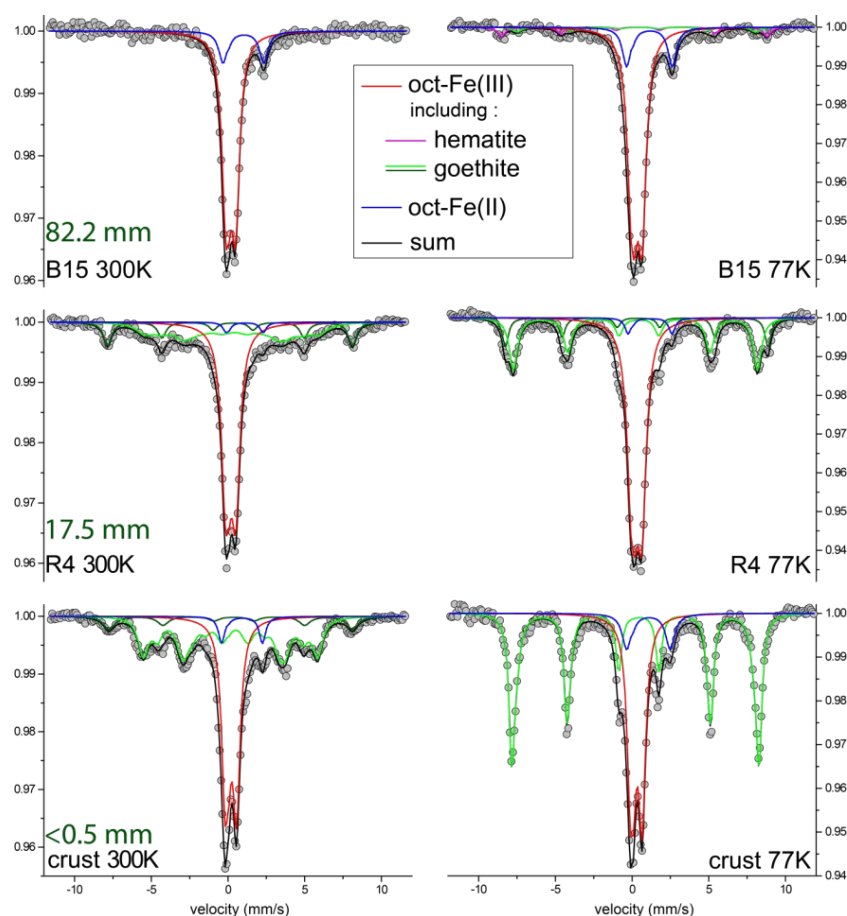


Fig. 73: Room temperature and 77K Mössbauer spectra of the raw FEBEX material and a series of 2 samples from block BM-B-41-1.

The hyperfine parameters are displayed in Appendix C, Tab. 3 and Tab. 4.

Data, collected on sample R4 at 17.5 mm from the contact, contrast even more with raw material. A significantly higher content in magnetic oxides, mainly present as goethite, is observed. The reduction level of iron is however unchanged compared to bulk material. XRF data suggest a significant increase of the Fe content in this sample (+ 46 %). Most of the additional Fe is present as Fe^{3+} in this case. If one assumes that the additional Fe is present as superparamagnetic goethite only (taking into account that a portion originates from the original material, i.e. at most 14 %), an increase of + 41 % is found. This is consistent with XRF data. In that case, notable amounts of additional paramagnetic Fe^{3+} are also found. Observations show no net change in Fe^{2+} content.

Finally, the crust sample displays a significantly higher content of magnetic species (55 %, mainly goethite) and slightly higher reduction levels (8 %) than the raw sample. EDX data indicate a dramatic increase of the Fe content in this sample, of at least + 220 %. This increase may even be higher, since the above inferred value is averaged over the first 1.4 – 4 mm at the contact with the steel liner (i.e. the first mapped row in the profile), while the crust sample originates from the first few hundred micrometers of the block. Again, if one assumes that the additional Fe is present as paramagnetic goethite only (taking into account that a portion originates from the original material, i.e. at most 5 %), an increase of + 100 % is found. This is still below the minimal predicted value of 220 %. An important part of the increase is thus due to additional paramagnetic Fe as well. A mass balance calculation of paramagnetic Fe content indicates the presence of at least an additional 14 % of Fe^{3+} and at least 6 % of Fe^{2+} .

The main observations from the Mössbauer survey are listed in Tab. 6.

Tab. 6: Data relative on Fe redox speciation inferred from ^{57}Fe Mössbauer spectrometry.

Sample	Distance	Colour	Fe increase*	Para Fe red.%**	Super-para***	Mag****	Comments on additional fe pool
	mm		% of init. Fe	% of total Fe			
Raw	-	Pale grey	-	5 %	20 %	12 %	<i>Up to 20 % of initial Fe is accessory Fe oxides (goe:hem 2:1)</i>
Crust	< 0.2	Black	> + 220 %	18 %	< 2 %	54 %	Mainly magnetic and paramagnetic goethite
R4	25	Red	+ 4 6 %	7 %	< 2 %	4 5 %	Mainly superpara-magnetic goethite
B15	75	Blue	+ 1 2 %	18 %	10 %	< 2 %	Paramagnetic Fe ²⁺
B20	100	Blue	+ 13 %	17 %	10 %	< 2 %	
G30	150	Green	+ 6 %	10 %	10 %	< 2 %	

* Expressed in % of initial Fe, determined from xrf profile of Fe/Al (edx in the case of the crust samples)

** Reduction level of paramagnetic iron ($\text{Fe}^{2+}/(\text{Fe}^{2+}+\text{Fe}^{3+})$)

*** Percentage of total Fe present as superparamagnetic Fe

**** Percentage of total Fe present as magnetic Fe

Three groups of samples can be discriminated:

- The green and blue samples (B15, B29 and G30) show weak Fe increase and a moderate increase of the reduction level of paramagnetic Fe compared to the raw material, without any net change in paramagnetic Fe^{3+} content. The additional presence Fe can be attributed to Ferrous hydroxide, sorbed Fe^{2+} and/or sorbed Fe^{3+} (following sorption of Fe^{2+} and reduction of clay structural Fe (Schaefer et al. 2011)).
- The red sample (R4) displays a net increase in Fe content, occurring mainly as superparamagnetic goethite (i.e. with grain size of 5 to 25 nm). There is a slight increase in paramagnetic Fe^{3+} content and no change in paramagnetic Fe^{2+} .
- Finally, the crust sample displays the most dramatic increase. Most of the Fe (> 70 %) is in fact additional, and it is mainly shared between magnetic goethite (large goethite grains > 25 nm) and paramagnetic Fe^{3+} (probably nano-sized goethite). The small amounts of

additional paramagnetic Fe^{2+} might account for similar species than in the green/blue group, or also for siderite.

4.4.4 Discussion

The study of Fe speciation in the original FEBEX matrix shows that Fe is mainly (75 %) present as clay octahedral Fe^{3+} . The other important pools consist of magnetic goethite (up to 13 %) and paramagnetic oxides (mainly hematite, < 9 %). A small portion (5 %) of paramagnetic Fe^{2+} is initially present, presumably in illite/mica minerals, ilmenite and pyroxenes. Smectite is the main component of the bentonite (at least 75 %, interstratified I-S might be in fact present). The smectite is more concentrated in the light-coloured parts of the matrix.

Post-mortem analyses of block BM-B-41-1 show that the main change at the end of the FEBEX experiment with regard to Fe is related to the diffusion of Fe into the bentonite. Data also suggest a slight exchange of interlayer Na for Ca and Mg, rather homogenous throughout the whole profile. Fig. 74 displays the chemical profile of Fe as a function of distance from the interface with the liner. Data points and error bars were coloured according the macroscopic aspect of the bentonite.

This profile shows that a correlation exists between the colouration of the bentonite, the amount of additional Fe and the nature of the accumulated species. Although Fe accumulation is more obvious in the red-orange zone (first 45 mm), data suggest that Fe diffused deeper into the bentonite, i.e. throughout the entire blue area, and even into a portion of the green area. This is seen by the slight difference between the red line and the EDX data on a large portion of the profile. The red line in 74 represents the average bulk value in the outermost and thus presumably less perturbed zone (by Fe diffusion) of the block. The value inferred from EDX is slightly lower than the average XRF reference value (NAB 16-68) but still falls within the region of error bars. XRF data are in fact more consistent with reference values, and the small gaps observed between both profiles indicate that EDX data might be slightly underestimated (underestimated SEC factor).

XRD data on profiles samples suggest that a slight increase in the basal spacing occurred during the experiment. This could be for instance induced by a slight exchange of Na for Ca and or Mg. CEC measurements on samples retrieved in the partial dismantling of the FEBEX experiment in 2002 tend to support such an assumption (Villar et al. 2006) However, XRF data on Ca, Mg and Na (Fig. 64, Appendix C, Tab. 1 and Tab. 2) indicate that their content is slightly depleted, especially at the vicinity of the interface (at distance < 100 mm). Thus, the slight increase in basal spacing can be also induced by an exchange of Na/Ca/Mg for Fe. XRF data on trace elements (Appendix C, Tab. 1 and Tab. 2, Appendix) also indicate that Sr and Mn contents decrease progressively toward the interface (starting at distance < 100 mm). Therefore, Sr and Mn might also have been exchanged for Fe in the Fe enriched zone.

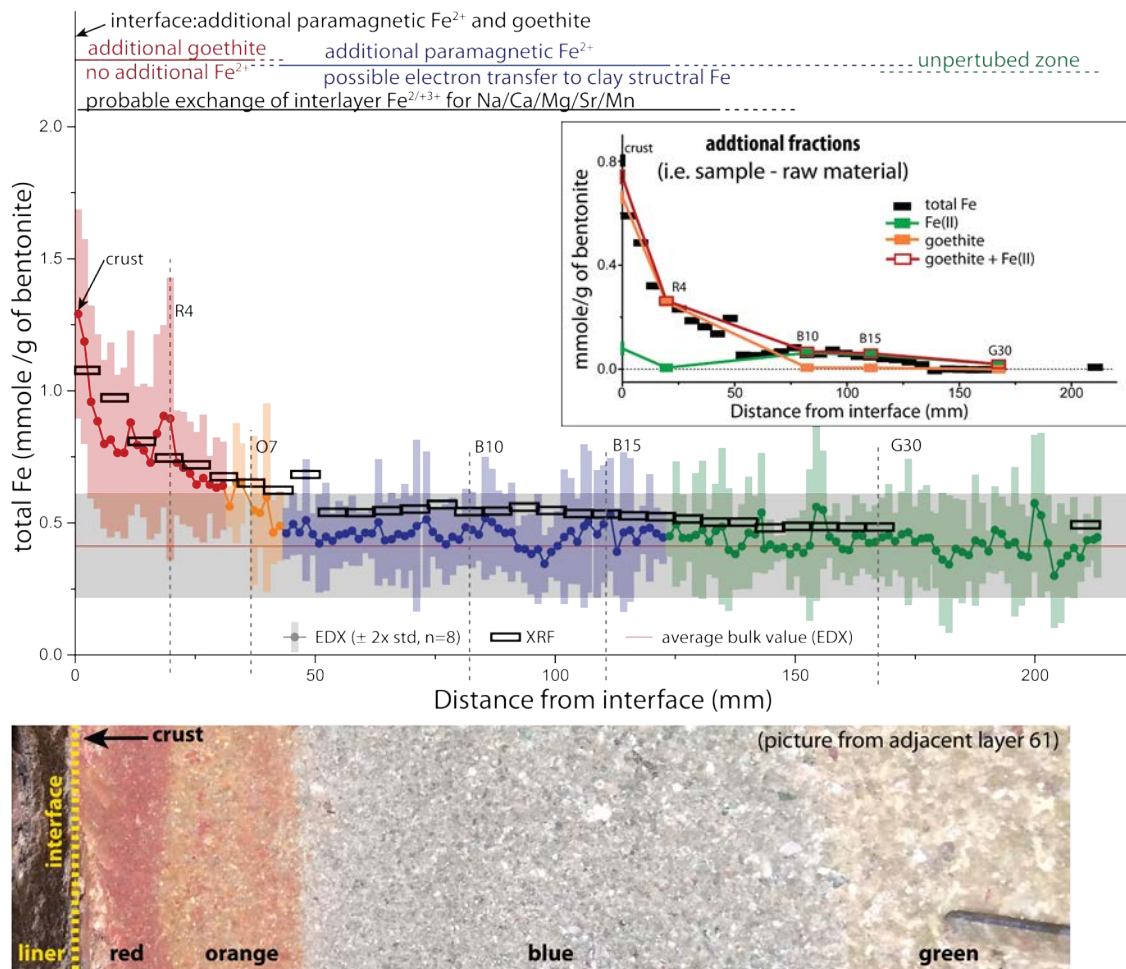


Fig. 74: Chemical profile of Fe perpendicular to the interface (here normalized by the Al atomic proportions) in block BM-B-41-1.

Al-normalized data were converted to mmol of Fe per gram of bentonite, using the weight content in Al in the original material (22.55 wt% (NAB 16-68) and a bulk dry density of $1.6 \text{ g}\cdot\text{cm}^{-3}$. The colours account for the colour of the sampled powder. Blue line represents the average reference value in raw material, and the dark grey rectangle accounts for two times the standard deviation (NAB 16-68). The horizontal red line represents the average value in the outermost zone of the block (at a distance between 180 and 220 mm). Vertical grey lines indicate the first series of samples analysed by Mössbauer spectrometry and XRD. The picture shows a bentonite block at contact with the liner in an adjacent layer 61 (chosen for its better resolution); the extents of the various-coloured halos slightly vary (Few cm) from those in the studied block.

The insert shows a chemical profile of "excess" portions of Fe(II), goethite, and total Fe as determined by XRF and Mössbauer data.

Quantification of Fe transfer process

The amount of Fe transferred to the clay (ΔM_{Fe}) can be roughly estimated from Al-normalized excess profiles through the following equation (taking account a cylindrical symmetry, as proposed in (Wersin et al. 2015)):

$$\Delta M_{Fe} = \sum_{n=1}^z (r_n^2 - r_{n-1}^2) \cdot \pi h \rho_b [Fe]_n^{excess} \quad \text{Eq. 1}$$

where n is the number of the area where excess Fe concentration $[Fe]_n$, is counted (in wt%), r_n is the distance of a given area to the Fe source (r_0 is the radius of the Fe source, 485 mm), z is the total number of areas taken into consideration (in the present the entire profiles), ρ_b is the density of the bentonite ($1.6 \text{ g}\cdot\text{cm}^{-3}$ (Villar et al. 2006)) and h is the height of the cylinder taken into consideration. The excess Fe concentration $[Fe]_n$ (expressed in wt%) in a given sector n was deduced from the Al-normalized excess profiles through the following expression:

$$[Fe]_n^{excess} = \frac{(Fe/Al)_n^{excess}}{(Fe/Al)_{bulk}} \cdot [Fe]_{raw}^{XRF} \quad \text{Eq. 2}$$

where $[Fe]_{raw}$ is the content of Fe (in wt%) measured in the raw dry material (XRF (Wersin et al. 2015)), $(Fe/Al)_{bulk}$ is the average ratio determined in the outermost section of the block (red line on Fig. 74) and $(Fe/Al)_n^{excess}$ is the excess ratio in the sector n . The amount of Fe transferred to the clay can be converted to the average corrosion depth d_{corr} of the Fe source:

$$d_{corr} = \frac{\Delta M_{Fe}}{\rho_{Fe}} \cdot \frac{1}{A_s} \quad \text{Eq. 3}$$

where ρ_{Fe} is the density of the heater's steel (here $7.7 \text{ g}\cdot\text{cm}^{-3}$ for 15Mo3 steel) and A_s is the unit surface of the Fe source, equal to

$$A_s = 2\pi r_0 h \quad \text{Eq. 4}$$

Eq. 1, Eq. 3 and Eq. 4 can be further combined and simplified in the following expression of d_{corr} as a function of the amount of excess Fe:

$$d_{corr} = \frac{\rho_b}{\rho_{Fe}} \cdot \frac{1}{2r_0} \sum_{n=1}^z (r_n^2 - r_{n-1}^2) \cdot [Fe]_n^{excess} \quad \text{Eq. 5}$$

In the present case, such a calculation results in a corrosion depth of $0.18 - 0.25 \text{ mm}$ (respectively using XRF and EDX data). This corresponds to an averaged corrosion rate of $10 - 14 \text{ }\mu\text{m}/\text{year}$ (considering the total time of experiment, including both aerobic and anaerobic phases), which falls in the range of rates previously estimated for corrosion of steel (in the $0.1 - 10 \text{ }\mu\text{m}/\text{year}$ range (Schlegel et al. 2014, Wersin et al. 2015, Xia et al. 2005)). Such a calculation allows determining the relative amount of Fe accumulated in the different zones. It appears that the amount of Fe accumulated in the blue zone (and a portion of the green zone) represents about half the amount accumulated in the red zone and the crust.

Impact on bentonite chemistry

Although clay (smectite and/or illite-smectite) makes up more than 90 % of the material, the morphology of the FEBEX bentonite is quite heterogeneous, representing a large range from micro- up to millimeter-sized aggregates of contrasting colours, scattered in a clay matrix of pale grey colour. Dark-coloured aggregates consist mostly of accessory minerals (quartz, cristobalite, Feldspars, pyroxenes olivine, oxides, carbonates, volcanic ashes etc. (Villar et al. 2006)), while light coloured ones (white, yellow, and pink) consist mostly in smectite. XRD data suggest that the type of smectite is almost the same in the aggregates and in the matrix, although slight variations in basal spacing suggest probable variation in composition of interlayer and/or structure. Chemical mappings show that Fe has been accumulated in the clay matrix, at the boundary with the accessory minerals, but only in a portion of the clay-rich aggregates. Fe did not diffuse into the white aggregates. The main difference with the other light-coloured aggregates is the notable presence of amorphous silica, as suggest by XRD data on the powdered sample (Fig. 70). These aggregates might in fact consist of clay aggregates coated by a layer of amorphous silica which would deter Fe(II) from diffusing.

Although Fe is expected to diffuse into the bentonite as Fe^{2+} , (Fe^{3+} being poorly soluble in the conditions of the experiment, i.e. pH of the bentonite medium > 6), data only show the presence of additional Fe^{2+} in the crust (the first hundreds of micrometer) or much further away in the blue and green zone (at least at distance > 20 mm). All the Fe accumulated in the red zone (and perhaps orange) is present as goethite and paramagnetic Fe^{3+} (most probably nano-sized grains of goethite, and perhaps lepidocrocite). The additional Fe found in the crust is also mainly in goethite. The identity of paramagnetic Fe^{2+} -bearing species in the crust sample is still difficult to determine (could be siderite, Ferrous hydroxide, green rust, sorbed Fe^{2+} , reduced clay). Dealing with the blue zone, Mössbauer data clearly show the addition of only paramagnetic Fe^{2+} to the system (no net changes in Fe^{3+}). Two processes can explain such a change. Either Fe^{2+} is sorbed without electron transfer or there is an associated redox reaction with structural Fe^{3+} being reduced and sorbed Fe^{2+} being oxidized. This would in fact result in no apparent net change in the amount of paramagnetic Fe^{3+} . Eventual release of the sorbed Fe^{3+} would likely be followed by direct *in-situ* precipitation of nano-sized goethite, and would thus have no impact on the amount of paramagnetic Fe^{3+} . The presence of green rust, magnetite or other mixed-valence compounds can be ruled out because of the absence of additional Fe^{3+} . However, the presence of Fe^{2+} as a separate phase such as siderite or Ferrous hydroxide cannot be ruled out.

The exact conditions and time sequence of the accumulation of Fe in block BM-B-41-1 are yet to be determined. The reason for this asymmetric Fe diffusion front might be related to a clear contrast in the water saturation of the bentonite (Villar et al. 2017, further discussed below).

A phenomenological description of the Fe diffusion mechanism

The proposed mechanism is based on the interplay between the Fe released by the corrosion process of steel (diffusing Fe), the Fe initially present in the bentonite material (background Fe) and the varying redox conditions.

It is generally accepted that corrosion of steel in Fe-bentonite *in-situ* experiments proceeds in two sequences: first an aerobic sequence where Fe^{3+} (and thus corrosion products) is generated at the surface of steel, followed by an anaerobic phase (once O_2 has been depleted from the system) where Fe^{2+} is generated (Kaufhold et al. 2015). It is thus generally considered that Fe^{2+} diffusion into bentonite will occur during the anaerobic period and will mainly interact with the bentonite medium through ion exchange (Wilson et al. 2015, Xia et al. 2005). One could thus expect a monophasic diffusion of Fe^{2+} . In fact, a biphasic diffusion front is generally observed

(as in Xia et al. 2005 and in the present study) and a significant amount of additional Fe^{2+} is found at larger distances from the interface, deeper in the bentonite while Fe is mainly found as Fe^{3+} at the vicinity of the interface (up to several cm inside the bentonite).

One could argue that this high amount of Fe^{3+} would stem from a methodological artefact in the dismantling/subsampling/analysing approach, i.e. that mainly Fe^{2+} was present *in situ*, but would have been oxidized prior to analysis. Partial oxidation of the studied sample cannot be ruled out completely. Nevertheless, there is evidence that the observed low reduction level of the additional Fe pool found close to the interface is actually the normal result of such Fe-bentonite interaction in such experimental settings. Similar observations have been made in samples retrieved from analogous longterm experiments, such as the ABM2 experiment (Hadi et al. 2017). Because of the different shape, size, position and the shorter dismantling time in the ABM2 experiment, one should expect less of such oxidative perturbation than in the FEBEX experiment (e.g. longer dismantling time, presence of the gap between the liner and the heater, presence of holes in the liner). Moreover, very similar patterns could be observed in other locations of the present experiment (Fig. 75).

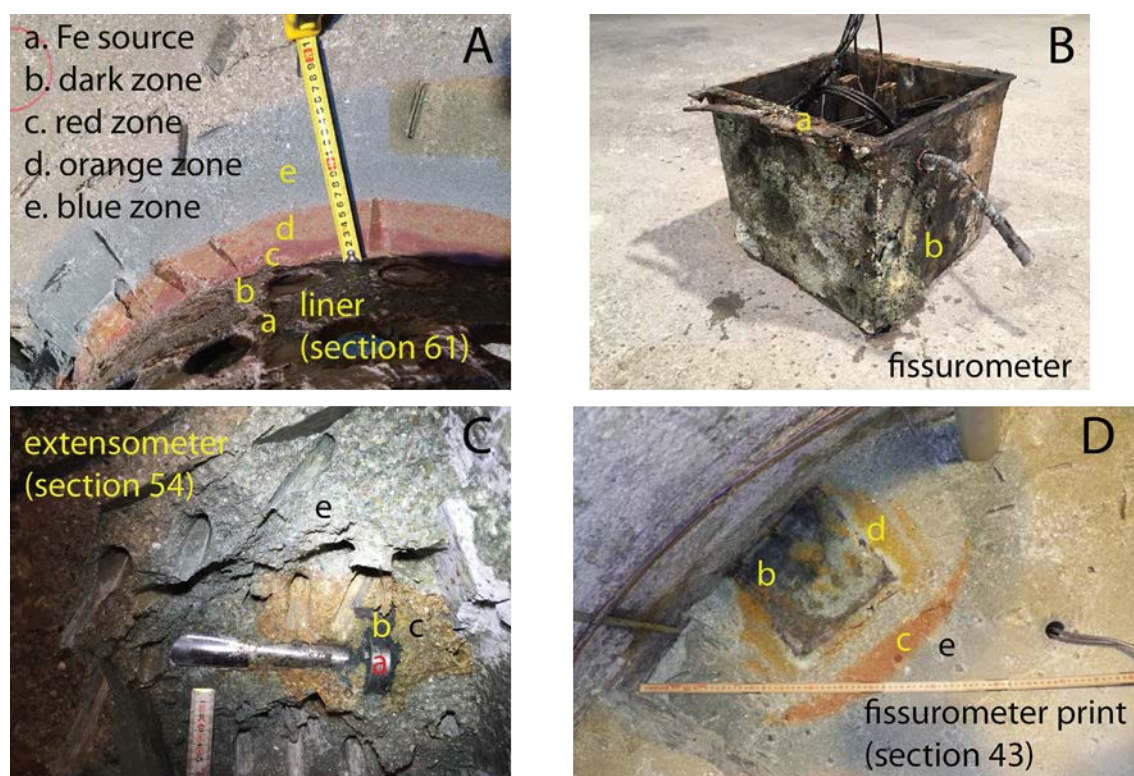


Fig. 75: Coloured corrosion halos observed around various steel components retrieved upon dismantling of the FEBEX-DP experiment.

The presence of a Fe^{3+} -rich orange coloured bentonite rim (several centimeters wide) right around a steel piece, surrounded by a larger and blue coloured bentonite rim (Fe poorer, but more reduced) further away, could be observed at various locations, such as the tip of both vertical and horizontal extensometers installed in Section 54 or the fissurometer in Section 43. This pattern seems to be in fact the typical result of aerobic followed by anaerobic corrosion of steel enclosed in bentonite.

In the proposed mechanism, Fe^{2+} diffusion is first hindered by O_2 present in the bentonite. A recently reported small-scale laboratory experiment involving bentonite gel and native iron showed in fact that the corrosion will proceed anaerobically, even under normal laboratory conditions (i.e. in the presence of oxygen around the gel) (Kaufhold et al. 2015). As a consequence, Fe^{2+} is oxidized to Fe^{3+} and precipitates mainly as goethite as soon as it diffuses into the aerobic bentonite. It is thus first accumulated close to the interface, and will diffuse further inside as soon as O_2 is depleted in the bentonite too.

Diffusing Fe^{2+} can further interact with the Fe initially present in the starting material (raw industrial bentonite), which mainly consists of structural Fe^{3+} in octahedral smectite layers. This pool is considered to be immobile but can however undergo reversible redox reactions with the diffusing Fe^{2+} , through the reduction by Fe^{2+} sorbed on the clay edges (Schaefer et al. 2011, Soltermann et al. 2014, Soltermann et al. 2013), and also on basal surfaces (Latta et al. 2017). Moreover, sorption of diffusing Fe^{2+} on pre-existing Fe^{3+} -bearing oxides (e.g. on hematite (Kerisit et al. 2015, Rosso et al. 2010, Yanina & Rosso 2008) or goethite (Handler et al. 2014) followed by an electron transfer inside the oxide and a release of Fe^{2+} from another crystallographic site is also possible. Redox interaction with clay might lead to the formation of strongly sorbed Fe^{3+} and immobile structural Fe^{2+} . While sorption on oxides (followed by oxidation) leads to the fixation of Fe^{3+} in oxides, it also induces the release of mobile Fe^{2+} from another crystallographic plane (thus no net accumulation). Both processes are thus not equivalent to a simple Fe^{2+} diffusion process inside the bentonite medium. The former process would slow down Fe^{2+} diffusion and lead to accumulation, whereas the latter enables further Fe diffusion (from another crystallographic site of the same grain).

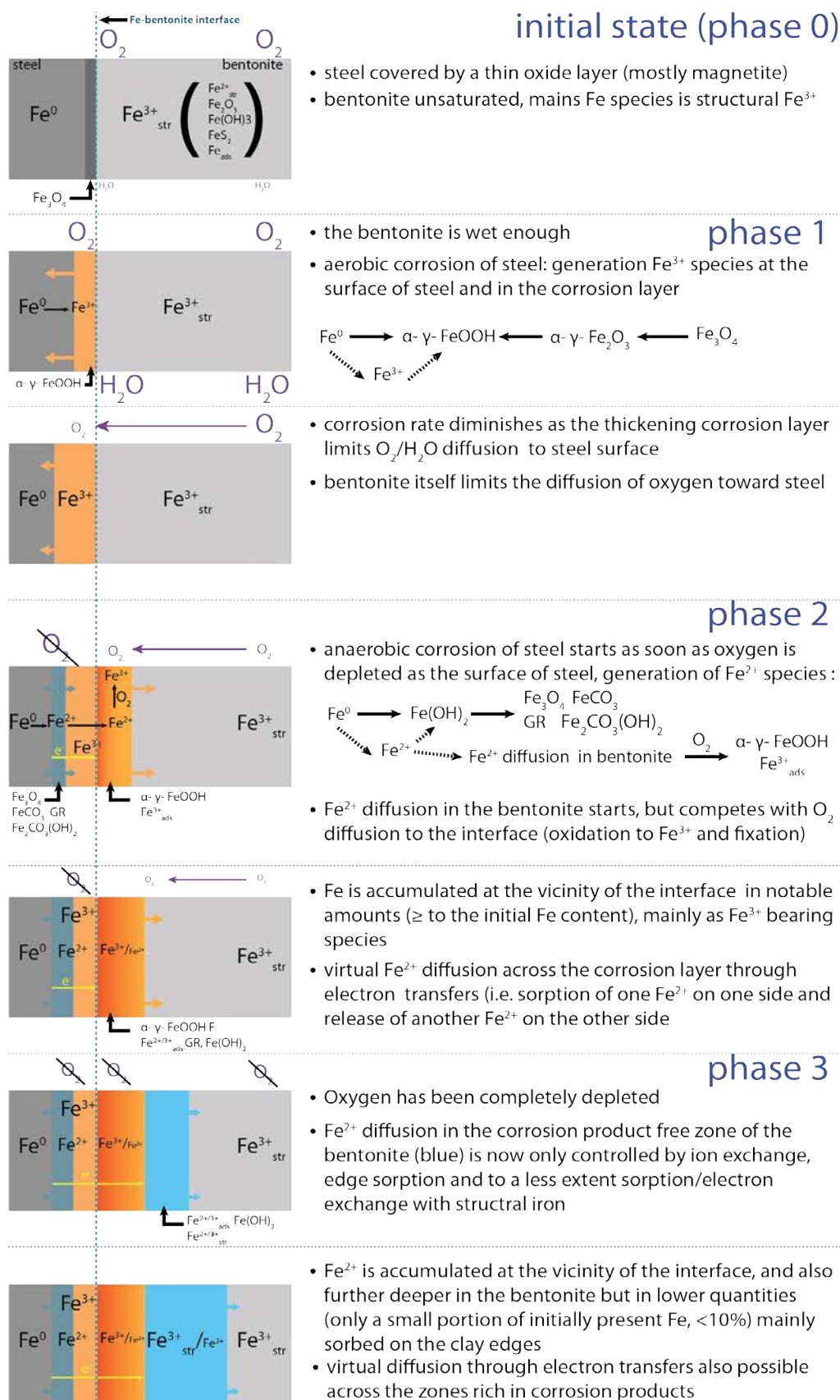


Fig. 76: Proposed Fe diffusion mechanism at the Fe-bentonite interface.

A simplified scheme of the proposed mechanism for Fe diffusion in the bentonite is displayed in Fig. 76. It is proposed that the additional Fe^{3+} is generated *in situ*, as Fe^{2+} start to diffuse in the bentonite while low levels of oxygens are still present.

Results from experimental (Schlegel et al. 2014) and modelling (Wilson et al. 2015) studies suggest that the aerobic phase (phase 1 in Fig. 76) is generally short and would only last about a month under closed conditions as suggested from a lab-scale experiment. As outlined in the introduction of this report, the FEBEX-DP experiment does not reflect a closed system (potential pathways for air through the plug, the cable ducts and the gas and water pipes, the effects of the dismantling of FEBEX I and the potential presence of fractures in the host rock). Still, various features related to anaerobic corrosion were observed throughout the various samples. In particular, notable amounts of additional Fe^{2+} were found not only in the vicinity of the interface but also further away in the blue halo. This indicates that anaerobic conditions were reached during the FEBEX-DP experiment. A recently reported small-scale laboratory experiment involving bentonite gel and native iron in fact showed that the corrosion will proceed anaerobically, even under normal laboratory conditions (i.e. in the presence of oxygen around the gel) (Kaufhold et al. 2015). In the proposed mechanism (Fig. 76) diffusion of Fe^{2+} starts as soon as anaerobic conditions are reached at the surface of the steel and in the corrosion layer (phase 2). Aerobic conditions would still be prevailing in the bentonite. Most of the diffusing Fe^{2+} is thus oxidized and immobilized as soon as it enters the bentonite, mainly as Fe^{3+} paramagnetic oxides (e.g. goethite or lepidocrocite) and to a lesser extent as sorbed Fe^{3+} (actually Fe^{2+} is first sorbed and then oxidized by O_2). Thus, during phase 2, the diffusion of Fe^{2+} inside the block competes with the diffusion of oxygen toward the interface. Diffusivity of Fe^{2+} would increase as soon as O_2 concentration decreases. At some point (phase 3), O_2 levels in the block are low enough to enable effective diffusion of Fe^{2+} over larger distances in the clay. Diffusion of Fe^{2+} is then controlled by sorption onto clay minerals and by redox processes with structural Fe^{3+} in clay or Fe^{3+} oxides (sorption followed by oxidation). The former process (sorption only) would be predominant, as sorption-reduction sites make up only a small portion of the sorption sites (at most 0.6 on 4 octahedral sites are structural Fe). Either Fe^{2+} is sorbed without e- transfer or there is an associated redox reaction with structural Fe^{3+} being reduced and sorbed Fe^{2+} being oxidized. Under such conditions, Fe^{2+} diffuses further away from the interface and the local accumulation is more limited. The residence time of Fe^{2+} in the Fe^{3+} -enriched zone close to the interface would be shortened, as electron conduction through oxide can enhance the diffusivity of Fe^{2+} . This can explain the absence of additional Fe^{2+} observed in the sample R4 collected in this zone. As a consequence, this latter process would lead to a progressive tailing of the Fe^{2+} profile. This means that the accumulation process of Fe^{3+} at the vicinity of the interface is stopped, and already accumulated Fe^{3+} is slowly displaced further away from the interface.

It must be emphasized that the described phenomena were very localised and did not occur all along the liner. It was only observed along a portion of the liner located in between the two heaters, and along other steel pieces located closer to the wall than to the heater. This is assumed to be related to varying water saturation conditions in the experiments. At the vicinity of the heaters, the bentonite was not humid enough to allow such processes to occur.

4.5 Fe-bentonite interface study of SKB

4.5.1 Introduction

The focus in this work was on mineralogical and chemical changes in the 0 – 5 cm zone from the iron contact. The mineralogy was studied by X-ray diffraction (XRD) with as main target to search for any formation of trioctahedral smectite, as seen in the ABM2 experiment at Äspö hardrock laboratory, Sweden (Svensson 2015). The overall chemistry was studied with X-ray fluorescence spectroscopy (XRF), and the montmorillonite content was studied using cation exchange capacity (CEC), as an indicator of alteration of the montmorillonite to other phases. This work was performed by the authors at the clay science laboratory at Äspö, Sweden.

4.5.2 Samples

The sample received was BM-S-42-4 (heater section). The sample showed a strong discolouration of the bentonite that had been in contact with the corroding iron (Fig. 77). Approximately 1 – 2 cm of the bentonite was discoloured (Fig. 77b). Under a microscope reddish-yellowish and very dark phases were observed (Fig. 78).

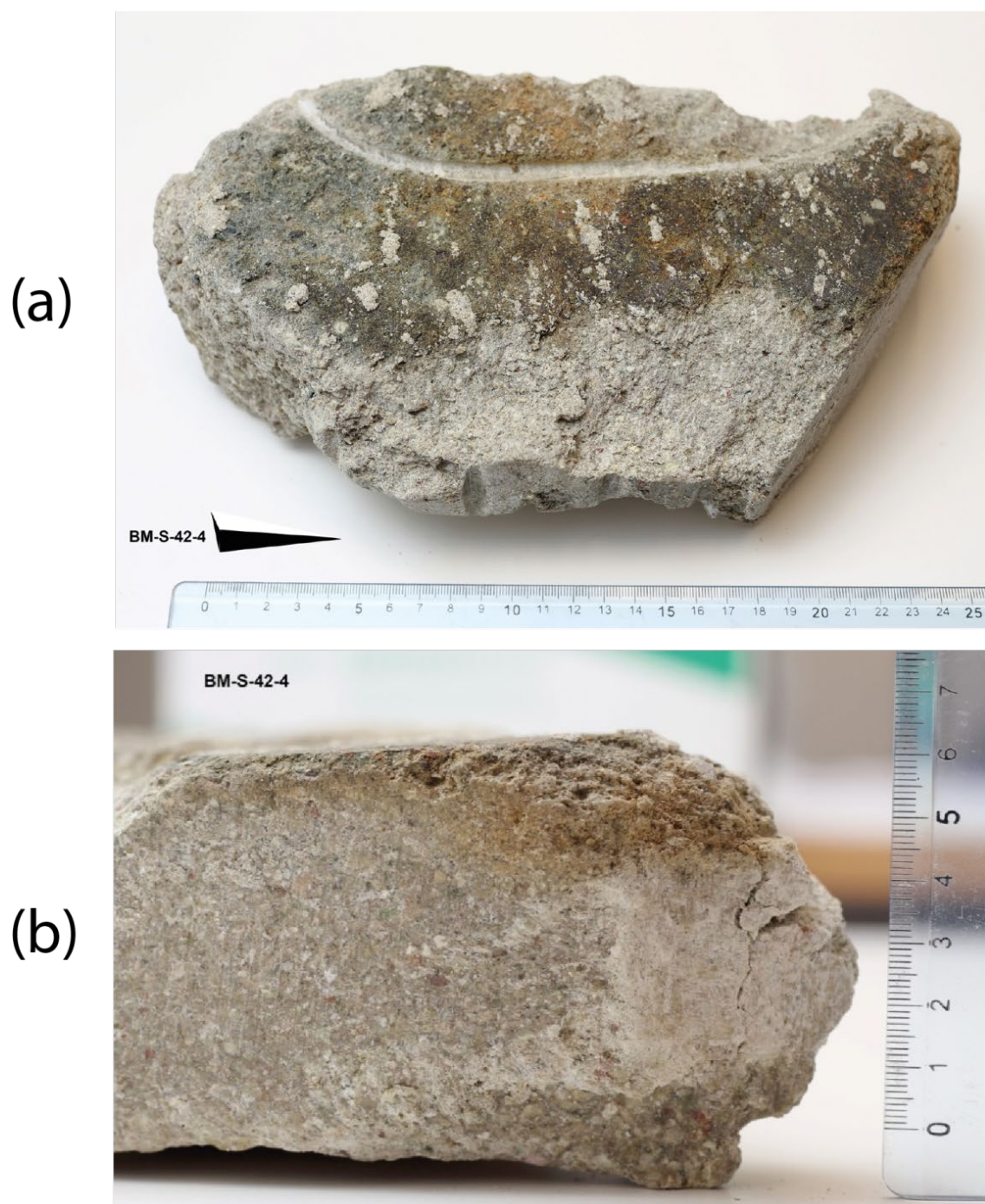


Fig. 77: The received sample BM-S-42-4.
The surface towards the corroding iron from the top (a) and from the side (b). Scale in cm.

(a)



(b)



Fig. 78: The bentonite-iron contact zone in the received sample BM-2-42-4.
(a) represents about 2×3 cm and (b) represent about 5×3 mm. Reddish-yellowish and very dark phases are present.

4.5.3 Methods

X-ray diffraction (XRD)

Randomly oriented samples were prepared by backfilling the sample holders. Measurements were done in reflection mode (theta-theta) using a Panalytical X'Pert Pro diffractometer equipped with Co-broad focus X-ray source and a PIXcel1D line detector, operating at 40 kV and 40 mA. The interval 4 – 80 deg was measured in 3h, a programmable divergence slit was used with an irradiated length of 8.5 mm. A 0.016 mm beta-filter of iron was used to decrease the Co k-beta radiation. No monochromator was used to increase the X-ray intensity. Soller slits of 0.04 rad and a fixed incident beam mask of 20 mm was used.

X-ray fluorescence spectroscopy (XRF)

Bentonite powder was compacted to a disc with a diameter of about 3 cm and a thickness of about 5 mm, and placed within the sample carousel in the XRF. The method is based on the commercial Omnia method, developed by the equipment supplier Panalytical. XRF data was collected under helium atmosphere at different systematic conditions controlled by a program in which different acceleration voltages and filters were used. The method was modified to measure low energy at longer time in order to improve the sensitivity to sodium.

Cation exchange capacity (CEC)

CEC was measured using the exchange reaction with copper triethylenetetramine complex evaluated colourimetrically by UV/Vis spectroscopy, as described by Meier and Kahr (1999) and Ammann et al. (2005).

4.5.4 Results and conclusions

Mineralogy

No dramatic differences between samples could be seen with XRD when comparing the innermost sample (0 – 1 mm from the iron) with the samples further away from the iron (Fig. 79). Subtle effects were seen in the low angle region (Fig. 79, left arrow); a weak reflection around 14 degrees, most likely corresponding to the 002 reflection of the smectite basal reflection. In the area about 1.5 Å also a minor difference was observed (Fig. 79; right arrow). This could indicate a very low level of formation of a trioctahedral clay mineral, something that has been observed earlier in a similar field experiment but to a much larger extent (ABM2 experiment, Äspö Sweden, e.g. Svensson 2015).

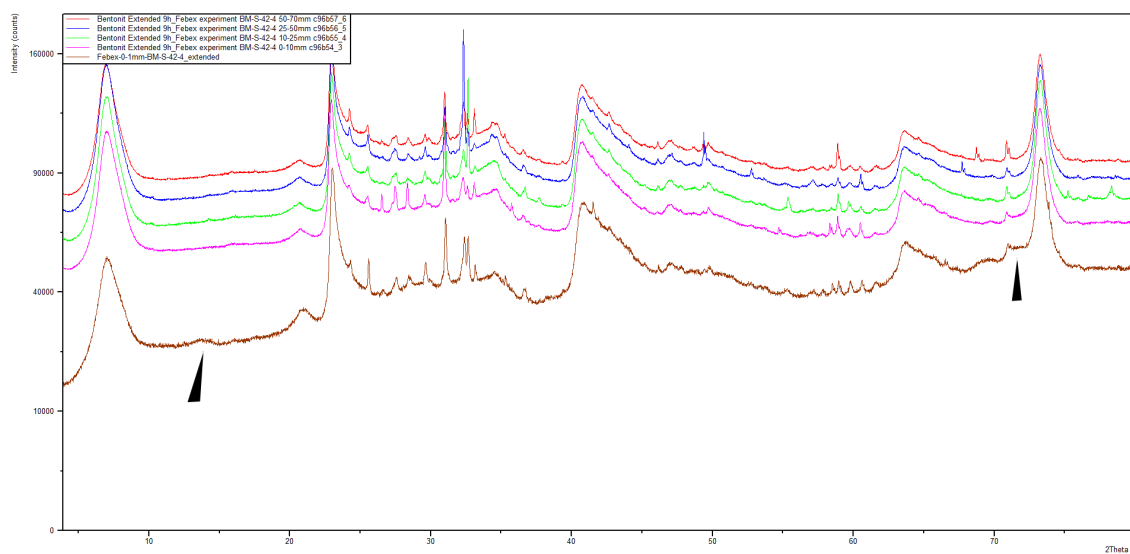


Fig. 79: X-ray diffractogram of samples from the following distances from the iron surface in the BM-2-42-4 sample (from above): 50 – 70, 25 – 50, 10 – 25, 0 – 10, 0 – 1 mm. The 0 – 1 mm diffractogram is marked with two arrows indicating details in the data.

Chemistry

A strong accumulation of Fe and Mg was observed towards the iron surface (Fig. 80). The accumulation of Fe has its origin in the corrosion of metallic Fe in the construction, while the reason for Mg increase is less clear, but very well documented from earlier field experiments (e.g. Svensson 2015). The Mg is expected to be present as exchangeable interlayer Mg^{2+} and/or as newly formed phases, e.g. saponite. Minor increase was seen in the Ca/Na ratio towards the Fe-surface, which could be a sign of possible ion exchange reactions.

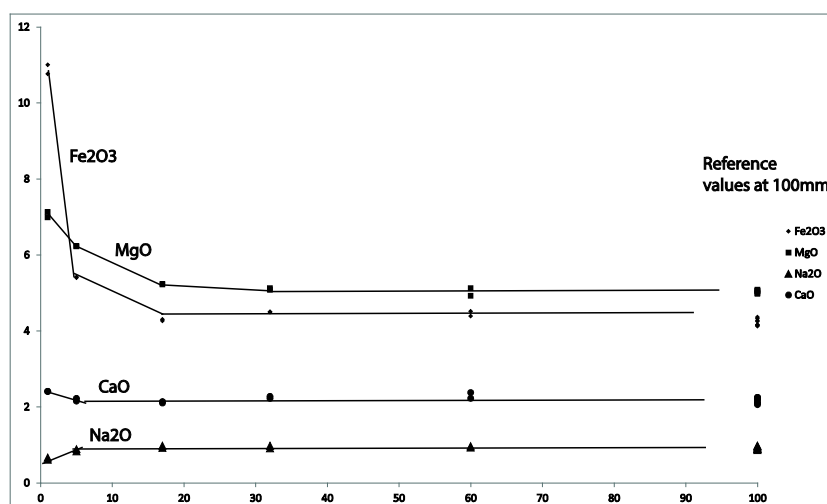


Fig. 80: X-ray fluorescence data (in wt%) of Fe_2O_3 , MgO , CaO and Na_2O as a function of the distance from the corroding iron (mm).

Reference values are given at 100 mm distance.

Sulphur (S) and Cl were found to be higher in the field compared to the reference samples (Fig. 81, most likely due to the interaction with groundwater. Accumulation of Ca (Fig. 80) and S (Fig. 81) indicate that gypsum/anhydrite could be present close to the iron interface.

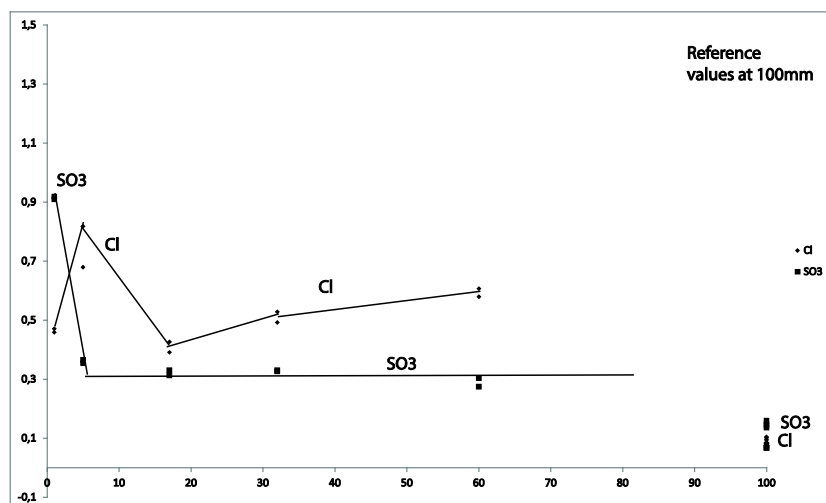


Fig. 81: X-ray fluorescence data (in wt%) of SO_3 and Cl as a function of the distance from the corroding iron (mm).

Reference values are given at 100 mm distance.

A significant decrease of CEC at the iron surface was observed (Fig. 82). This CEC reduction can be explained by the dilution of montmorillonite in the sample due to the presence of corrosion products. The Fe_2O_3 content (Fig. 4) increased from 4 to 12 wt%. Hence about 8 wt% of the iron in the sample was added from the corrosion process. Hence, only approximately 92 % ($100 \% - \text{average } 8 \%$) of the innermost bentonite represents the original sample. If this is taken into account the dilution effect expects the CEC to be about $92 \% \times 102 = 94$, which is what was observed (Fig. 82).

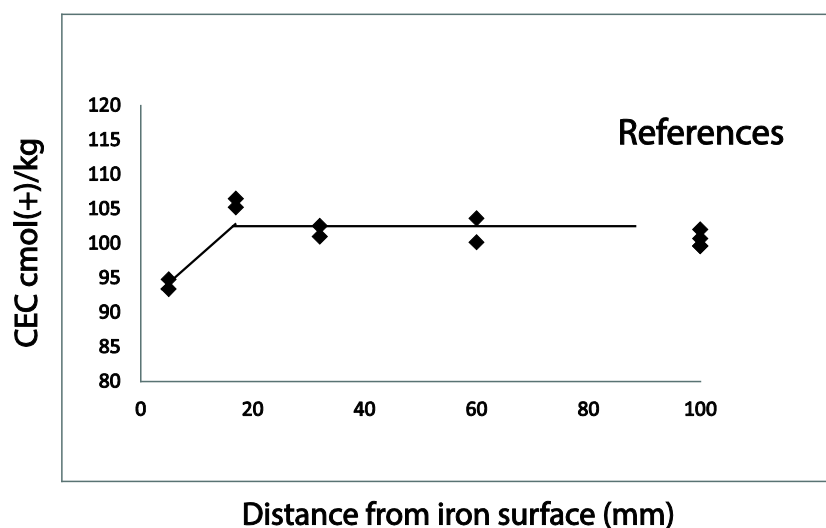


Fig. 82: Cation exchange capacity of the bentonite as a function of the distance from the corroding iron (mm).

Reference values are given at 100 mm distance.

4.5.5 Conclusions

Small changes were observed with X-ray diffraction in the 060 region at about 1.5 Å (Fig. 79), possibly indicating the formation of trioctahedral clay minerals. This has been observed in several previous field experiments at Äspö hard rock laboratory, Sweden, and may indicate the formation of a trioctahedral Mg-rich smectite such as saponite.

Chemical data indicate increase in Fe and Mg towards the iron surface, and a general increase in S and Cl compared to the reference clays. This is very typical also for previous field experiments that were analysed.

A small decrease of CEC was observed at the iron surface that could be explained by dilution effects due the presence of Fe – corrosion products.

Generally, the FEBEX experiment look very much like the ABM and TBT experiments at Äspö (Svensson 2015). All observations were more or less predicted, but all are not yet understood.

4.6 Interface study of BGR

4.6.1 Introduction

FEBEX experiment

The "Full-scale Engineered Buffer EXperiment" (FEBEX) was the first real scale test of a horizontal disposal system for high-level radioactive waste (HLRW, NAB 13-96). It consisted of two heaters embedded in compacted bentonite blocks. The heater of the FEBEX experiment started operating in 1997. The first parts of the experiment were removed in 2002 (partial dismantling). The second part was dismantled in 2015. Details about the experiments were summarised previously (e.g. Nagra NAB 13-96). All sensor data were compiled in the Nagra report NAB 16-19.

BGR Objective

BGR is investigating the reactions taking place at the bentonite-metal surface. The aim is to identify the mechanism of mineral alteration reactions so as to finally be able to model them. Laboratory experiments, however, are commonly restricted to a few years and it is difficult to mimic the actual conditions present in a repository in a laboratory. The investigation of large scale tests is, therefore, of particular scientific value. Because of the especially long time of heating, the FEBEX experiment represents a unique possibility to study the longterm performance of bentonite in contact with a heated metal tube. BGR's research was focused on the identification of mineralogical reactions taking place at different interfaces.

4.6.2 Materials and methods

Methods

At BGR bentonite blocks from 8 sections were studied but not all were relevant for studying the bentonite-iron interface. In addition to the official FEBEX-samples, some samples were collected directly from the heater and the liner. These samples are referred to as (E-samples; "E" = extra). The samples were analysed by X-ray fluorescence spectroscopy (XRF), C- and S-analysis (LECO), and cation exchange capacity (CEC). Selected samples were additionally analysed by X-ray diffraction (XRD), scanning electron microscopy (SEM), infrared spectroscopy (IR), and simultaneous thermal analysis coupled with a mass spectrometer to study also the evolved gas (STA).

For XRF analysis of powdered samples, a PANalytical Axios spectrometer was used (ALMELO, The Netherlands). Samples were prepared by mixing with a flux material (lithium metaborate Spectroflux, Flux No. 100A, Alfa Aesar) and melting into glass beads. The beads were analysed by wavelength-dispersive XRF. To determine loss on ignition (LOI), 1'000 mg of sample material were heated to 1'030 °C for 10 min.

The organic carbon (OC) content was measured with a LECO CS-444-Analysator after dissolution of the carbonates. Carbonates had been removed by treating the samples several times at 80 °C with HCl until no further gas evolution could be observed. Samples of 170 – 180 mg of the dried material were used to measure the total carbon (TC) content. TIC (total inorganic carbon) was calculated by the difference of TC-TOC. The samples were heated in the device to 1'800 – 2'000 °C in an oxygen atmosphere and the CO₂ was detected by an infrared

detector. The device was built by LECO (3000 Lake Avenue, St. Joseph, Michigan 49085, USA).

The CEC was measured using the Cu-Triethylenetetramine (Cu-trien) method (Meier & Kahr 1999). The FEBEX-samples were analysed using 30 mL Cu-trien solution and no additional water. Two different sample masses were analysed and average values were calculated. The error (± 3 sigma) of values determined using Cu-trien_{5xcalcite} method for bentonites (Dohrmann & Kaufhold 2009) is different for different cations and the CEC. The scattering is the lowest for K^+ (± 0.3 meq/100 g), followed by Mg^{2+} (± 0.8 meq/100 g), Ca^{2+} (± 0.8 meq/100 g), Na^+ (± 1.9 meq/100 g), and the CEC (± 3.1 meq/100 g). These values can be used approximately to evaluate differences in this study.

XRD powder pattern were recorded using a PANalytical X'Pert PRO MPD Θ - Θ diffractometer (Co-K α radiation generated at 40 kV and 40 mA), equipped with a variable divergence slit (20 mm irradiated length), primary and secondary soller, diffracted beam monochromator, point detector, and a sample changer (sample diameter 28 mm). The samples were investigated from 1° to 75° 2Θ with a step size of 0.03° 2Θ and a measuring time of 12 s per step. For specimen preparation, the back-loading technique was used.

Oriented mounts for XRD (texture slide XRD) were prepared using 15 mg per cm^2 clay. An aliquot of 1.5 mL of suspension was deposited on the circular (diameter = 2.4 cm) ceramic tiles which were 3 mm thick. The suspension was filtered through the tile using a vacuum filter apparatus. XRD patterns of the oriented mounts were recorded using a PANalytical X'Pert PRO MPD Θ - Θ diffractometer (Co-K α radiation generated at 40 kV and 40 mA), equipped with a variable divergence slit (20 mm irradiated length), primary and secondary soller, diffracted beam monochromator, and a point detector. The air-dried samples were investigated from 1° to 65° 2Θ with a step size of 0.03° 2Θ and a measuring time of 5 s per step. Furthermore, the specimens were stored overnight in an ethylene glycol atmosphere at $60^\circ C$ (EG treatment). The clay films were measured from 1° to 40° 2Θ (stepsize 0.03° 2Θ , 5 s per step) after cooling to room temperature, representing EG conditions.

For SEM investigation, a FEI Quanta 600 F operating in low-vacuum mode (0.6 mbar) was used. Therefore, sputtering of the samples with gold or carbon is not necessary. The microscope is equipped with the EDX-system Genesis 4000 of EDAX. A freshly broken surface of the unprocessed air-dried sample was fixed on the carbon grid and used for SEM inspection.

For measuring mid (MIR) infrared spectra the KBr pellet technique (1 mg sample/200 mg KBr) was applied. Spectra were collected on a Thermo Nicolet Nexus FTIR spectrometer (MIR beam splitter: KBr, detector DTGS TEC). The resolution was adjusted to 2 cm^{-1} . Measurements were conducted before and after drying of the pellets at $150^\circ C$ in a vacuum oven for 24 h. The spectrometer was built by Nicolet Instruments, Madison, Verona Road, Wisconsin, USA.

Simultaneous thermal analyses (STA) were performed using a Netzsch 449 F3 Jupiter thermobalance equipped with a DSC/TG sample holder linked to a Netzsch QMS 403 C Aeolus mass spectrometer (MS). 100 mg of powdered material previously equilibrated at 53 % relative humidity (RH) was heated from $25 - 1150^\circ C$ with a heating rate of $10K/min$. The devices were manufactured by Netzsch (Gebrüder-Netzsch-Straße 19, 95100 Selb, Germany).

The water content was gravimetrically determined after oven drying for 1 week at $60^\circ C$.

Reference Material

The FEBEX-bentonite used for the ABM test (Dohrmann et al. 2013, Kaufhold et al. 2013) was used as reference. In addition, 22 samples of those investigated in the present study were selected and the values were averaged to calculate a reference. These selected samples were taken at a distance of more than 10 cm from the heater and from the granite and did not show any variation with respect to the chemical composition. Both reference values, the FEBEX-ABM data, and the "average reference" are compared in Tab. 7 and Tab. 8. No deviations were found for exchangeable Na^+ and K^+ . The slightly lower content of exchangeable Mg^{2+} is close to insignificant. The larger content of exchangeable Ca^{2+} , however, reflects the systematic differences between two slightly different methods used. The ABM reference clay was investigated using the so called "Cu-trien5xcalcite" method in which the exchange solution was pre-saturated with respect to calcite in order to avoid further calcite dissolution during the CEC experiment (Dohrmann et al. 2013). This method however requires a larger sample mass. For the present study, this method could not be applied because less sample mass was available. Generally, CEC values can be best compared when measured within one measurement series (same solutions, same calibration of photometer, same temperature, same solid/liquid ratio, same time of shaking, and so on). Therefore, the values obtained by averaging 22 samples, all with appreciable distance to both heater and granite, are better suited as reference values to follow changes during the 18 years of operation. The 5x-calcite-values are marked in grey.

The carbonate content of the "reference material" based on XRD Rietveld analysis (calcite 1 mass%) is in good agreement with the LECO data (0.1 mass% C which equals 0.8 – 0.9 % calcite). The evolved gas analysis of thermally-induced gases indicated the presence of at least traces of a sulfate mineral; sulfide minerals could not be identified (< 0.01 mass%). The K_2O content can be explained by 5 % K-Feldspar resulting in about 0.85 mass% K_2O and some exchangeable K^+ of the smectite (about 0.14 mass% K_2O). No K is available for illitic layers in a hypothetical interstratified mineral. Instead FEBEX bentonite as used in the ABM test in Äspö contains smectite with different hydration states when analysed in air-dry conditions. This can be described as a kind of interstratification of smectite with different water layers. Ferrage et al. (2005) demonstrated that the coexistence of different hydration states is a common phenomenon in smectites. Overall the chemical data confirms the mineralogical composition determined by Rietveld analysis. The quantitative mineralogical composition is given in Tab. 9. The results are in good agreement with those published by Nagra (NAB 13-96) except for the different Feldspar contents. BGR Rietveld refinement yielded 14 mass % Feldspar while about 3 mass % were reported in previous studies.

The mineralogical composition as determined by Rietveld analysis could be slightly modified based on chemical data but the data was used as it is because for Rietveld refinement the same parameters were used for all samples. This is the prerequisite for a possible identification of differences of samples based on quantitative XRD.

Tab. 7: Chemical composition of the references.

ABM: FEBEX-bentonite from ABM test, SKB Sweden, FEB AVG.: average of 22 samples which were at least 10 cm away from both heater and granite.

	SiO ₂	TiO ₂	Al ₂ O ₃	Fe ₂ O ₃	MnO	MgO	CaO	Na ₂ O	K ₂ O	P ₂ O ₅	(SO ₃)	LOI	Sum		C _{total}	C _{org}	C _{carb}	S _{total}
	[mass%]	[mass%]	[mass%]	[mass%]	[mass%]	[mass%]	[mass%]	[mass%]	[mass%]	[mass%]	[mass%]	[mass%]	[mass%]		[mass%]	[mass%]	[mass%]	[mass%]
REF ABM	55.2	0.2	17.2	3.1	0.0	4.4	1.8	1.1	1.0	0.0	0.1	16.0	100.2		0.1	0.0	0.1	0.0
REF FEB AVG.	54.8	0.2	17.2	3.3	0.0	4.4	1.9	1.1	1.0	0.0	0.0	15.7	99.9		0.1	0.1	0.1	0.0

Tab. 8: CEC data of the CEC references.

	Na ⁺	K ⁺	Mg ²⁺	Ca ²⁺	sum	CEC
	[meq/100g]					
REF ABM (5x-Cc)	27.3	2.9	37.0	33.8	100.0	101.0
REF averg. (n=22)	27.6	2.6	35.7	40.9	107.0	98.1

Tab. 9: Mineralogical composition of the ABM references.

	Febex REF (ABM)
	[mass%]
quartz	1
K-fsp	5
smectite	84
plagioclase	9
calcite	1
sum	100

In this study, the "average reference" values were usually abbreviated as "FEB".

4.6.3 Results

Section 36

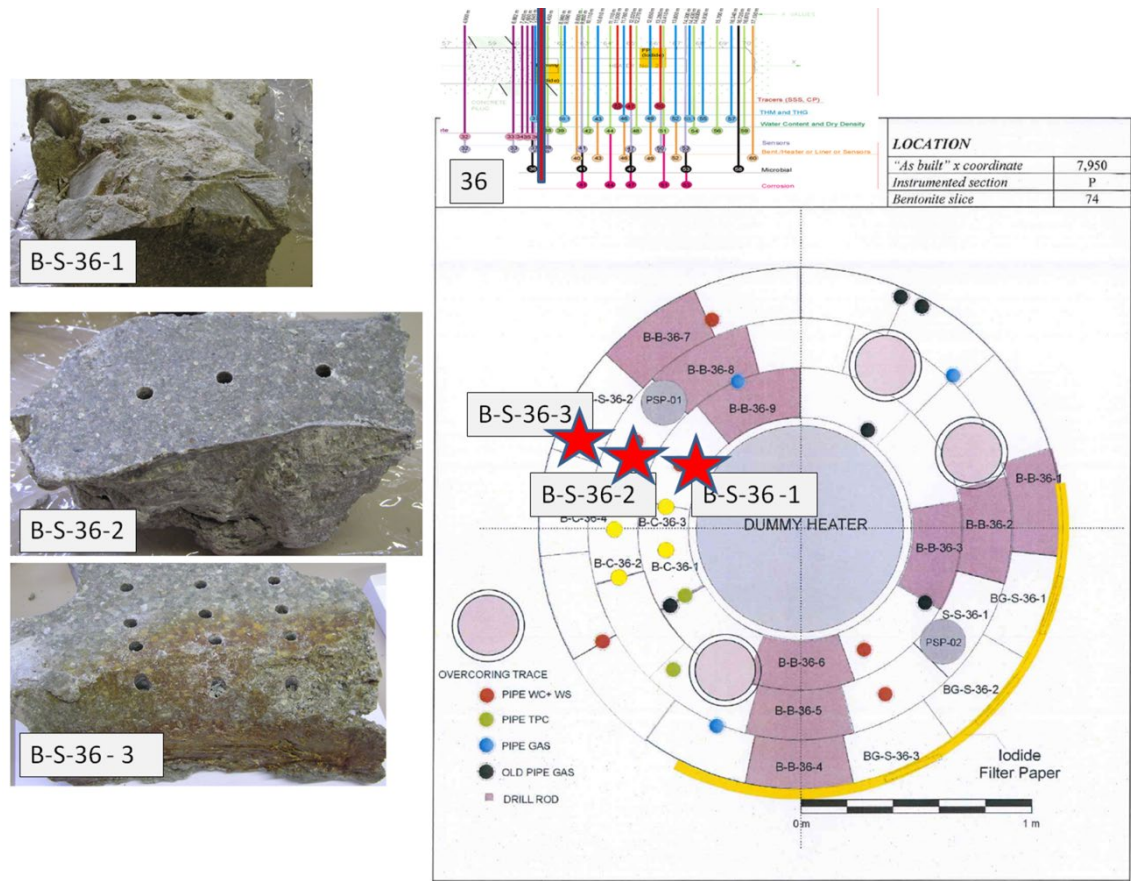


Fig. 83: Sample location and sampling of FEBEX Section 36.

Samples taken in Section 36 were selected to investigate the bentonite-iron interface (Fig. 83). Therefore, a block with direct contact to the heater (heated liner) surface was taken. To investigate the interface, one sample was taken from this block by scratching off material from the contact using a sharp knife ("1 mm sample"). The other samples were taken with increasing distance to the contact. Blocks 2 and 3 were only sampled in the center because no specific interfaces were present.

Tab. 10: Chemical composition of samples taken from Section 36.

Marked numbers indicate significant changes.

	distance from contact water (60°C)	SiO ₂	TiO ₂	Al ₂ O ₃	Fe ₂ O ₃	MnO	MgO	CaO	Na ₂ O	K ₂ O	P ₂ O ₅	(SO ₃)	LOI	Sum	C _{total}	C _{org}	C _{carb}	S _{total}	
		[mass%]	[mass%]	[mass%]	[mass%]	[mass%]	[mass%]	[mass%]	[mass%]	[mass%]	[mass%]	[mass%]	[mass%]	[mass%]	[mass%]	[mass%]	[mass%]	[mass%]	
REF ABM		55.2		17.2	3.1		4.4	1.8	1.1	1.0	0.0	0.1	16.0	100.0	0.1	0.0	0.1	0.0	
REF FEB AVG.		54.8	0.2	17.2	3.3	0.0	4.4	1.9	1.1	1.0	0.0	0.0	15.7	99.9	0.1	0.1	0.1	0.0	
B-S-36-1	1 mm	17.6	52.5	0.2	16.3	7.3	0.0	4.2	1.7	1.1	1.0	0.0	0.1	15.6	99.9	0.2	0.1	0.1	0.0
B-S-36-1	1 cm	17.6	55.4	0.2	17.3	3.3	0.0	4.4	1.7	1.1	1.0	0.0	0.0	15.3	99.9	0.1	0.1	0.1	0.0
B-S-36-1	3 cm	17.2	55.6	0.2	17.3	3.4	0.0	4.4	2.1	1.1	1.0	0.0	0.0	14.6	99.9	0.2	0.1	0.1	0.0
B-S-36-1	5 cm	17.3	55.1	0.2	17.3	3.3	0.0	4.5	2.0	1.2	1.0	0.0	0.0	15.2	99.9	0.2	0.1	0.1	0.0
B-S-36-1	8 cm	17.3	55.2	0.2	17.4	3.2	0.0	4.5	1.8	1.1	1.0	0.0	0.1	15.3	99.9	0.2	0.1	0.1	0.0
B-S-36-2	center	17.3	55.5	0.2	17.6	3.3	0.0	4.4	2.1	1.2	1.1	0.0	0.1	14.3	99.9	0.2	0.1	0.1	0.0
B-S-36-3	center	20.3	55.9	0.2	17.5	3.3	0.0	4.7	2.3	1.3	1.1	0.0	0.0	13.3	99.9	0.2	0.1	0.1	0.0

At the contact a reddish colour was observed which corresponded to an increase of the Fe-content from about 3 mass% Fe₂O₃ to about 7 mass% Fe₂O₃. (Tab. 10). This difference is supposed to result from corrosion at the bentonite/iron interface.

Tab. 11: Cation exchange data of samples taken from Section 36.

Marked numbers indicate significant changes.

	distance from heater surface [cm]	Na ⁺	K ⁺	Mg ²⁺	Ca ²⁺	sum	CEC
		[meq/100g]					
REF ABM (5x-Cc)		27.3	2.9	37.0	33.8	100.0	101.0
REF avg.		27.6	2.6	35.7	40.9	107.0	98.1
B-S-36-1	0.1	23.9	4.0	36.3	38.6	102.7	90.0
B-S-36-1	1	26.0	4.1	38.8	40.2	108.9	99.0
B-S-36-1	3	24.3	3.7	37.1	39.4	104.4	93.2
B-S-36-1	5	25.0	3.9	38.3	39.8	107.0	97.0
B-S-36-1	8	25.3	3.7	38.3	39.4	106.6	97.9
B-S-36-2	center	27.8	3.6	34.2	41.7	107.3	98.5
B-S-36-3	center	31.3	4.8	20.3	47.0	103.3	97.6

A decrease of the CEC of about 10 % was found at the contact (Tab. 11). The exchangeable Ca²⁺ was unchanged for most samples. A slight decrease of the content of exchangeable Na⁺ was found which, however, was probably within the analytical error of the method Na⁺ (± 1.9 meq/100 g, 3 sigma). The most striking change was found for the Mg content in sample B-S-36-3, which was far away from the heater. In this block, the content of exchangeable Mg²⁺ dropped by about 50 % which was not observed in any other block. At the same time an increase of the Ca²⁺ value was found (only in this sample). The CEC measurements were conducted with double specimen which provided similar results. An analytical error can, therefore, be excluded.

Tab. 12: Mineralogical analysis of selected samples from Section 36.

Marked numbers indicate significant changes.

	B-S-36-3 1mm	B-S-36-3 8cm	FEB
	[mass%]	[mass%]	[mass%]
quartz	2	2	1
K-fsp	4	5	5
smectite	82	83	84
plagioclase	10	9	9
calcite	0	1	1
goethite	2		
sum	100	100	100

For the contact sample a slightly lower calcite content was found. The most significant difference, however, was the appearance of goethite at the contact. The mineralogical composition was further investigated by STA (Fig. 84) and IR (Fig. 85).

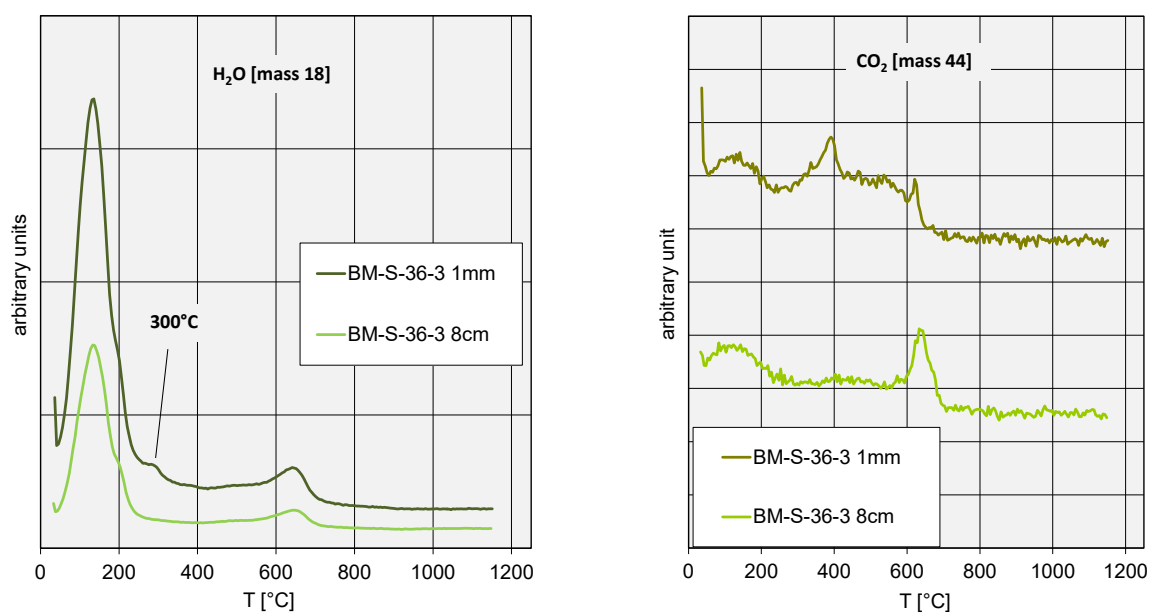


Fig. 84: STA mass spectrometer curves of two samples taken from Section 36.

The sample taken from the contact showed a small but clearly observable H₂O peak at 300 °C (thermal analysis). This peak position is typical of both goethite dehydroxylation and organic carbon oxidation. A new peak was observed in the CO₂ curve at 400 °C indicating the accumulation of organic matter near the heater. This peak, however, is close to the detection limit and, therefore, represents traces of organic matter which could not be resolved by LECO analysis. The H₂O peak, at 300 °C, therefore can be assigned to goethite which is in agreement with the XRD results.

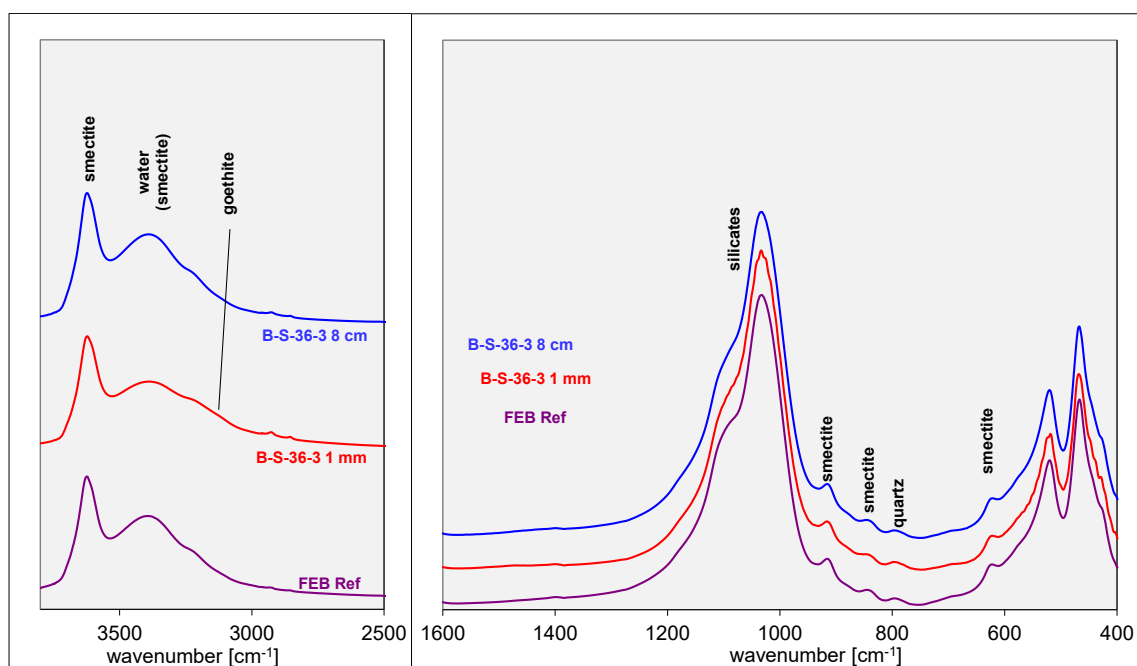


Fig. 85: IR spectra of two samples taken from Section 36 (compared with the reference material).

The spectra collected from other Section 36 blocks are similar. Only a weak inflection in the spectrum of the contact sample was found at 3140 cm^{-1} which points towards the presence of goethite. At the contact of Section 36 the formation of goethite was proven by STA, IR (Fig. 84, Fig. 85), and XRD. The Fe_2O_3 content increased by about 4 mass% Fe_2O_3 and XRD Rietveld analysis calculated an increase of 2 mass% goethite. A slightly larger value would have been expected based on the XRF results.

In the sample from the outermost blocks a marked decrease of exchangeable Mg^{2+} was found (along with an increase of exchangeable Ca^{2+}) which cannot be explained yet. The heater and corrosion are not supposed to play a role with respect to the loss of Mg^{2+} because of the large distance.

Section 42 a

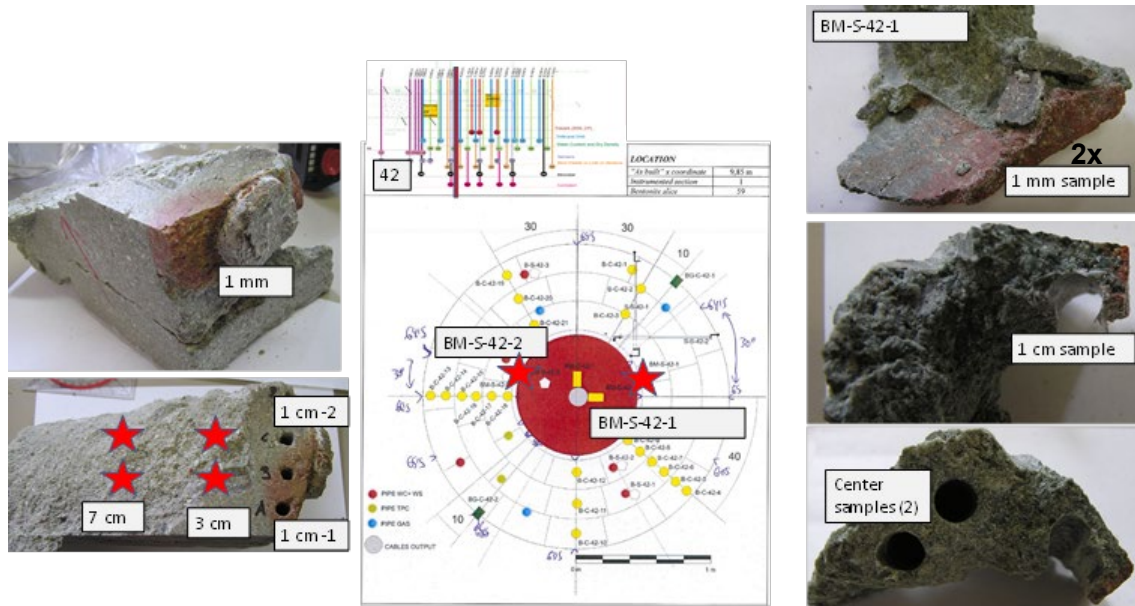


Fig. 86: Sample location and sampling of FEBEX Section 42a.

From Section 42 different samples from the "BM-series" were available (Fig. 86), some from the contact and some in larger distance (42b) from the liner. The samples with obvious contacts to the heater/liner (42a) were sampled at various distances. The contact was scratched off with a sharp knife ("1 mm sample") and the other samples were taken at larger distances. The chemical composition is shown in Tab. 13.

Tab. 13: Chemical composition of samples taken from Section 42a.

Marked numbers indicate significant changes.

	distance	water (60°C)	SiO ₂	TiO ₂	Al ₂ O ₃	Fe ₂ O ₃	MnO	MgO	CaO	Na ₂ O	K ₂ O	P ₂ O ₅	(SO ₃)	LOI	Sum	Ctotal	Corg	Ccarb	Stotal
		[mass%]	[mass%]	[mass%]	[mass%]	[mass%]	[mass%]	[mass%]	[mass%]	[mass%]	[mass%]	[mass%]	[mass%]	[mass%]	[mass%]	[mass%]	[mass%]	[mass%]	[mass%]
REF ABM		55.2		17.2	3.1			4.4	1.8	1.1	1.0	0.0	0.1	16.0	100.0	0.1	0.0	0.1	0.0
REF FEB AVG.		54.8	0.2	17.2	3.3	0.0		4.4	1.9	1.1	1.0	0.0	0.0	15.7	99.9	0.1	0.1	0.1	0.0
BM-S-42-1	1 mm	16.4	53.6	0.2	17.1	5.0	0.0	4.3	1.4	1.1	0.9	0.0	0.0	16.1	99.9	0.1	0.1	0.0	0.0
BM-S-42-1	1 cm	16.3	54.7	0.2	17.2	3.7	0.0	4.3	1.5	1.1	0.9	0.0	0.0	16.2	99.9	0.1	0.1	0.0	0.0
BM-S-42-1 (2)	1 mm	15.9	53.4	0.2	16.8	4.8	0.1	4.9	1.7	1.1	0.8	0.0	0.0	16.1	99.8	0.1	0.1	0.1	0.0
BM-S-42-1	center	17.0	54.9	0.2	17.3	3.5	0.0	4.4	1.5	1.1	0.9	0.0	0.0	15.9	99.9	0.1	0.1	0.0	0.0
BM-S-42-2	1 mm	14.1	53.2	0.2	16.8	6.7	0.0	4.3	1.5	1.1	0.9	0.0	0.0	15.1	99.9	0.1	0.1	0.0	0.0
BM-S-42-2 a+b	1 cm	14.4	54.9	0.2	17.1	4.6	0.0	4.3	1.5	1.1	1.0	0.0	0.0	15.1	99.9	0.1	0.1	0.0	0.0
BM-S-42-2 (2) c+d	1 cm	14.7	55.1	0.2	17.3	3.4	0.0	4.4	1.6	1.1	1.0	0.0	0.0	15.5	99.9	0.1	0.1	0.0	0.0
BM-S-42-2 a+b	3 cm	14.6	55.3	0.2	17.5	3.5	0.0	4.5	1.8	1.2	1.0	0.0	0.0	14.8	99.9	0.1	0.1	0.1	0.0
BM-S-42-2 (2) c+d	3 cm	14.9	55.3	0.2	17.5	3.3	0.0	4.5	1.8	1.2	1.0	0.0	0.0	15.1	99.9	0.1	0.1	0.1	0.0
BM-S-42-2 ab	7 cm	14.9	55.1	0.2	17.4	3.3	0.0	4.6	1.9	1.2	1.0	0.0	0.0	15.2	99.9	0.1	0.1	0.1	0.0
BM-S-42-2 (2) cd	7 cm	15.0	54.9	0.2	17.4	3.2	0.0	4.4	1.8	1.1	0.9	0.0	0.0	16.0	99.9	0.1	0.1	0.1	0.0

As in Section 36 an increase of the Fe content was found in all three "1 mm samples". In addition, a slightly larger MgO content was found for sample BM-S-42-1(2)-1mm. Also, a slightly lower CaO was observed which possibly correlates with a small decrease of the inorganic carbon content. These changes, however, were rather small and are, hence, not interpreted further. One contact sample and the sample taken at 1 cm distance which also showed an increase of the Fe content were investigated with XRD Rietveld (Tab. 14). The sample taken at 7 cm distance to the contact was investigated as reference.

Tab. 14: Mineralogical composition as determined by XRD Rietveld analysis of Section 42a.

	BM-S-42-2 1mm	BM-S-42-2 1cm	BM-S-42-2 7cm	FEB
	[mass%]	[mass%]	[mass%]	[mass%]
quartz	1	2	1	1
K-fsp	4	4	4	5
smectite	83	84	84	84
plagioclase	9	9	9	9
calcite	0	0	1	1
goethite	2	1		
sum	100	100	100	100

As in case of the samples taken from Section 36 goethite was found by XRD at the contact. In this section, however, goethite was also found in the sample taken in 1 cm distance to the contact. A decrease of the carbonate content was found as well (as observed for the contact samples of Section 36).

Tab. 15: CEC data of the samples taken from Section 42a.

	distance from heater surface [cm]	Na ⁺	K ⁺	Mg ²⁺	Ca ²⁺	sum	CEC
		[meq/100g]					
REF ABM (5x-Cc)		27.3	2.9	37.0	33.8	100.0	101.0
REF averg.		27.6	2.6	35.7	40.9	107.0	98.1
BM-S-42-1	0.1	25.9	2.9	37.0	36.6	102.4	98.2
BM-S-42-1	1	26.2	2.5	36.6	37.2	102.6	97.3
BM-S-42-1 (2)	0.1	25.6	2.5	36.8	41.2	106.1	97.3
BM-S-42-1	center	26.8	2.6	37.7	39.1	106.1	101.2
BM-S-42-2	0.1	25.4	2.4	36.3	37.4	101.4	94.8
BM-S-42-2 a+b	1	26.0	2.4	37.3	37.8	103.5	96.6
BM-S-42-2 (2) c+d	1	26.1	2.2	38.3	39.7	106.2	98.0
BM-S-42-2 a+b	3	26.1	2.4	37.3	40.4	106.2	98.0
BM-S-42-2 (2) c+d	3	26.5	2.3	38.0	40.7	107.4	97.8
BM-S-42-2 ab	7	26.3	2.7	38.5	40.1	107.5	98.0
BM-S-42-2 (2) cd	7	26.8	2.5	39.1	40.1	108.4	98.8

A CEC decrease of about 5 % was found for the contact sample with the largest increase of Fe (Tab. 15). The CEC decrease of the other contact samples, however, was nearly insignificant. Interestingly, no significant change of exchangeable Na⁺ and exchangeable Mg²⁺ was found. No systematic variation of the content of exchangeable Ca²⁺ could be identified either.

An increase of the Fe content of the contact samples and of one "1 cm sample" was observed. At the contact, goethite was found by XRD. A slight CEC drop (5 %) was found for one sample. The CEC decrease of the other two contact samples was insignificant in this section. Fe accumulation was accompanied by a small decrease of the calcite content (as already observed in Section 36).

The results were considered to be consistent. Therefore, no further analysis (e.g. IR, STA) was conducted on these samples.

Section 54

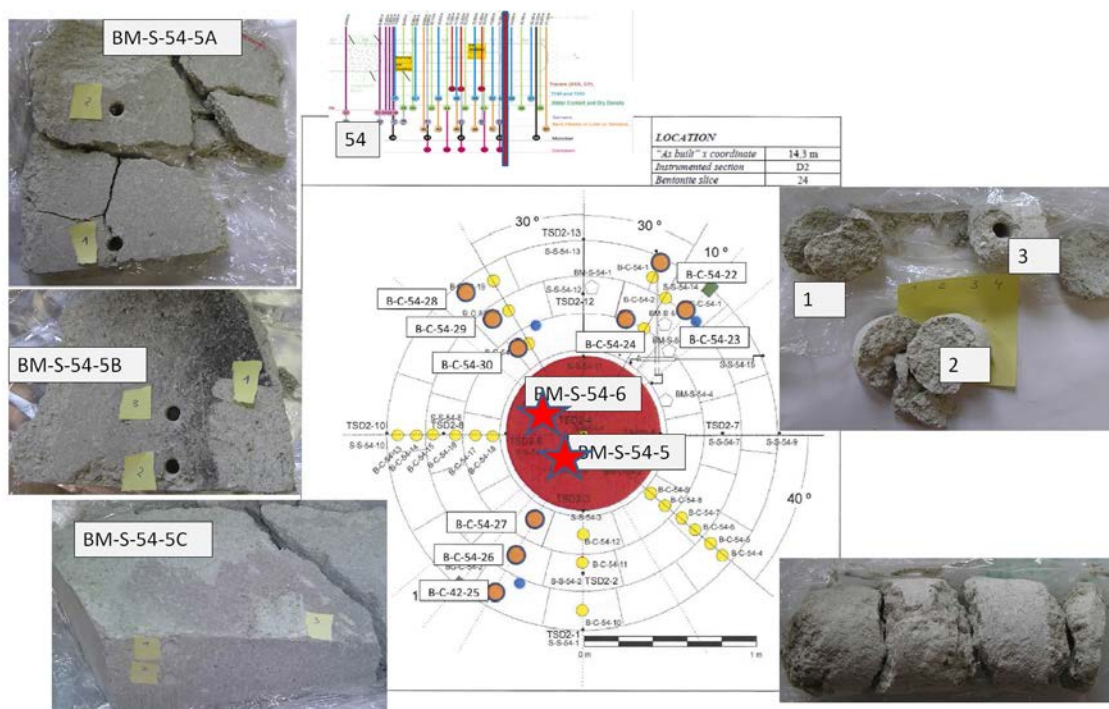


Fig. 87: Sample location and sampling of FEBEX Section 54.

Because a larger amount of sample mass was required, additional samples were taken at the interface (BM-S-54-5B2 + BM-S-54-1NH).

Section 54 was sampled because these blocks were in direct contact to the heater, without the liner in between (Fig. 87). Interestingly no reddish contact was found. Instead even surfaces covered with a dark to greenish coating indicated the contact to the heater. The chemical composition is given in Tab. 16.

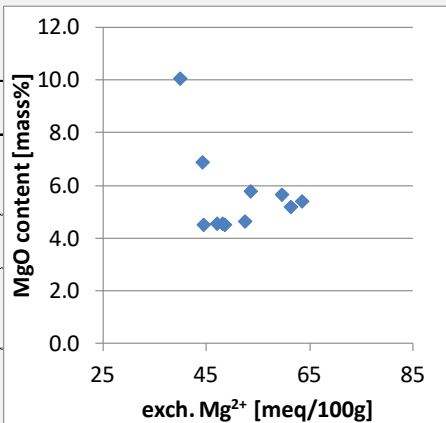
Tab. 16: Chemical composition of samples taken from Section 54.

	distance to heater [cm]	water (60°C) [mass%]	SiO ₂ [mass%]	TiO ₂ [mass%]	Al ₂ O ₃ [mass%]	Fe ₂ O ₃ [mass%]	MnO [mass%]	MgO [mass%]	CaO [mass%]	Na ₂ O [mass%]	K ₂ O [mass%]	P ₂ O ₅ [mass%]	(SO ₃) [mass%]	LOI [mass%]	Sum [mass%]	C _{total} [mass%]	C _{org} [mass%]	C _{carb} [mass%]	S _{total} [mass%]
REF ABM			55.2		17.2	3.1		4.4	1.8	1.1	1.0	0.0	0.1	16.0	100.0	0.1	0.0	0.1	0.0
REF FEB AVG.			54.8	0.2	17.2	3.3	0.0	4.4	1.9	1.1	1.0	0.0	0.0	15.7	99.9	0.1	0.1	0.1	0.0
BM-S-54-6 1		10.6	53.8	0.2	16.8	3.1	0.0	4.6	2.1	1.1	0.9	0.0	0.0	17.3	99.9	0.1	0.1	0.1	0.0
BM-S-54-6 2		10.8	53.7	0.2	16.9	3.0	0.0	4.6	1.9	1.0	1.0	0.0	0.0	17.5	99.9	0.1	0.1	0.1	0.0
BM-S-54-6 3		11.0	54.3	0.2	16.8	3.0	0.0	4.5	1.8	1.0	0.9	0.0	0.0	17.3	99.9	0.1	0.1	0.1	0.0
BM-S-54-5A 1		11.3	52.9	0.2	16.6	3.0	0.0	5.4	1.8	0.8	0.9	0.0	0.1	18.1	99.9	0.1	0.1	0.0	0.0
BM-S-54-5A 2		10.7	52.9	0.2	16.3	3.0	0.0	5.6	1.9	0.9	1.1	0.0	0.0	17.9	99.9	0.1	0.1	0.1	0.0
BM-S-54-5B 1	0.1	7.6	50.4	0.2	15.5	3.2	0.1	10.1	2.1	0.8	0.9	0.0	0.0	16.6	99.9	0.3	0.1	0.2	0.0
BM-S-54-5B 2		10.6	52.9	0.2	16.2	3.0	0.1	5.8	1.9	0.8	1.0	0.0	0.1	18.0	99.9	0.1	0.1	0.1	0.0
BM-S-54-5B 3		11.1	53.1	0.2	16.6	3.0	0.0	5.2	1.8	0.9	1.0	0.0	0.0	18.0	99.9	0.1	0.1	0.0	0.0
BM-S-54-5C 1		11.2	53.3	0.2	16.8	3.0	0.0	4.6	2.0	1.0	0.9	0.0	0.0	18.0	99.9	0.1	0.1	0.0	0.0
BM-S-54-5C 2		11.1	53.7	0.2	16.7	3.0	0.0	4.5	2.0	1.0	1.0	0.0	0.1	17.7	99.9	0.1	0.1	0.1	0.0
BM-S-54-5C 3	0.1	9.8	52.0	0.2	16.3	2.9	0.1	6.9	2.2	0.9	0.9	0.0	0.0	17.5	99.9	0.2	0.1	0.1	0.0

No increase of the Fe content was found which explains the absence of reddish colour. Instead, some samples showed an increased MgO content. The highest MgO contents were observed for the samples which were scratched off the contact surface. Moreover, the increase by almost 6 mass% of sample BM-S-54-5B1 was higher than in the LOT, PTR, ABM, or Heater-D test (e.g. Kaufhold et al. 2013). Therefore, a detailed mineralogical analysis was carried out on this material. A minor part of the Mg could be explained by cation exchange. The CEC data is given in Tab. 17.

Tab. 17: CEC data of the samples taken from Section 54.

	distance from heater [cm]	Na ⁺	K ⁺	Mg ²⁺ [meq/100g]	Ca ²⁺	sum	CEC
REF ABM (5x-Cc)		27.3	2.9	37.0	33.8	100.0	101.0
REF averg.		27.6	2.6	35.7	40.9	107.0	98.1
BM-S-54-6 1		23.9	2.9	48.2	54.2	129.6	97.6
BM-S-54-6 2		24.1	2.9	47.2	50.9	125.4	100.1
BM-S-54-6 3		23.8	2.9	44.6	45.1	116.7	99.1
BM-S-54-5A 1		18.1	3.4	63.6	49.5	134.9	95.2
BM-S-54-5A 2		17.1	3.6	59.8	46.1	127.0	88.5
BM-S-54-5B 1	0.1	15.7	3.2	40.1	35.9	95.0	63.9
BM-S-54-5B 2		17.5	3.1	53.6	45.0	119.6	83.3
BM-S-54-5B 3		19.5	3.3	61.4	48.6	133.2	94.2
BM-S-54-5C 1		22.4	2.9	52.6	56.5	134.9	95.4
BM-S-54-5C 2		22.2	2.9	48.6	52.0	126.1	96.2
BM-S-54-5C 3	0.1	19.8	3.0	44.4	51.5	119.1	82.9



The highest MgO increase was found in subsample 5B1. The content of exchangeable Mg of this sample increased by only 5 meq/100 g. Most of the MgO increase, therefore, has to be explained by processes other than cation exchange. Other subsamples, as 5A1, showed an increase of exchangeable Mg by about 20 meq/100 g explaining approximately 0.4 mass% MgO. Accordingly, the MgO decrease cannot be explained by exchangeable Mg variation as in the case of Section 48. A marked decrease of the CEC of the contact samples was found as well. The most pronounced CEC drop was found for the samples with the largest MgO increase. These samples were investigated further (Fig. 88).

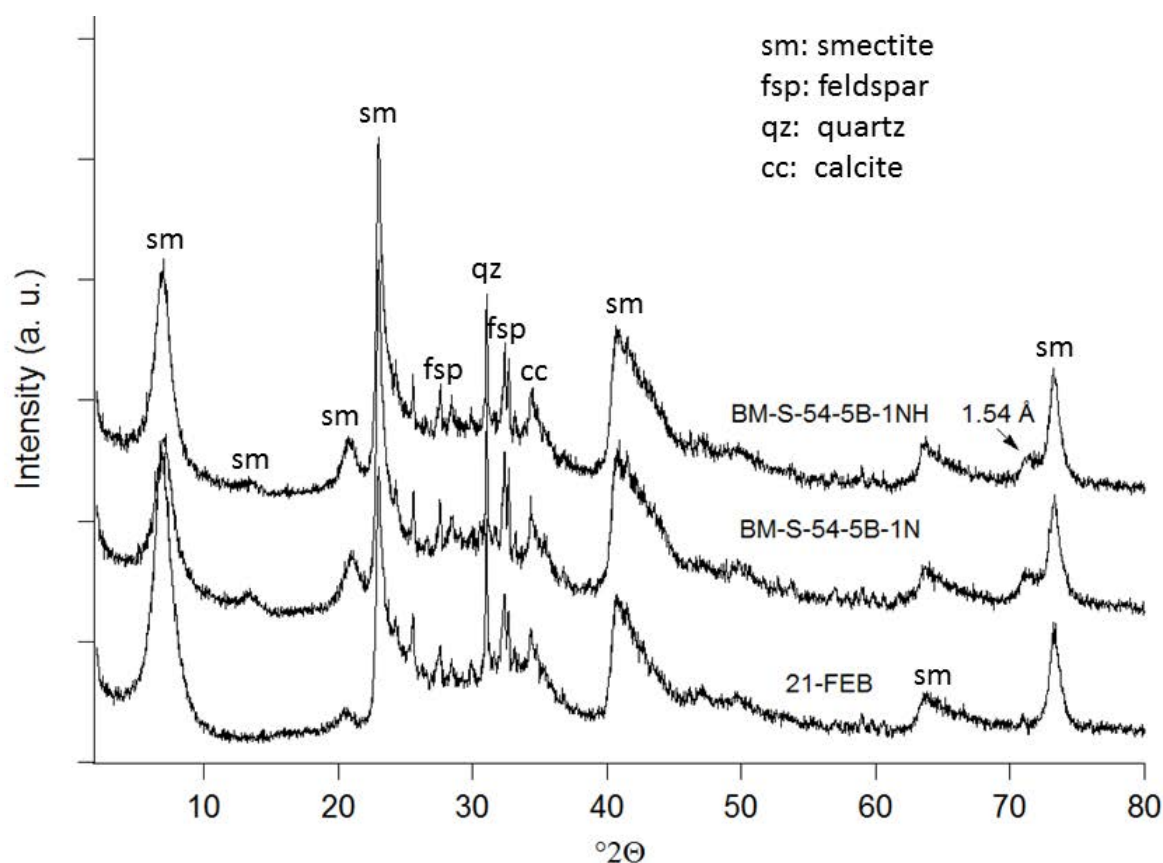


Fig. 88: XRD powder pattern of selected samples of Section 54 (samples BM-S-54-5B-1N(H) were taken at the same position as BM-S-54-5B-1 from which not enough material was left for XRD Rietveld analysis).

For sample 5B1 with the largest MgO increase a new peak was found at 1.54 Å which indicates the presence of trioctahedral domains or phases. The formation of trioctahedral domains in bentonites containing dioctahedral smectites at the very contact to a heater surface was described before (Kaufhold et al. 2013, Svensson 2015). However, such a significant drop of the CEC as in case of sample 5B1 (almost 40 %) was not observed before (for samples with MgO increase only).

Tab. 18: Mineralogical composition as determined by XRD Rietveld refinement.

	BM-S-54-5B2	BM-S-54-5C2	BM-S-54-5C3	BM-S-54-5B-1N	BM-S-54-5B-1NH	FEB
	[mass%]	[mass%]	[mass%]	[mass%]	[mass%]	[mass%]
quartz	2	2	2	2	4	1
K-fsp	4	4	4	2	2	5
smectite	86	84	86	87	85	84
plagioclase	8	9	8	6	6	9
calcite	1	1	1	0	1	1
brucite				2	2	
sum	100	100	100	100	100	100

XRD Rietveld refinement of the pattern shown in Fig. 88 revealed the presence of brucite in the contact samples. The presence of kaolinite could be ruled out based on the oriented mount XRD (Fig. 90). The brucite, however, does not explain the change of the d_{060} reflection. XRD, therefore, indicated the formation of both, brucite and trioctahedral smectite. Interestingly XRD Rietveld refinement did not reveal a decrease of the smectite content although the CEC was markedly reduced. The expandability was, therefore, further investigated by XRD analysis of texture slides (Fig. 89). All samples showed full expandability (upon ethylene glycol (EG) treatment the peaks moved to about 17 \AA). Even a close look at the comparison of subsample 5B1 (resp. 54-1NH) with the reference (Fig. 90) did not reveal the formation of any other clay mineral. Kaolinite formation could be ruled out which also helped to interpret the IR spectra (Fig. 92). Differences in peak positions of the two patterns are mainly caused by a small sample displacement error during XRD analysis. Sample 54-1NH shows a sharper and more symmetrical main reflection in the powder pattern and additionally a weak reflection at $13.5^\circ 2\theta$. This sample has a stronger tendency towards the bihydrated state during the measurement than the reference sample. This is not an indication for a structural change and may be caused by slightly different measurement conditions (temperature and relative humidity) and/or varying interlayer cation population.

Another interesting observation is the poor degree of preferred orientation hk band at approximately $23^\circ 2\theta$ of the samples "0" and "2" in Fig. 89 compared with the reference material "21". This has to be investigated in the future.

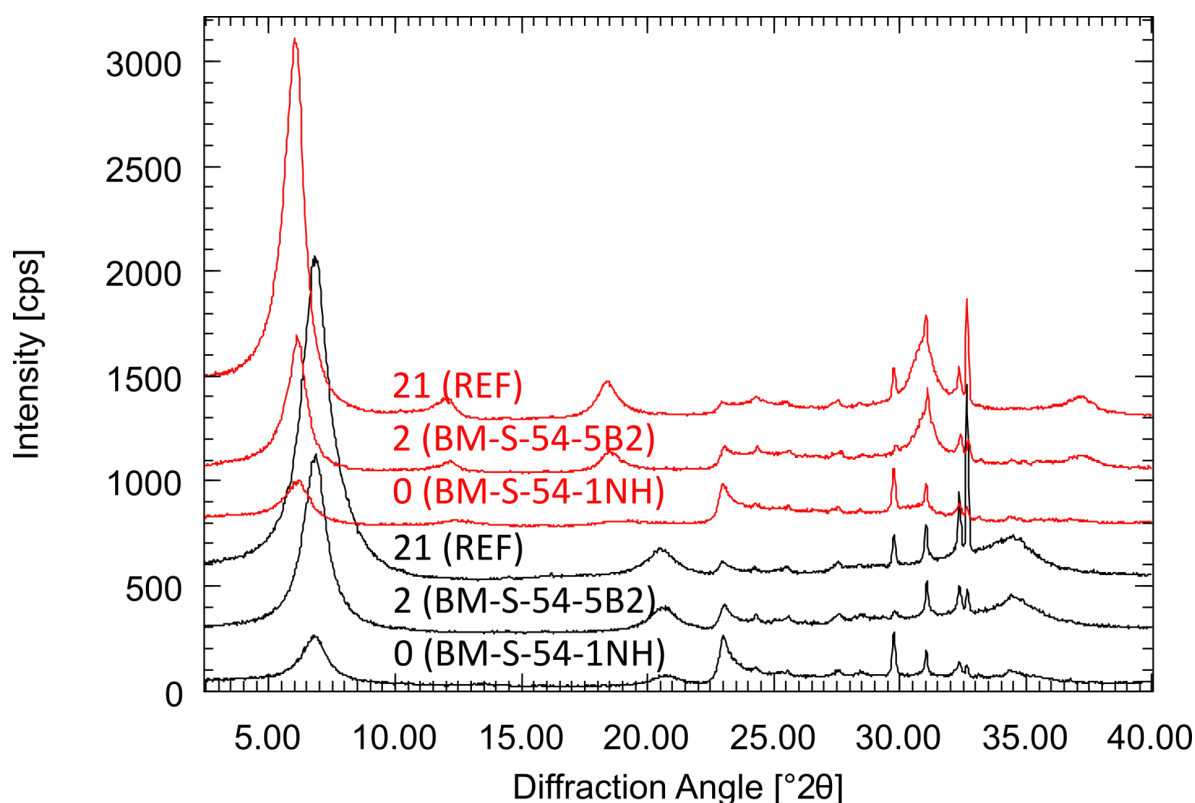


Fig. 89: XRD texture slides of selected samples of Section 54 (black: air dried, red: ethylene glycol treated).

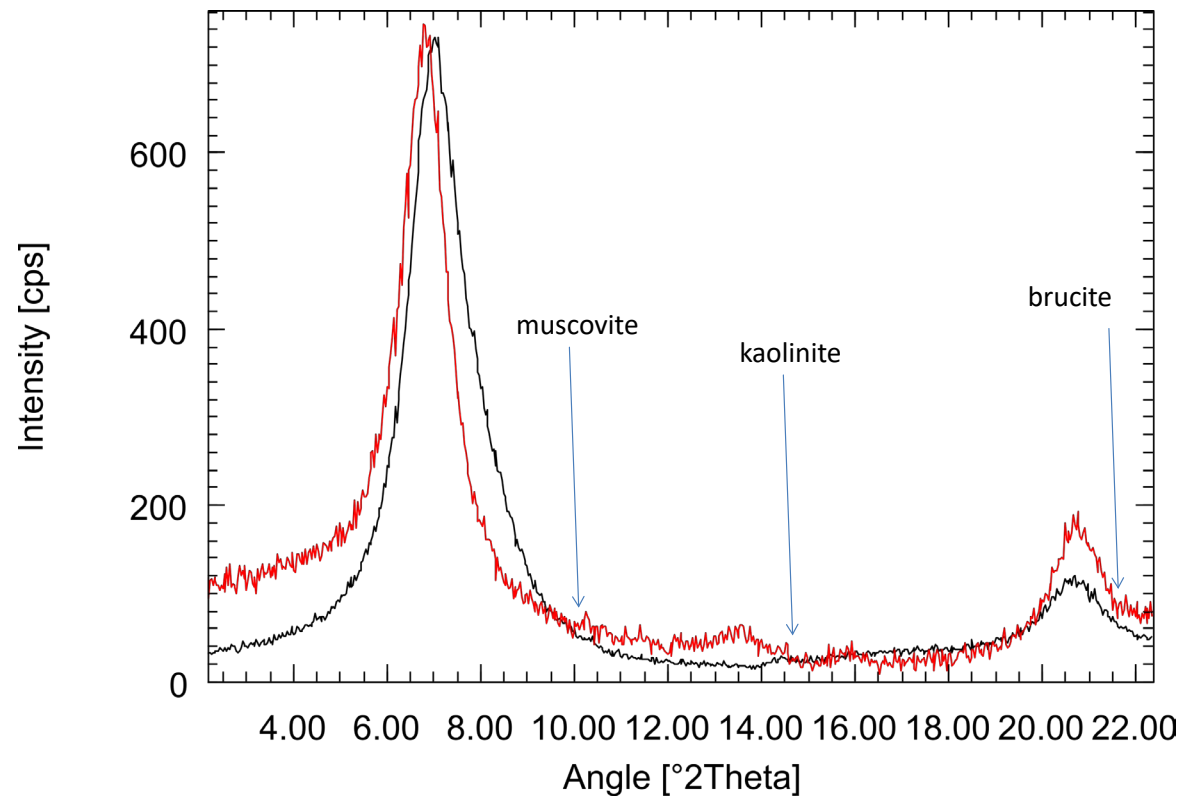


Fig. 90: XRD texture slides, black: REF, red: BM-S-54-1NH.

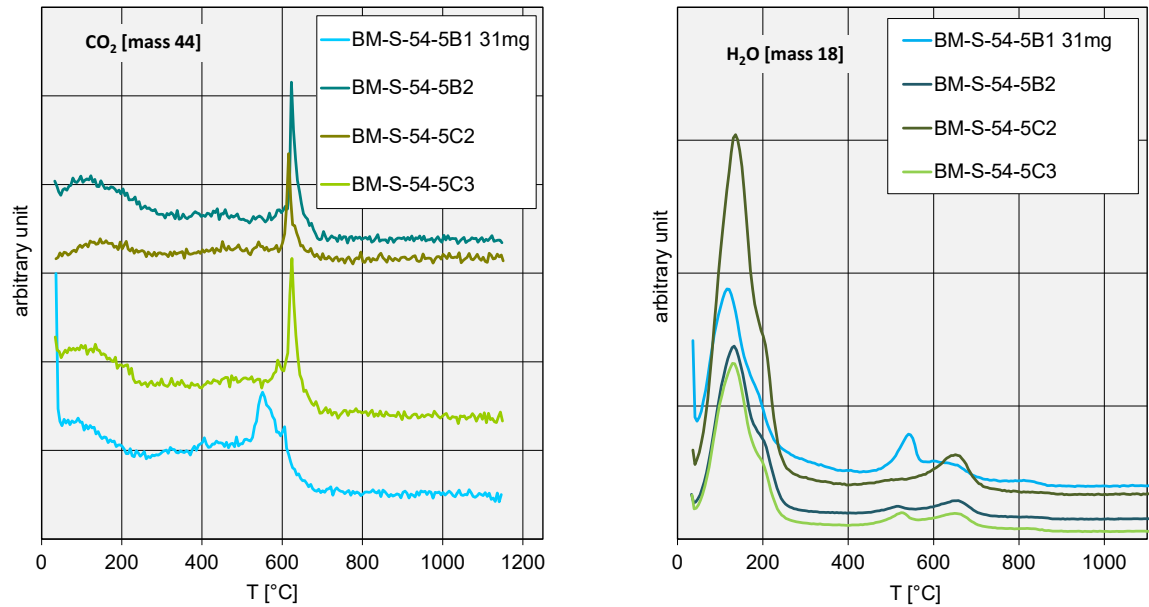


Fig. 91: STA curves of selected samples taken from Section 54.

For thermal analysis of the contact samples only 31 mg were left (compared to 70 mg used to record the other curves; Fig. 91). This probably led to the small shift of the carbonate peak at about 600 °C. In the water curve a new peak appeared at about 530 °C (described already in Section 35). This peak could be assigned to either kaolinite or brucite. Thermal analysis, therefore, did not provide further information on the brucite or kaolinite formation. Further investigations were performed by IR spectrometry (Fig. 92).

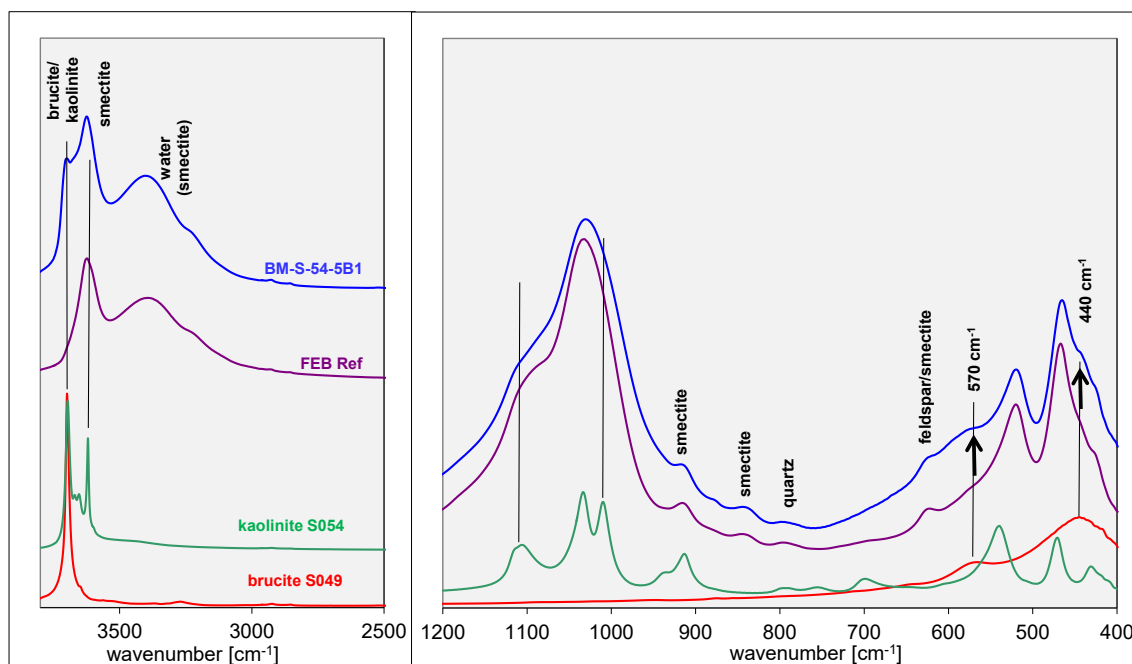


Fig. 92: IR spectra of the sample with the largest MgO increase.

In the IR spectra of sample BM-S-54-5B2 (second largest MgO increase) no additional features were found. The focus was, therefore, set on sample BM-S-54-5B1. In the spectra of this sample, the reference material, and of the two references S054 and S049 (BGR reference materials) were given. The most prominent new spectral feature of sample 5B1 is the band at 3698 cm^{-1} . This band can be assigned to brucite or kaolinite. The second characteristic band of kaolinite is masked by the smectite band at 3'630 cm^{-1} and hence cannot be used for unambiguous mineral identification. No spectral differences were found in the SiO-stretching region where additional kaolinite should have caused some changes of the band shape (between 1000 and 1100 cm^{-1}). In contrast, slight changes were observed in the spectrum of sample 5B1 in the oxide deformation range (400 – 600 cm^{-1}). Both these additional humps (570 + 440 cm^{-1}) can be explained by a larger brucite content because the pure brucite also revealed bands at these positions. Based on XRD results, however, the formation of kaolinite could be ruled out.

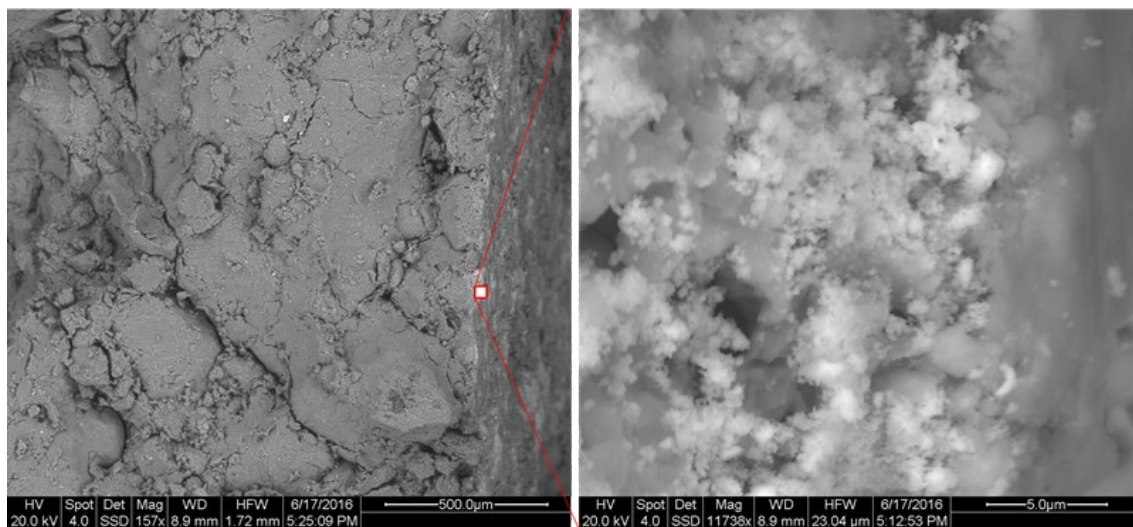


Fig. 93: SEM images of the contact surface towards the heater.

The contact was investigated using SEM (Fig. 93). The contact is represented by an even surface with small white spots. As expected, the Mg content is slightly larger at the surface, but actual values differ depending on the considered location. The bright spots at the surface are rather small (Fig. 93). Their primary particle diameter is < 100 nm. These particles can be brucite or a Mg-rich clay mineral. Interestingly, the zone in which the white spots formed is rather thin (about $5\text{ }\mu\text{m}$).

A significant MgO increase was found for the samples scratched off the surface of the contact to the heater. Notably, these blocks were in direct contact with the heater and not with the liner as samples considered before. Formation of brucite and trioctahedral smectite domains were indicated.

Corrosion samples directly from liner

In addition to the bentonite samples taken from the blocks additional samples were taken directly from the metal surfaces of the liner (Fig. 94, Tab. 19, Tab. 20).

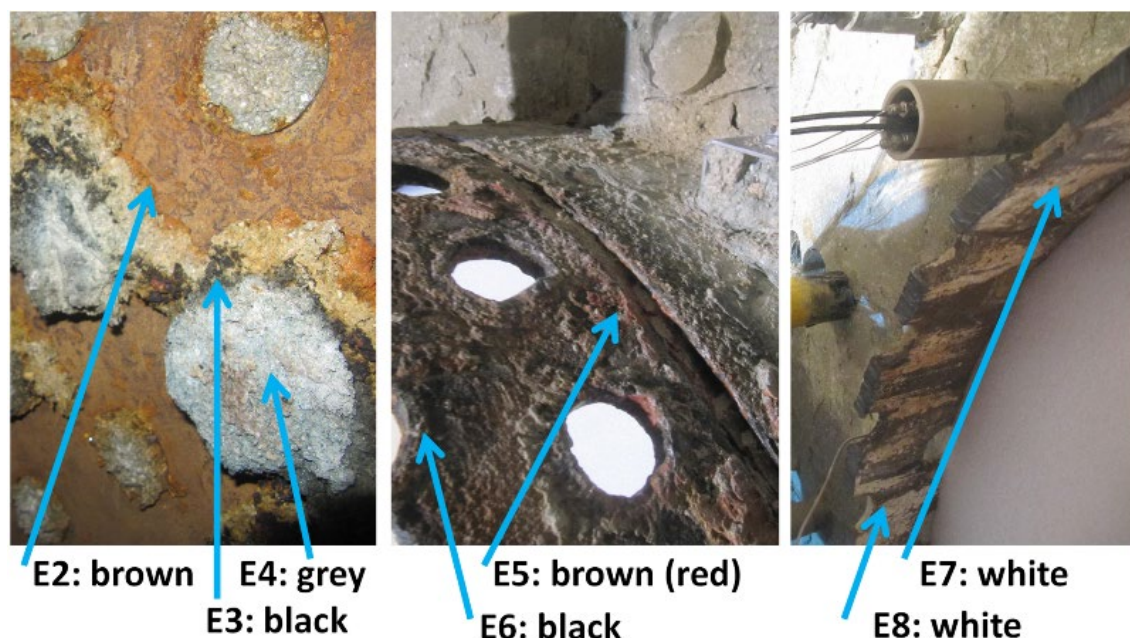


Fig. 94: Samples taken directly from or at the liner.

Tab. 19: Chemical composition of the samples taken directly from the surface of the metal (liner).

Marked numbers indicate significant changes.

	SiO ₂	TiO ₂	Al ₂ O ₃	Fe ₂ O ₃	MnO	MgO	CaO	Na ₂ O	K ₂ O	P ₂ O ₅	(SO ₃)	LOI	Sum	C _{total}	C _{org}	C _{carb}	S _{total}
	[mass%]	[mass%]	[mass%]	[mass%]	[mass%]	[mass%]	[mass%]	[mass%]	[mass%]	[mass%]	[mass%]	[mass%]	[mass%]	[mass%]	[mass%]	[mass%]	[mass%]
REF ABM	55.2		17.2	3.1		4.4	1.8	1.1	1.0	0.0	0.1	16.0	100.0	0.1	0.0	0.1	0.0
REF FEB AVG.	54.8	0.2	17.2	3.3	0.0	4.4	1.9	1.1	1.0	0.0	0.0	15.7	99.9	0.1	0.1	0.1	0.0
E2	50.3	0.2	16.7	8.5	0.0	4.3	1.5	1.1	0.9	0.0	<0.01	16.3	99.9	0.1	0.1	0.0	0.0
E3	52.4	0.2	15.8	6.2	0.0	4.3	1.9	1.3	0.9	0.0	<0.01	16.8	99.9	0.1	0.1	0.0	0.0
E4	52.7	0.2	16.8	3.2	0.1	5.9	2.0	1.0	0.9	0.0	0.1	17.1	99.9	0.1	0.1	0.1	0.1
E5	52.7	0.2	16.5	7.8	0.0	4.2	1.4	1.1	0.9	0.0	0.0	15.1	99.9	0.1	0.1	0.0	0.0
E6	29.6	0.1	9.3	37.1	0.5	3.1	3.1	0.5	0.5	0.0	0.1	15.9	99.6	1.6	0.1	1.5	0.1
E7	33.0	0.1	10.4	4.1	0.2	5.1	18.5	0.8	0.6	0.0	0.1	27.0	99.7	4.4	0.1	4.3	0.1
E8	38.4	0.2	12.0	2.8	0.1	4.1	15.9	0.8	0.7	0.0	0.1	24.6	99.7	3.3	0.2	3.2	0.1

The MgO increase of the E-samples was low despite the fact that the E-samples were taken directly from the liner. A slight increase of MgO was found in the grey material collected between heater and liner. Samples E2, E3, and E5 showed elevated Fe-contents. By far the largest Fe-increase was found for sample E6. For samples E7 and E8 (white crust inside liner) a marked increase of both C and CaO was observed pointing towards the presence of carbonates.

Tab. 20: Mineralogical composition as determined by Rietveld analysis. 0 means < 1 mass% but present.

	E2 [mass%]	E3 [mass%]	E4 [mass%]	E5 [mass%]	E6 [mass%]	E7 [mass%]	FEB [mass%]
quartz	2	1	2	2	2	1	1
K-fsp	4	5	4	4		4	5
crystalite							
smectite	83	84	86	81	52	55	84
plagioclase	8	10	8	8	9	5	9
calcite	0	0	1	0		2	1
goethite	3			5	4		
siderite					7		
magnetite					13		
maghemite					5		
iron					0		
muscovite					7		
aragonite						30	
dolomite						2	
	100	100	100	100	100	100	100

In sample E2 (reddish, scratched off from the inside of the liner) goethite was found by XRD. Samples E3 and E4 were similar compared to the reference (within the analytical accuracy and despite a somewhat lower calcite content). No newly-formed Fe phases were found in E3 although the Fe_2O_3 -content increased by about 3 %. The black crust scratched off the liner (E6) contained siderite and magnetite and still the primary components of the bentonite (as smectite). Traces of native Fe were also found in this sample. For Rietveld refinement, it was advantageous to add a maghemite structure (yielded a better fit). The actual presence of maghemite, however, is difficult to verify. Interestingly, sample E6 contains 10 Å intensities which were described as muscovite in XRD Rietveld analysis. This can be explained either by sample heterogeneity (larger illite content because of natural variation) or some smectite collapsed upon dehydration to 10 Å and hence had to be described as muscovite in the Rietveld refinement. It may also be possible that real muscovite formed but the K-content decreased which would not correspond to the formation of muscovite. In the white crust, more than 30 % carbonates were found, dominated by aragonite. The results of thermal analysis are shown in Fig. 95.

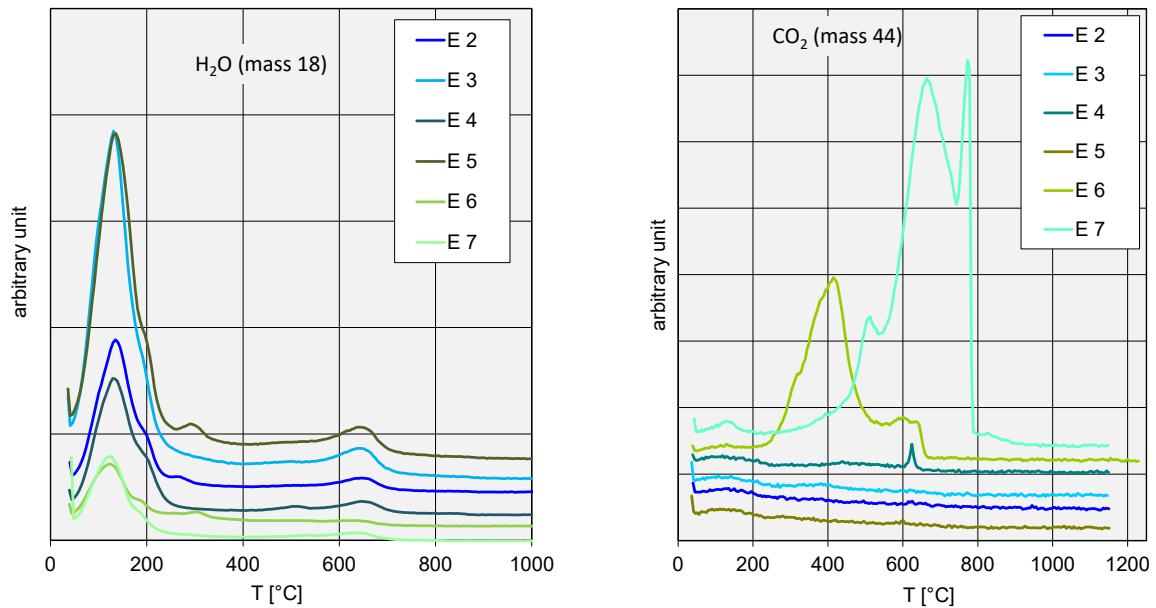


Fig. 95: STA curves of the E-samples taken directly from the metal surface.

The thermal analysis (evolved gas analysis) H₂O curve (Fig. 95) of the E samples confirmed the presence of goethite (dehydroxylation at 300 °C) which was found by XRD (E2, E5, E6). The CO₂ curves confirmed the presence of carbonates (siderite: E6, aragonite: E7). Thermal analysis confirmed the XRD and XRF results and did not provide further information.

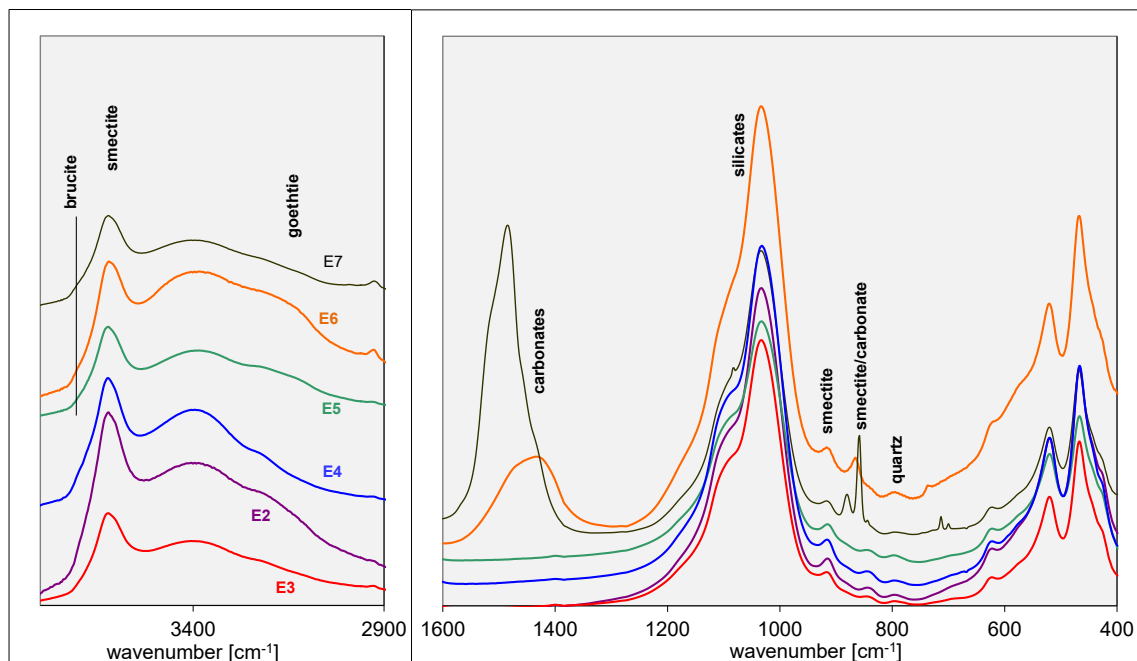


Fig. 96: IR spectra of the E-samples taken directly from the metal surface.

The IR spectra (Fig. 96) of the E samples proved the absence of brucite and confirmed the presence of goethite (most significant in sample E6) and the presence of carbonates (E6, E7).

Tab. 21: CEC data of the E-samples taken directly from the metal surface.

	distance from heater surface [cm]	Na ⁺	K ⁺	Mg ²⁺	Ca ²⁺	sum	CEC
		[meq/100g]					
REF ABM (5x-Cc)		27.3	2.9	37.0	33.8	100.0	101.0
REF averg.		27.6	2.6	35.7	40.9	107.0	98.1
E2	0	27.4	3.0	38.5	41.2	110.1	90.6
E3	0	31.1	2.5	32.8	44.4	110.9	86.8
E4	0	24.2	2.7	54.1	53.6	134.6	91.0
E5	0	25.3	2.8	36.3	36.8	101.2	93.2
E6	0	8.8	1.2	16.4	32.2	58.7	37.6
E7	0	16.3	1.7	24.7	28.8	71.5	53.9
E8	0	16.8	2.3	28.1	31.9	79.1	60.4

The CEC of the clayey samples E2-E5 (Tab. 21) scratched off from the metal decreased only slightly (approximately 10 %). The black metallic sample (E6) still contained appreciable smectite as well as the white crusts which are dominated by carbonates. This points to an intimate mixing of primary phases (smectite) and secondary phases (magnetite, goethite, siderite, aragonite).

4.6.4 Discussion

The FEBEX project showed similar mineral reactions as determined in other large scale tests (e.g. Kaufhold et al. 2013). Carbonates were partly dissolved and precipitated elsewhere. Fe increase was observed at the contact to the heater/liner accompanied by precipitation of goethite. Some samples showed an increase of Mg obviously accompanied by the formation of trioctahedral minerals and/or domains. Finally, a redistribution of exchangeable cations was observed.

Corrosion

Corrosion is expected to occur when bentonite and iron are contacted. In most of the large-scale tests highly compacted bentonite is in contact with an even iron surface. Such contacts existed at both circular faces of the FEBEX heater. The cylindrical part of the heater was surrounded by a metal liner. At these (cylindrical) surfaces highly compacted bentonite was in contact with the liner surface and some bentonite which has swollen through the perforation of the liner, which in turn reduced the dry density. This lower-density bentonite was in direct contact with the heater even in the cylindrical part. Results presented in the present study suggest that different reactions have taken place which probably result from the fact that more oxygen was entrapped in the volume between heater and liner (in the cylindrical part) compared to the circular faces of the heater. In the cylindrical part, magnetite was found as an intimate mixture with bentonite particles and native iron. This material was scratched off the liner. The clay samples which were previously taken away from the metal surfaces ("contact samples") were analysed as well. This

clay material which was close to the heater was often reddish and contained slightly more Fe compared to the reference bentonite. By XRD, IR, and thermal analysis goethite was found which is probably responsible for the reddish colour. In one instance goethite was found even at 1 cm distance from the heater. Mostly, goethite appearance and Fe increase were restricted to the very surface and, hence, could only be detected in samples scratched off the contact face of the clay samples. Interestingly no Fe increase was found at the circular face of the heater, where highly compacted bentonite was in direct contact to the heater. The amount of oxygen there was probably low and electron transfer processes did, therefore, occur in the cylindrical part. The water content may also be important here. The largest MgO increase ever detected by the authors (in such large-scale bentonite heater experiments), however, was found at the circular contact face.

Mg increase

In many of the contact samples a significant MgO increase was found. Small variations of the MgO content could be explained by cation exchange processes but in case of the more significant MgO increase structural modifications of the smectite were indicated. The most interesting sample in this respect was derived from the heater face. Although being in direct contact to the iron of the heater no Fe increase was found but an increase of MgO by almost 6 %. In many HLRW deposition tests conducted with bentonite, some Mg accumulation was found. In the ABM test, unambiguous proof was found for the formation of trioctahedral minerals and/or domains (Kaufhold et al. 2013). The sample taken from the face contact also showed formation of trioctahedral domains but for the first time brucite was also found there. Yet it is not clear if both reactions took place at the same time or if conditions changed throughout the project facilitating different reactions. The most important difference to the ABM test is the lower water content and the low ionic strength of the groundwater. Hence it may be possible that the lower water content led to the formation of brucite. It may also be that brucite formed in other experiments as well but has not been detected so far. Finally, it has to be investigated in the future how the distribution of exchangeable Mg^{2+} is related to the mineral reaction in which Mg is obviously involved. The larger content of exchangeable Mg^{2+} near the heater suggests a larger Mg^{2+} concentration in the porewater of the bentonite near the heater. This reaction has to be investigated further.

4.6.5 Conclusions

The analysis of the FEBEX-DP samples proved that the Mg enrichment in the bentonite close to the heater, which was observed in several large-scale deposition tests, is not related to the corrosion. As in most of the other tests, indications for trioctahedralisation were observed. The reaction mechanism, however, has yet to be discovered. Heater/liner corrosion, on the other hand, was apparently restricted to the areas in which oxygen was entrapped (between liner and bentonite). No corrosion was observed where the heater was in direct contact to the compacted blocks. The heater-liner-bentonite interfaces apparently acted as sacrificial anode. Different water contents may also have been important in this respect.

At the very contact, intimately mixed with the iron, magnetite was observed which is often claimed to be the first corrosion product at the bentonite iron interface. Most of the increase of the Fe-content, however, can be explained by formation of goethite which in turn indicates that appreciable oxygen was entrapped in the system – probably mainly between canister and liner.

4.7 Fe-bentonite interface study of Ciemat

4.7.1 Introduction

The Deep Geological Repository (DGR) is currently the most accepted management option for the longterm isolation of High-Level Radioactive Waste (HLRW) (NEA-OCDE 2003, US-DOE 2014). Regardless of the geological options considered for the DGR, they are all based on a multi-barrier system (Engineered barrier system, EBS) in order to achieve the safety requirements for limiting the eventual release of radionuclides to the biosphere. This system consists of: the metallic canister containing the radioactive waste, the bentonite barrier surrounding the canister and the concrete to seal the galleries. In addition to the barrier, a set of other components (e.g. a variety of sensors) are placed to monitor the evolution of the system.

This report regroups the post-mortem characterisation of the bentonite in contact with some metallic components of the FEBEX experiment: the heater/liner and one sensor (fissurometer) that monitored the EBS. The specific aim of the post-mortem characterisation is the analysis of the physical, physico-chemical, mineralogical and chemical changes that occurred in the clay as a consequence of the interaction with metal components.

4.7.2 Dismantling of the barrier and metal-bentonite interface sampling

Sample selection was carried out in such a way as to achieve a good representation of the effect of TH gradients on the metal/bentonite interaction under realistic disposal conditions. For that reason, interface samples were collected at different distances from the heater. Consequently, these sampling areas were subjected to different temperatures, saturation degrees and chemical environments. These factors might influence corrosion processes and the nature and transport of corrosion products into the compacted bentonite. The extension of the chemical and mineralogical changes caused by the metal/bentonite interaction might also be affected by these parameters. So, in order to evaluate the impact of environmental conditions on Fe-related processes, samples were taken from (Fig. 97):

- *Heater/bentonite interface*: one bentonite sample is taken at the contact with the front lid of the heater (B-B-42-5) and another bentonite sample at the contact with the back lid of the heater (BM-S-54-7).
- *Liner/bentonite interface*: four bentonite samples at the liner contact; two from Section 45 (BM-D-45-2, ML-45-3) and two from Section 52 (BM-D-52-2, ML-52-4).
- *Other metallic components/bentonite interface*: one bentonite sample from the filling of the gap between the liner and the dummy in Section 37 (B-S-37-1) and one sample of bentonite in contact with a fissurometer (B-C-47-10).

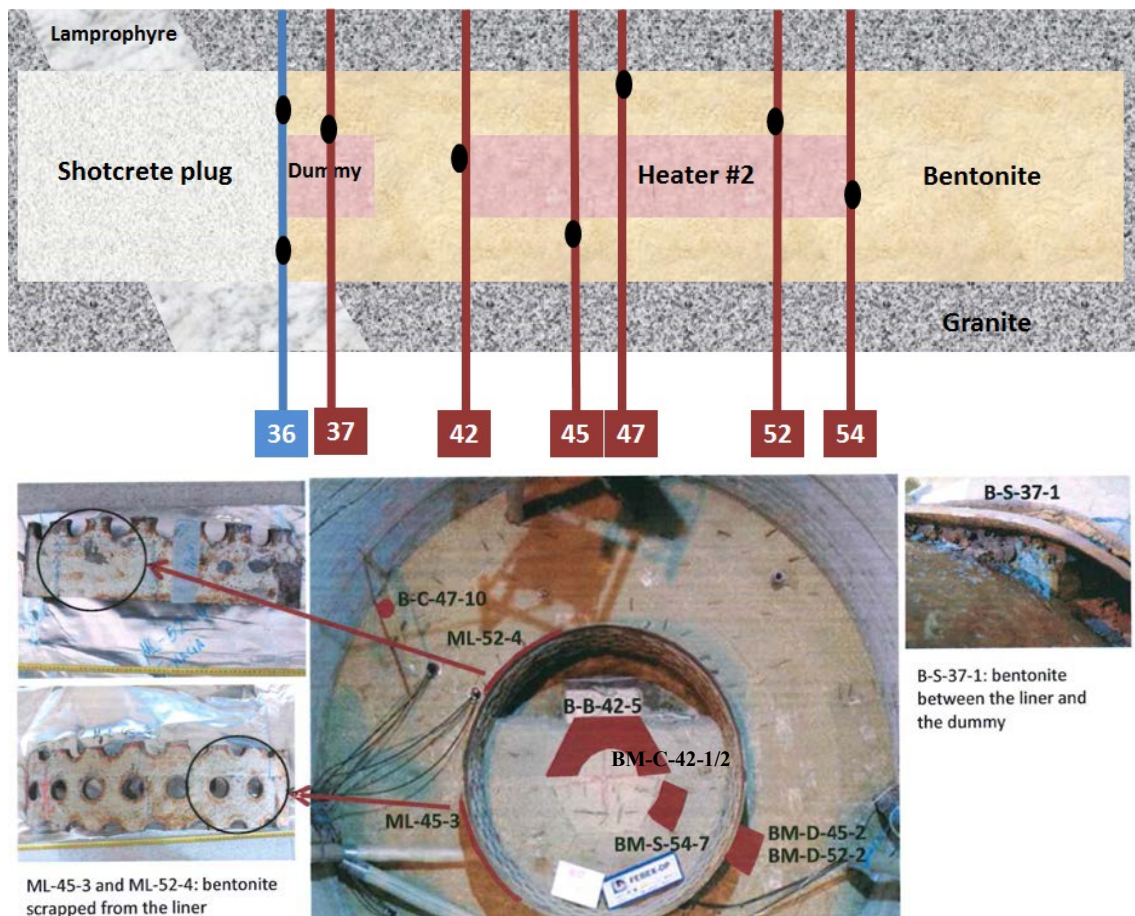


Fig. 97: Position of the bentonite samples studied by CIEMAT in the FEBEX *in-situ* experiment.

Details on each sample can be found in Appendix D.

The samples were preserved in plastic film, two layers of aluminised PET-sheets and vacuum sealed plastic bags immediately after their extraction. The PET-sheets were vacuum-sealed. The samples were referred to according to the key given in the Sampling Book (AITEMIN 2015).

Samples exhibit different appearances as a function of their position in the FEBEX *in-situ* test (Appendix D). Differences in colour and texture depend mainly on water content and, probably, the nature of the corrosion products precipitated. In samples collected at the contact with the heater and liner, reddish brown corrosion products were found on the surface of the bentonite block. In these areas, subjected to low relative humidity and high temperatures for over 18 years, bentonite remained unsaturated and, apparently, penetration of the corrosion products into bentonite blocks seemed to be restricted to the first millimeter. Samples from saturated areas of the bentonite barrier, such as B-S-37-1 and B-C-47-10, exhibited a bright orange colour. Sample B-S-37-1 corresponds to saturated bentonite protruded through liner holes, whereas sample BC-47-10 is a bentonite core drilled in the proximity of the granite.

Tab. 22 lists the bentonite samples studied by Ciemat that have been in contact with metal components. The table covers the most relevant details about sampling date, shipping, sealing conditions at arrival and time elapsed from *in situ* to laboratory sampling.

Tab. 22: Bentonite samples studied by CIEMAT for the characterisation of the metal/bentonite interface.

Section	Reference	Sampling GTS	Arrival CIEMAT	Sampling CIEMAT	Time elapsed (days)	Vacuum
37	B-S-37-1	19/05/15	27/05/15	27/10/15	161	Yes
42	B-B-42-5	03/06/15	21/08/15	22/10/15	141	No
42	BM-C-42-1/2, 3	03/06/15	07/08/15	22/10/15	141	No
45	BM-D-45-2	23/06/15	07/08/15	19/10/15	118	Yes
45	ML-45-3 ^a	25/06/15	28/10/15	02/03/16	251	Yes
47	B-C-47-10	26/06/15	07/08/15	21/10/15	117	Yes
52	BM-D-52-2	13/07/15	21/08/15	21/10/15	100	Yes
52	ML-52-4*	22/07/15	28/10/15	02/03/16	224	Yes
54	BM-S-54-7	17/06/15	07/08/15	27/10/15	101	Yes

* Samples sent by Tecnalia

From the time of their arrival the samples were kept in a RH-controlled room (Fig. 98). The RH was initially set to 70 % and then to 80 %, although because the samples were vacuum sealed, this value is not considered relevant. Some of the samples used for the interface studies were kept in a refrigerator.



Fig. 98: RH-controlled room for the storage of samples.

Tab. 23 summarises the position and temperature reached at the bentonite/metal interface samples in the FEBEX gallery. Position and temperature data presented in this table are approximate values. Temperature values were extrapolated from data provided by thermocouples installed in the FEBEX experiment (Martínez et al. 2016).

Tab. 23: Position and temperature of the metal/bentonite interfaces studied by CIEMAT for the characterisation of the metal/bentonite interface.

Section	Reference	Temperature (°C)	Distance from the axis of the gallery (cm)
37	B-S-37-1	30	45
42	B-B-42-5	85	10
42	BM-C-42-1	85	10
42	BM-C-42-2,3	85	10
45	BM-D-45-2	90	48.5
45	ML-45-3*	90	48.5
47	B-C-47-10	45	103
52	BM-D-52-2	90	48.5
52	ML-52-4 ^a	90	48.5
54	BM-S-54-7	105	20

* Samples sent by Tecnalia: bentonite scrapped from the external surface of the liner

4.7.3 Methods of analysis

The laboratory determinations presented in this report have been carried out at CIEMAT facilities from August 2015 to August 2016.

The sampling logs used for the study of the interfaces are shown in Appendix D.

Density and water content

The gravimetric water content (w) is defined as the ratio between the mass of water and the mass of dry solid expressed as a percentage. Consequently, all the values given in this report are weight percentages. The mass of water was determined as the difference between the mass of the sample and its mass after oven drying at 110 °C for 48 h (mass of dry solid). Dry density (ρ_d) is defined as the ratio between the mass of the dry sample and the volume occupied by it prior to drying. The volume of the specimens was determined by immersing them in a recipient containing mercury and by weighing the mercury displaced. The precision of this measurement is between 0.01 and 0.02 g/cm³. The same samples whose volumes had been determined were used for the water content determination. The saturation degree (S_r) was computed from the dry density and water content determined in the laboratory, taking a value for the density of solid particles of 2.70 g/cm³. This is the average value of numerous determinations carried out on FEBEX bentonite following an optimised technique (Villar 2002).

Pore size distribution

The pore size distribution of each subsample was determined by mercury intrusion porosimetry (MIP). This technique allows the determination of porosity and pore size distribution by injecting mercury into the sample at different pressures while controlling the volume intruded. The porosimeter used was a Micromeritics AutoPore Series IV 9500, allowing the exploration of pore diameter sizes between 0.006 and 600 μm . Consequently, the mercury does not intrude the microporosity (pores size less than 0.002 μm , according to the classification of Sing et al. 1985). The mercury intrusion method allows access to be gained only to the macroporosity and to part of the mesopores. Before the samples were inserted in the porosimeter, the water was removed from the pores by freeze-drying. Samples smaller than 3 cm^3 were lyophilised to eliminate the water in the pores.

Specific surface area

Classical nitrogen adsorption/desorption isotherms were obtained by Ciemat on a discontinuous volumetry sorptometer, Micromeritics ASAP 2020. Approximately 2 – 4 grams of total sample were ground in an agate mortar. The samples were dried at 90 °C during at least 24 h before the tests. Prior to the nitrogen adsorption, the samples were out-gassed by heating at 90 °C for 18 hours using a mixture of helium and nitrogen under a residual vacuum between 500 and 6 – 10 mmHg. The tests were performed at the boiling point of liquid nitrogen (77 K) considering a molecular cross section area of 0.162 nm for the nitrogen molecule. External specific surface areas were calculated using the standard N_2 -BET method, using a series of data points over the P/P_0 range from 0.02 to 0.25 on the nitrogen adsorption isotherm (Gregg & Sing 1982). An average value was determined by the measurement of two or three aliquots of each subsample.

Mineralogy

XRD

XRD diffraction patterns were obtained from random powders and oriented aggregates in order to identify the mineralogical species in the samples.

The grinding of the bulk sample to produce the powders was made in a RETSCH RM 100 mortar grinder with an agate pestle after drying the samples at room temperature. Next, the size fraction of less than 63 μm was obtained after sieving the powder through a nylon ASTM sieve.

The preparation of oriented clay specimens (air-dried, ethylene-glycol solvated and heated at 550 °C) for quantitative analysis was made using the suction-onto-ceramic technique (Shaw 1972). The size fractionation was made in deionized water by settling (Stokes Law). The final clay suspension was ultrasonically dispersed using 1 g in 5 mL of deionized water. The oriented mounts were prepared by suction of the dispersion through 3 mm thick ceramic tiles.

The XRD patterns registered from bulk, randomly-oriented powders were recorded in an angular range (2θ) of 3 – 70° a $\theta/2\theta$ X-PERT Panalytical instrument with an X-CELERATOR detector. This set-up allowed taking measurements equivalent to 0.016° angular steps during 100 s each step. Voltage and Intensity of the operated X-ray Cu tube were 45 kV and 40 mA, respectively. The equipment uses monochromatic radiation provided by a Ge 111 monochromator. The slit settings were: soller slit (0.04 rad); divergence and antiscatter slits both of 0.5°. The XRD database used for mineral identification was the Power Diffraction Files from the International Center for Diffraction Data (ICDD).

SEM and TEM

Electron microscopy was used to study morphology, mineralogy and microstructure of some samples. Prior to scanning electron microscope (SEM) imaging samples were dried at 60 °C during 48h and sputter coated with gold to reduce sample charging and improve secondary electron emission. A SEM JEOL JM-6400 coupled to a dispersive X-ray energy spectrometer X LINK LZ_5 was used at the National Center for Electron Microscopy of the Complutense University of Madrid.

For TEM examination a JEOL 2100FX with 200 kV acceleration voltage (3.4 Å point- to-point resolution) coupled to an OXFORD ISIS X-ray energy dispersive spectrometer giving a resolution of 136 eV at 5.39 keV was used at the National Center for Electron Microscopy of the Complutense University of Madrid. Bentonite samples were dispersed in acetone and dropped on a carbon coated copper grid.

FTIR

Fourier transform infrared spectrometry (FTIR) was used to further characterise the bentonite at the interface. Bentonite samples were homogenized in a Retsch RM200 mortar grinder with an agate pestle and mixed with KBr (2 mg of clay or shotcrete sample and 100 mg of KBr). FTIR spectra were obtained using a Nicolet 6700 FTIR spectrometer in transmission mode with a DTGS KBr detector and recording over the middle-IR region spectral range (4'000 – 400 cm⁻¹) with a resolution of 2 cm⁻¹ in an atmosphere continuously purged from water and atmospheric CO₂. Measured FTIR spectra were processed by Omnic (Version 3.1) software (Nicolet Instruments Co., Madison, USA).

Soluble ions by aqueous leaching

Aqueous extracts were obtained from the bentonite samples. Sample powders were obtained by grinding the samples in a Retsch RM200 mortar grinder with an agate pestle to a size of less than 63 µm after drying them overnight in an oven at 105 °C. Next, they were placed in contact with deionized and degassed water at a solid to liquid ration of 1:4 (2 mg of clay in 8 mL of water), shaken end-over-end and allowed to react for 24 hours. Separation was made by centrifugation (30 minutes at 12'500 rpm) and the supernatant was filtered by a 0.45-µm pore size filter and analysed. pH and E_h were not determined in the extracts because they do not represent reliable environmental conditions regarding the actual cell system, but the method is assumed to give a useful indicator for the content of soluble ions. Duplicates were made for all samples.

Cations in supernatants were analysed by Inductive Coupled Plasma - Optical Emission Spectrometry (ICP-OES) in a Spectro ARCOS spectrometer after acidification of the samples to pH < 2 with HNO₃ (8 mL/L). Anions were analysed using ion chromatography (Dionex DX-4500i).

Determination of exchangeable cations

For the analysis of the exchangeable cations, the CsNO₃ 0.5N displacement method was used (Sawhney 1970). FEBEX bentonite was equilibrated with CsNO₃ 0.5 N using a S:L ratio of 1:8 in a glove box. Samples were shaken end-over-end for 1 day. After phase separation by centrifuging, the supernatant solutions were decanted.

For the chemical analysis of the supernatants, an IC Metrohm (Switzerland) with Metrosep C3-250 and A SUPP 4-250 columns was used.

Determination of the Cation Exchange Capacity (CEC)

Cation Exchange Capacity (CEC) of bentonite was determined by using the photometric method with the Copper(II)-trien complex (Meier & Kahr 1999). 200 mg of clay sample were added to 35 ml of distilled water and dispersed by ultrasonic treatment (20 kHz, 400 W, 5 min). The suspension was diluted in a 50 ml volumetric flask to 50 ml, then completely transferred into a 100 ml beaker. While stirring the suspension, 10 ml of the solution of the Cu complex was added. After 3 min reaction time, the suspension was centrifuged at 13'000 rpm for 3 min. The supernatant solution was carefully removed and the extinction was measured at 620 nm in a 10 mm cuvette against water as a blank.

Fe measurements

One of the aims of this work was to identify and quantify the different contributions to total Fe content measured in the analysed bentonite samples.

Therefore, during this work, three major contributions were considered:

- Fe in exchange positions: determined with the CsNO_3 0.5N displacement method.
- Fe sorbed in edge surfaces: citric acid 0.3M was used as extractant
- Fe from iron oxides and (oxy)hydroxides precipitated in the bentonite samples: analysed according to the dithionite-citrate-bicarbonate (CBD) method

Total Fe content was measured by means of Total Reflection X-Ray Fluorescence Spectroscopy (TR-XRF).

Sample preparation for Fe measurements

Samples for Fe determination were prepared under anoxic conditions inside a glove box. Interface samples were sampled and grounded in an agathe mortar under an N_2 inert atmosphere. Water content corrections were made from gravimetric determination after heating at 105 °C.

Sorbed iron

A solution of citric acid 0.3M was used as extractant to quantify Fe sorbed at edge surfaces of bentonite. For the extraction, FEBEX bentonite was equilibrated with citric acid 0.3M using a S:L ratio of 1:10 in a glove box purged with N_2 . Samples were shaken end-over-end for 1 day. After centrifugation, supernatants were decanted and analysed by ICP-OES after acidification of the samples to $\text{pH} < 2$ with HNO_3 (8 ml/l).

Amorphous iron oxides and (oxy)hydroxides

The determination of free iron oxides (amorphous Fe oxides) in bentonite was made according to the dithionite-citrate-bicarbonate (CBD) method proposed by Mehra and Jackson (1960). For this, 1 g of clay was placed in a 100 mL centrifuge tube and 40 mL of 0.3 M Na-citrate solution

and 5 mL of 1 M NaHCO_3 solution was added. Temperature was brought to 80 °C in a water bath, then 1 g of solid Na_2SO_4 was added and the mixture was stirred for a total of 15 minutes. At the end of the digestion period, 10 mL of saturated NaCl solution and 10 mL of acetone were used to promote flocculation. The suspension was warmed in a water bath and centrifuged for 5 min. at 2500 rpm. The supernatant was decanted and kept for Fe determinations by ICP-OES.

Total Fe content

Total Fe content was measured by means of Total Reflection X-Ray Fluorescence Spectroscopy (TR-XRF). For the analysis of Fe in the bentonite samples, a TXRF S2 PicoFox spectrometer was used.

4.7.4 Results

Density and water content

Water content and dry density of specific samples of bentonite just contacting the metallic components were determined and the results are given in Tab. 24. An exhaustive analysis of water content and dry density of the bentonite in different radii and sections around the heater/liner and other metallic components can be found in "NAB 16-12 – FEBEX-DP on-site analyses report". Results coincide fairly well with those presented here ($\pm 5\%$).

The average dry density of bentonite in the proximity of the heater is $1.65 \pm 0.03 \text{ g/cm}^3$ and the average water content is $16.8 \pm 0.6\%$, which corresponds to a saturation degree around 72 %. The average dry density of the bentonite in contact with metallic components located in the coldest areas of the bentonite barrier, is $1.44 \pm 0.13 \text{ g/cm}^3$ and its average water content is $30.6 \pm 6.4\%$, corresponding to a saturation degree around 95 %. The water content in sample B-S-37-1, which was sampled in the gap between the dummy and the liner, seems to be higher than the rest of the samples whereas the dry density is very low. After the complete dismantling of the experiment, it was observed that the zone where the sample was taken is an area of water inflow, which could explain the determined water content and dry density values.

In general, differences in dry density and water content in samples located at different distances of the heater can be explained by the temperature effect.

Swelling capacity was determined in two samples collected from Section 36, in the proximity of the liner, and Section 59, close to an extensometer, according to the methodology described in NAB 16-17, where the results are also presented. The swelling strain values measured are less than 1 % lower than the values expected for the reference sample with the same initial state in terms of dry density and water content. However, for the rest of the tested samples not affected by interfaces, the decrease in swelling capacity with respect to the theoretical one was even higher (NAB 16-17). Hence, it is considered that the oxidation effects had no effect on the swelling capacity of the bentonite. Nevertheless, it is also acknowledged that the number of samples analysed was small.

Tab. 24: Dry density, water content and saturation degree determined for the samples studied in this work.

Section	Reference	ρ_d (g/cm ³)	w (%)	S _r (%)
37	B-S-37-1	1.30	37.6	94
42	B-B-42-5	1.55	25.1	91
45	BM-D-45-2	1.67	16.5	72
45	ML-45-3*	-	-	-
47	B-C-47-10	1.47	29.1	94
52	BM-D-52-2	1.67	16.4	72
52	ML-52-4 ^a	-	-	-
54	BM-S-54-7	1.61	17.4	70

* Samples sent by Tecnalia. The samples were too scarce for dry density and water content determinations.

Pore size distribution

The pore size distribution of each subsample was determined by Mercury Intrusion Porosimetry (MIP). Total intruded porosities and pore size distribution for each sample are given in Tab. 25. Due to the limitation of the method only part of the macropores ($50\text{--}6\cdot 10^5$ nm) and mesopores (6 – 50 nm) are accessible. Assuming that the percentage of pores not intruded by mercury corresponds entirely to the micropore size, an estimation of the percentage of micropores can be made from the percentage of pores intruded. This was done for all the bentonite samples and the total porosity as well as the percentage of each pore size was recalculated by comparing the actual void ratio of the samples (computed from their dry density and density of solid particles) and the apparent void ratio calculated from mercury intrusion, the same methodology as used in NAB 16-17 (Villar et al., in prep.) and NAB 16-18 (Turrero et al., in prep.).

Tab. 25: Total intruded porosity and pore size distributions measured for bentonite samples collected at the interfaces with metallic elements.

Position in the gallery	Reference	Total porosity (%)	Pore size distribution (%)		
			Macro	Meso	Micro
Heater	BM-S-54-7	46	25	13	62
Liner	BM-D-45-2a	55	9	39	52
	BM-D-52-2	43	22	15	63
Cable cap	B-B-42-5B	45	21	15	64
Granite	B-C-47-10	35	16	15	69
Dummy	B-S-37-1	22	8	12	81

No significant differences in total intruded porosity values were observed in the six samples studied. Porosity ranges from 22 to 55 %, with an average value of 42 ± 10 %, a value quite close to that of the raw FEBEX bentonite. Microporosity increases with saturation degree (samples B-C-47-10 and B-S-37-1). On the other hand, the maximum macroporosity value was reached in sample BM-S-54-7, which is possibly related to the formation of retractive cracks and the desiccation processes occurring in areas close to the heater.

Regarding pore size distribution, all analysed samples present a bimodal distribution, with a well-defined maximum in the mesopore region centered on 10 to 20 nm. The macropore population varies significantly as a function of water content of the bentonite sample (Fig. 99).

In order to evaluate the existence of a porosity gradient along the studied samples, three subsamples of samples BMD-45-2 and BB-42-5 were analysed. Intruded porosity values measured in the six subsamples are given in Tab. 26. Slight variations on total porosity and pore size distribution were observed in the studied subsamples; but apparently, no porosity gradients are observed in the samples (Fig. 100).

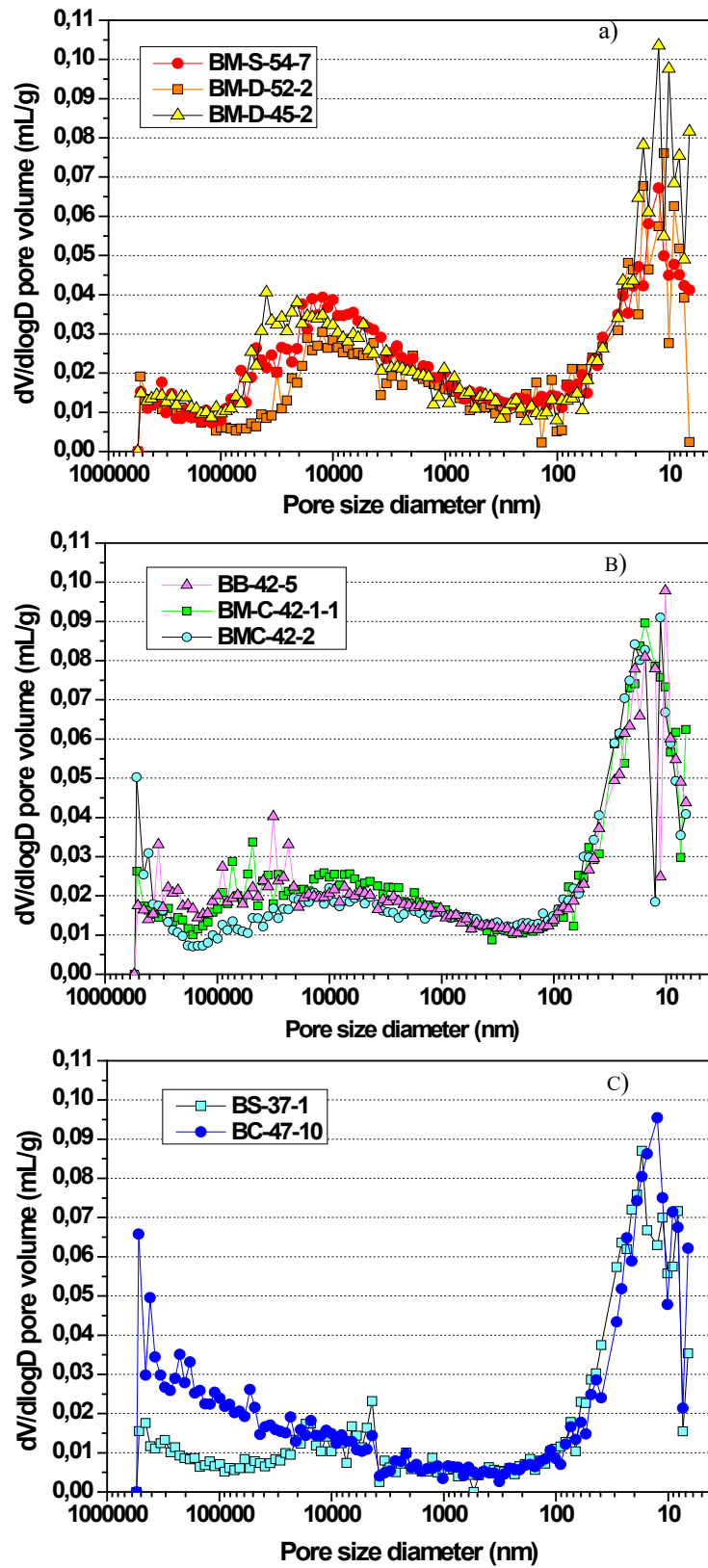


Fig. 99: Pore size distributions measured for samples collected in the vicinity of: A) heater (BMS-54-7) and liner (BMD-45-2 and BMD-52-2); B) cable cap and C) saturated areas (BS-37-1-dummy and BC-47-10-granite).

Tab. 26: Total intruded porosity profiles measured in sample BMD-45-2 and BB-42-5.

Position in the gallery	Sample	Total porosity (%)	Pore size distribution (%)		
			Macro	Meso	Micro
Liner	BM-D-45-2-0 cm	55	9	39	52
Liner + 2 cm (axis z)	BM-D-45-2-2 cm	62	8	44	47
Liner + 4 cm (axis z)	BM-D-45-2-4 cm	60	9	43	47
Contact cable cap	B-B-42-5-0 cm	45	21	15	64
Contact + 2 cm (axis z)	BM-C-42-1	46	20	18	62
Contact + 2 cm (axis y)	BM-C-42-2	42	18	17	64

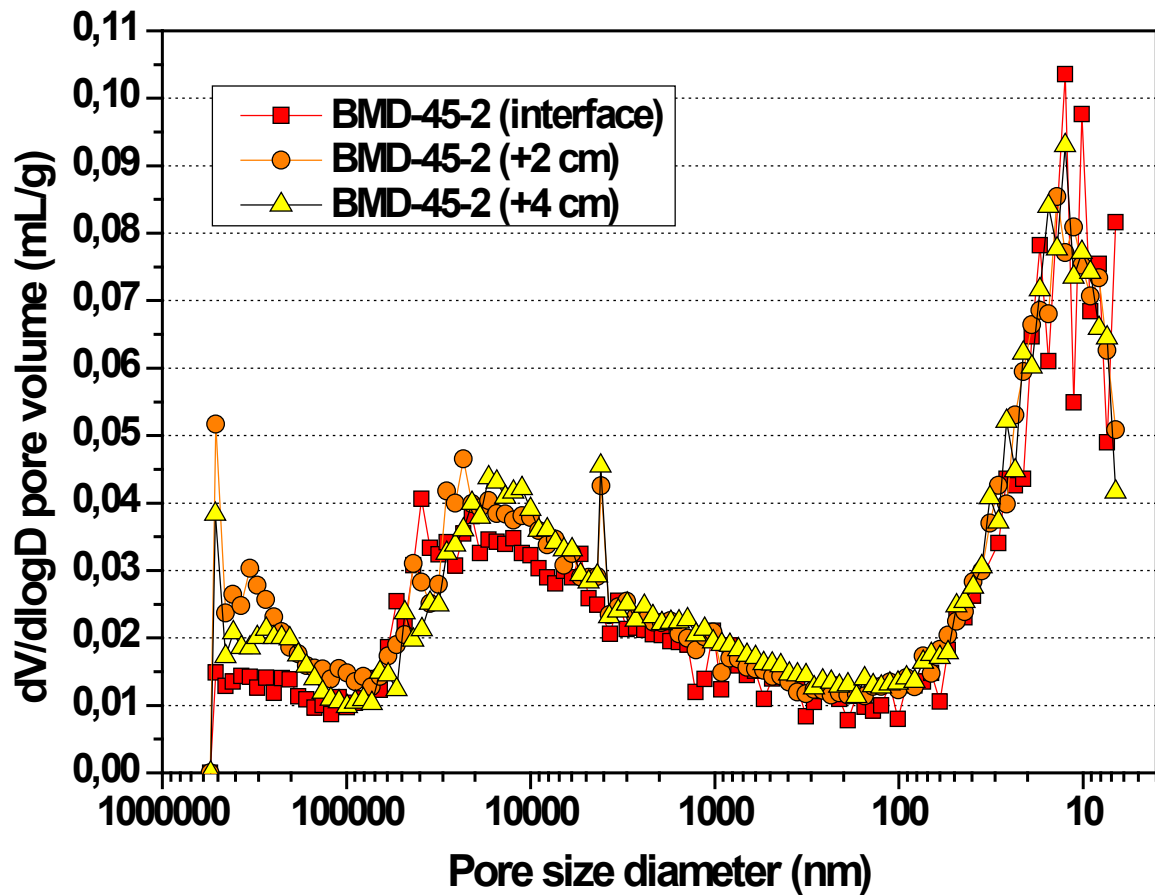


Fig. 100: Pore size distributions measured along sample BMD-45-2.

Specific surface area

BET Specific Surface Area was measured in ten samples collected at different distances from the heater. Measured BET values are shown in Tab. 27.

BET values measured in bentonite samples from the FEBEX *in-situ* test are notably lower than the ones measured in raw FEBEX bentonite. BET-SSA decreases nearly 75 % towards the heater, possibly due to desiccation processes. Near the granite, BET-SSA values decrease, but to a lesser extent (~25 %). BET values can decrease as a consequence of the cementation of bentonite particles by the precipitation of FeOOH. However, no correlation with total Fe or FeOOH content (%wt.) was found.

The thermo-hydraulic gradient imposed in the bentonite barrier can also lead to a reduction of both porosity and specific surface area. Near the heater, high temperatures can lead to modifications in the intergranular network, favouring the clustering of montmorillonite particles. In saturated areas close to the granite, the increase in microporosity will lead to higher specific surface values. Although the BET values are notably higher than the ones measured in high temperature areas, they are still lower than in raw FEBEX bentonite. This difference might be related to full saturation and the compaction effect.

Tab. 27: BET- Specific Surface Area values measured in bentonite samples from the FEBEX *in-situ* test.

Position in the gallery	Sample	BET Specific Surface (m ² /g)
Heater	BM-S-54-7	11.1
Liner	BM-D-52-2	15.3
	ML-45-3	16.1
	ML-52-4	17.6
	BM-D-45-2a	24.7
Cable cap	BM-C-42-1-1	38.1
	BM-C-42-2,3	41.3
	B-B-42-5B	44.5
Granite	B-C-47-10	44.0
Dummy	B-S-37-10-1	44.4
	FEBEX natural	60.3 ± 0.3

Mineralogy

XRD - Bulk sample

XRD characterisation of the metal-bentonite interface samples received in CIEMAT confirmed that the mineralogical composition of bentonite in contact with metal did not change significantly with regard to the original bentonite.

The montmorillonite content of FEBEX bentonite is above 90 wt. % (92 ± 3 %). The smectitic phases are actually made up of a smectite-illite mixed layer, with 10 – 15 wt. % of illite layers (Cuadros and Linares 1995). Besides, the bentonite contains variable quantities of quartz (2 ± 1 wt. %), plagioclase (3 ± 1 wt. %), K-Feldspar (traces), calcite (1 ± 0.5 wt. %), and cristobalite-trydimite (2 ± 1 wt. %).

Phase identification and quantitative analysis were performed with the commercial Match! software. Initially, phase identification was done automatically by comparing the diffraction pattern of each sample to the COD database. In order to refine the phase identification, other clay phases, including illite, and the most frequent iron oxides and FEBEX accessory minerals were introduced manually. No results for illite were obtained in any of the samples. The mineralogical composition of the analysed samples is given in Tab. 28. Montmorillonite is the prevailing mineral phase. Calcite and quartz were detected in all samples, together with traces of K-Feldspar and plagioclase.

Regarding iron oxides, anhydrous Fe oxides are most likely to form in the hottest areas of the bentonite barrier. By contrast, Fe oxyhydroxides will precipitate in saturated areas of the bentonite barrier, where temperature is lower. Maghemite is the major phase in bentonite samples collected in the contact with the heater and the liner. In the case of samples B-S-37-1 and B-C-47-10, Fe oxyhydroxides (goethite and lepidocrocite) prevail over anhydrous oxides (maghemite).

Tab. 28: Semi-quantitative XRD analysis performed in the samples studied.

Phases (wt%)	B-B-42-5	BM-D-52-2	B-C-47-10	B-S-37-1	ML-45-3	ML-52-4	BM-S-54-7
Montmorillonite	88	85	89	85	86	82	86
Calcite	Traces	3	2	2	3	Traces	4
Quartz	Traces	4	Traces	3	3	Traces	4
Goethite	1	2	3	6	-	3	-
Maghemite	7	6	2	2	8	13	6
Lepidocrocite	4	Traces	2	2	-	2	-
Ferrihydrite	-	-	2	-	-	-	-

XRD - Oriented clay films

In order to study the characteristics of the clay fraction ($< 2 \mu\text{m}$) of the previous samples (Tab. 28), 0.2 g of bulk powder of each sample was dispersed in distilled water and allowed to sediment in a 250 cm^3 test tube in order to separate $> 2 \mu\text{m}$ size particles. The operation was repeated three times and the supernatant was collected every time to concentrate the clay fraction above $2 \mu\text{m}$. The obtained suspension was flocculated by adding MgCl_2 0.5M and centrifuged. The clay was then washed three times with pure alcohol and then dried at room temperature. The amount of clay separated was in the order of 0.1 g, which was suspended in 4 cm^3 of distilled water. Approximately 3 portions of 1 cm^3 suspension were smeared in glass tiles in order to prepare oriented clay films. These oriented aggregates were air-dried, treated with ethylene-glycol and heated to 550°C for 2 hours (Moore & Reynolds 1989).

All the studied samples show a complete swelling to 17\AA when they are solvated by ethylene-glycol and dehydrate to 9.7\AA when they are heated to 550°C (Fig. 101 to Fig. 104). This behaviour seems to support the fact that bentonite is fully expandable, and neoformation of non-swelling phases has not occurred.

Air-dried clay oriented films (Fig. 105) reveal that Mg grows notably in samples taken at the contact with the heater (BMS-54-7) and the liner (BMD-52-2). Peak broadening in the 14\AA basal spacing indicates a non-homoionic nature of smectite in samples from the coldest areas of the barrier (BS-37-1 and BC-47-10). In the 30° region ($3,10\text{\AA}$), well-separated peaks were observed for Mg-Ca bentonite (liner and heater) and Na-Mg-Ca bentonite (dummy and granite).

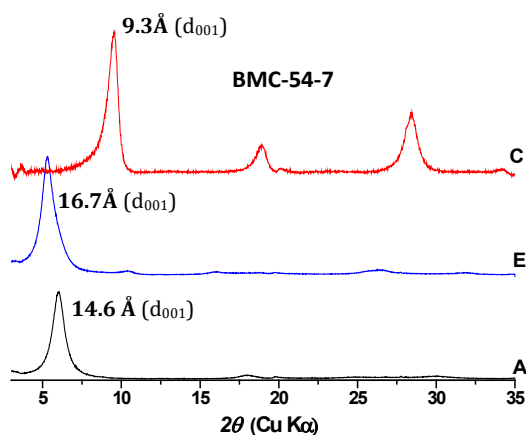


Fig. 101: X-ray diffraction patterns of oriented aggregates prepared for sample BM-S-54-7: A) air-dried, E) ethylene-glycol solvated and C) heated to 550 °C.

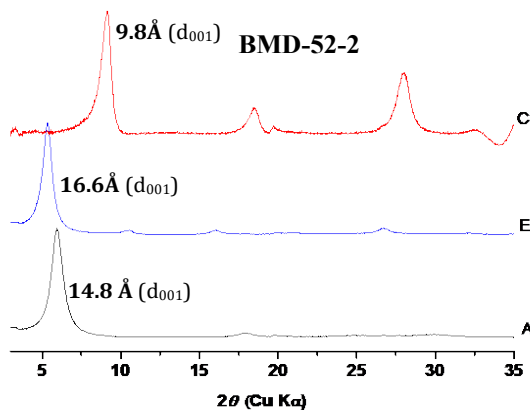


Fig. 102: X-ray diffraction patterns of oriented aggregates prepared for sample BMD-52-2: A) air-dried, E) ethylene-glycol solvated and C) heated to 550 °C.

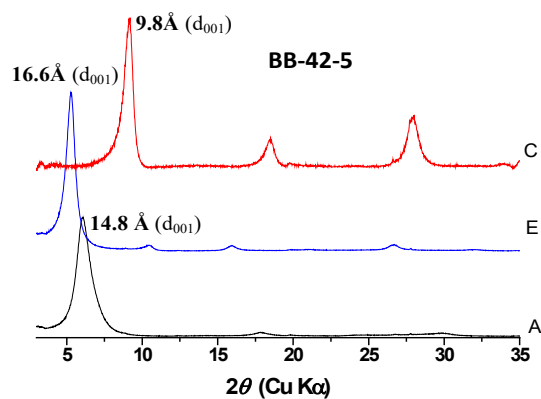


Fig. 103: X-ray diffraction patterns of oriented aggregates prepared for sample BMD-42-5: A) air-dried, E) ethylene glycol solvated and C) heated to 550 °C.

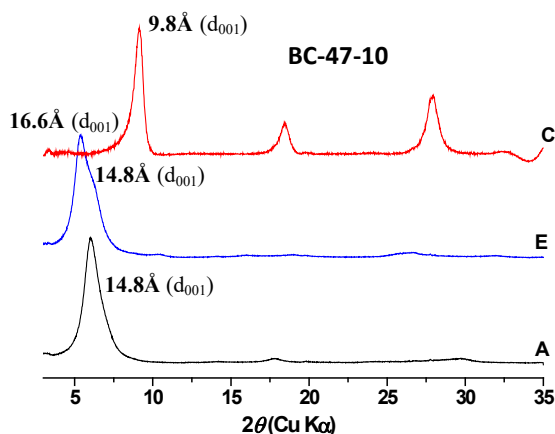


Fig. 104: X-ray diffraction patterns of oriented aggregates prepared for sample BC-47-10: A) air-dried, E) ethylene-glycol solvated and C) heated to 550 °C.

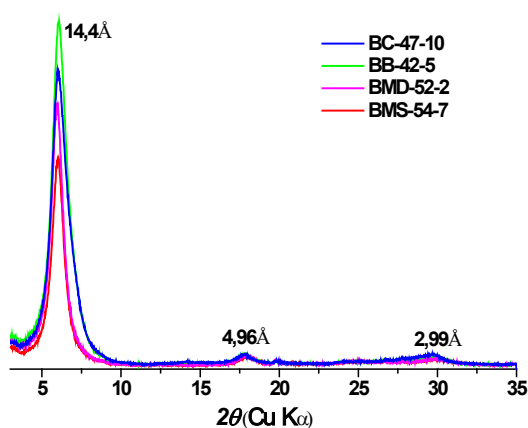


Fig. 105: X-ray diffraction patterns of air-dried oriented aggregates for samples: BMS-54-7, BMD-52-2, BB-42-5 and BC-47-10.

Ethylene-glycol solvated patterns (Fig. 106) exhibited a high saddle to peak ratio in the 16,7Å basal spacing of samples in contact with the liner (i.e. BMD-52-2). This effect could be attributed to a small but perceptible illite/smectite mixed layering increase regarding the original clay, which is also revealed by the existence of a shift to lower d-spacing values in bentonite samples subjected to higher temperatures.

In sample BC-47-10 (near granite), the 16,7Å peak can be deconvoluted into two peaks: a major peak centered in 16,7Å and a secondary one centered in 14,4Å. Though, the shoulder in the 16,7Å peak could be related to the formation of a non-swellable phase, this peak collapses totally to 9,3Å (Fig. 107). For that reason, the existence of high layer charge minerals cannot be discarded in sample BC-47-10.

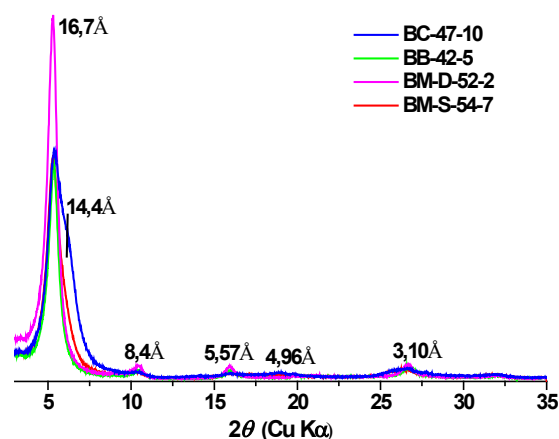


Fig. 106: X-ray diffraction patterns of oriented aggregates glycolated with ethylene-glycol.

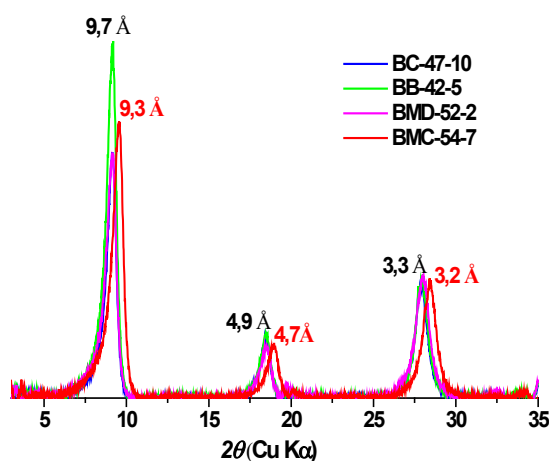


Fig. 107: XRD patterns of oriented aggregates heated to 550 °C.

SEM and TEM

SEM-EDS analyses

Due to the low importance of Fe-related processes at the metal/bentonite interfaces, cross-sections of bentonite samples BM-S-54-7 (contact with heater) and B-C-47-10 (near granite) were prepared for SEM and EDS analyses. According to EDS profiles and spot analyses conducted in the proximity of the heater, the alteration zone was restricted to the first 500 μm (Fig. 108). Maximum Fe contents were reached in the first 50 μm . Magnesium, as well as sodium, increases significantly towards the interface (Fig. 109).

This alteration front observed in samples consisted basically of a mechanical mixture of corrosion products and compacted bentonite enriched in Na, Mg, Cl and Ca (Fig. 110 and Fig. 111).

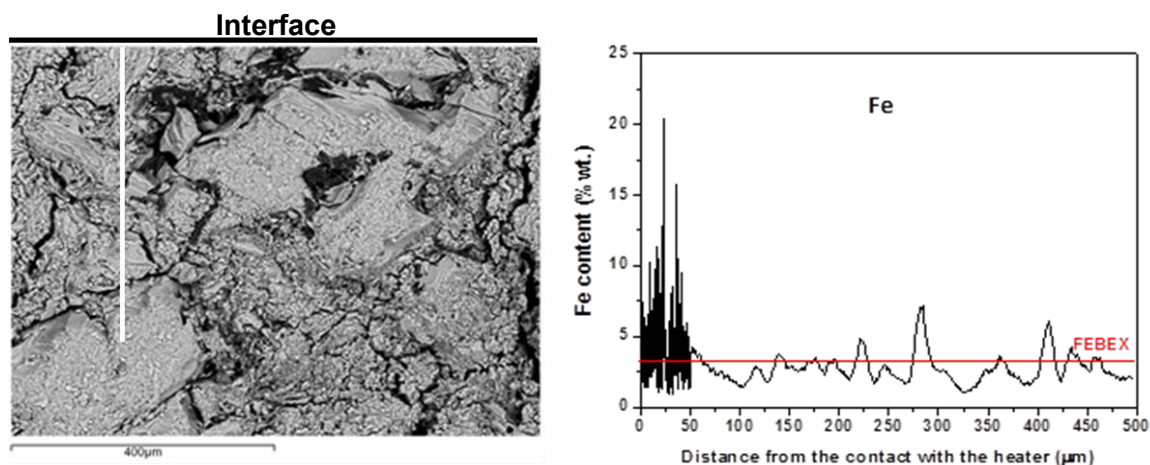


Fig. 108 (Left) Back-scattered cross-section SEM micrograph of the heater/bentonite interface in sample BM-S-54-7, (right) EDS line profile analysis corresponding to Fe (%wt.).

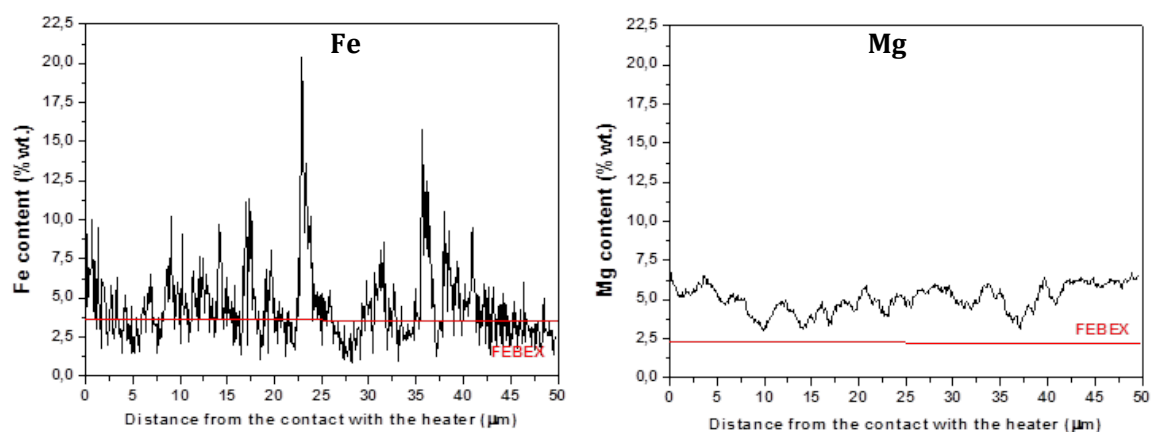


Fig. 109: EDS line profile analysis corresponding to Fe (left) and Mg (right) performed in the heater/bentonite interface in sample BM-S-54-7.

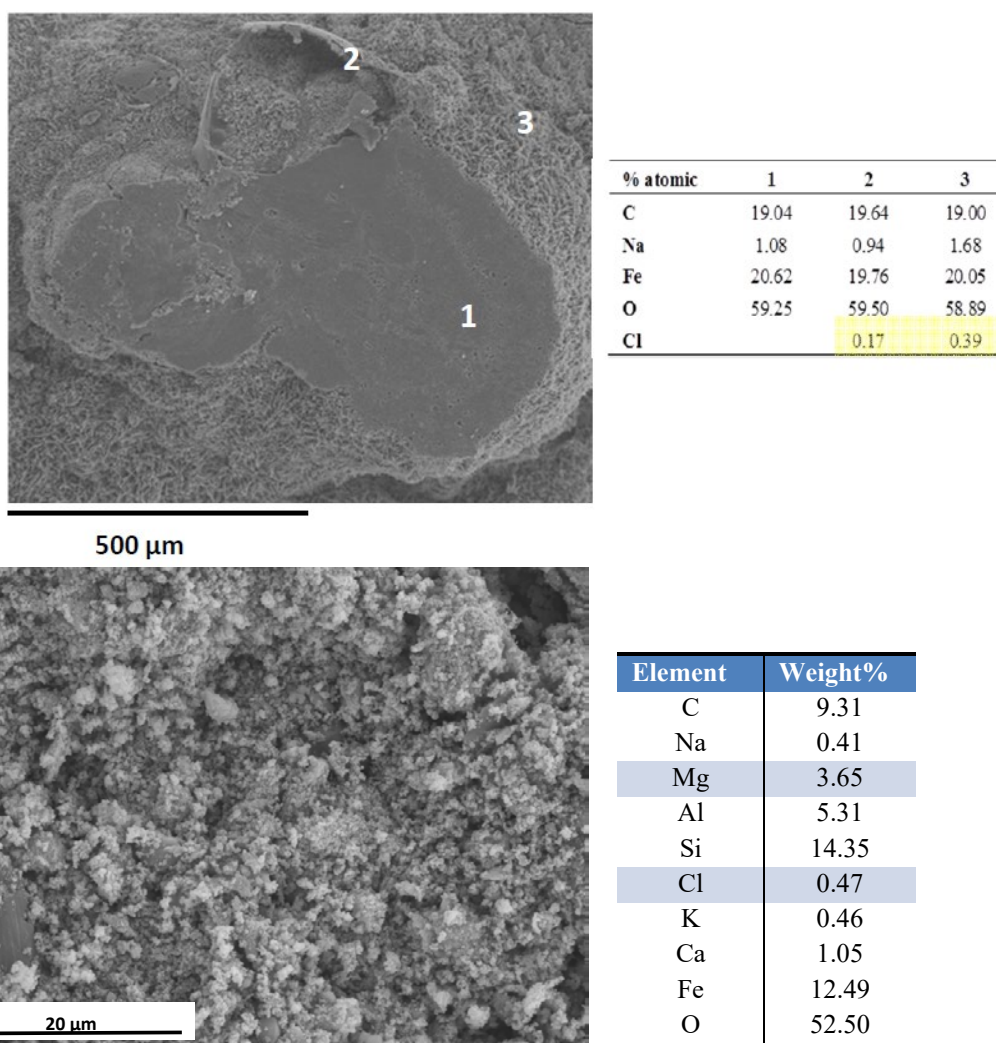


Fig. 110: SEM micrograph of the iron oxide layer found in sample B-B-42-5 (bentonite in contact with the front lid of the heater) and in sample BM-S-54-7 (bentonite in contact with the back lid of the heater).

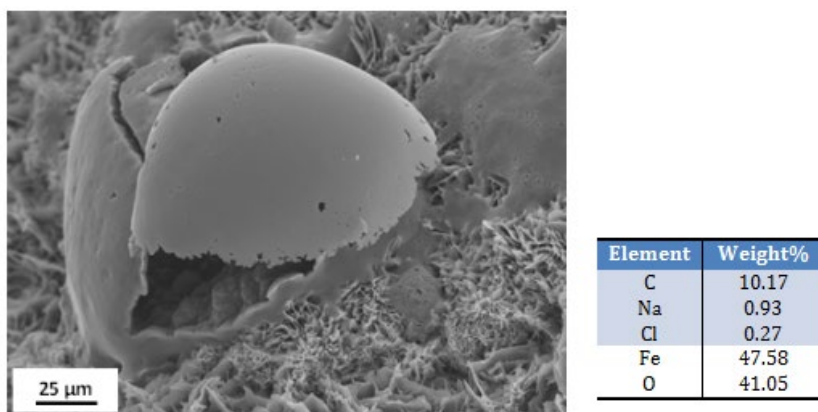


Fig. 111: (Left) Egg-like structure found in the oxide layer of sample BM-D-45-2; (right) EDS analysis of the outer shell.

High temperature ($> 85\text{ }^{\circ}\text{C}$) favors the evaporation and subsequent precipitation of salts, such as carbonates or sodium chloride. Precipitation of carbonates was observed in bentonite in contact with the heater and liner (Fig. 112). Calcite (aragonite) and siderite (ankerite) have been detected in samples BM-S-54-7, BM-D-45-2, M-L-45-3 and M-L-52-4.

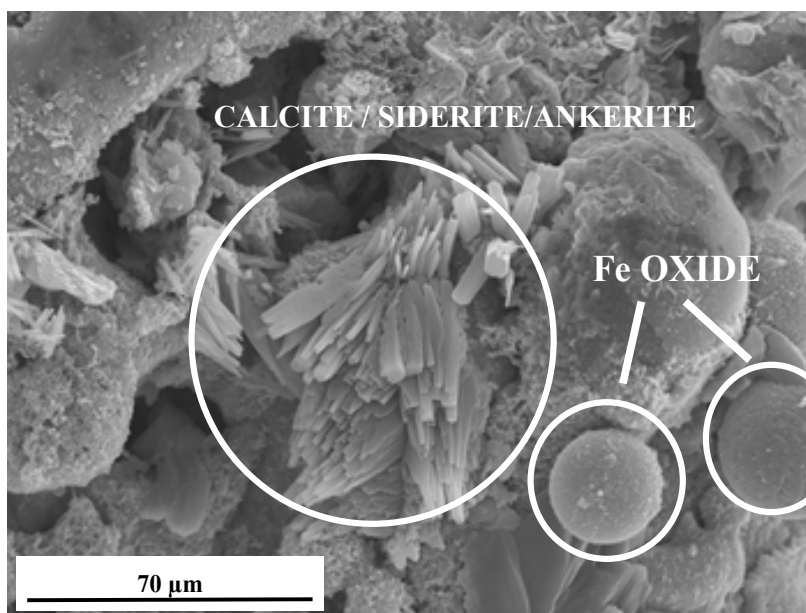


Fig. 112: Precipitation of carbonates (calcite, siderite or ankerite) in sample BM-D-45-2 (liner).

Regarding the morphology of Fe oxides, in samples taken at the contact with the liner (BM-D-45-2, B-B-42-5 and ML-45-3) and the cable cap (BM-C-42-1), similar globular forms were found. EDS analysis shows that globular Fe oxides found in samples BM-D-45-2 and BM-C-42-1 are quite similar (Tab. 29). In sample B-B-42-5, the chemical composition differs, as carbon is not detected. Nevertheless, the shape and size of the particles are similar ($\sim 5\text{ }\mu\text{m}$).

Therefore, these observations suggest that the movement of colloidal Fe oxides in the vicinity of the cable cap and the liner cannot be discarded.

Tab. 29: EDS analyses of globular Fe oxides shown in Fig. 112 and Fig. 113 (b) and (c).

Element	Weight%		
	BM-D-45-2	BM-C-42-1 (Fig. 113b)	B-B-42-5 (Fig. 113c)
C	12.95	13.50	8.42
Mg	-	0.53	-
Si	0.26	0.75	1.80
Ca	12.13	16.85	-
Fe	26.15	19.01	69.92
O	47.38	49.35	18.82
Al	-	-	1.04
Mn	0.85		
Cl	0.27		

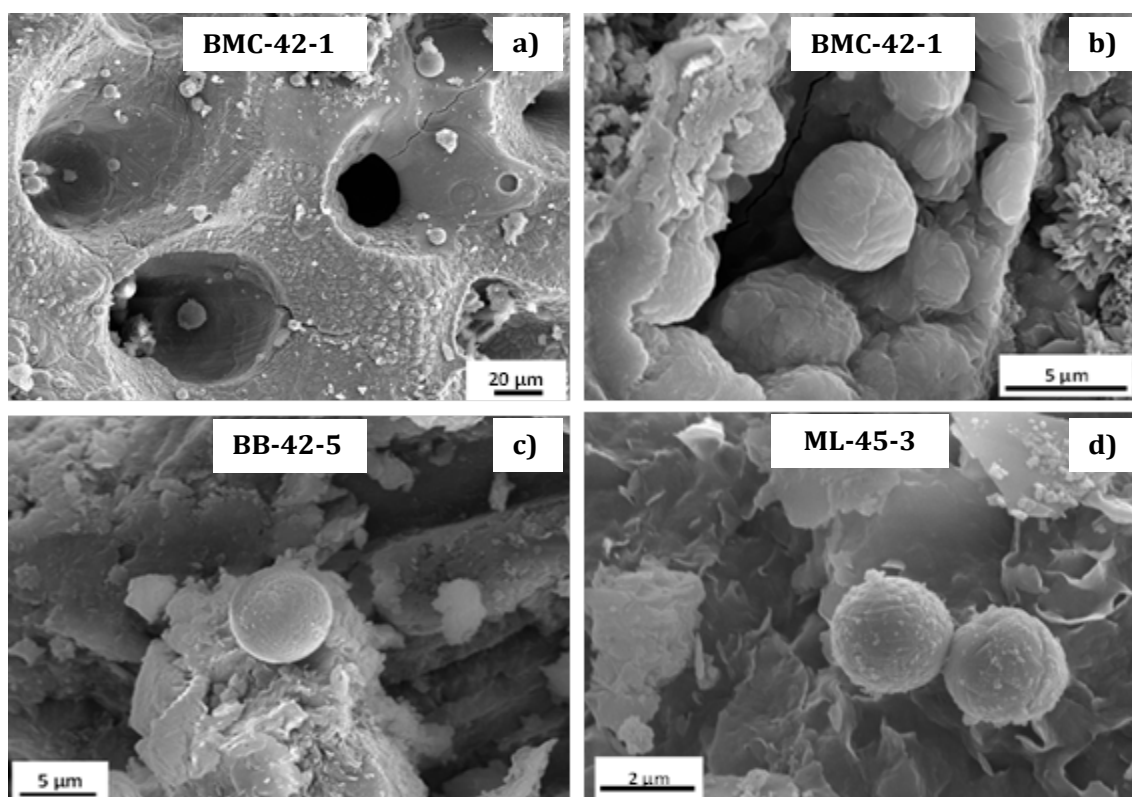


Fig. 113: Micrometric globular iron oxides found in samples in contact with the cable cap: (a) and (b) BM-C-42-1 and the liner (c) B-B-42-5 and (d) M-L-45-3.

In sample BC-47-10, EDS line profiles show a notable increase in Fe in the first 50 μm , possibly due to the precipitation of FeOOH particles in the interface (Fig. 114).

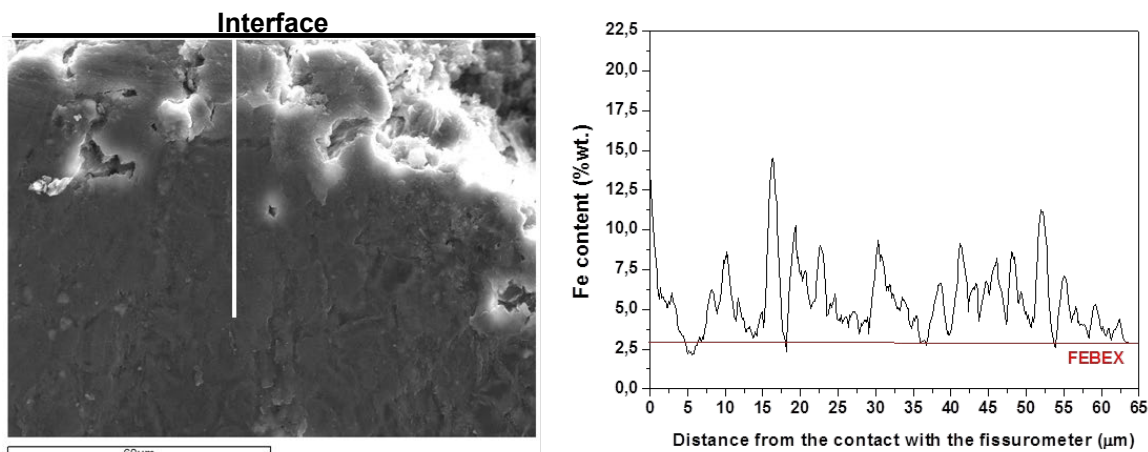


Fig. 114: Cross-section SEM micrograph of the fissurometer/bentonite interface in sample B-C-47-10, (right) EDS line profile analysis corresponding to Fe (%wt.).

TEM and SAED analyses

In highly-saturated zones of the clay barrier, newly-formed clay phases were not detected. Smectite and illite were the only clay phases identified by Selected Area Electron Diffraction (SAED) analysis (Fig. 115). In these zones, smectite particles seem to have undergone dissolution processes. TEM analysis confirmed the existence of amorphous SiO_2 gels.

In sample B-C-47-10, significant precipitation of iron oxyhydroxide occurred in bentonite in contact with stainless steel of the fissurometer in the vicinity of the granite. TEM analysis confirmed the formation of colloidal particles of maghemite (Tab. 30), goethite and Ferrihydrite (Fig. 117), which contained traces of Ni, Zn and Mn (Tab. 31). These particles could have been formed either by the co-precipitation *in situ* of Fe released from the corrosion of the cable cap and the alloying elements released during corrosion or by the spalling and transport from the corrosion products layer.

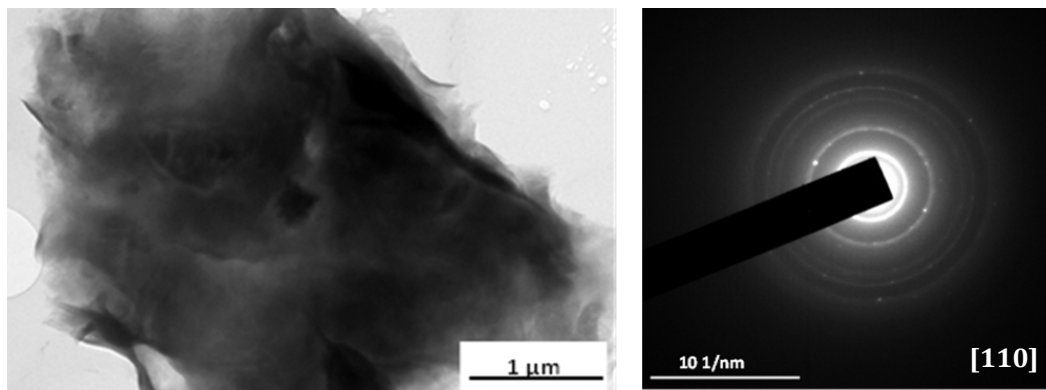


Fig. 115: (Left) Transmission electron micrograph of a clay particle in sample B-C-47-10, (right) Ring SAED pattern from an illite domain.

Tab. 30: EDS-TEM analysis of the illite particle shown in Fig. 115.

Element	Weight%
O	32.89
Na	0.39
Mg	3.42
Al	12.03
Si	36.30
K	2.82
Ca	0.95
Ti	0.74
Fe	10.46

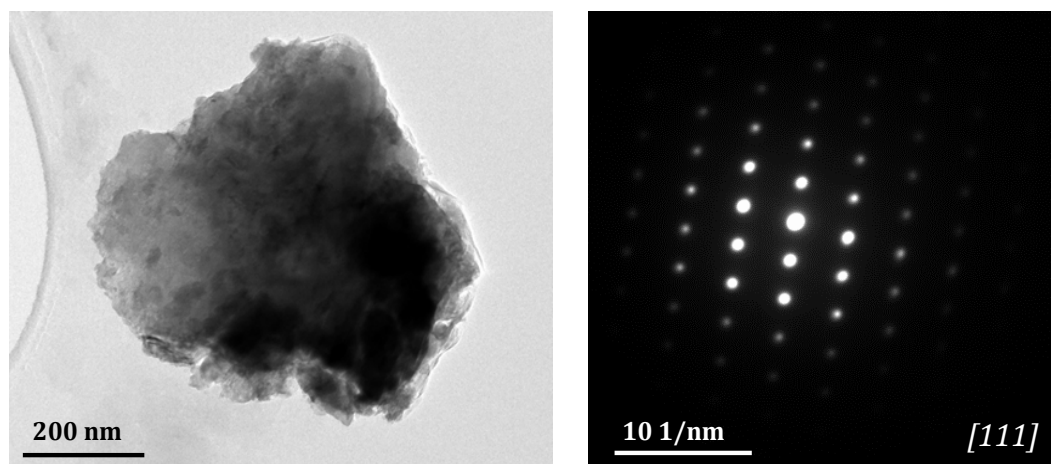


Fig. 116: (Left) Transmission electron micrograph of an iron oxide particle found in sample B-C-47-10, (right) Spot SAED pattern assigned to maghemite.

Tab. 31: EDS -TEM analysis of the maghemite particle shown in Fig. 116.

Element	Weight%
O	41.63
Mg	0.25
Si	0.56
Ca	0.34
Mn	1.51
Fe	49.39
Ni	0.24
Zn	6.07

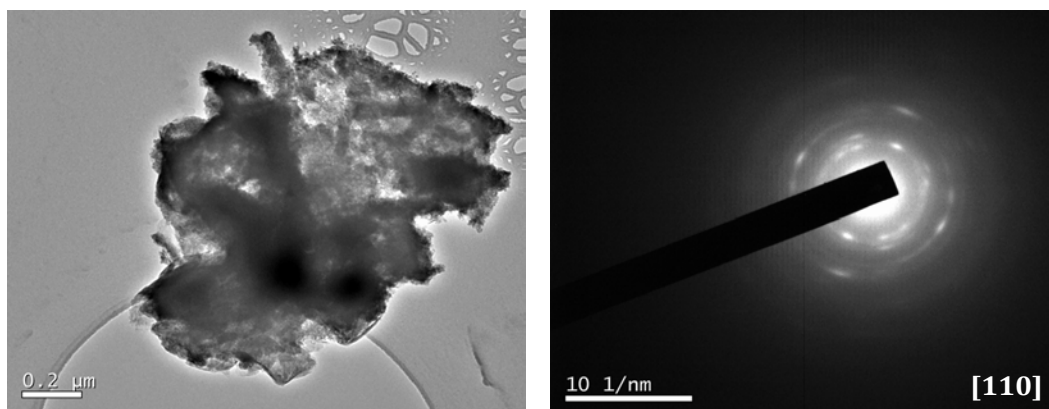


Fig. 117: (Left) TEM micrograph of a Fe oxide particle found in sample B-C-47-10, (right) corresponding SAED pattern assigned to Ferrihydrite.

At the contact with the heater, smectite is the predominant clay phase (Fig. 118). Other clay minerals, such as chlorite (Fig. 119), have been identified. EDS analyses confirmed the presence of traces of Cl in the analysed clay particles. Mg content increased compared to unaltered FEBEX bentonite.

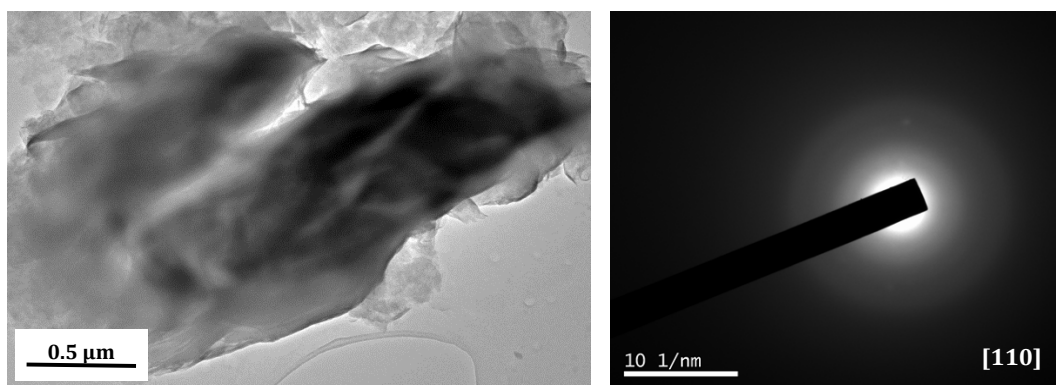


Fig. 118: (Left) Transmission electron micrograph of a clay particle sampled at the contact with the heater, (right) Ring SAED pattern from the montmorillonite particle.

Tab. 32: EDS analysis of the montmorillonite particle shown in Fig. 118.

Element	Weight%
Na	0.15
Mg	10.83
Al	10.34
Si	27.04
Cl	0.18
K	0.25
Ca	0.51
Ti	0.11
Mn	0.12
Fe	2.02
O	48.43

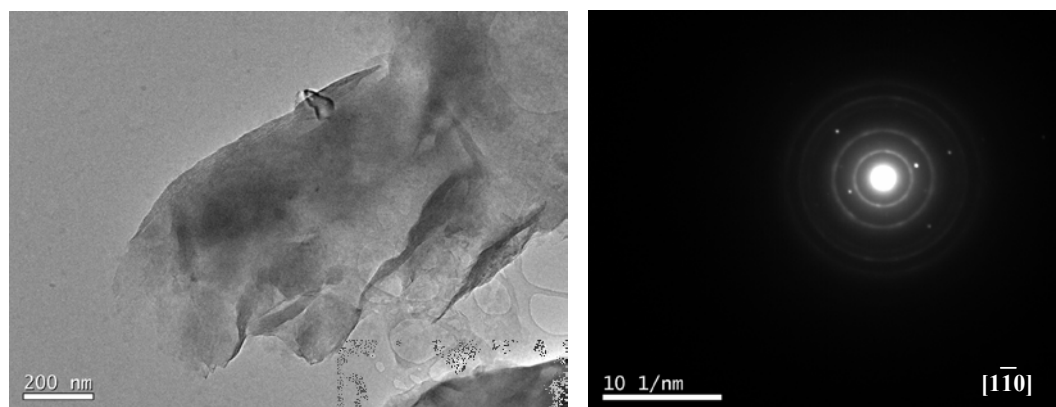


Fig. 119: (Left) Transmission electron micrograph of a chlorite particle in sample BM-S-54-7, (right) corresponding ring SAED pattern.

Tab. 33: EDS analysis of the chlorite particle shown in Fig. 119.

Element	Weight%
Mg	9.47
Al	8.36
Si	27.95
Cl	0.18
K	0.87
Ca	0.50
Fe	4.75
O	47.93

Precipitation of calcite seems to have occurred to a significant extent at the contact with the heater (Fig. 120). Calcite and aragonite phases have been identified by SAED analysis. EDS has shown that Ca has co-precipitated with Mg and Sr, possibly displaced from the bentonite exchange complex.

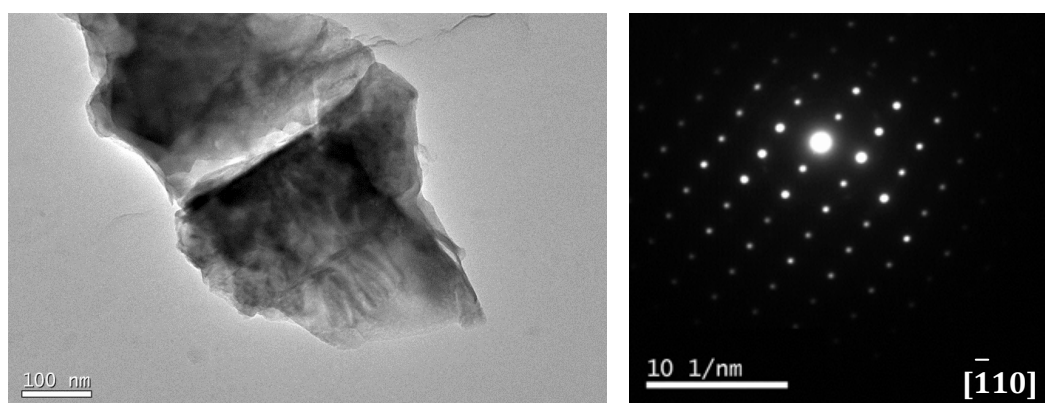


Fig. 120: (Left) Transmission electron micrograph of an aragonite particle in sample BM-S-54-7, (right) Spot SAED pattern from the aragonite particle (see also Tab. 34).

Tab. 34: EDS analysis of the aragonite particle shown in Fig. 120.

Element	Weight%
Mg	1.33
Al	0.61
Si	1.73
Cl	0.37
Ca	64.17
Fe	0.34
Sr	1.95
O	29.50

In the hottest areas of the bentonite barrier, exchangeable and soluble magnesium increased significantly (Tab. 38 and Tab. 41, respectively). Mg-rich silicate phases were occasionally found (Fig. 121). SAED diffraction patterns of these phases were in good agreement with Mg-rich zeolites (Mg-chabazite).

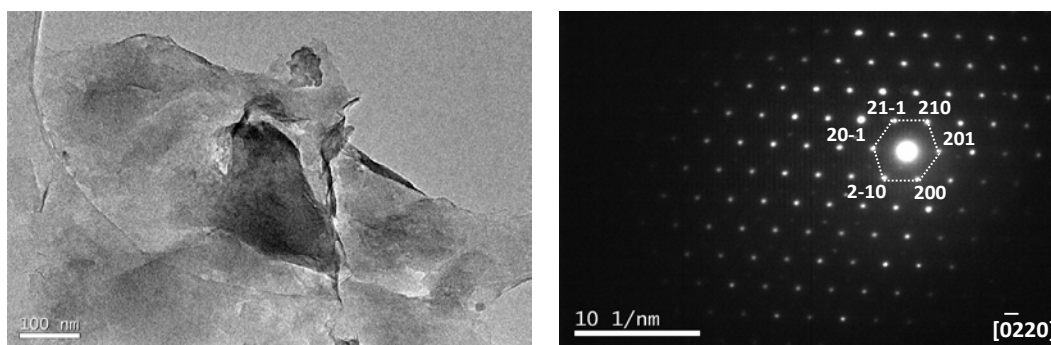


Fig. 121: Transmission Electron micrograph and SAED pattern of a Mg-chabazite crystal found in sample BM-S-54-7, at the contact between bentonite and the heater.

Tab. 35: EDS analysis corresponding to Mg-rich phase shown in Fig. 121.

Element	Weight %
Mg	11.72
Al	9.17
Si	27.98
Ca	0.50
Fe	0.88
O	48.75

FTIR

FTIR spectroscopy was used to study the octahedral cation distribution of smectites, especially in the 1'100 – 550 cm⁻¹ region of the MIR. This region corresponds to the octahedral cation-OH lattice deformation bands.

According to FTIR spectra no significant changes are observed in the position and intensity of the $\delta_{\text{Al-Me}^{2+}\text{-OH}}$ bands in the bentonite that have been in contact with the heater and the liner (Fig. 122). In these zones the bentonite does not seem to have undergone significant structural changes or Fe enrichment.

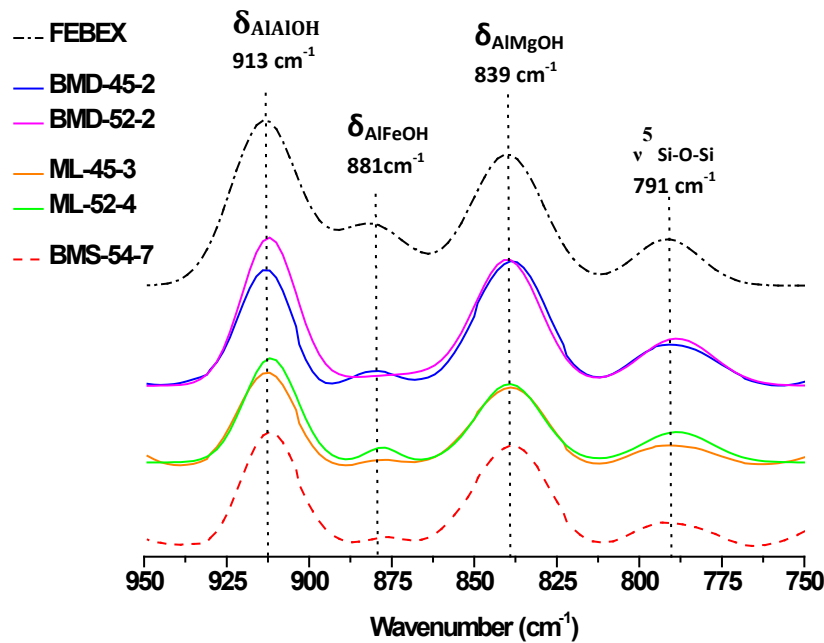


Fig. 122: FTIR spectra in the 950 – 750 cm⁻¹ region corresponding to heater/bentonite and liner/bentonite interfaces.

However, a slight decrease in intensity of these bands was observed in saturated bentonite sampled in cold areas of the bentonite barrier (BS-37-1 and BC-47-10) (Fig. 123). This might suggest the occurrence of dissolution processes related to the long-term saturation of bentonite in that area.

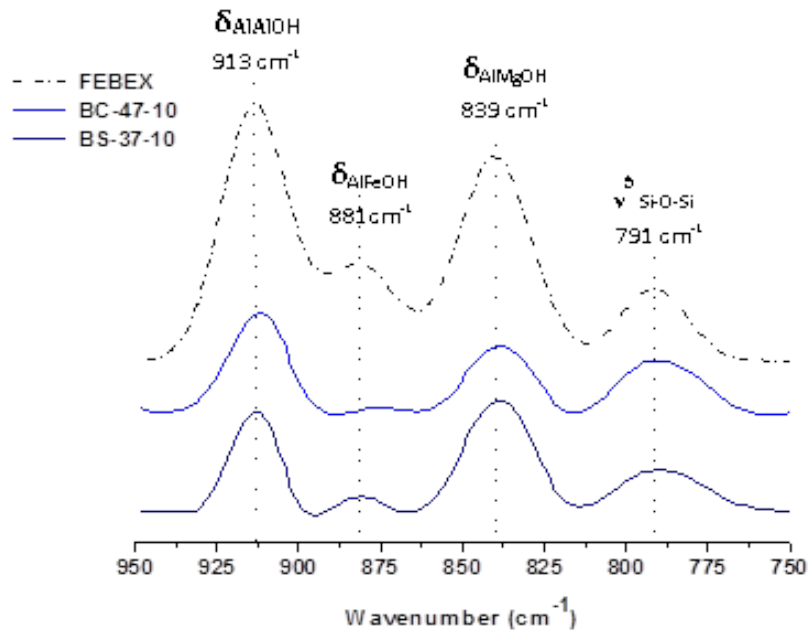


Fig. 123: FTIR spectra in the 950 – 750 cm^{-1} region for saturated bentonite samples.

Fig. 124 displays a sequence of spectra from the initial FEBEX natural to the samples in contact with the liner/heater and the sample close to the granite. The sequence quite evidently shows the difference between the spectra of the area far away from the heater and those of the heater/liner zone.

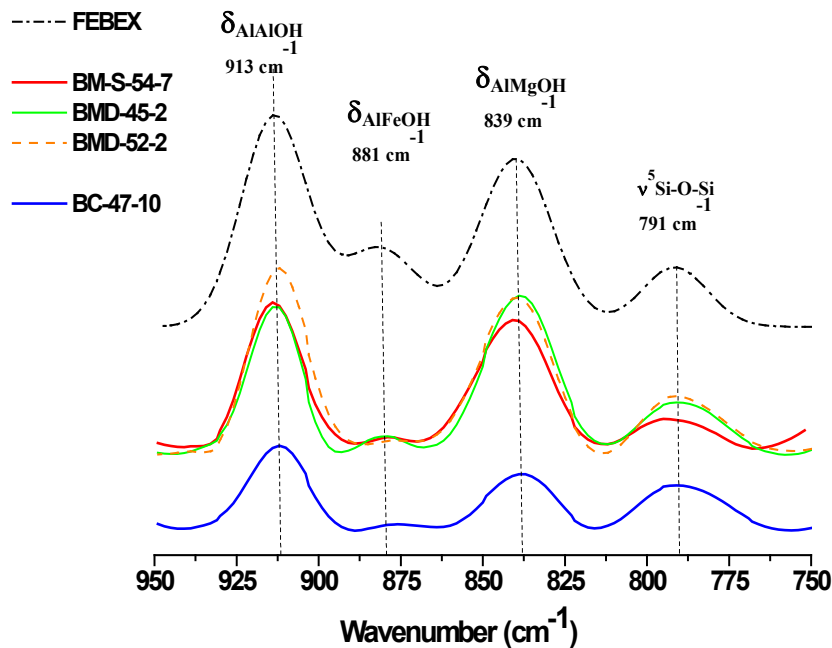


Fig. 124: FTIR spectra in the 950 – 750 cm^{-1} region obtained for the metal/bentonite interfaces in samples: FEBEX natural, BM-S-54-7, BMD-45-2, BMD-52-2 (heater/liner) and B-C-47-10 (fissurometer close to granite).

Cation Exchange Capacity

Cation Exchange Capacity (CEC) was measured in eleven samples. CEC values determined in these samples range from 86.5 to 90.6 cmol(+)/kg (Tab. 36). These values are similar to average CEC measured for unaltered FEBEX bentonite (89.1 ± 0.5 cmol(+)/kg).

Tab. 36 Cation exchange capacity (CEC) determined with Cu-triethylenetetramine in samples corresponding to the metal/bentonite interfaces.

Position in the gallery	Reference	CEC cmol(+)/Kg
Heater	BM-54-7	88.2
	BM-D-45-2	88.1
Liner	M-L-45-3	86.5
	BM-D-52-2	87.0
	M-L-52-4	87.5
	B-B-42-5	86.7
Cable cap	BM-C-42-1	87.6
	BM-C-42-2	90.6
	BM-C-42-3	89.9
Granite	B-C-47-10	90.1
Dummy	B-S-37-1	90.3
	FEBEX	89.1 ± 0.5

Tab. 37: CEC profiles along the studied samples.

Position	Reference	CEC (cmol(+)/kg)
Heater	<i>BM-S-54-7</i>	
	Interface (0 cm)	88.0
	1.5 cm	88.4
	<i>BM-D-45-2A</i>	
	Interface (0 cm)	85.4
	1 cm	87.9
	2 cm	88.1
	3 cm	88.6
	4 cm	89.0
	6 cm	90.3

Tab. 37: Cont.

Position	Reference	CEC (cmol(+)/kg)
Liner	<i>BM-D-52-2</i>	
	Interface (0 cm)	86.0
	1.5 cm	88.0
Cable cap	<i>B-B-42-5</i>	
	Interface (0 cm)	91.3
	0.75 cm	90.1
	1.5 cm	89.5
	2.5 cm	89.4
	3.5 cm	89.4
	4.5 cm	89.3
	6 cm	88.7
	<i>BM-C-42-1</i>	
	Interface (0 cm)	84.2
	1 cm	86.8
	2 cm	87.3
	3 cm	88.3
	4 cm	88.6
	6 cm	90.1
	<i>BM-C-42-2.3</i>	
	Interface (0 cm)	90.9
	1 cm	90.3
	2 cm	89.9
	4 cm	89.8
	6 cm	89.4
	8 cm	88.9
Granite	<i>B-C-47-10</i>	
	Interface (0 cm)	89.0
	1.5 cm	89.3
	3 cm	89.4
	5 cm	90.1

Exchangeable cations

Cation population in the exchange complex varies as a function of the thermal gradient (Tab. 37). Magnesium is the major exchangeable cation in the hottest areas of the bentonite barrier at the expense of sodium, whereas it remains similar to unaltered FEBEX bentonite in low-temperature saturated zones (Fig. 125). Exchangeable sodium increases near the granite and drops at the contact with the heater. On the contrary, magnesium increases significantly near the heater.

Some authors have reported the change in the selectivity coefficients as a function of temperature. In the case of K, the increase of selectivity was explained by an increase of charge density in the smectites rather than the effect of temperature (Shainberg et al. 1987). According to longterm lab tests carried out with compacted FEBEX bentonite, the selectivity of magnesium in smectite increases with temperature in relation to sodium (Cuevas et al. 1997).

Magnesium is released from the interlayers to the porewater in low-temperature areas of the bentonite barrier and transported towards the heater. Magnesium-complexes seem to be more stable at high temperatures than the complexes formed by the rest of the exchangeable cations. To date, we have not found any evidence of significant structural modifications in order to explain these changes.

The average value of calcium remains constant in the exchange complex in the 11 bentonite samples (35 ± 3 cmol(+)/kg). However, Ca slightly decreases at the contact with the heater. Ca is replaced by Mg in the bentonite exchange complex and released into porewater solution. Once, Ca concentration in porewater exceeds the solubility limit, it precipitates together with dissolved bicarbonate as calcite. Precipitation of siderite, calcite and aragonite has been observed in samples in contact with the heater, the liner and the cable cap.

Similar variations in the exchange complex were described from previous experiments with simultaneous heating and hydration lasting for 8 years in large-scale cells (60 cm) (Fernández & Villar 2010). Further discussion on the related processes is given in the cited publication. Exchangeable cation profiles show that cation populations are quite homogeneous along the studied bentonite samples (Tab. 40). No gradients are observed as a function of temperature or distance to the interface.

Tab. 38: Distribution of exchangeable cations in the studied samples (cmol(+)/kg).

Data correspond to average values from all the subsamples analysed for each sample.

Position in the gallery	Samples	Na ⁺ (cmol(+)/kg)	K ⁺ (cmol(+)/kg)	Mg ²⁺ (cmol(+)/kg)	Ca ²⁺ (cmol(+)/kg)	Σ _{exchange}
Heater	BM-S-54-7	8.8	2.2	47.4	31.5	89.8
Liner	BM-D-45-2A	16.2	2.6	42.6	38.2	99.6
	M-L-45-3	15.1	2.3	45.3	33.3	96.0
	BM-D-52-2	16.0	2.0	44.0	35.8	97.7
	M-L-52-4	15.1	2.8	46.0	32.3	96.3
Cable cap	B-B-42-5	26.3	1.8	31.0	39.9	99.0
	BM-C-42-1	23.6	2.2	32.7	39.1	97.6
	BM-C-42-2	23.5	1.7	30.4	41.9	97.4
	BM-C-42-3	24.6	1.7	31.0	41.8	99.0
Granite	B-C-47-10	27.2	2.1	34.0	34.9	98.1
Dummy	B-S-37-1	23.7	2.0	37.8	34.9	98.4
	FEBEX	24 ± 1	2.6 ± 0.4	31 ± 3	35 ± 3	92.6 ± 2

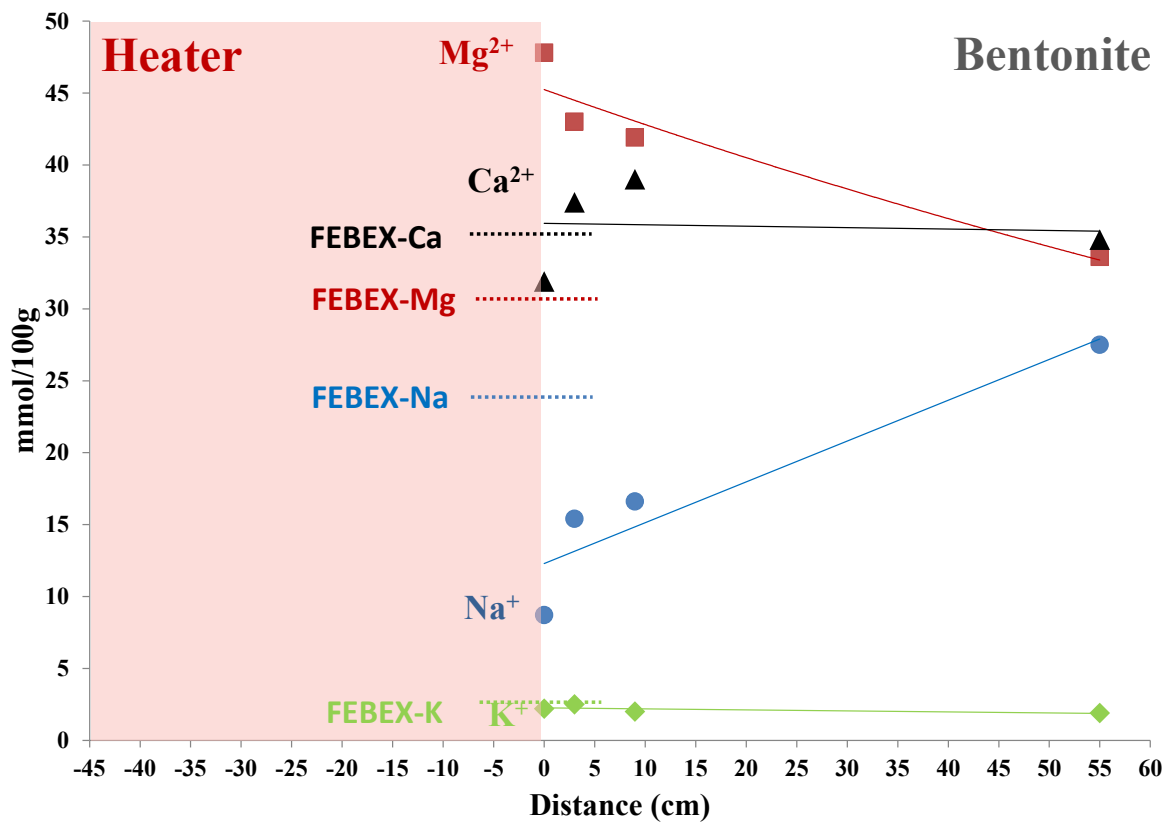


Fig. 125: Distribution of exchangeable cations as a function of the distance to the heater.

Only samples of Sections 45, 47, 52 and 54 (heater sections) are represented.

Tab. 39: Exchangeable Fe measured after its displacement by CsNO₃ 0.5N method.

Position in the gallery	Reference	Fe (cmol(+)/kg)
Heater	BM-54-7	0.003
Liner	BM-D-45-2A	0.003
	M-L-45-3	<d.l.
	BM-D-52-2	0.003
	M-L-52-4	<d.l.
Cable cap	B-B-42-5	<d.l.
	BM-C-42-1	<d.l.
	BM-C-42-2	<d.l.
	BM-C-42-3	<d.l.
Granite	B-C-47-10	0.03
Dummy	B-S-37-1	<d.l.
	FEBEX	<d.l.

Tab. 40: Distribution profiles of exchangeable cations along the studied samples.

Shadowed cells are considered for Fig. 125.

Position	Reference	cmol (+)/kg				
		Na ⁺	K ⁺	Mg ²⁺	Ca ²⁺	Σ _{exch. cat}
Heater	BMS-54-7					
	Interface (0 cm)	8.7	2.2	47.8	31.9	90.6
	1.5 cm	8.9	2.1	46.9	31.1	89.0
Liner	BMD-45-2A					
	Interface (0 cm)	15.4	2.5	43.0	37.4	98.5
	1 cm	15.7	2.4	42.3	38.1	98.5
	2 cm	16.8	3.8	42.3	37.9	100.8
	3 cm	16.6	2.4	42.2	38.4	99.6
	4 cm	16.2	2.5	43.8	38.3	100.7
	6 cm	16.6	2.0	41.9	39.0	99.5
	BMD-52-2					
	Interface (0 cm)	15.6	1.9	42.3	35.3	95.1
	1.5 cm	16.3	2.0	45.7	36.3	100.3

Tab. 40: Cont.

Position	Reference	cmol (+)/kg				
		Na ⁺	K ⁺	Mg ²⁺	Ca ²⁺	Σ _{exch. cat}
Cable cap	<i>BB-42-5</i>					
	Interface (0 cm)	26.0	2.0	30.9	39.7	98.7
	0.75 cm	25.9	1.8	30.9	39.8	98.4
	1.5 cm	26.4	1.8	31.0	39.6	98.7
	2.5 cm	27.2	1.7	31.7	41.6	102.1
	3.5 cm	27.3	1.7	31.9	41.2	102.1
	4.5 cm	25.8	1.6	30.0	39.3	96.8
	6 cm	25.8	1.8	30.3	38.1	96.1
	<i>BMC-42-1</i>					
	Interface (0 cm)	23.4	2.4	33.0	38.5	97.4
	1 cm	24.7	1.9	30.8	39.8	97.2
	2 cm	20.7	3.0	38.0	35.8	97.4
	3 cm	24.5	2.6	30.7	39.5	97.3
	4 cm	24.0	1.7	32.0	41.3	98.9
	6 cm	24.2	1.7	31.5	39.9	97.2
	<i>BMC-42-2.3</i>					
	Interface (0 cm)	23.5	1.7	30.4	41.9	97.4
	1 cm	24.3	1.8	30.3	42.1	98.4
	2 cm	23.9	2.0	31.4	41.3	98.6
	4 cm	24.8	1.9	31.3	40.8	98.7
	6 cm	24.6	1.7	31.0	41.8	99.0
	8 cm	24.9	1.8	30.4	41.3	98.4
Granite	<i>BC-47-10</i>					
	Interface (0 cm)	27.5	1.9	33.6	34.8	97.8
	1.5 cm	26.1	2.4	34.8	35.0	98.4
	3 cm	27.2	1.8	33.7	35.3	98.0
	5 cm	27.9	2.1	33.7	34.5	98.2

Soluble ions by aqueous leaching

Soluble ions determined for bentonite samples collected at the metal/clay interfaces are shown in Tab. 43 and Tab. 44. A notable increase of soluble salts is observed in the proximity of the heater (Fig. 124 and Fig. 126). Chloride, and sodium as its counterion, are the prevailing ions in the vicinity of the heater and liner (hot zones). Ca and Mg tend to concentrate near the heater as well, but to a lesser extent than Na and Cl. The cause of the increase of salinity in the proximity of the heater is uncertain. Pusch et al. (1985) described the movement of salts due to suction gradients in compacted clay. The presence of solutes in bentonite porewater creates an osmotic potential. Gradients in osmotic pressure could induce significant flows of water in bentonite under conditions of high solute concentrations and low water content. Cuevas et al. (2002), however, proposed that the driving force for salt transport would be the increase of salt concentration on the mesopore "external" water with respect to the "surface-influenced" (anion exclusion) micropore water. The preservation of primitive interfaces between the stacks of montmorillonite lamellae and the macrograins (i.e. quartz) upon saturation supports the preservation of preferential pathways for salt migration (Tab. 41 and Tab. 42).

Soluble salt profiles determined along the bentonite samples are given in Tab. 43 and Tab. 44. Soluble Na and Cl gradients are observed in samples subjected to higher temperatures. Soluble Na and Cl increase towards the interface with metal (higher temperature) in bentonite samples taken from the contacts with the heater and the liner (BM-54-7, BM-D-45-2, BM-D-52-2).

Tab. 41: Soluble cations determined in aqueous extracts (S:L 1:4).

Position in the gallery	Reference	Na ⁺ (mmol/100 g)	K ⁺ (mmol/100 g)	Mg ²⁺ (mmol/100 g)	Ca ²⁺ (mmol/100 g)
Heater	BM-S-54-7	11.71	0.48	6.32	3.80
Liner	BM-D-45-2A	4.81	0.14	0.44	0.41
	ML-45-3	4.46	0.31	0.59	0.44
	BM-D-52-2	6.01	0.22	1.13	0.91
	ML-52-4	4.20	0.19	0.46	0.33
Cable cap	B-B-42-5	4.10	0.11	0.20	0.20
	BM-C-42-1	4.75	0.90	0.14	0.21
	BM-C-42-2	5.26	0.06	0.11	0.16
	BM-C-42-3	4.11	0.04	0.05	0.09
Granite	B-C-47-10	0.59	0.02	0.01	0.01
Dummy	B-S-37-1	9.48	0.19	0.17	0.21
	FEBEX	3.32	0.03	0.03	0.04

Tab. 42: Soluble anions determined in aqueous extracts (S:L 1:4).

Position in the gallery	Reference	F ⁻ (mmol/100 g)	Cl ⁻ (mmol/100 g)	SO ₄ ²⁻ (mmol/100 g)
Heater	BM-54-7	0.01	29.03	0.75
Liner	BM-D-45-2A	0.02	5.63	0.31
	ML-45-3	0.02	4.65	0.47
	BM-D-52-2	0.02	9.24	0.36
	ML-52-4	0.02	4.38	0.30
Cable cap	B-B-42-5	0.03	2.47	0.38
	BM-C-42-1	0.02	2.11	0.59
	BM-C-42-2	0.01	2.32	1.29
	BM-C-42-3	0.02	2.35	0.63
Granite	B-C-47-10	0.01	0.09	0.19
Dummy	B-S-37-10	0.05	8.58	0.09
	FEBEX	0.07	1.29	0.59

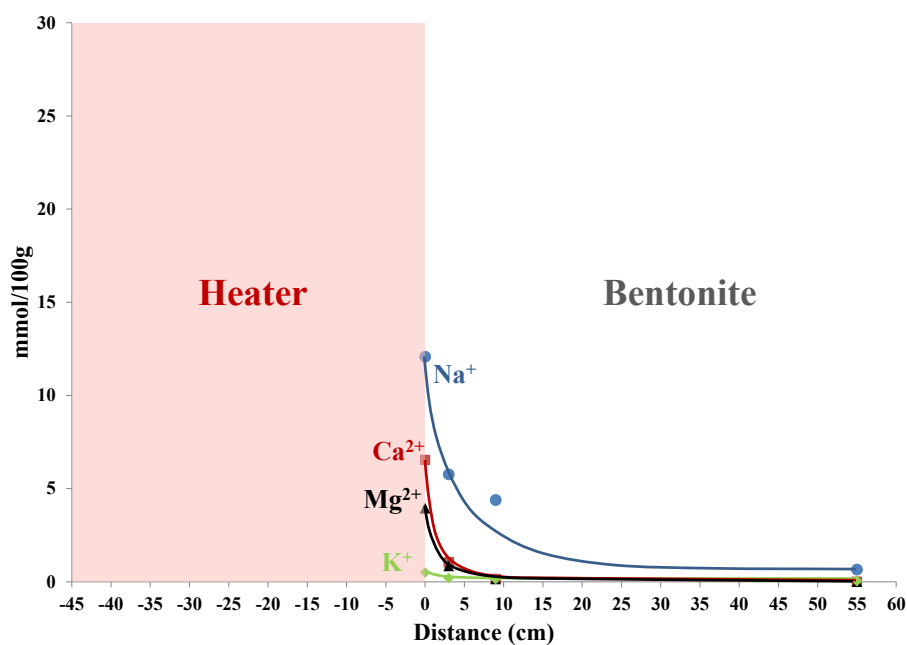


Fig. 126: Distribution of soluble cations as a function of the distance to the heater.
Only samples of Sections 45, 47, 52 and 54 (heater sections) are represented.

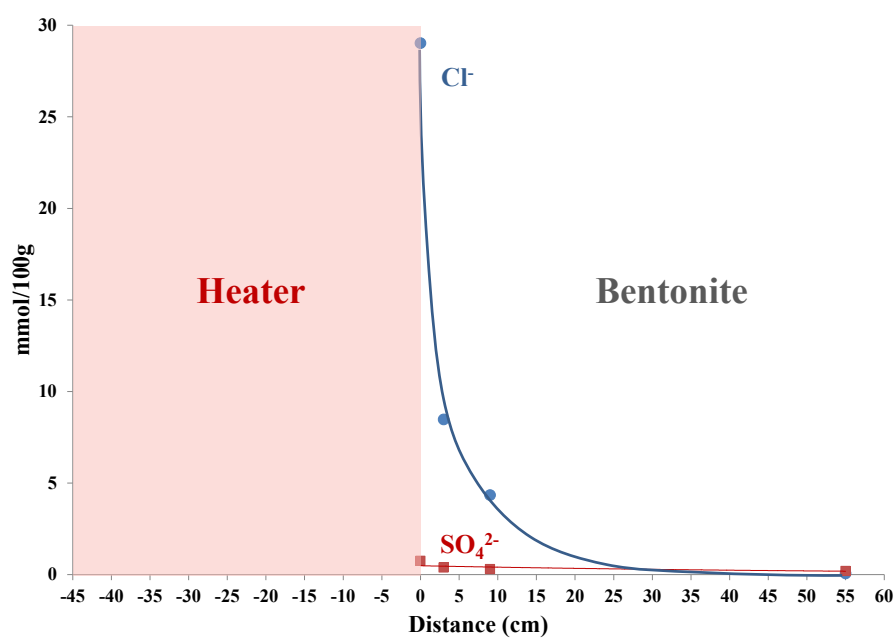


Fig. 127: Distribution of soluble anions as a function of the distance to the heater. Only samples of Sections 45, 47, 52 and 54 (heater sections) are represented.

Tab. 43: Distribution profiles of soluble cations along the studied samples.

Shadowed cells are considered for Fig. 126.

Position	Reference	Na ⁺ (mmol/100 g)	K ⁺ (mmol/100 g)	Mg ²⁺ (mmol/100 g)	Ca ²⁺ (mmol/100 g)
Heater	BM-S-54-7				
	Interface (0 cm)	12.08	0.49	6.54	3.95
	1.5 cm	11.34	0.47	6.10	3.66
Liner	BM-D-45-2A				
	Interface (0 cm)	5.26	0.17	0.84	0.75
	1 cm	5.21	0.14	0.41	0.40
	2 cm	5.06	0.16	0.70	0.60
	3 cm	4.47	0.14	0.46	0.42
	4 cm	4.45	0.06	0.09	0.10
	6 cm	4.39	0.14	0.15	0.16
	BM-D-52-2				
	Interface (0 cm)	6.27	0.23	1.23	0.96
	1.5 cm	5.76	0.21	1.03	0.86
Cable cap	B-B-42-5				
	Interface (0 cm)	4.12	0.16	0.37	0.31
	0.75 cm	4.03	0.18	0.09	0.11
	1.5 cm	4.12	0.16	0.58	0.52
	2.5 cm	4.33	0.08	0.13	0.14
	3.5 cm	4.16	0.05	0.08	0.09
	4.5 cm	3.93	0.07	0.08	0.10
	6 cm	4.04	0.06	0.08	0.10
	BM-C-42-1				
	Interface (0 cm)	5.51	5.09	0.05	0.09
	1 cm	4.90	0.10	0.51	0.68
	2 cm	4.52	0.04	0.06	0.11
	3 cm	4.20	0.05	0.07	0.10
	4 cm	4.19	0.04	0.06	0.09
	6 cm	5.20	0.05	0.10	0.16
	BM-C-42-2.3				
	Interface (0 cm)	5.26	0.06	0.11	0.16
	1 cm	4.59	0.04	0.07	0.11
	2 cm	4.93	0.05	0.08	0.13

Tab. 43: Cont.

Position	Reference	Na ⁺ (mmol/100 g)	K ⁺ (mmol/100 g)	Mg ²⁺ (mmol/100 g)	Ca ²⁺ (mmol/100 g)
Cable cap	4 cm	4.26	0.05	0.06	0.10
	6 cm	4.11	0.04	0.05	0.09
	8 cm	3.62	0.04	0.07	0.14
Granite	<i>B-C-47-10</i>				
	Interface (0 cm)	0.66	0.04	0.00	0.01
	1.5 cm	0.50	0.02	0.00	0.00
	3 cm	0.63	0.01	0.01	0.01
	5 cm	0.57	0.01	0.01	0.01

Tab. 44: Distribution profiles of soluble anions along the studied samples.

Shadowed cells are considered for Fig. 127.

Position	Reference	F- (mmol/100 g)	Cl- (mmol/100 g)	SO ₄ ²⁻ (mmol/100 g)
Heater	<i>BM-S-54-7</i>			
	Interface (0 cm)	0.01	30.00	0.77
	1.5 cm	0.01	28.07	0.73
Liner	<i>BM-D-45-2A</i>			
	Interface (0 cm)	0.02	7.64	0.42
	1 cm	0.02	6.38	0.34
	2 cm	0.02	5.81	0.20
	3 cm	0.02	5.11	0.28
	4 cm	0.03	4.48	0.30
	6 cm	0.03	4.35	0.30
	<i>BM-D-52-2</i>			
	Interface (0 cm)	0.01	9.31	0.36
	1.5 cm	0.02	9.16	0.36
Cable cap	<i>B-B-42-5</i>			
	Interface (0 cm)	0.03	2.96	0.39
	0.75 cm	0.04	2.65	0.37
	1.5 cm	0.03	2.49	0.36
	2.5 cm	0.03	2.39	0.42
	3.5 cm	0.02	2.31	0.40

Tab. 44: Cont.

Position	Reference	F- (mmol/100 g)	Cl- (mmol/100 g)	SO ₄ ²⁻ (mmol/100 g)
Cable cap	4.5 cm	0.03	2.26	0.35
	6 cm	0.02	2.22	0.34
	<i>BM-C-42-1</i>			
	Interface (0 cm)	0.02	2.02	0.58
	1 cm	0.03	1.90	0.39
	2 cm	0.02	2.19	0.62
	3 cm	0.02	2.40	0.64
	4 cm	0.02	2.11	0.66
	6 cm	0.02	2.06	0.64
	<i>BM-C-42-2.3</i>			
	Interface (0 cm)	0.01	2.32	1.29
	1 cm	0.03	2.28	1.29
	2 cm	0.02	2.28	0.84
	4 cm	0.03	2.47	0.91
	6 cm	0.02	2.35	0.63
	8 cm	0.03	2.20	0.59
Granite	<i>B-C-47-10</i>			
	Interface (0 cm)	0.01	0.07	0.20
	1.5 cm	0.01	0.07	0.19
	3 cm	0.01	0.16	0.20
	5 cm	0.01	0.07	0.15

Total and free iron

Extraction of amorphous iron oxides

Determination of amorphous Fe oxides in bentonite was made according to the dithionite-citrate-bicarbonate (CBD) method (Mehra & Jackson 1960). Distribution of citrate-dithionite extractable iron does not seem to follow any clear pattern (Tab. 45). Maximum value is measured in sample BS-37-1 (filling the gap between the liner and the dummy), whereas the minimum content was found in sample BMS-54-7 (heater).

Tab. 45: Extracted Fe from amorphous Fe oxides in the studied metal/bentonite interfaces according to the Dithionite-Citrate-Bicarbonate (CBD) method.

Position in the gallery	Reference	Fe (mmol/100 g) (adsorbed Fe, carbonates)
Heater	BM-S-54-7	0.02
Liner Cable cap	BM-D-45-2	0.05
	ML-45-3	0.03
	BM-D-52-2	0.03
	ML-52-4	0.03
	B-B-42-5	0.36
	BM-C-42-1	0.17
	BM-C-42-2	0.11
	BM-C-42-3	0.08
Granite	B-C-47-10	1.55
Dummy	B-S-37-10	0.24
	FEBEX natural	0.05 ± 0.04

Extraction of adsorbed iron

Extraction of adsorbed Fe was performed with a solution of citric acid 0.3N. Citrate-extractable Fe is highest in sample B-C-47-10 (near granite). On the contrary, at the contact with the heater and the liner, where temperature is higher, extractable Fe is below the value measured for unaltered FEBEX bentonite. According to Tab. 46, extractable Fe seems to be distributed as a function of temperature and saturation degree. Citrate-extractable Fe tends to increase in saturated zones whereas it decreases or remains close to the extractable Fe value measured for the original FEBEX bentonite.

Tab. 46: Citrate-extractable Fe in the studied metal/bentonite interfaces using a solution of citric acid 0.3N as extractant.

Position in the gallery	Reference	Fe (mmol/100 g) (adsorbed Fe, carbonates)
Heater	BM-S-54-7	0.02
Liner	BM-D-45-2	0.05
	ML-45-3	0.03
	BM-D-52-2	0.03
	ML-52-4	0.03
	B-B-42-5	0.36
Cable cap	BM-C-42-1	0.17
	BM-C-42-2	0.11
	BM-C-42-3	0.08
Granite	B-C-47-10	1.55
Dummy	B-S-37-10	0.24
	FEBEX natural	0.05 ± 0.04

Total Fe content

Total Fe content was measured by means of Total Reflection X-Ray Fluorescence Spectroscopy (TR-XRF). Total Fe content measured range from 3.0 (BS-37-1) to 4.6 %wt. (B-C-47-10) (Tab. 47). These values are slightly higher than the Fe content measured for the unaltered FEBEX bentonite. The highest contents were found in samples B-C-47-10 (near granite) and BMS-54-7 (heater). This increase is a consequence of the precipitation of FeOOH and anhydrous Fe oxides.

Tab. 47: Total Fe content measured in the bentonite samples studied by Total Reflection X-Ray Fluorescence Spectroscopy (TR-XRF).

Position in the gallery	Reference	Fe content (wt %)
Heater	BM-S-54-7	4.4 ± 0.1
Liner	BM-D-52-2	3.3 ± 0.1
	ML-52-4	3.2 ± 0.1
	BM-D-45-2	3.7 ± 0.1
	ML-45-3	4.0 ± 0.1
Cable cap	BM-C-42-1	3.1 ± 0.1
	B-B-42-5	4.2 ± 0.1
Granite	B-C-47-10	4.6 ± 0.1
Dummy	B-S-37-1	3.0 ± 0.1
	FEBEX natural	2.9 ± 0.1

An overall Fe enrichment is observed in the analysed samples (Tab. 48). Fe(II) in exchange positions and citrate-extractable Fe are negligible in all cases, below 0.1 %wt. On the other hand, Fe extracted from amorphous oxides ranges from 0.2 to 2.3 %wt. Despite the fact that structural Fe has not been quantified, the increase in Fe content seems to be related to the precipitation of anhydrous Fe oxides near the heater and liner and Fe oxyhydroxides in saturated areas of the barrier.

Tab. 48: Distribution of total Fe content measured in the studied samples (wt%): in the exchange complex, sorption sites and precipitated as amorphous iron oxides.

Position in the gallery	Reference	Fe (wt %)			
		Exchangeable	Adsorbed	Amorphous oxides	Fe total* (TR-XRF)
Heater	BM-S-54-7	2E-4	1E-3	0.2	5.3
Liner	BM-D-45-2	2E-4	3E-3	0.2	4.4
	ML-45-3	< 1E-4	2E-3	0.9	4.8
	BM-D-52-2	3E-4	2E-3	0.2	3.9
	ML-52-4	< 1E-4	2E-03	0.8	3.8
Cable cap	BM-C-42-1	< 1E-4	1E-2	0.3	4.1
	BM-C-42-2	< 1E-4	6E-3	0.2	4.1
	BM-C-42-3	< 1E-4	4E-3	0.2	4.1
	B-B-42-5	< 1E-4	2E-2	0.9	5.6
Granite	B-C-47-10	2E-3	9E-2	0.5	6.5
Dummy	B-S-37-1	< 1E-4	1E-2	2.3	4.8
	FEBEX	< 1E-4	3E-3 ± 2E-3	0.2 ± 0.02	3.4

* A after water content correction

4.7.5 Summary and discussion

Fe Distribution

Understanding the fate of iron released by corrosion was one of the primary aims of this work. According to the apparent diffusion coefficients measured for iron in compacted bentonite (10^{-12} and 10^{-14} m²/s, for the fast and slow diffusion pathway, respectively) (Idemitsu et al. 2002), iron would rather precipitate in the corrosion scales at the interfaces than migrate into compacted bentonite. Diffusion rates in compacted bentonite will depend on several factors (e.g. redox conditions, available water content). Based on the results obtained, differences in chemistry and mineralogy between bentonite sampled in saturated and unsaturated areas of the bentonite barrier were observed. However, in both cases, Fe released during corrosion mostly precipitated in the corrosion layer and the first mm from the metallic surface.

In the bentonite samples received by CIEMAT, diffused iron in bentonite was mostly precipitated as nanometric or colloidal iron oxides and oxyhydroxides (> 97 wt% of non-structural Fe). According to results obtained, sorbed iron, either on clay or iron oxides sites, is below 0.1 wt% of the total sample in all cases (< 2.4 wt% of non-structural Fe). According to the data, maximum Fe contents are found in the first mm from the metal surface. However, discrete Fe precipitates were also found in several samples at distances exceeding 2 cm. In principle, this accumulation beyond the Fe/bentonite contact may have resulted from colloid transport (Kurosawa et al. 1997) or by diffusion of Fe(II) and subsequent reaction with O₂ in the

still oxidizing bentonite. The latter process has been postulated in the studies of Obayashi (Section 4.3) and Uni Bern (Section 4.4).

Effect of Fe-related processes on the physical, chemical and mechanical properties of the bentonite barrier

Physical, chemical and mechanical properties of the clay buffer may be affected by Fe-related processes, such as the reduction of structural Fe in bentonite or the precipitation of Fe oxides. Alteration of montmorillonite to non-swelling 1:1 or 2:1 phyllosilicates could result in loss of swellability. However, in the light of existing data, corrosion of metallic elements seems to have no significant effect on the swelling capacity of bentonite (Part 4.7.4 and NAB 16-17).

BET-SSA values measured in bentonite samples from the FEBEX *in-situ* test are notably lower than the ones measured for raw FEBEX bentonite. BET-SSA decreases nearly 75 % at the contact with the heater. Near the granite, BET-SSA values decrease, but to a lesser extent (~25 %). BET-SSA values can decrease as a consequence of the cementation of bentonite particles through precipitation of FeOOH. However, no correlation with total Fe or Fe from amorphous phases content (%wt.) was found. The thermo-hydraulic gradient imposed in the bentonite barrier can lead to a reduction of both porosity and specific surface area, as well. Near the heater, high temperatures can trigger the clustering of montmorillonite particles caused by the displacement of interlayer water towards macropores (Villar & Lloret 2004). Close to granite, in areas disturbed by the insertion of metallic elements, water flow from granite can favor the dissolution of mineral phases and the formation of secondary amorphous solids, leading to a decrease in SSA. However, this decrease in the SSA values compared to raw FEBEX bentonite might also be related to thermo-hydraulic factors such as high saturation degrees and the effect of compaction.

Regarding porosity, precipitation of Fe phases would result in a decrease of porosity. However, no remarkable differences in total intruded porosity values were observed among the samples. MIP values do not seem related to an increase of the Fe content or to FeOOH precipitation. According to MIP results, Fe enrichment does not seem to modify the pore size distribution in the studied samples. Changes in pore size distribution are mostly related to the degree of saturation of each sample. Regarding the distribution of pore size, microporosity increases with saturation. On the contrary, macroporosity reaches its maximum at the contact with the heater. The increase in macroporosity is probably related to the formation of retractive cracks and desiccation processes occurring in high temperature areas.

Reduction of structural Fe can lead to significant changes in parameters such as layer charge or cation exchange capacity (CEC). CEC values measured for raw FEBEX bentonite, however, are similar to the ones obtained for samples from dismantling.

Based on the obtained results, temperature and degree of saturation seem to have a far more relevant effect on the chemical, physical and mechanical properties of bentonite than the effect of Fe-related alteration processes at the centimetre scale.

Salt distribution and cation exchange

The effect of the thermal and hydraulic gradient established along the bentonite barrier favours the movement of soluble salts towards the heater. Chloride, and sodium as its counterion, are the prevailing soluble ions in the vicinity of the heater and liner (hot zones). Ca and Mg tend to concentrate as well near the heater, but to a lesser extent than Na and Cl. High chloride contents

measured in the proximity of the heat source could have favoured the initialization and significantly enhanced the corrosion of the metallic elements in the EBS. In fact, according to the study by TecNALIA (NAB 16-54 and Section 4.2), chloride is detected in almost all the corrosion products analysed on the surface of the heater and is one of the factors for the corrosion of the liner. Corrosion products examined in the stainless steel coupons and Cu, Cu-Ni coupons revealed quite significant amount of chloride, which could influence the corrosion damage of the coupons.

The cation population in the exchange complex varies as a function of the thermal gradient, as well. Magnesium is the major exchangeable cation in the hottest areas of the bentonite barrier. Soluble Mg content is also high near the heater and the liner. These two conditions could have favoured the formation of Mg-rich silicate phases in the hottest areas of the bentonite barrier.

Mineralogy

Maghemite is the major phase in bentonite samples collected at the heater and liner contacts. In the case of samples farther away from the heater, Fe oxyhydroxides (goethite and lepidocrocite) prevail over anhydrous oxides (maghemite).

High temperature ($> 85\text{ }^{\circ}\text{C}$) also favours the evaporation and subsequent precipitation of salts, such as carbonates or sodium chloride; calcite (aragonite) and siderite (ankerite) have been detected in bentonite in contact with the heater or the liner.

4.8 Study of the University of Bristol

4.8.1 Objectives

Data on montmorillonite-iron interaction are very scarce and uncertainties with regard to the likelihood of bentonite alteration driven by possible interactions between the smectite component of bentonite and the corrosion products on metallic containers exist. Therefore, the present work was undertaken.

The overall aim of this work was to determine the plausible effects of anaerobically corroding iron on montmorillonite stability. In order to accomplish the proposed goal, several relevant samples from the FEBEX-DP project were analysed.

The changes to bentonite under the experimental conditions to which it was exposed, and plausible alterations in its thermo-hydro-mechanical (THM) and thermo-hydro-geochemical (THG) properties occurring during the experiment due to blended effects of temperature, water content, engineering structural components and solutes were measured. The objective was to obtain a greater knowledge of these processes through detailed sample characterisation.

Characterisation will mainly focus on corrosion-related alterations combined with thermal effects, since the dominant smectite in bentonite is montmorillonite, and the octahedral sheet is composed of Fe, Al and Mg. If the Fe (III) is reduced to Fe (II), this event can impact the layer charge and in turn the safety properties.

During the FEBEX field experiment, bentonite was emplaced at considerable depths in underground laboratories. Oxygen partial pressure was therefore much lower than at the earth's surface, and combined with ion water composition and contact with the metallic components, this could potentially lead to a chemically reducing atmosphere.

4.8.2 Materials and analytical methods

Materials: The FEBEX experiment-background and sample description

The University of Bristol (UoB) has received a series of seven FEBEX bentonite samples from the FEBEX-DP to analyse as part of a PhD project (Tab. 51).

- S-S-54-15-A/B/C/D/E
- M-S-48-1
- BM-B-41-1

All seven samples analysed in the current report are from the dismantling of Heater No. 2. This specific field test was conceived and performed within a horizontal shaft, 70.39 m long, driven into the granite host rock, with a total bentonite backfilled test length of 17.00 m. Heater No. 2 was located approximately 14 m into the backfilled volume (Fig. 3). Samples from the bentonite were retrieved from different slices or layers; each slice or layer corresponded to a different sampling section.

Samples **S-S-54-15-A/B/C/D/E** were received in sealed aluminium packages (freshly sealed at site to maintain conditions). Samples S-S-54-15-A/B/C/D (core samples) of similar provenance were extracted by hammering steel Shelby Tubes into the sampling face of the bentonite edifice. Each steel Shelby Tube has an approximate diameter of 35 mm (Fig. 128). Sample S-S-54-15-E

was described as "loose material" and was in direct contact with one of the extensometer sensors. The bulk density, thickness, volume and weight of each core sample have been estimated (Tab. 49).



Fig. 128: Bentonite samples embedded in steel Shelby tubes (Hadi 2016).

Tab. 49: Parameters extensometer samples (Hadi 2016).

Samples S-S-54-15-A/B/C/D		
Bulk Density	1'950	kg/m ³
Thickness (L)	0.2	m
Radius (r)	0.017	m
Volume (V)	2×10^{-5}	m ³
Weight	0.0354	kg
Weight	35.4	g

The five samples were extracted from the zone immediately adjacent to extensometer SH-SD2-03 (Fig. 129, Fig. 130), in what is known as the "halo" zone, characterised by a visibly distinguishable discolouration assumed to result from the corrosion suffered on the extensometer. Each core sample and sample S-S-54-15-E was collected in bentonite slice (or layer) 24, corresponding to sampling Section 54 (Fig. 131, Fig. 132) at a horizontal distance of 14.60 m into the backfilled test volume (Fig. 133). The sensor was part of the instrumentation used to read in continuous parameters during the operational test period, and is described as an extensometer used to measure possible displacements of Heater No. 2 (Enresa 1998). According to data supplied in Technical Publication n°: 12/98 (Enresa 1998), the extensometer was protected by an external tube manufactured from AISI 316 stainless steel (Fig. 132).

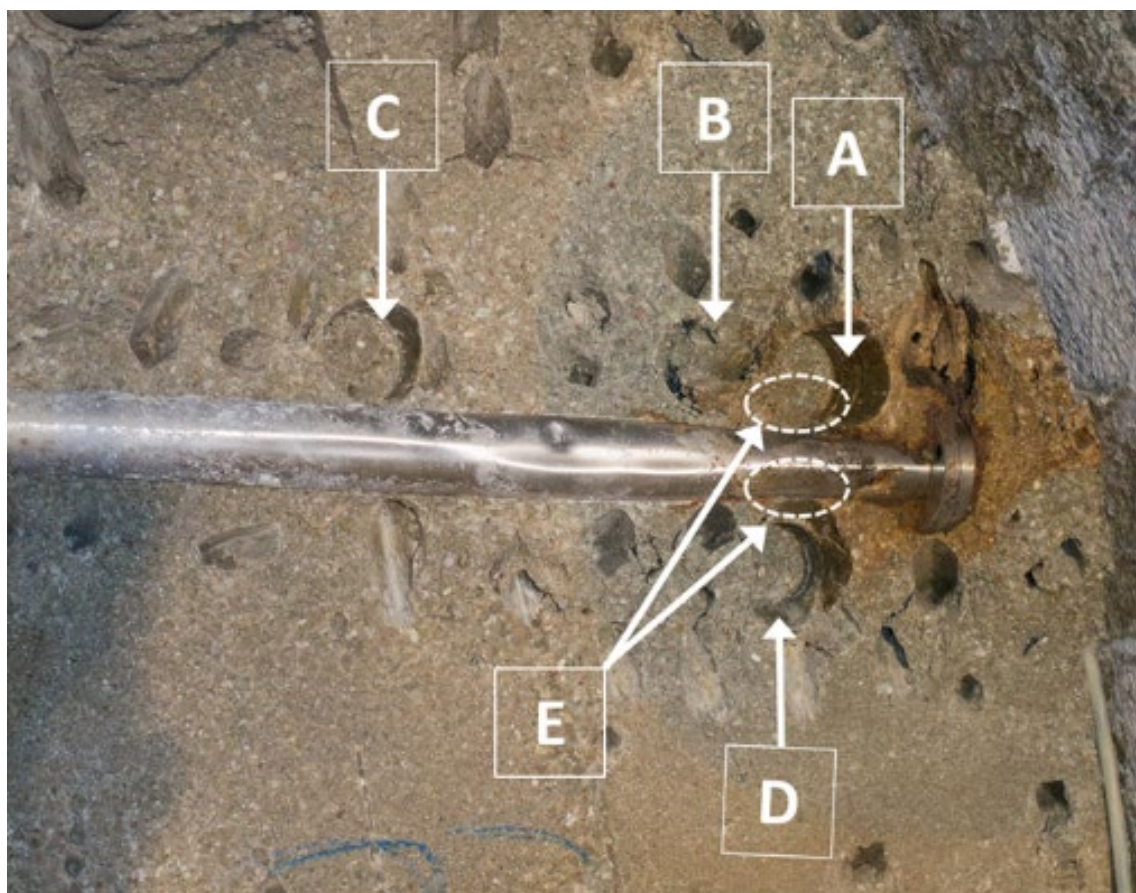


Fig. 129: Extensometer sample positions (Hadi 2016).

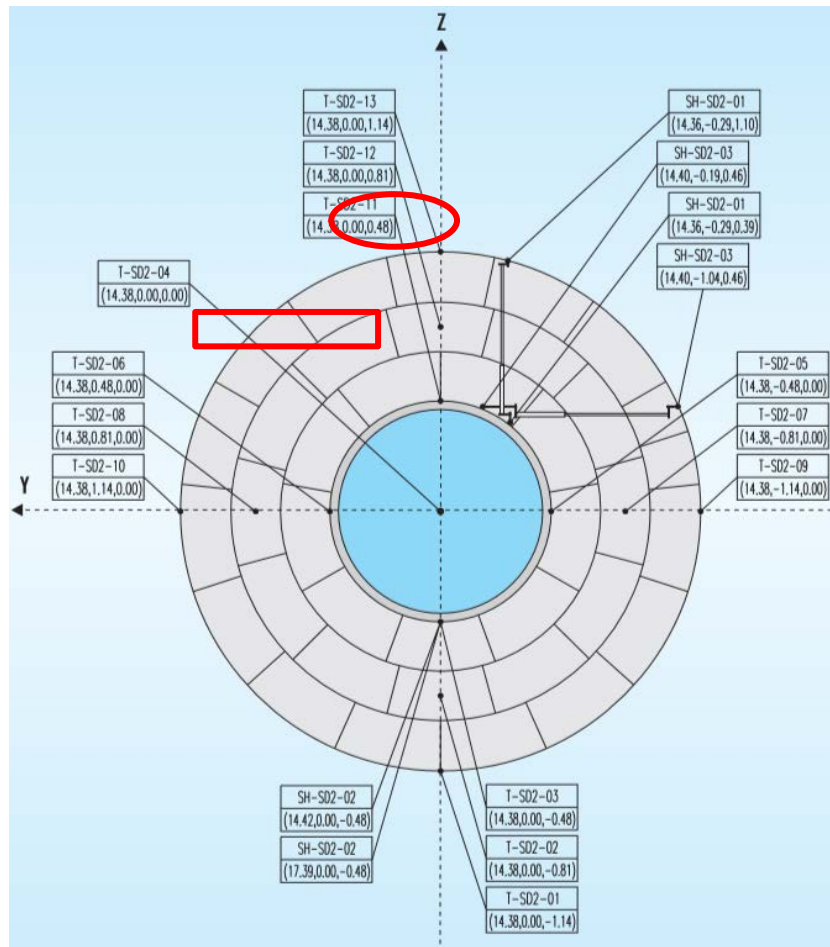


Fig. 130: Position of the sensor SH-S02-03, slice/layer 24 (NAB 16-11).

The core samples and their colouration at the time of sampling (Fig. 5) were as follows:

- S-S-54-15-A was collected in a "red" corroded zone.
- S-S-54-15-B was collected at the interface of the "blue" and "red" corroded areas.
- S-S-54-15-C was taken next to the corroded "blue" area but with normal grey bentonite colouration (characteristic of the FEBEX bentonite).
- S-S-54-15-D was taken from the interface of the "blue" and "red" corroded areas (similar to S-S-54-15-A/B).

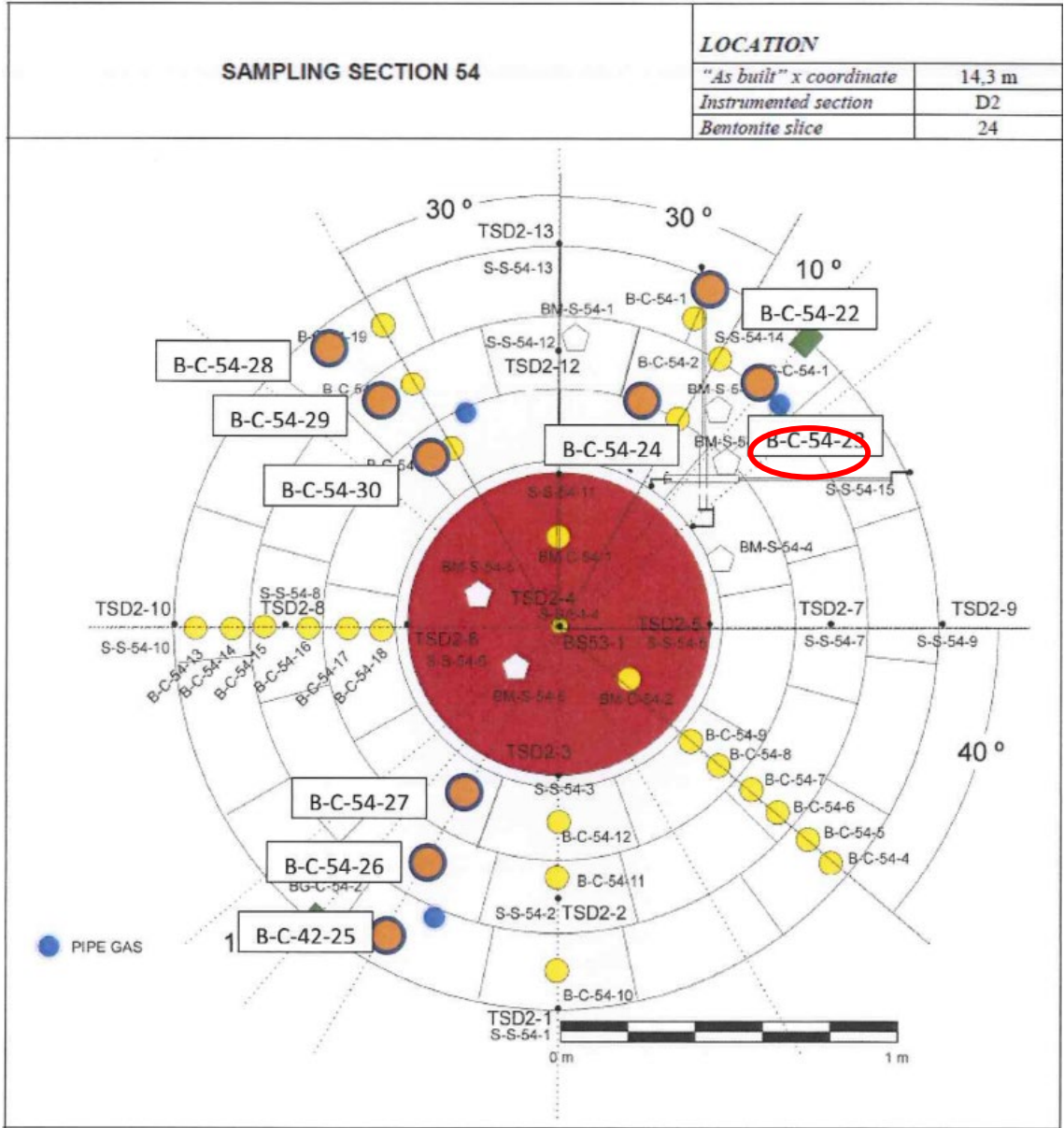


Fig. 131: Sampling Section 54, bentonite 24 slice (NAB 16-11).



Fig. 132: Sampling Section 54, bentonite slice 24 Heater No. 2 (NAB 16-11).

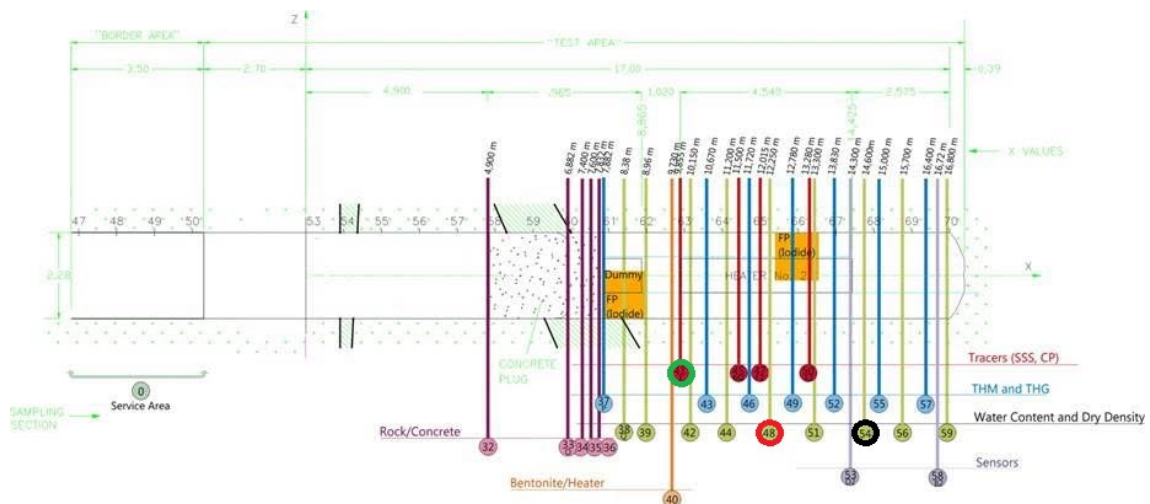


Fig. 133: Layout of sampling in Heater No. 2 (NAB 16-11) .

Sample **M-S-48-1** was collected following the protocol described in report NAB 16-11 (Nagra 2016), and is defined as a "metal coupon" or "corrosion probe". The coupons are different candidate wall metals for manufacturing the high activity containers and were included in the experiment to evaluate the bentonite behaviour when gradual corrosion of the metal occurs. During the experiment, four racks with metallic coupons (TStE355 Carbon Steel, AISI 316L austenitic stainless steel, titanium alloys grade 2, 7 and 12, and pure copper and cupronickel alloys) were installed (Fig. 134 and Fig. 135) into rectangular cavities around the liner margins and backfilled with powdered bentonite to seal them in place.

Sample M-S-48-1 was taken from Rack 1A, located in bentonite slice/layer 42 (also known as sampling Section 48) at a horizontal distance of 12.015 m into the backfill volume (Fig. 133 and Fig. 134). Sampling of M-S-48-1 was conducted on July 1, 2015.

It is noteworthy that a period of one month separated the excavation process and physical sample retrieval. Over this period, the inner liner and surrounding excavated face of bentonite were exposed to air, possibly resulting in chemical alteration of the outermost material, through drying, and/or corrosion.

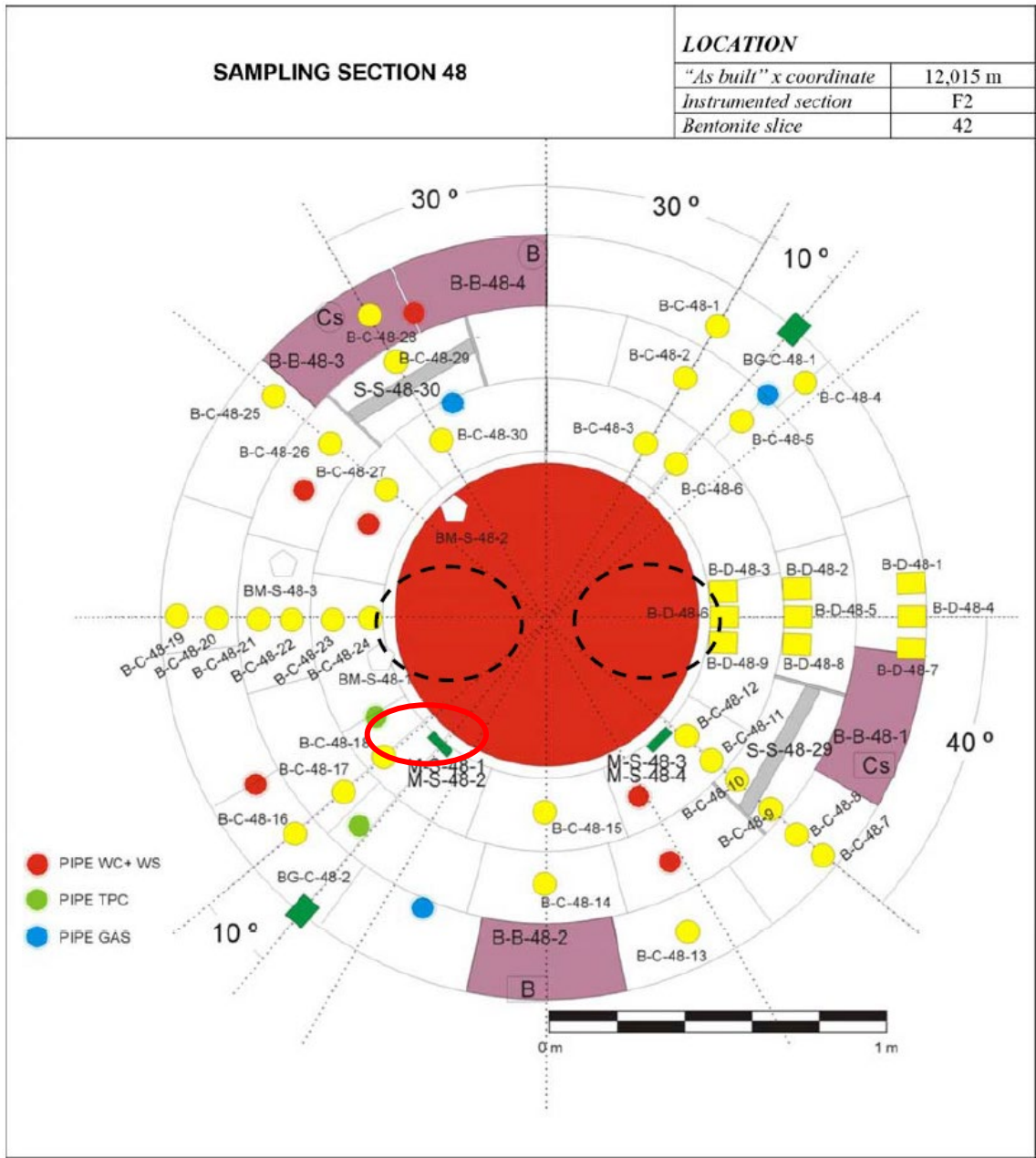


Fig. 134: Location of corrosion coupon, M-S-48-1, in sampling Section 48 (Bárcena & García-Siñeriz 2015a).



Fig. 135: M-S-48-1, metallic coupon or corroded probe (Nagra 2016).

The last sample analysed from FEBEX-DP was tagged as BM-B-41-1. This sample was collected following the protocol described in report NAB 16-11 (Nagra 2016) and the collection data is described in Tab. 50.

This sample was extracted from bentonite slice/layer 63, sampling Section 41 (Fig.136), at a horizontal distance of 9.450 m (Fig. 133). The sample was extracted close to the "liner" (Fig. 137 and 138), and belongs to a 20 kg block which was packaged within 20 minutes of extraction. Following the field sampling process, the sample was cut into 5 slabs, which involved a further 30 minutes' atmospheric exposure.

The guide tube or "liner" used in the experiment was a perforated steel tube, 970 mm in diameter and 15 mm thick. The liner was used to construct the storage receptacle and facilitate the insertion of the heat generating container in its experimental storage position. The liner was designed and constructed with 11 segments. Each segment was made of a conventional alloyed steel plate more typically used for boilers and pressure vessels (15 Mo 3 after DIN 17155) (Enresa 2006).

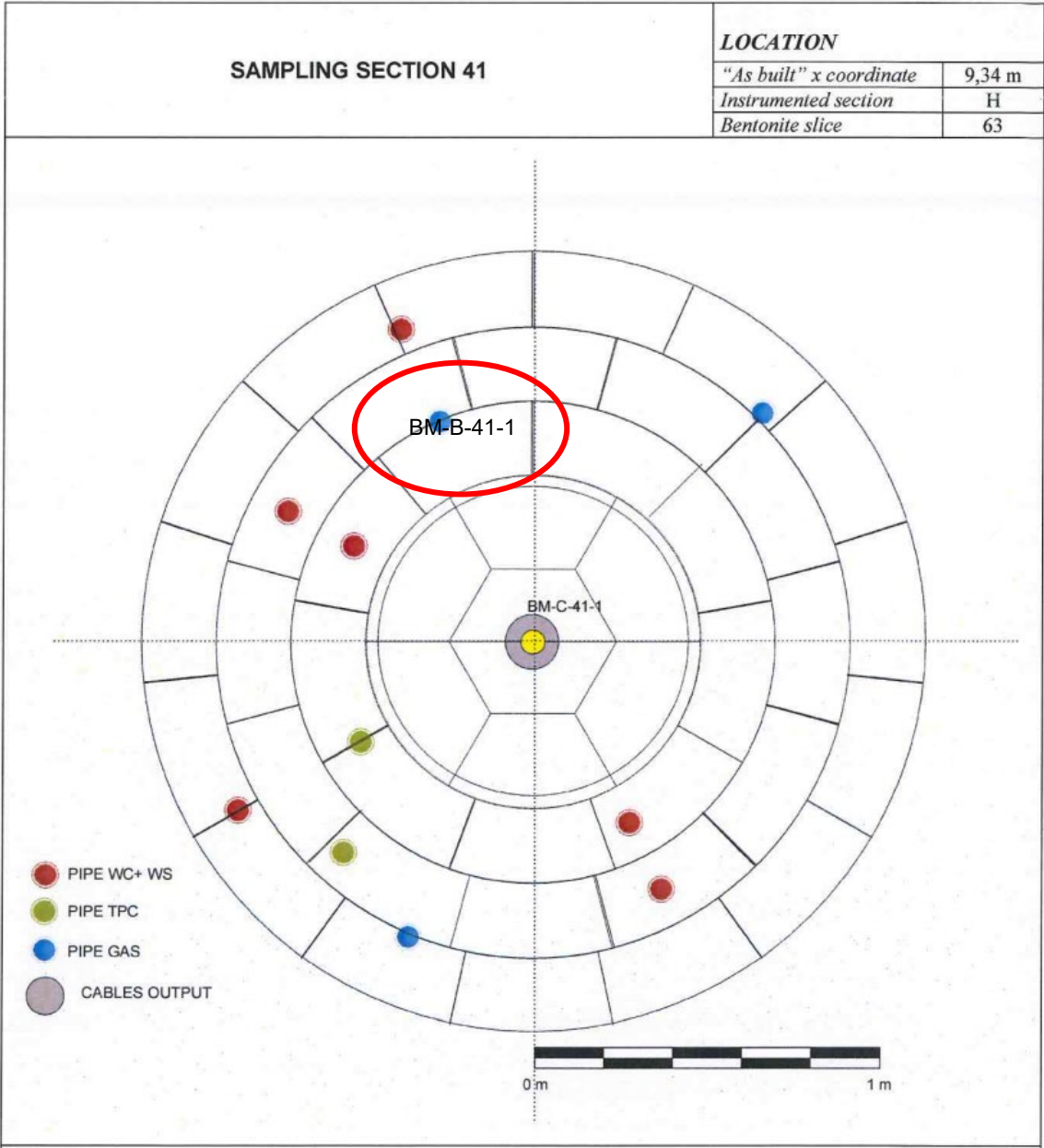


Fig. 136: Location of sample BM-B-41-1 (NAB 16-11).



Fig. 137: Sample BM-B-41-1. Detail of the aureoles formed as a consequence of corrosion close to the liner.

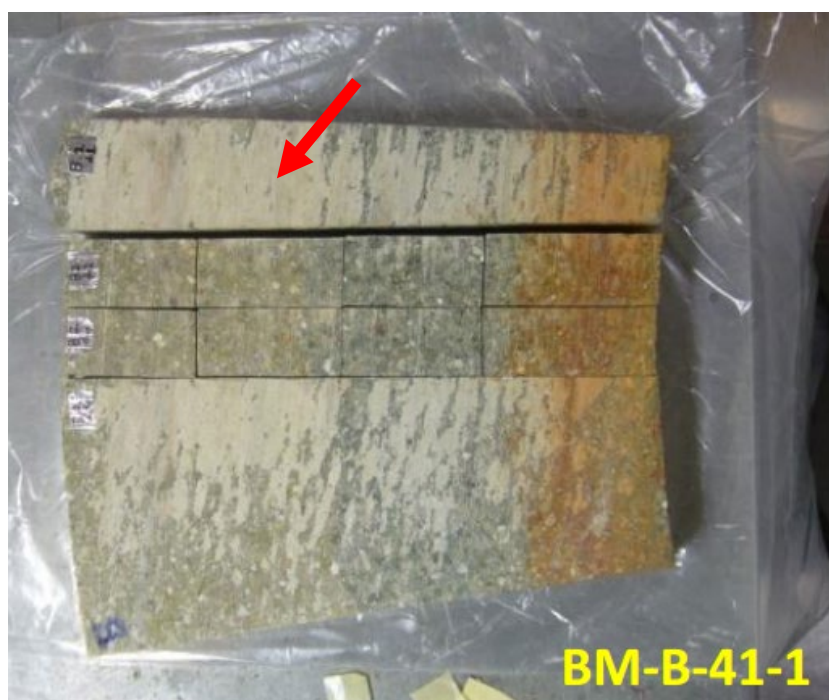


Fig. 138: Sample BM-B-41-1.

Tab. 50: BM-B-41-1 sample data collection.

Collection Data		
Date	29/05/2015	
Time	14:05	
Air Exposure Approximate Time (min)	10 min	
Temperature (°C)	13.5	
Humidity (%)	55	
Dimensions (cm)	Δx	13.5
	Δy	54
	Δz	22

Tab. 51: List of samples studied by the University of Bristol.

Sample Type	Sample Code	Sampling Section	Description
Bentonite (vicinity of sensor SH-SD2-03)	S-S-54-15-A	54	Bentonite samples taken near sensor SH-SD2-03 ("halo" zone).
	S-S-54-15-B	54	
	S-S-54-15-C	54	
	S-S-54-15-D	54	
	S-S-54-15-E	54	
Corrosion coupon probe	M-S-48-1	48	Coupon of TStE355 carbon steel. Candidate material placed in the bentonite barrier.
Bentonite (interface bentonite/liner)	BM-B-41-1	41	Bentonite in contact with the liner.

Analytical methods and work programme

The present chapter describes the analytical methods used to date, and further analytical methods that are planned to study the alteration induced by corrosion of metallic components in bentonite.

Bentonite Samples: S-S-54-15-A/B/C/D/E and BM-B-41-1

X-Ray Diffraction

One of the techniques commonly used for the analysis of clay minerals is X-Ray Diffraction (XRD). This analytical technique provides information about the mineralogical phases present in the bentonite samples from the FEBEX project. In the case of bentonites, it is necessary to examine both the bulk material to determine subsidiary mineral phases and the clay fraction isolated by sedimentation to determine the clay mineralogy of bentonite. Consequently, XRD analyses were performed on random powders samples and on oriented mounts.

1. Random powders

To minimise the air exposure, the samples were handled in a nitrogen-purged glove box (Saffron Scientific Equipment Ltd). Sample preparation was performed under an inert atmosphere to limit air exposure and, thereby, limit oxidative alteration of the materials. Each sample was analysed as rapidly as possible.

To analyse the bulk mineral composition of the samples, random powder XRD was performed. The powders were obtained by grinding 1 g of each sample in an agate mortar to a size less than 53 μm , to ensure that the grain size is less than 53 μm , each sample was sieved using a 53 μm nylon mesh. Through this sample preparation, the samples all have the crystals arranged in every possible crystallographic direction, so that there will always be a larger number of crystals non-oriented, and it is possible to identify maximum diffractions for a given group.

Random powder diffraction analysis allows the identification of bentonite minerals by their crystalline structure. This method is an indirect method to estimate the mineral composition of the analysed samples, with a good approximation of the major mineral phase content. As a first approximation, random powder diffraction allows the qualitative identification of bentonite bulk mineralogy.

Subsequently, a semi-quantitative analysis was performed, considering that the data obtained in the random powder diffraction should not be taken as an absolute value of quantity, only as relative indicators of concentration of each mineral. With the purpose of conducting this semi-quantitative analysis, the reflected powers method (Barahona 1974) was considered.

Randomly-oriented samples were measured using a Bruker D8 Advance diffractometer equipped with a $\text{CuK}\alpha$ X-ray source and energy dispersive Sol-X detector, operating at 40 kV and 40 mA. Scans were carried out over 2 to 65° in 2θ with a time step of 1s and a step size of 0.02°.

2. Oriented mounts

The morphology of clay minerals is mainly phyllosilicates with 00 l orientation. Random powder XRD for this group of minerals is not as conclusive and unequivocal as in many other groups, which do not present the preferred orientation evident in clay minerals. Therefore, it is essential to arrange a spatial mineral order. This additional arrangement for clay minerals is achieved by taking advantage of the fact that these minerals, due to their laminar structure, develop two-dimensional shapes which, through suitable preparation, can be arranged in parallel layers, "like the leaves of a book".

The oriented mounts aim to intensify the basal reflections of clay minerals present in bentonite. Oriented samples are meant to lay up phyllosilicates perpendicular to their c -axis by having them resting on their basal cleavages and crystal faces. Oriented samples intensify the diffraction peaks resulting from the d -spacing of these 00 l planes, making clay mineral identification more likely.

Bearing in mind, everything discussed in the previous paragraphs, to accomplish a semi-quantitative analysis of the bentonite samples, it is very important to separate the clay fraction ($< 2 \mu\text{m}$) from the bulk sample. Overall, the decantation technique is used to "force" the clay bentonite mineral particles to lie flat based on Stokes' law to achieve a separation of the fraction less than $2 \mu\text{m}$. To analyse the clay mineralogy in the oriented mounts, the following treatments were performed; air drying, solvation with ethylene glycol, and thermal treatment to 550°C . To perform oriented mounts preparation, we followed the description given by Moore & Reynolds (1997).

For each sample three oriented aggregates (OA) are prepared, which are allowed to air-dry. The first OA is analysed directly, the second OA is analysed once subjected to an ethylene glycol (EG) atmosphere at 60°C for at least 24 hours. Finally, the third OA is analysed once heated at 550°C for at least two hours. By comparing the three treatments obtained, the clay minerals are identified. Once the nature of each clay phases is known, such phases can be semi-quantified using a specific reflection for each of them and their reflective power.

Oriented mount samples were measured using a Bruker D8 Advance diffractometer equipped with a $\text{CuK}\alpha$ X-ray source and energy dispersive Sol-X detector, operating at 40 kV and 40 mA. Scans were carried out over 2 to 35° in 2θ with a time step of 1s and a step size of 0.02° .

Scanning Electron Microscopy/Energy Dispersive X-Ray Analysis (SEM/EDX)

Scanning electron microscopy (SEM) is used to define the microstructural morphology of the clay minerals, identify minor chemical elements and perform an analysis of iron diffusion through bentonite, as well as, possible alteration product formation as a result of contact with the metallic components, high temperatures and groundwater. However, the microscope resolution, specific sample preparation and aggregate nature of clays are insufficient to allow observation of individual clay mineral grains with this technique.

SEM/EDX analysis is performed using a Zeiss Sigma HD field emission SEM with EDAX EBSD and Octane Plus EDX. Backscattered electron and variable pressure detectors were used to optimise the data quality of the secondary electron images, backscatter electron images and EDX chemical analysis. A small piece ($0.5 \text{ cm} \times 0.5 \text{ cm}$) of each bulk sample will be gold-coated prior to SEM analysis to ensure that the samples are sufficiently conductive. The instrument was operated in high vacuum (HV).

One of the objectives of the investigation of alteration induced by corrosion in the FEBEX-DP components is to examine diffusion of the corrosion products released from the metallic components into the bentonite. Cross-sections of each samples were prepared. First, samples were ground in an agate mortar under an inert atmosphere (Saffron Scientific Equipment Ltd.). Afterwards, the samples were mounted in an aluminium ring and affixed using a mixture of epoxy and hardener. The samples were dried at least 24 hours, and subsequently each sample was polished until a sufficiently flat surface was achieved. Once the mounting sample process complete, each sample was coated with a film of a conductive material, carbon coating, to obtain better results. With the purpose of acquiring good results, SEM was operated under variable pressure mode (VP) to allow imaging with little charging of the sample. In addition, elemental analysis was obtained using the energy dispersive X-ray detector.

Transmission Electron Microscopy (TEM)

To perform the observation and analysis at the scale of an individual clay particle and thus possible alterations, Transmission Electron Microscopy (TEM) was used. To perform a single clay mineral observation, preparation requires that the grains must lie parallel to the surface preparation. The conventional method is to prepare a suspension and drop it on a TEM metal grid.

To accomplish this laboratory analysis, there are several methods of sample preparation. Specimens of bentonite clay grains for TEM analysis were prepared following the method described by Arroyo *et al.* 2016.

To avoid air exposure of the specimens, sample preparation was performed under an inert atmosphere within a nitrogen purged glove box (Saffron Scientific Equipment Ltd.). Up to 10 mg of each sample was used to prepare a suspension with an inorganic solvent 1 – 2 ml (ethanol or isopropanol), the purpose of which is to assure that the iron present in bentonite is not oxidized. Afterwards, the suspension was dispersed and then deposited onto a TEM metal grid. The metal grid was then covered with a fine formvar film.

Through this sample preparation the physical integrity of each specimen is degraded. Therefore, information about textural relationships is lost. However, this preparation method allows the analysis of a single grain and the determination of the iron present in each specimen and is commonly used to study the shape and morphology of clay mineral phases displayed in bentonite.

Fourier Transform Infrared Spectroscopy (FTIR)

Fourier Transform Infrared Spectroscopy (FTIR) is a suitable technique to investigate the chemistry and structure of compounds. Although, bentonite is chemically very complex. FTIR allows the comparison between samples. One key purpose of this technique is to study the corrosion evolution among the samples retrieved in the extensometer region (S-S-54-15-A/B/C/D/E) and the sample taken from contact with the liner (BM-B-41-1), as these samples were exhibited to different temperatures and groundwater conditions.

To perform this laboratory analysis, samples were prepared using the KBr pressed disc technique as described by Madejová (2003). This sampling method requires the pelletisation of the bentonite samples. As recommended two different sample/KBr ratios were used to press the pellets:

- 2 mg of sample and 200 mg of KBr to record optimal spectra in the region of 4'000 – 3'000 cm^{-1} .
- 0.6 mg of sample and 200 mg of KBr to record optimal spectra in the region 4'000 – 400 cm^{-1} .

Samples were ground in an agate mortar, under vacuum conditions (Saffron Scientific Equipment Ltd. glove box), and mixed with the KBr without pulverising the mixture. Afterwards, the mixture was pressed by applying a force between 6 – 8 tons for at least a minute.

The pressed pellets were heated in a furnace overnight at 150 °C to minimise the amount of the adsorbed water. The analysis was performed in the fraction around 53 μm . The exact amount of sample is recorded to enable comparison of samples with each other. When IR is used for quantification, the sample/KBr ratio in the pellet must be taken into account.

Mössbauer Spectroscopy

Although FTIR provided information about the amount of iron present in the octahedral sheets of bentonite in different samples, much more information about the iron oxidation state and identification of the type of coordination polyhedron occupied by iron atoms (tetrahedral and octahedral sheets) in bentonite can be achieved by Mössbauer Spectroscopy. Mössbauer Spectroscopy is a reliable technique for determining the oxidation state of iron present in bentonite. Iron is present in two oxidation states in bentonite, Fe^{2+} and/or Fe^{3+} . In addition, bentonite may contain other Fe-bearing mineral like pyrite (FeS_2) and iron oxides (hematite, Fe_2O_3) or oxyhydroxides (goethite, $\alpha\text{-FeOOH}$).

To prevent exposure of samples to air, samples were prepared and stored under vacuum conditions (Saffron Scientific Equipment Ltd. glove-box) until transferred to the Mössbauer instrument.

Each sample was ground in an agate mortar and spread across a sample holder with a diameter equal to that of the window in the detector. The amount of sample used affects the resultant spectrum. The known chemical composition of bentonite random powder XRD is used to estimate the amount of sample needed for the Mössbauer spectroscopy analysis.

Laser Raman Spectroscopy

Laser Raman Spectroscopy was performed on the S-S-54-15-A/B/C/D/E (extensometer samples) and BM-B-41-1 (liner sample) to identify the chemical composition and phases present in bentonite exposed to corroded metallic components.

To avoid specimen oxidation, sample preparation was done under vacuum conditions (Saffron Scientific Equipment Ltd. Glove box). Samples were ground in an agate mortar until they reached a grain size less than 53 μm . Subsequently, each sample was deposited in a specially

manufactured glass holder and vacuum-sealed by using an epoxy resin to avoid any oxygen exposure.

Raman spectra were obtained using a Renishaw Ramanscope Spectrometer model 2000. The system was equipped with He-Ne and Ar⁺ lasers (20 mV) with an excitation wavelength of 543.365 nm (green) which was focused on each powdered surface sample as the Raman signal was collected in reflection mode. Each analysis was performed by focusing the laser with objective magnification 50x onto the sample surface through a Leica Optical microscope, corresponding to a laser spot diameter of about 4 µm. Spectra were measured in Raman shift intervals of 100 – 1700 cm⁻¹ with an acquisition time for each step of 10s with laser power of 4 mW.

Exchangeable Cations and Cation Exchange Capacity (CEC)

The sample extraction was performed in a glove box, in an inert atmosphere (Saffron Scientific Equipment Ltd) with an oxygen concentration around 2 ppm. The reagent solutions were prepared using deionised water.

The CEC was measured following the method by Meier & Kahr method (1999). 200 mg of sample was dispersed in 35 ml of distilled water by ultrasonic treatment and 10 ml of 0.10 M Cu(II)-triethylenetetramine (Cu-tri) was added to the suspension, which is left to react. After 1 hour of centrifugation (15'000 rpm during 20 min), 3 mL of the supernatant was extracted and the absorbance at 620 nm of all supernatant solutions was measured in a spectrophotometer. The CEC (cmol+/kg dry weight) was calculated from the total Cu loss in the supernatant.

The exchangeable cation analysis was performed by using the Sawhney (1970) method. 5 g of the bulk sample was dispersed in 40 ml of 0.5 N CsNO₃ which was stirred for 24 hour. After 1 hour of centrifugation (15'000 rpm during 20 min), the supernatant was extracted and filtered by 0.45 µm. The exchangeable cations were then measured by ionic chromatography.

Metal coupons sample: M-S-48-1 (Tab. 53)

Scanning Electron Microscopy/Energy Dispersive X-Ray Analysis (SEM/EDX)

Corrosion analysis of the metallic coupon sample using SEM/EDX was performed on a Zeiss Sigma HD VP Field Emission SEM with EDAX EBS AND Octane Plus EDX, with backscattered electron and variable pressure detectors. The goal of this analysis was to determine the extent of the corroded surfaces in the metallic coupon and identifying the nature of corrosion products released.

X-Ray Diffraction

The corrosion products raised from the metallic coupons (TStE355 carbon steel) was also analysed using X-ray diffraction (XDR).

Each sample was examined with a Philips model X'PERT diffractometer, using a CuKα anode. Scans were carried out over 20 to 90° in 2θ with a time step of 20s per point and a step size of 0.02°.

Laser Raman Spectroscopy

Laser Raman Spectroscopy was undertaken for the corrosion products on each metallic coupon. Raman spectroscopy is an optical technique through which chemical and specific phase information can be achieved non-destructively. After removal and visual inspection of each metallic coupon from the Rack 1A, no sample preparation was required. The positions of the bands and the intensity in Laser Raman spectra depend on the crystal phase and chemical composition of the samples.

Raman spectra were obtained using a Renishaw Ramanscope Spectrometer model 2000. The system was equipped with a He-Ne and Ar⁺ lasers (20 mV) with an excitation wavelength of 543.365 nm (green) which was focused on each powdered surface sample, with the Raman signal collected in reflection mode. Each analysis was performed by focusing the laser with an objective magnification 50x onto the sample surface through a Leica Optical microscope, corresponding to a laser spot diameter of about 4 µm. Spectra were measured in Raman shift intervals of 100 – 1700 cm⁻¹ with an acquisition time for each step of 10s with laser power of 4 mW.

4.8.3 Results

The present chapter describes the results obtained to date.

FEBEX DP Bentonite Samples: S-S-54-15-A/B/C/D/E and BM-B-41-1.

Visual inspection

Bentonite samples S-S-54-15-A/B/C/D/E (close to the extensometer SH-SD2-03) and BM-B-41-1 (in contact with the liner) were examined visually. Bentonite samples were received packaged inside an aluminium sealed pouch. The visual examination of each sample was performed in an inert atmosphere (Saffron Scientific Equipment Ltd. glove box) to minimise air exposure.

Fig. 139 shows the external appearance of bentonite samples retrieved near extensometer SH-SD2-03. Samples B/C/D, as described in the report from the University of Bern (Hadi 2016), display a "blue colouration" associated with a corroded blue area. Sample A shows a "red colouration" which correlates with the description in the same report of a red corroded area. Finally, sample E consists of separate pieces of bentonite showing different colourations from reddish to dark brown.

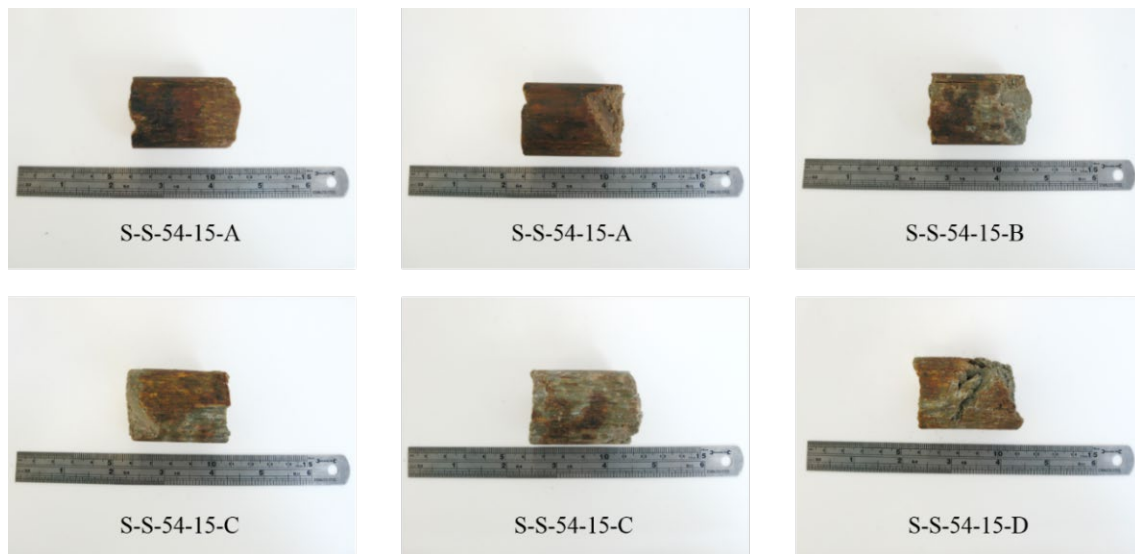


Fig. 139: External appearance of the samples retrieved in the vicinity of extensometer SH-SD2-03.

Fig. 140 presents the external appearance of bentonite sample BM-B-41-1 when received at the University of Bristol. Overall, the samples show different colouration areas that have been labelled/named as Area "A", "B" and "C". Area "A" was in direct contact with the liner and exhibits a reddish colouration. Area "B" displays a blue-greenish colouration. Finally, Area "C" shows a greyish-green colouration closer to the greyish colour characteristic of the FEBEX bentonite.

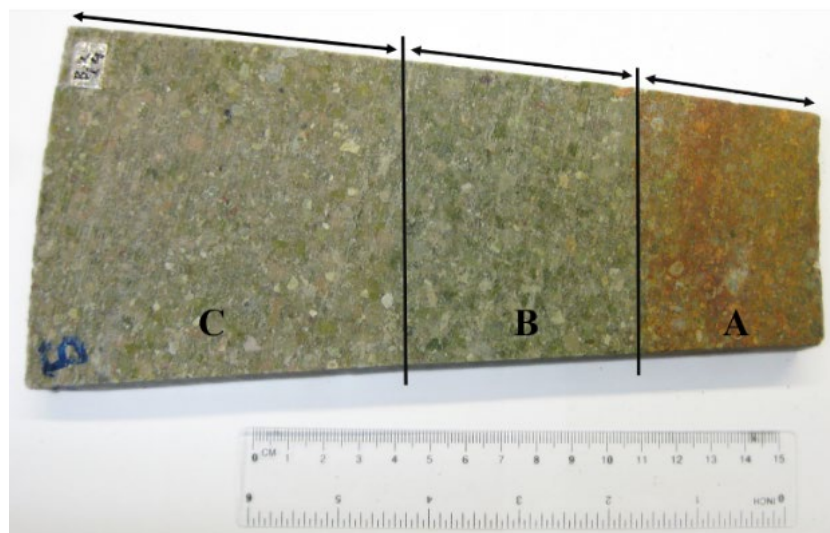


Fig. 140: External appearance of sample BM-B-41-1.

X-Ray Diffraction

XRD patterns were obtained in random powder and in oriented aggregates (OA) prepared from subsamples of each sample, and from the untreated FEBEX bentonite. Random powder diffraction analysis was performed in order to identify the minerals in each bentonite sample as a qualitative prior identification of the bentonite's bulk mineralogy.

In view of the mineralogy of the samples no differences between the untreated bentonite and the bentonite samples analysed from the FEBEX-DP was found (Fig. 141 and Tab. 52). The mineral phases observed in the XRD diffractograms were similar to those observed in the untreated sample.

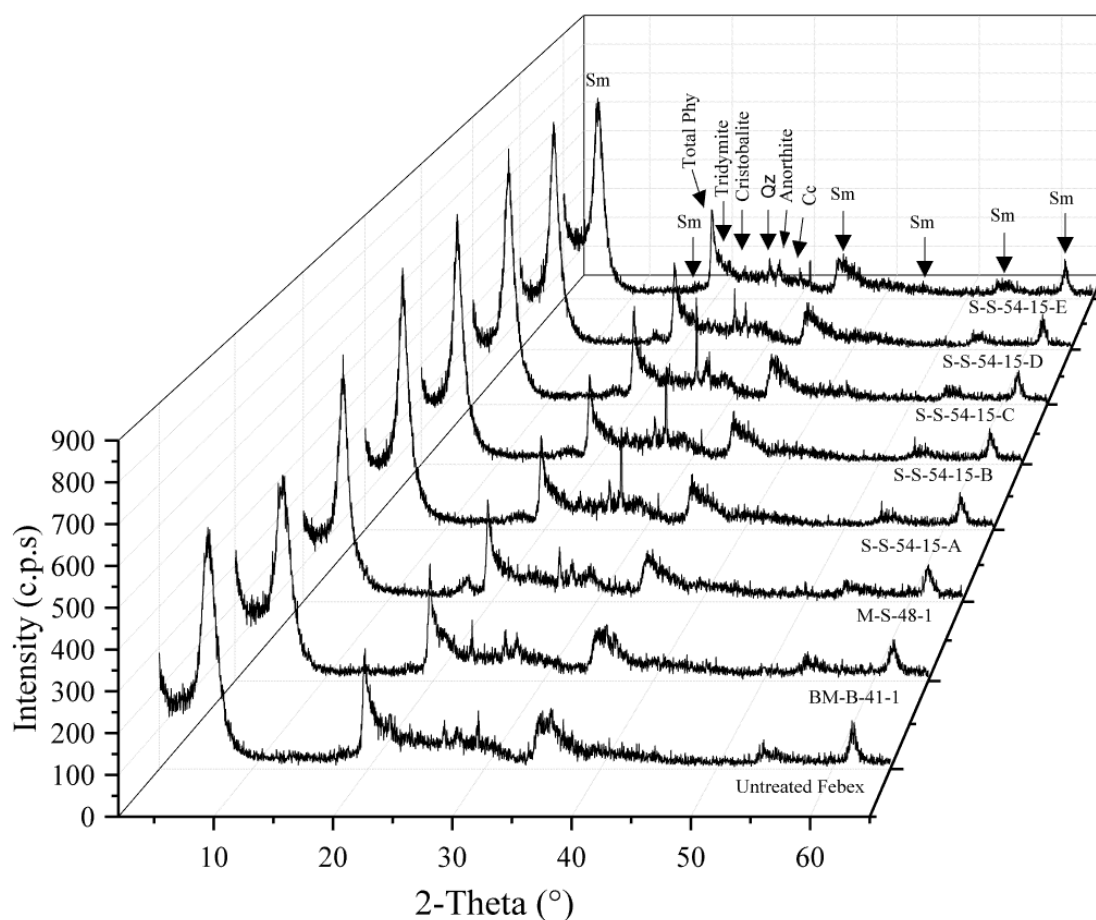


Fig. 141: XRD-Patterns of random powder samples of bentonite samples from FEBEX-DP (Sm: Smectite, Total Phy: Total Phyllosilicates, Qz: Quartz, Cc: Calcite).

Tab. 52: Main and accessory minerals in the FEBEX-DP samples.

Mineral Name	Untreated FEBEX (%)	BM-B-41-1 (%)	M-S-48-1 (%)	S-S-54-15-A (%)	S-S-54-15-B (%)	S-S-54-15-C (%)	S-S-54-15-D (%)	S-S-54-15-E (%)
Quartz	2	2	2	3	4	2	3	1
Tridymite	4	6	3	5	6	3	4	4
Phyllosilicates	88	86	87	87	85	87	84	86
Calcite	-	Traces	1	Traces	Traces	Traces	Traces	Traces
Plagioclase (Albite/Anorthite)	3	5	7	6	5	8	9	8
Cristobalite	1	1	Traces	Traces	Traces	Traces	Traces	1

From the clay mineralogy perspective, no observable dissimilarities between the untreated material and the samples were found (Fig. 142 and Fig. 143). Based on XRD and the positions ($\text{CuK}\alpha$) of the 001/002 and 002/003 reflections (Moore & Reynolds 1989), the smectitic phases of the FEBEX bentonite are actually made up of illite-smectite mixed layers (Cuadros & Linares 1996), with $\sim 10\%$ of illite layers (001/002: 10.45° , 002/003: 15.95° and full-size image $\Delta 2\theta = 5.50$). Small peaks of mica (illite) and kaolinite are observed but were not quantifiable ($< 1\%$ in both cases). In addition, the untreated bentonite and the samples from the FEBEX-DP contain variable quantities of quartz, plagioclase, cristobalite, calcite and tridymite.

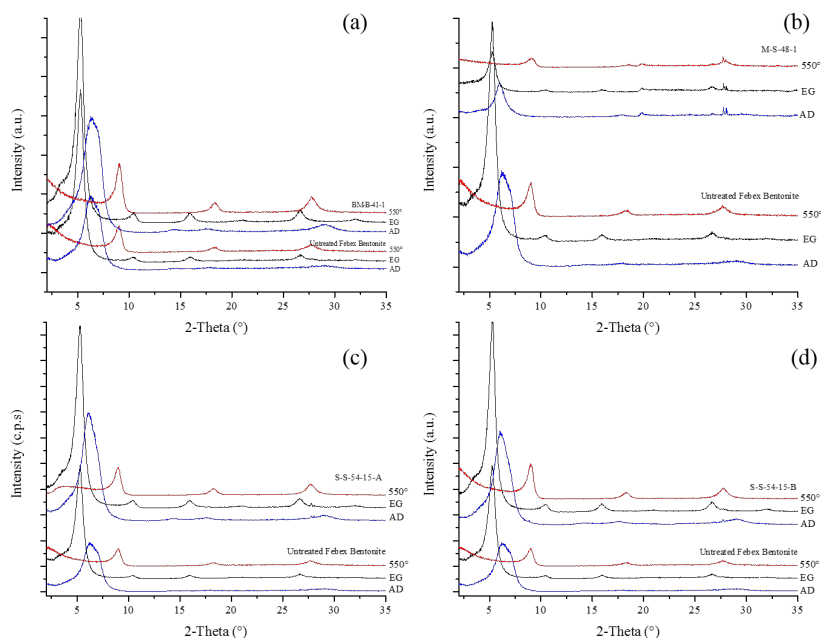


Fig. 142: XRD patterns of oriented aggregates bentonite samples from FEBEX-DP. (a) BM-B-41-1, (b) M-S-48-1, (c) S-S-54-15-A, (d) S-S-54-15-B (EG: Ethylene Glycol, AD: Air Dried).

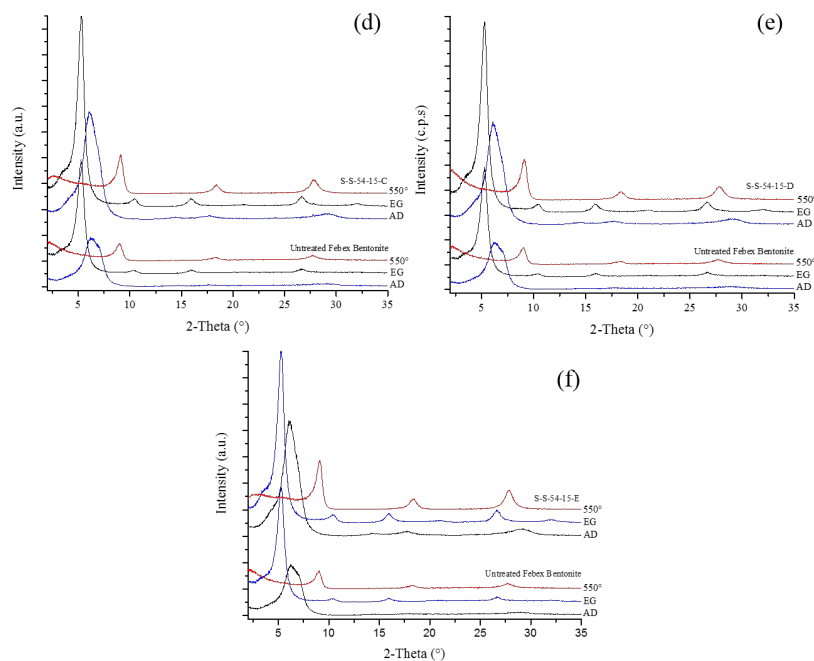


Fig. 143: XRD patterns of oriented aggregates bentonite samples from FEBEX-DP. (d) S-S-54-15-C, (e) S-S-54-15-D, (f) S-S-54-15-E (EG: Ethylene Glycol, AD: Air-Dried).

FEBEX DP corrosion coupons samples: Rack 14: TStE355 carbon steel

The corrosion coupons studied, consist of a series of rectangular coupons manufactured from TStE355 carbon steel. The coupons were designed with a hole in the upper part so they could be mounted together (Fig. 144). Each coupon was placed on Teflon supports at both ends and are separated by Teflon spacers which held each carbon steel piece.

Rack 1A contains: two base coupons, one coupon welded by Electron Beam Welding (EBW), one coupon welded by Plasma Arc Welding (PAW) and one coupon welded by Metal Active Gas Welding (MAGW) (Fig. 144). Each coupon was classified at reception as follows (Tab. 6): two base material coupons identified as 1A1 and 1A2 and three test coupons with welded joints identified as following: 1A3, 1A4 and 1A5. Fig. 145 displays the overall appearance of the Rack 1A.

Tab. 53: Properties metallic coupon sample, M-S-48-1 (Hadi & Wersin 2015).

Rack	Material	Type of coupon (and quantity)				Total
		Base (2)	EBW (1)*	PAW (1)**	MAGW (1)***	
1A	Carbon steel TStE355	Base (2)	EBW (1)*	PAW (1)**	MAGW (1)***	5

* Electro Beam Welding
** Plasma Arc Welding
*** Metal Active Gas Welding.

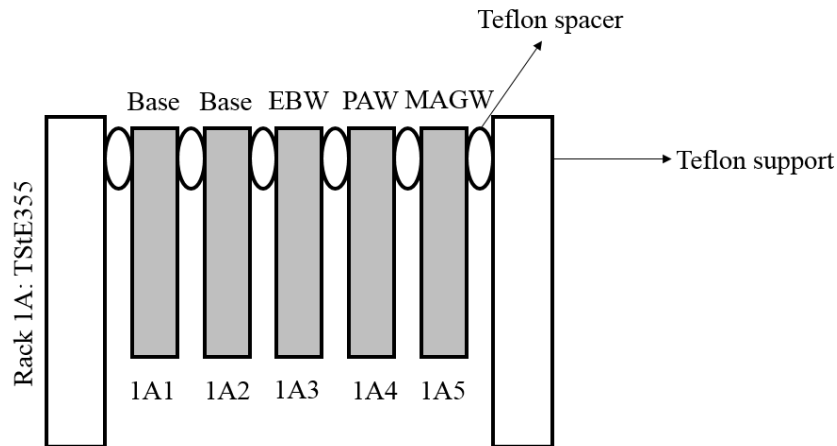


Fig. 144: Outline appearance of the corrosion coupon.



Fig. 145: Appearance of the Rack 1A on reception.

The corrosion coupon sample was received in an aluminium sealed pouch which in turn was sealed inside of two plastic pouches. The dismantling of the rack and the separation of each coupon was performed in a nitrogen purged glove box (Saffron Scientific Equipment Ltd. glove box) to keep air exposure to a minimum. Once the sample was open the bentonite powder remaining in the last plastic pouch was collected to perform the corresponding analysis. The bentonite powder collected is characterised by a high reddish colouration.

After each coupon separation, the weight and dimensions were measured Tab. 54.

Tab. 54: Dimensions and weight coupons belonging to the Rack 1A.

Rack	Coupons	Size	Weight (g)
1A. TStE 355 Carbon steel	1A1 Base	50 mm × 20 mm × 0.5 mm	34.1855
	1A2 Base	50 mm × 20 mm × 0.5 mm	34.3907
	1A3 EBW	50 mm × 20 mm × 0.5 mm	30.5722
	1A4 PAW	50 mm × 20 mm × 0.5 mm	31.1425
	1A5 MAGW	50 mm × 20 mm × 0.5 mm	33.4700

Visual inspection

Summarising, all the coupons were covered with rust and it was possible to distinguish different colouration types, the surface of each coupon showed black-reddish colouration, with greenish areas blended with the bentonite remaining on each coupon. Moreover, some coupons displayed bentonite adhered with a reddish colouration and a lesser degree of humidity than observed in samples S-S-54-15-A/B/C/D/E and BM-B-41-1.

Corrosion damage in the coupons, presented as general corrosion, was observed in all five carbon steel coupons (Fig. 146 to Fig. 150). In addition, the five coupons displayed areas of corrosion penetration; cracking was also seen.

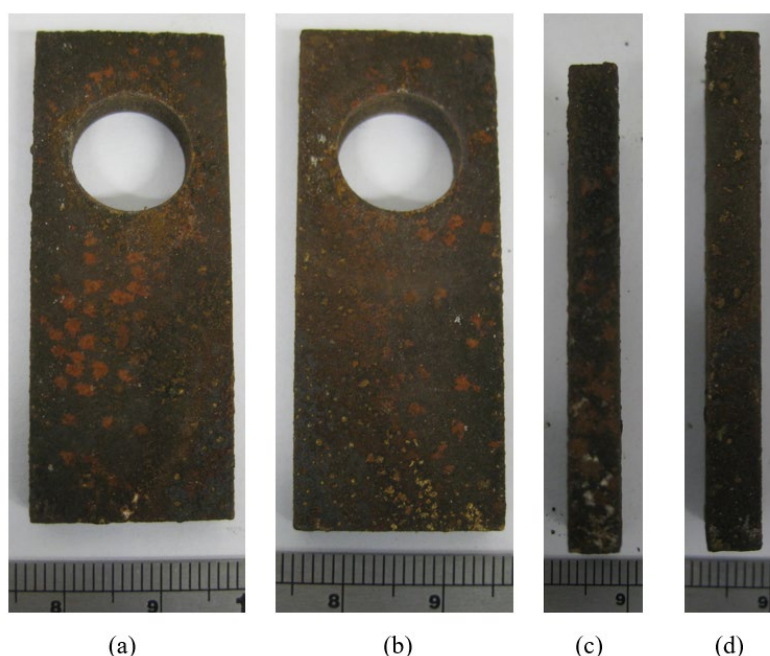


Fig. 146: Photographs of corrosion on the coupon 1A1 (base 1).

(a) Corrosion present on side "a", (b) Corrosion present on side "b", (c) and (d) Corrosion present on the lateral sides of the sample.

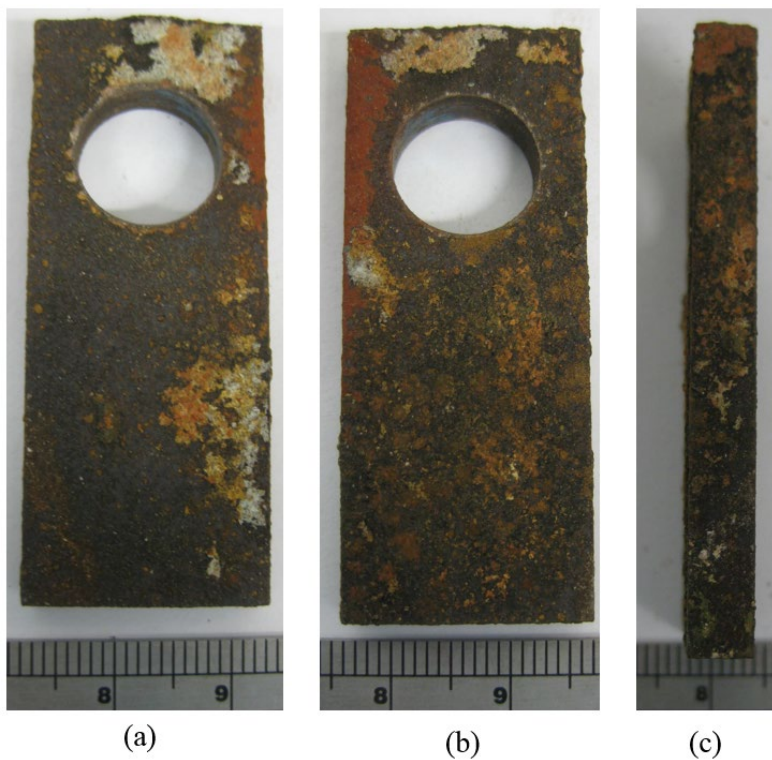


Fig. 147: Photographs of corrosion on the coupon 1A2 (base 2).

(a) Corrosion present on side "a", (b) Corrosion present on side "b", (c) and (d) Corrosion present on the lateral sides of the sample.

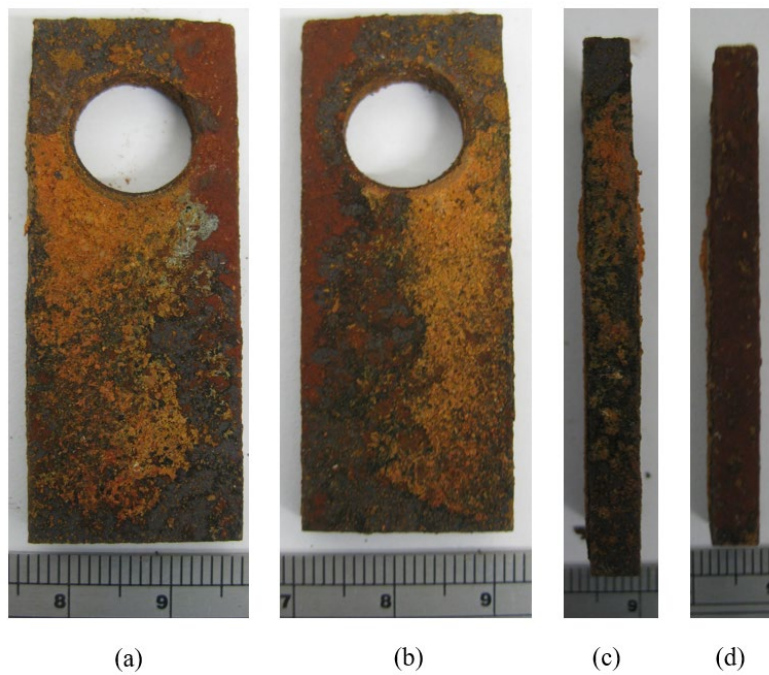


Fig. 148: Photographs of corrosion on the coupon 1A3 (EBW).

(a) Corrosion present on side "a", (b) Corrosion present on side "b", (c) and (d) Corrosion present on the lateral sides of the sample.

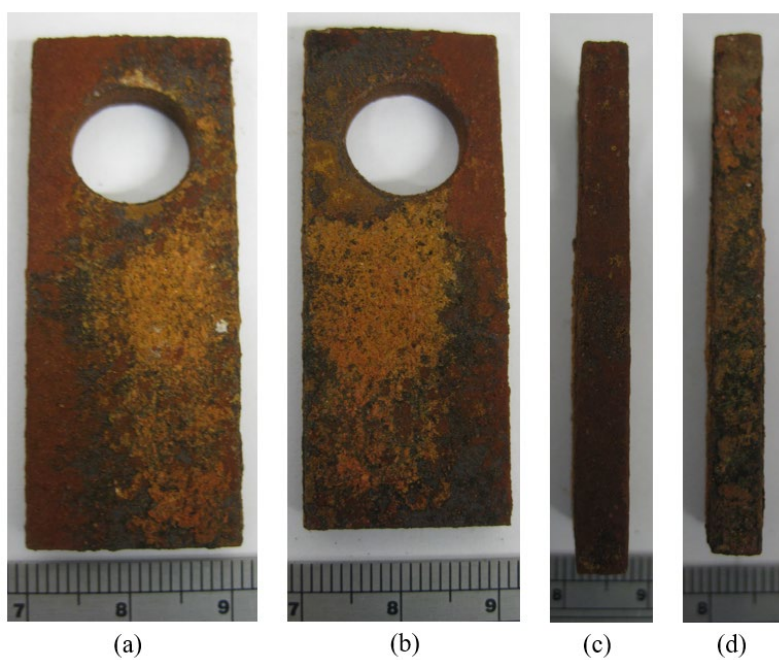


Fig. 149: Photographs of corrosion on the coupon 1A4 (PAW).
(a) Corrosion present on side "a", (b) Corrosion present on side "b", (c) and (d) Corrosion present on the lateral sides of the sample.

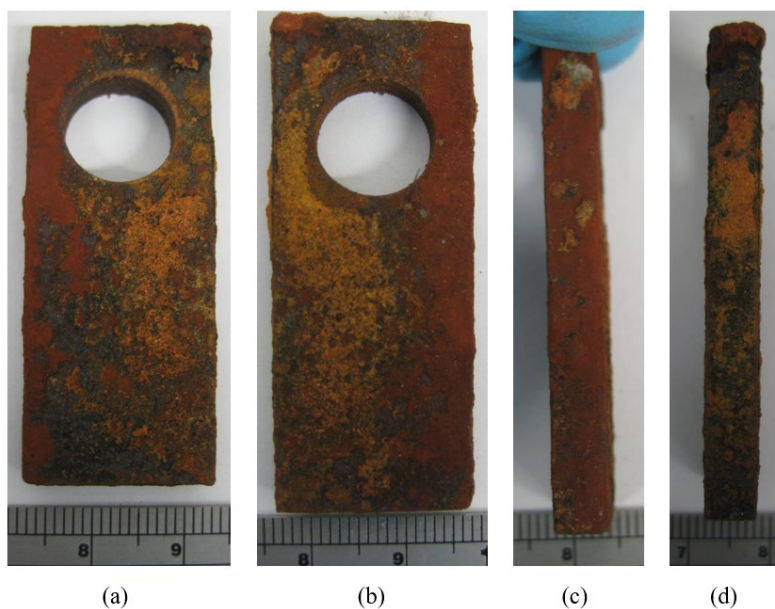


Fig. 150: Photographs of corrosion on the coupon 1A5 (MAGW).
(a) Corrosion present on side "a", (b) Corrosion present on side "b", (c) and (d) Corrosion present on the lateral sides of the sample.

Corrosion Products Analysis: Raman and SEM/EDX analysis

SEM micrographs were taken of each sample to obtain general information about the corrosion in the coupons. The corrosion products released from the carbon steel TSt355 were analysed by EDX. The analyses were performed once the samples were opened in an inert atmosphere and the bentonite remaining in the package was collected.

EDX analysis indicated that the surface of each coupon is composed principally of iron and oxygen. Chloride is also present on the surface of the five coupons examined. Silicon, aluminium, magnesium, calcium, sodium and traces of potassium were also detected on each coupon surface which is attributed to adhered bentonite.

EDX spectra from the carbon steel coupons, Fig. 151 to Fig. 155, shows a surface layer mostly enriched by oxygen and iron. The EDX analysis conducted on the surface of each coupon showed the presence of chlorine, in all the obtained spectra, and this peak is very predominant on some occasions. The spectra also showed the presence of manganese and traces of nickel.

Tab. 55 lists the semi-quantitative results of the minor elements, obtained by EDX analysis, present in the carbon steel coupons.

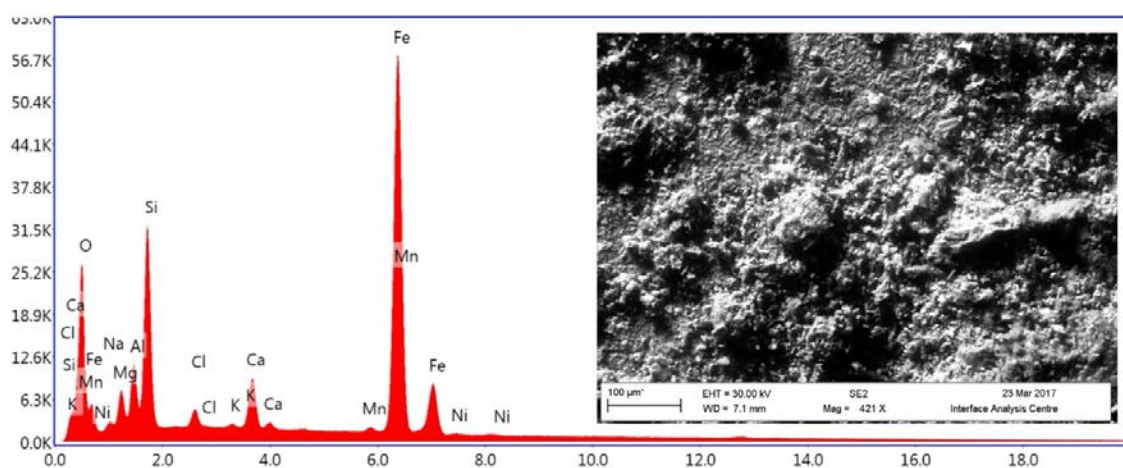


Fig. 151: Micrograph of Coupon 1A1 (base 1) surface, and its corresponding EDX spectrum.

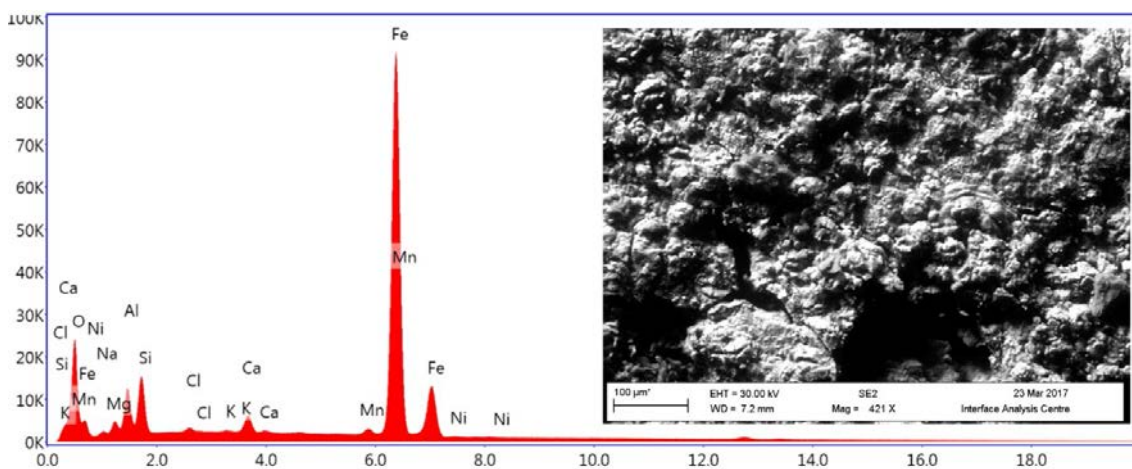


Fig. 152: Micrograph of Coupon 1A2 (base 2) surface, and its corresponding EDX spectrum.

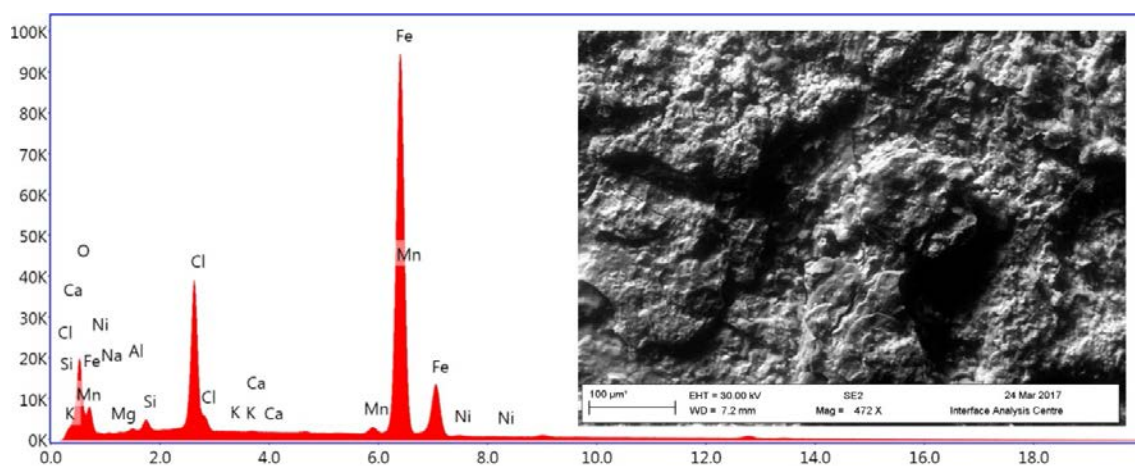


Fig. 153: Micrograph of Coupon 1A3 (EBW) surface, and its corresponding EDX spectrum. Cracking is apparent.

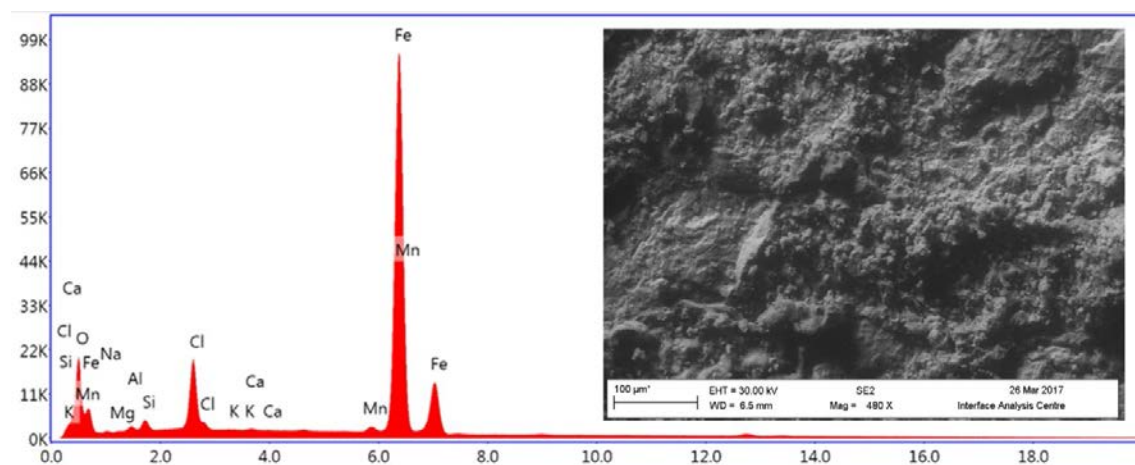


Fig. 154: Micrograph of Coupon 1A4 (PAW) surface, and its corresponding EDX spectrum.

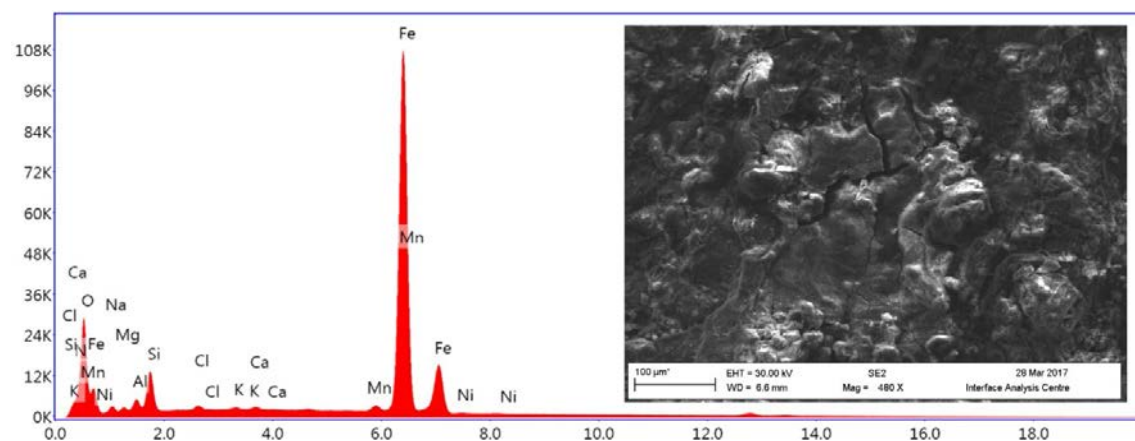


Fig. 155: Micrograph of Coupon 1A5 (MAGW) surface, and its corresponding EDX spectrum. Cracking is apparent.

Tab. 55: Semi-quantitative analyses of Coupons 1A1-1A5 from Fig. 27 – 31.

	O (%)	Na (%)	Mg (%)	Al (%)	Si (%)	Cl (%)	K (%)	Ca (%)	Mn (%)	Fe (%)	Ni (%)
1A1	36.07	4.93	5.2	5.7	13	0.79	0.16	2.37	0.31	31.44	0.02
1A2	26.78	5.95	2.42	4.74	2.78	0.26	0.04	0.77	0.8	55.28	0.17
1A3	25.9	0	0.83	0.08	0.34	13.22	0.06	0.25	1.32	58.13	0.11
1A4	20.28	0.8	0	0.36	0.58	5.27	0	0.21	1.48	71.02	0
1A5	32.3	4.78	1.35	1.6	3.28	0.16	0.16	0.24	0.86	55.1	0.18

In order to obtain more information about the corrosion of the coupons, optical micrographs and Raman spectra were collected and are presented in Fig. 156 to Fig. 158. To accomplish the stoichiometric characterisation of the corrosion products generated, Raman spectroscopy was performed using a 543.365 nm laser. Information about the chemical composition and phases present was obtained and is exposed in the figures below.

Fig. 156 revealed a well-resolved band position at $\sim 1087 \text{ cm}^{-1}$ which corresponds to the presence of calcite. The spectra also display the following bands corresponding to the presence of siderite (FeCO_3), hematite ($\alpha\text{-Fe}_2\text{O}_3$) and magnetite (Fe_3O_4); $\sim 184 \text{ cm}^{-1}$, at $\sim 223 \text{ cm}^{-1}$, $\sim 290 \text{ cm}^{-1}$, $\sim 409 \text{ cm}^{-1}$, $\sim 609 \text{ cm}^{-1}$ and $\sim 1'319 \text{ cm}^{-1}$.

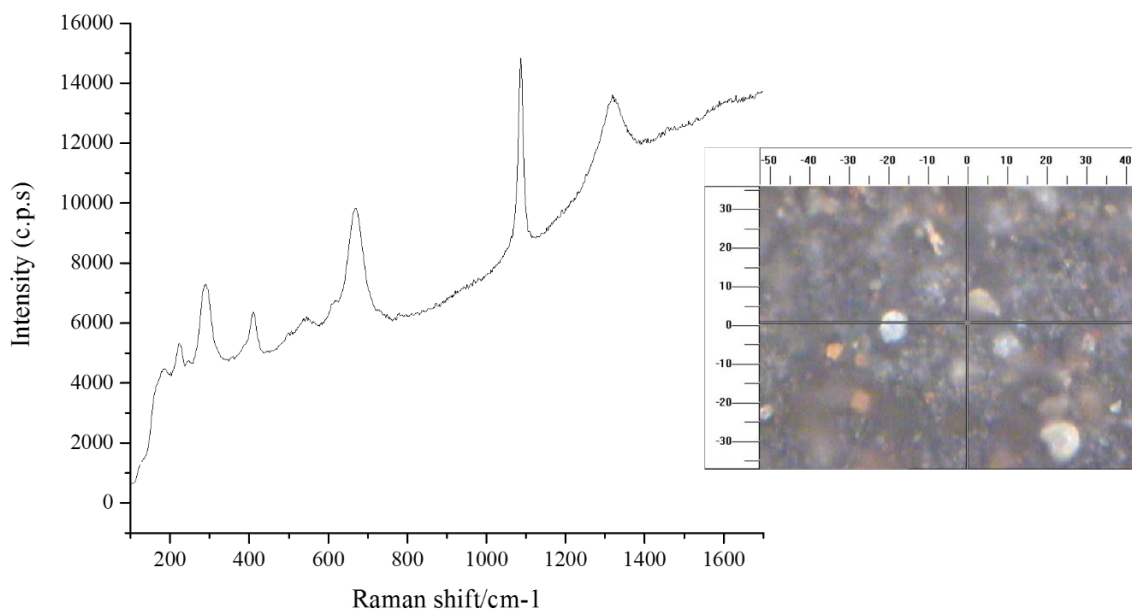


Fig. 156: Optical micrograph of corrosion coupon showing the location from where the Raman spectrum was collected, and Raman surface spectrum.

Fig. 157 shows the presence of hematite ($\alpha\text{-Fe}_2\text{O}_3$) bands at $\sim 223 \text{ cm}^{-1}$, $\sim 290 \text{ cm}^{-1}$ and $\sim 407 \text{ cm}^{-1}$ and magnetite at $\sim 1'319 \text{ cm}^{-1}$. The spectrum also reports a well resolved calcite band at $\sim 1'087 \text{ cm}^{-1}$.

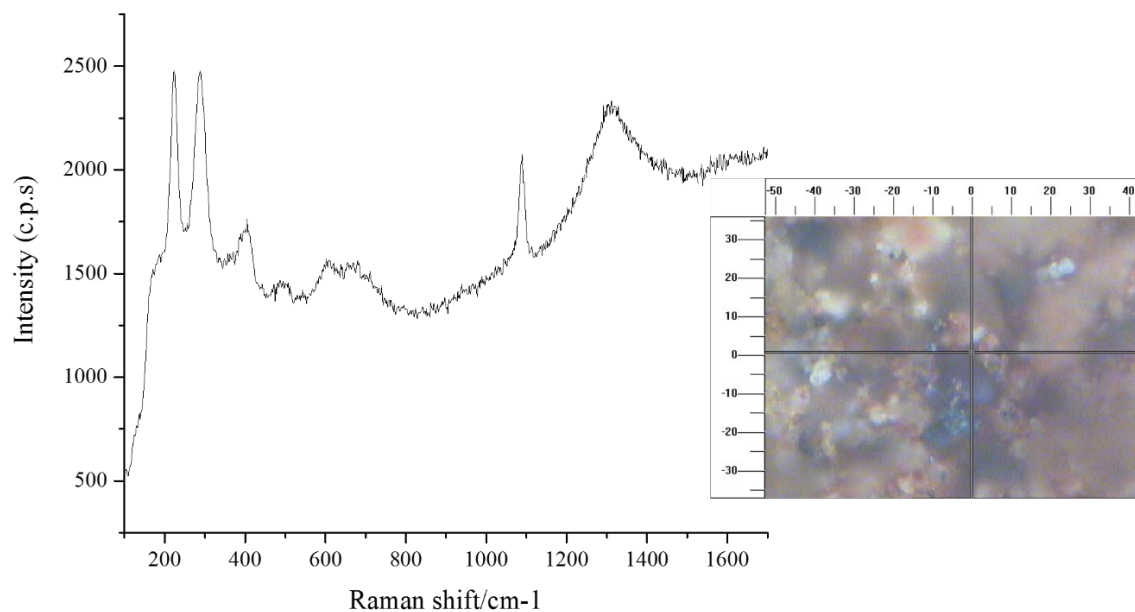


Fig. 157: Optical micrograph of corrosion coupon showing the location from where the Raman spectrum was collected, and Raman surface spectrum.

Fig. 158 exhibits the presence of hematite ($\alpha\text{-Fe}_2\text{O}_3$) bands at $\sim 220\text{ cm}^{-1}$, $\sim 290\text{ cm}^{-1}$ and $\sim 409\text{ cm}^{-1}$ and $\sim 609\text{ cm}^{-1}$ and magnetite at $\sim 667\text{ cm}^{-1}$ and $\sim 1319\text{ cm}^{-1}$. The spectra also show a well-resolved calcite band at $\sim 1087\text{ cm}^{-1}$.

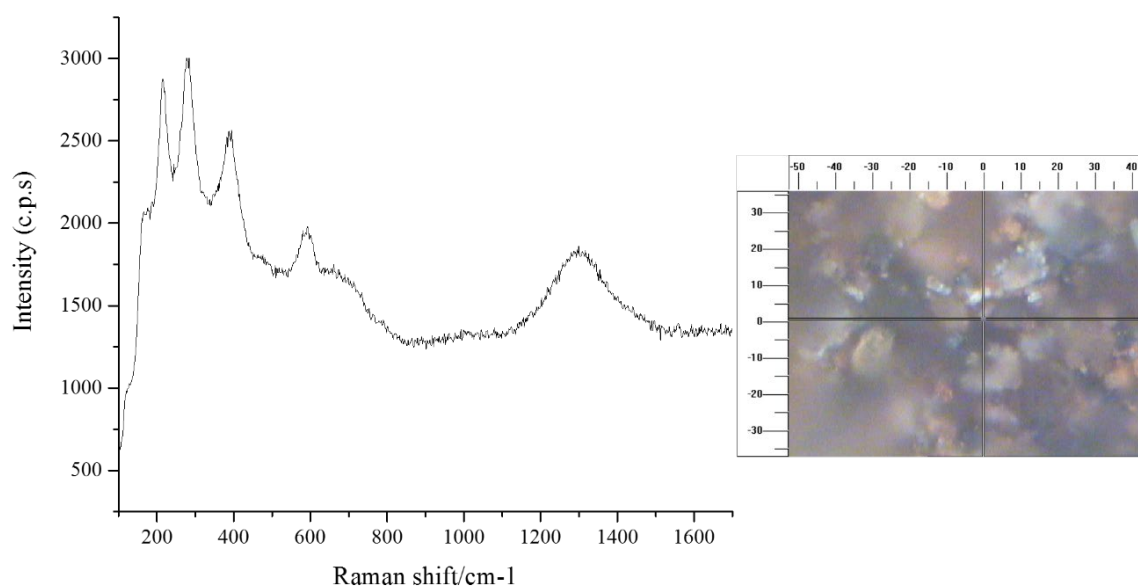


Fig. 158: Optical micrograph of corrosion coupon showing the location from where the Raman spectrum was collected, and the Raman surface spectrum.

Broadly, all the Raman spectroscopy patterns show the presence of hematite, magnetite and siderite. No appreciable differences were detected between the spectra obtained in the base and welded coupons.

4.8.4 Conclusions

The present work aimed to characterise samples of both FEBEX-DP bentonite and metallic coupons that were corroded within the bentonite. The intention was to achieve a greater understanding of the changes that may occur in the bentonite and corrosion coupons under the defined experimental conditions.

The following conclusions can be drawn based on the analyses performed and the data obtained:

- With respect to the bentonite samples, S-S-54-15-A/B/C/D/E and BM-B-41-1, XRD analysis was performed on random powders and OA. The obtained results do not reveal any significant difference between the untreated FEBEX bentonite and the samples analysed by the University of Bristol. It is worth mentioning that XRD analysis for this mineral group is not as precise and conclusive as for many other mineral groups.
- Random powder XRD patterns do not show significant variances between the untreated material and the samples analysed. From a qualitative perspective, the mineral phases identified in the XRD diffractograms were analogous to those observed in the XRD patterns of the untreated material.
- From the mineralogical point of view, OA XRD patterns do not reveal dissimilarities between the untreated material and the FEBEX-DP samples. OA XRD diffractograms also confirm that the smectitic phases on the FEBEX bentonite are actually made up of illite-smectite mixed layers, with approximately 10 % of illite layers.
- In relation to the analysis performed on the corrosion carbon steel (TStE355) coupons: Corrosion damage was observed. The corrosion damage can be defined as a generalised corrosion and is mostly manifested in each coupon as cracking damage.
- EDX analysis of the corrosion products reveals the presence of chlorine in each coupon. It is also worth highlighting the presence of manganese and nickel traces. In addition, the presence of silicon, aluminium, magnesium, calcium, sodium and potassium was detected, likely originating from the bentonite.
- Raman analysis was performed to obtain information about chemical and phases present in each corrosion coupon. Raman spectroscopy patterns reveal the presence of siderite, hematite, magnetite, and calcite.

However, EDX and Raman analyses did not reveal substantial differences between the base samples and the welded samples.

Based on the analysis performed and the obtained data, both from the bentonite samples and the corrosion coupons, it can be stated that no significant variations have been found between the untreated bentonite and the FEBEX-DP bentonite samples, nor between the base and welded corrosion coupons. Nevertheless, further analysis will be crucial as the analysis performed did not disclose enough information about possible iron-bentonite interactions and the effects on carbon steel as a result of exposure to an anaerobic environment over several years.

5 Discussion

5.1 Findings from corrosion studies

5.1.1 Carbon steel materials

The majority of the studies were focused on corrosion and/or metal-clay interaction phenomena involving carbon steel materials. From a macroscopic perspective, these phenomena are distributed in a heterogeneous way. This holds particularly for the Fe-clay interaction processes and the corresponding interaction zones which exhibit strong spatial variations. They appear to be correlated primarily to moisture content and its evolution during the experiment. Hence, areas with higher moisture content tend to display larger interaction zones. There seems to be less correlation with regard to temperature, although temperature has had an indirect impact, affecting moisture distribution. It should also be pointed out that the samples studied represent only a small fraction of the corroded surfaces and these samples mostly represent the heater/liner zone (Fig. 10).

From a macroscopic descriptive viewpoint, two layers adjacent to the iron metal can be distinguished: the corrosion layer attached to the iron surface and the interaction zone (Fig. 159). The latter will be described in the following section.

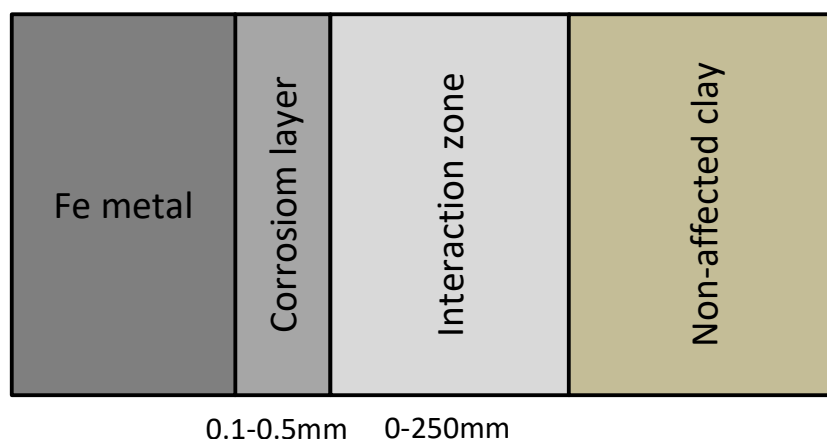


Fig. 159 Schematic view of the different compartment between carbon-based steels and the bentonite clay (not to scale).

The corrosion layer is dominated by iron oxides, but siderite was also encountered. The identified Fe phases in the corrosion layer by the different studies are listed in Tab. 56. The data obtained by the different teams is largely consistent and confirms the predominance of Fe(III) oxides, which already had been suggested through visual inspection. The two teams, Tecnia and Uni Bristol, which focused on the analysis of the corrosion layer in different types of carbon steel samples, largely observed the same corrosion products (Tab. 56). It should be noted that a considerable part of the corrosion products is expected to be nano-crystalline Fe(III) oxyhydroxides which are not detectable by conventional XRD analysis.

The predominance of Fe(III) in the corrosion layer points to the importance of aerobic corrosion, but the presence of newly formed magnetite and siderite highlights that anaerobic conditions were established after the aerobic phase. It should be kept in mind that contact with

air during dismantling, storage and sample preparation may have caused oxidation, thus affecting the Fe(III)/Fe(II) proportion. A further point to make is the initial corrosion layer when emplaced; according to the analysis of Obayashi on a liner sample this corrosion consisted of a thin layer of magnetite.

The thickness of the corrosion layer and thus of the corrosion depth is variable. According to the analysis by TecNALIA, the corrosion layer thickness of the liner is in the range of about 180 – 350 µm. The corrosion layer of the heater is slightly more homogeneous, with a thickness of about 200 µm and areas with localised corrosion at the end parts. The latter exhibits a corrosion layer of up to 400 µm. In general, very little localised corrosion was observed for all carbon steel parts and homogeneous corrosion was the dominant corrosion mode. Two phases of corrosion are proposed based on the analysis of the corrosion products. Due to contact with oxygen, iron(III) oxides precipitated on the outer surface of the iron surfaces and in the cracks of the pre-formed corrosion layer, partly replacing magnetite. In areas with low water content, anhydrous iron oxides (hematite and maghemite) were formed. Iron oxyhydroxides (goethite, lepidocrocite, Ferrihydrite) likely occurred in areas with higher moisture content. Salt accumulation at the heater during the evaporation process led to the formation of Cl-bearing oxides. After consumption of O₂ via corrosion close to the metal surface and decreased influx of O₂ from the bentonite, the corrosion rates decreased. In this phase, magnetite and siderite and possibly also non-identified microcrystalline green rust phases were formed, partly via reduction of previously formed Fe(III) oxides. A more elaborate phenomenological model combining corrosion and Fe-bentonite interaction processes is proposed in Section 5.2.1.

Tab. 56: Fe phases identified on carbon steel surfaces and in Fe/clay interface zone.

Object	Fe phases identified	Section	Team
Liner	mag, aka, hem, sid	45	TecNALIA
	hem, sid, goe, aka	35	Obayashi
	goe, (hem)	41	Uni Bern
	goe, mag	36,42	BGR
	mah, goe, lep	45,52	Ciemat
Heater	aka	var.	TecNALIA
	goe	54	BGR
	mah, goe, lep	42,54	Ciemat
Sensors	mag, sid	54	TecNALIA
	mah, goe, Fer	47	Ciemat
Coupon (TstE355)	mag, sid, hem	48	Uni Bristol

mag: magnetite; aka: akagenite; hem: hematite; sid: siderite; goe: goethite; mah: maghemite; lep: lepidocrocite; Fer: Ferrihydrite

Mass balance estimate

As outlined above, the predominant corrosion products in the corrosion layers are Fe(III) oxides which were formed by aerobic corrosion, thus through oxidation of carbon steel by molecular oxygen. It is instructive to compare the amount of O₂ in the tunnel after emplacement of the materials with the amount of oxidized Fe. Assuming a closed system, i.e. no influx of air during the experiment, the amount of O₂ should be in the same range or higher than the amount of Fe(III) resulting from the corrosion reaction:



Thus, 1 mol of O₂ may oxidize 4/3 mol of Fe to 4/3 mol of Fe³⁺.

Let us consider a 1 m section comprising the heater, liner and the main steel components. The amount of O₂ after emplacement in this section is present in (i) the gap between the heater and the (perforated) liner, the pores in the bentonite blocks only partially filled with water and gaps between them and (iii) the outer gap between the bentonite blocks and the tunnel wall. The calculated O₂ amounts and the corresponding dimensions and parameters are shown in Tab. 57. The total O₂ inventory derived is 6.5 mol. Hence, according to eq. (1) the maximum amount of corrodable Fe(III) is 8.7 mol. Using a density for carbon steel of 7690 m³/kg this corresponds to a volume 0.0075 m³ of Fe. The surface areas of the heater and liner for a 1 m long section are also shown in Tab. 57. The derived total surface area of the steel surfaces is 5.50 m². Thus, the average corrosion depth is 0.0075/5.50 = 1.1E-05 m or 11 μm.

The corrosion depths of the liner and heater can be roughly estimated from the measured corrosion layer (200 – 350 μm). Assuming that the corrosion layer density is 4.2 g/cm³ (density of goethite) and the density of carbon steel is 7.69 g/cm³, the derived corrosion depths are 109 – 191 μm. This is a factor of 10 – 20 larger than the corrosion layer derived from the amount of O₂ available. This strongly suggests that there was an external O₂ source contributing to steel corrosion keeping in mind that the main pool of corrosion production consists of Fe(III) oxides (see further discussion in Section 5.4).

Tab. 57: Calculated amounts of O₂ and Fe in a 1 m long section comprising the heater and the liner (see text).

Dimensions taken from Enresa (1998).

Oxygen	Air volume (m ³)	Amount O ₂ (mol)	Equiv. Amount Fe(III) (mol)	Assumptions
Gap heater -liner	0.085	0.77		Perforation degree = 60 %
Bentonite blocks	0.595	5.40		Av. Dry density 1'600 m ³ /kg av. Water content 14.36 %
Gap blocks-rock	0.036	0.32		
Total	0.715	6.49	8.66	
Iron		Surface area (m ²)	Av. Corrosion depth (µm)	
Heater		2.83		
Liner		2.67		Perforation degree = 60 %
Total		5.50	11.44	

5.1.2 Other metals

The corrosion of stainless steel (sensor, coupons), Ti alloys (coupons) and Cu alloys (coupons) was studied by TecNALIA. It is to note that the moisture content around the coupons seems to have been very low (NAB 16-12). Indeed, the bentonite surrounding the coupon racks had a dry powdery appearance.

Stainless steel: For the stainless steel tubes of the sensors, some mechanical damage was found but no signs of general or localised corrosion were noted. Analysis of 316L coupons also showed very little corrosion, but localised corrosion (pitting), and, in one specimen, cracking was detected. The pits contained brown, partly Cl-bearing iron oxides. Pitting depth was estimated to be about 300 µm, suggesting a fairly slow propagation of corrosion damage.

Titanium alloys: For the Ti coupons no corrosion phenomena at all were observed. Thus, no difference between unwelded and welded samples was noted.

Copper alloys: General corrosion was identified to be the main corrosion mode. Generally speaking, the effects of corrosion in the copper coupons were found to be rather small. Cu-Ni alloys showed less corrosion compared to the Ni-free ones. In the latter, some spots of localised corrosion were observed with maximum penetration depths of 20 – 100 µm. Cuprite was identified as corrosion product in all samples. Notable amounts of chloride were found in the corrosion layer. The estimated total corrosion depth from weight-loss measurements in one Cu sample was about 9 µm. The observed corrosion phenomena are explained by oxic corrosion. No signs of anaerobic corrosion (e.g. Cu sulphide) were found.

5.2 Findings from iron-bentonite interaction studies

5.2.1 Behaviour of iron released from carbon steel

Colour changes in the clay surrounding carbon steel components indicate the importance of Fe-bentonite interaction. It should be emphasised again that the extent of this interaction zone is very inhomogeneous, ranging from basically zero to hundreds of mm. In most parts of the experiment, this interaction zone is a few mm thick. When the zone is visible, it generally displays a duplex structure: a reddish inner layer and a blueish-greenish outer layer, suggesting an oxidized zone followed by a reduced outer zone. This was confirmed by Mössbauer spectrometry carried out on a sample in Section 41 (Section 4.4). The analysis of a nearby sample in the same section revealed basically no change in iron speciation relative to the unaffected clay. This is mainly due to the very heterogeneous spatial moisture distribution (see below). The general layered pattern of the iron-clay interaction zone is illustrated in a sketch (Fig. 160).

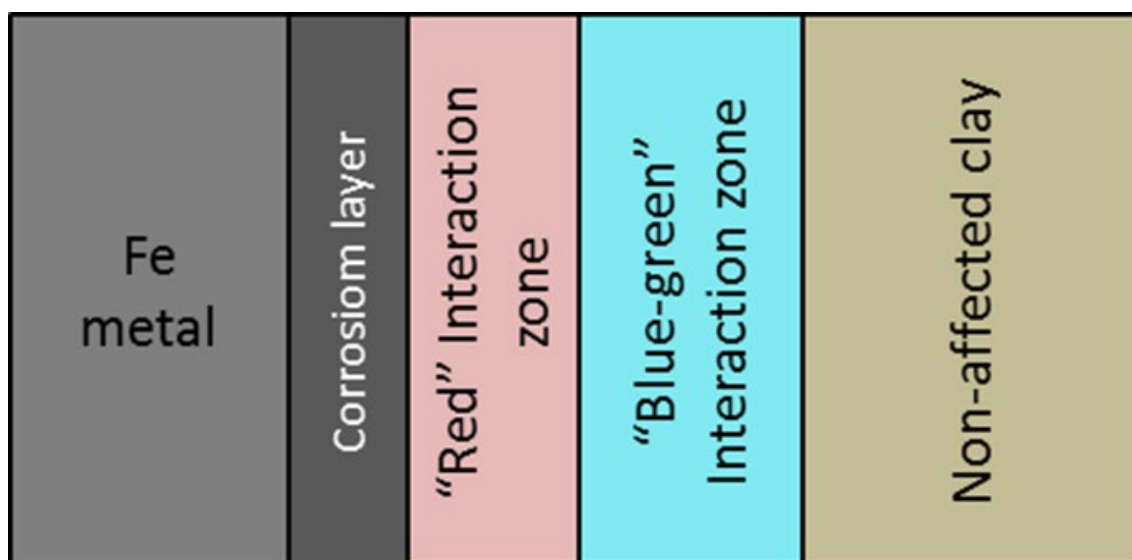


Fig. 160: Sketch showing layered structure of the Fe/clay interface area (not to scale).

The Fe content shows the same trend as the extent of the interaction zone: consequently, we can say that the larger the interaction zone, the larger the increase of Fe relative to the unaffected clay. The Fe content close to the iron source was found to be a factor 1.5 to 3 higher than further away. Conversely, in areas where no interaction is observed, no Fe increase in the clay occurred. This is illustrated in Fig. 161 which displays high-resolution EDX Fe profiles of two samples in Section 41. The sample with the large interaction zone exhibits an Fe front of about 30 mm whereas the sample with no visible interaction zone does not display any Fe enrichment. These two samples represent extremes with regard to the extension of the Fe front. The analyses from other locations, which were generally performed at much lower spatial resolution on bulk samples, exhibit Fe fronts ranging from zero to about 10 mm.

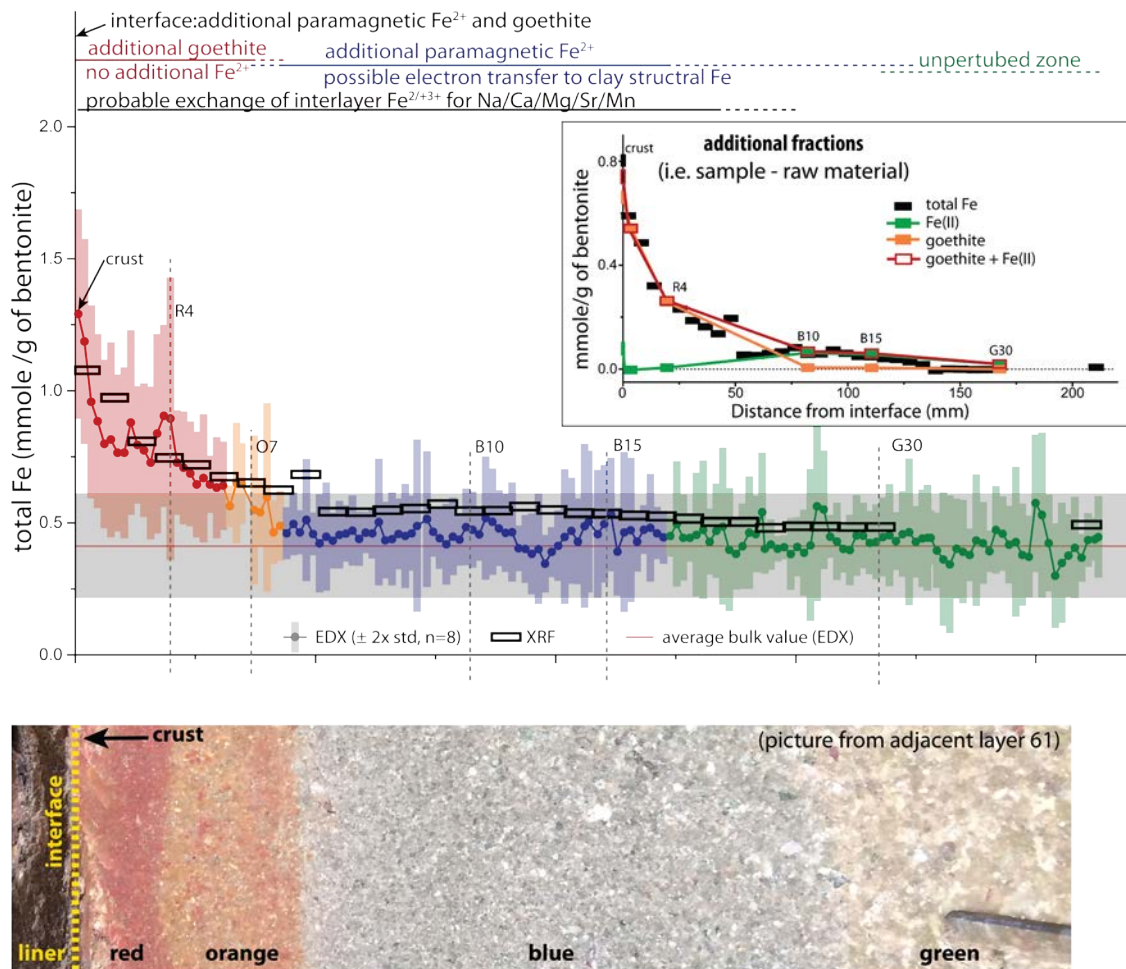


Fig. 161: Fe profiles perpendicular to liner in Section 41, in block BM-B-41-1 (EDX and XRF) and BM-B-41-2 (EDX).

The insert displays the excess amounts of Fe (compared to the natural clay) and the speciation determined from a combination of XRF and Mössbauer spectrometry for sample BM-B-41-1.

From the combined dataset of microscopic and spectroscopic analysis, the following phenomenological corrosion and Fe-clay interaction model has been suggested based on samples in the liner area (Section 4.4). Because similar features could be identified in other experiments (Section 5.3.1), it is suggested that the proposed model also applies to other areas in the FEBEX experiment.

- Phase 0: Carbon steel is covered with a thin oxide layer (mainly magnetite). Bentonite has a low moisture content; main species is structural Fe(III).
- Phase 1: Aerobic corrosion of steel leads to the formation Fe(III) oxides. Depending on moisture content, anhydrous Fe(III) oxides (hematite, maghemite) or Fe(III) oxyhydroxides (mainly goethite, lepidocrocite) are formed. O₂ and H₂O transfer to steel diminishes as corrosion proceeds and corrosion layer thickens.
- Phase 2: Anaerobic corrosion of steel at the inside of the corrosion layer leads to generation of Fe(II) and formation of magnetite and siderite in the corrosion layer. Furthermore, (rapid) electron transfer across the corrosion layer occurs, generating Fe(II) at the corrosion layer/bentonite interface which reacts with remaining O₂ to further produce Fe(III) oxides.
- Phase 3: Anaerobic conditions everywhere: Continuation of anaerobic steel corrosion, generation of Fe(II) (and magnetite/siderite) and (rapid) electron transfer across the corrosion layer. Diffusion of Fe(II) into bentonite and accumulation of Fe(II) in clay. Further transport of small fluxes of Fe(II) into clay. Mechanism of this transfer process still needs to be established. It probably involves redox reaction with structural Fe(III) and previously formed (and pre-existing) Fe(III) oxides.

The proposed mechanism is presented in more detail in Fig. 76. It should be emphasised again that major drivers affecting the corrosion process were the availability of water and O₂.

5.2.2 Other findings in the bentonite

The heating of the bentonite in conjunction with the limited amount of water induced evaporation close to the heater. Moreover, the corrosion reaction itself consumed water, thus enhancing water loss at the Fe surface. This led to the accumulation of Cl and, to a lesser extent, of sulphate and carbonate salts, as indicated from leaching tests. Cl in fact is known to be a strong corrodant under oxidic conditions and the evaporation process likely enhanced corrosion rates at the steel and liner surfaces. Calcite and aragonite precipitates were observed close to the heater.

The cation exchange capacity (CEC) showed no or only small changes as a function of distance from the heat source. The slight decrease (max. 10 %) noted for some of samples located at the interface has been explained by dilution of the clay with iron corrosion products. This suggests that alteration of smectite was very limited. This is supported on the one hand by the constant Al/Si ratio noted in the large interaction zone (see Section 4.4). On the other hand, the amount of newly identified silicate phases is very limited. The formation of minor trioctahedral smectite (saponite) "domains" in some samples in direct contact to the heater was indicated from XRD. In one sample in contact with the heater, a Mg-rich zeolite (chabazite) was identified.

Mg increase towards the iron contact was observed in some samples. This increase is not correlated with the increase in Fe, and hence, does not appear to be related to the corrosion process. This effect is rather related to temperature since there is trend of increasing Mg towards the heater whereas no Mg increase was observed in colder sections. At the heater, besides Mg-rich zeolite, brucite was identified. Also, exchangeable Mg shows a slight increase towards the heater.

5.3 Significance of results in relation to other studies

5.3.1 Comparison with similar types of in-situ studies

Generally speaking, the FEBEX-DP experiment revealed the same type of corrosion and iron-bentonite phenomena as observed in other in-situ experiments; for example, the Äspö-based experiments ABM (Alternative Buffer Materials) and TBT (Temperature Buffer Test) which are described shortly below.

The ABM experiment consists of a series of boreholes in which different bentonite materials were emplaced as ring-shaped blocks (thickness ~ 10 cm) around a steel heater. In the ABM1 and ABM2 boreholes, the bentonite was both saturated with artificial groundwater and heated to temperatures up to 140 °C (Svensson et al. 2011, Svensson 2015) for 2.5 and 5 years, respectively. A systematic strong increase of Fe close to the steel/bentonite interface (~ 5 – 10 mm) was observed. In parallel, the Fe(II)/Fe(III) ratio showed an increase toward the heater (Hadi et al. *subm.*). The identified corrosion products were magnetite, siderite and Fe(III) oxides. The alteration of smectite was generally very limited. At the heater contact, some newly formed trioctahedral smectite, which in one sample could be identified as Ferrous saponite (Svensson 2015) was identified. In many samples, an increase in Mg towards the heater was observed.

The TBT experiment was similar in design to the ABM experiment. MX-80 ring-shaped blocks (thickness ~ 50 cm) were placed around a steel heater and heated to temperatures up to 155 °C for a period of about 7 years (Åkesson et al. 2012). Contrary to ABM1 and ABM2, the clay close to the heater did not achieve full saturation during the test. Total Fe showed an increase in the innermost sample (~ 10 mm from Fe surface), but the Fe(II)/Fe(III) ratio in the clay showed no or only slight increase. The iron corrosion products were dominated by Fe(III) oxides. The observed differences with regard to the ABM1 and ABM2 tests were explained by the less reducing conditions and the higher O₂ amounts in the TBT experiment (Svensson & Hansen 2013). This is related to the larger bentonite blocks, the higher temperature and the longer saturation time in the TBT experiment. Both experiments showed no or very limited smectite alteration.

The main differences of FEBEX-DP compared to the ABM and TBT experiments are the longer test period (~ 18 years), the lower temperature (~ 100 °C) at the heater surface and the higher amount of air as well as of iron metal parts introduced to the system. Furthermore, ABM and TBT were artificially wetted whereas natural (slow) wetting from the granite rock occurred in the FEBEX experiment. This explains the more heterogeneous nature and the partly larger extent of the iron-bentonite interaction zones in the latter experiment. The corrosion features are more like those of the TBT experiment (predominance of Fe(III) oxides), which is related to the longer impact of O₂ and to the prevailing non-saturated conditions close to the heater. However, both ABM and FEBEX-DP indicate that both oxidizing and reducing conditions have occurred, whereas in the case of TBT there were no clear indications that reducing conditions had occurred.

5.3.2 Links with geochemical and microbiological studies within FEBEX-DP

Microbiological studies

Microbial studies performed by Micans (S) and BGR (D) have been reported in NAB 16-15 (Bentsson et al. 2017). These were focused on bacterial cell number and cultivation tests on a number of clay samples in the tunnel. The main finding was that a large number of cells could be grown in the colder and wetter parts of the tunnel, but not in the hotter and dryer parts (i.e. in the heater area). Keeping in mind that most samples studied for corrosion were from heater/liner area, the absence of any indication of microbially-induced corrosion at the heater/liner surfaces corroborates the microbial findings from Bentsson et al. (2017).

A cultivation test was also conducted on clay samples surrounding an extensometer in Section 54 and documented in NAB 16-54 (Madina 2016). No culturable bacteria could be found, although corrosion features adjacent to carbon steel parts suggested that microbially-induced corrosion had occurred.

Gas and porewater composition measurements

The evolution of gases and, to a lesser extent, of porewater composition was monitored via a sampling campaign during the FEBEX test (NAB 16-13, Fernández & Giroud 2017). The general result for the gasses is the increase in CO₂, N₂, H₂, CH₄ and other hydrocarbons and the decrease in O₂ levels. This was explained by the authors by corrosion processes on the one hand and biodegradation processes on the other. From the gas evolution, it was inferred that the redox conditions changed from oxic to reducing after about 2 years until the dismantling of Heater 1. After this oxic disturbance, reducing conditions were re-established in the Heater 2 tunnel.

A closer look at the gas measurements reveals considerable variations, as for example illustrated for O₂ and H₂ (Fig. 162). The evolution of these gases in fact shows considerable overlap suggesting apparently inconsistent redox conditions. A possible explanation for this could be spatially variable redox conditions, with reducing conditions occurring in the saturated outer parts and oxidizing conditions in the central unsaturated parts. Transport and mixing of gasses in the partly saturated medium under the thermo-hydraulic gradient can be expected to be rapid.

Few porewater data were acquired, in particular regarding redox sensitive species, such as SO₄²⁻, HS⁻, or Fe²⁺. This makes interpretation of redox evolution from porewater data difficult.

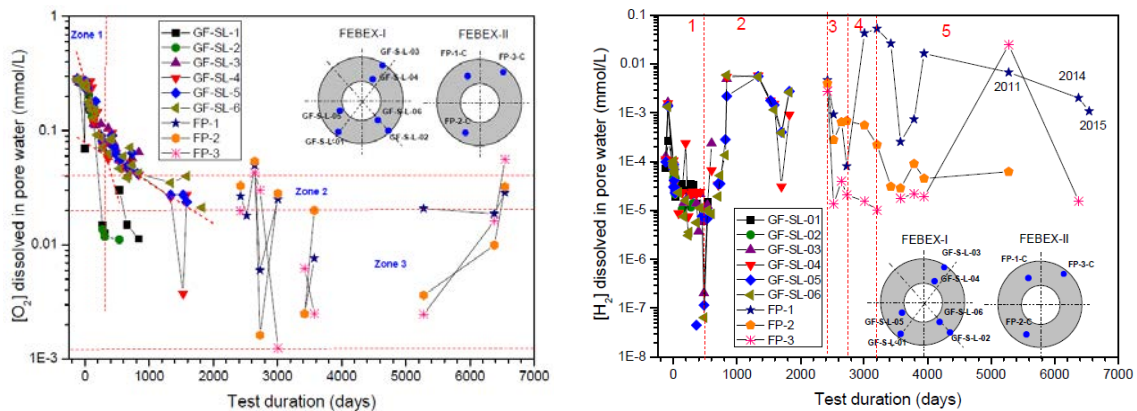


Fig. 162: Evolution of O_2 (left) and H_2 (right) based on gas measurements (Fernández & Giroud 2017).

Geochemical data from post-mortem samples

The THM and THC data obtained from analysis of clay samples in the FEBEX-DP experiments have been synthesised in NAB 16-17 (Villar et al. 2017). A lot of data and parameters were generated, but here only findings related to those from the corrosion studies are discussed:

- A strong increase in chloride concentration towards the heater is manifested. With regard to sulphate no clear trend can be discerned. This is largely supported by the data presented in this report.
- Exchangeable cations show a slight increase in Ca, a strong increase in Mg and a decrease in Na toward the heater. In the cooler sections the trends are generally less pronounced. These observations are also in line with the corrosion-related studies.
- The CEC does not show any clear trend as a function of distance to the heater and there is a considerable spread in values obtained from the different laboratories. This is also in line with studies presented above. Note that a slight decrease observed in SKB close to contact with heater was interpreted as dilution by iron oxides present in the sample.
- No major mineralogical changes were found. Notably, no modification in the crystal chemical properties of smectite as function of distance from the heater was observed. This supports the results obtained in the corrosion-related studies.

5.3.3 Comparison with corrosion study of FEBEX I

A similar type of corrosion study as reported in Section 4.2 was carried out by Tecnalia for FEBEX I (Madina & Azkarate 2004). Otherwise, very little work on the properties of the bentonite contacting the metal parts was performed. Therefore, the discussion here is limited to the comparison of both corrosion studies.

Corrosion processes were studied on the surfaces of the heater, the liner, metal coupons and sensors. In general, results for carbon steel materials showed the predominance of Fe(III) oxides as corrosion products and essentially no indications of Fe(II) mineral formation, thus indicating predominating oxidizing conditions during FEBEX I. However, corrosion phenomena observed on sensor samples and microbial analysis indicated sulphate reduction and formation of iron sulphides. This suggests that anaerobic conditions had occurred in parts of FEBEX I. The

presence of Fe(II) minerals (e.g. magnetite and siderite) and blue halos in FEBEX II points to the larger importance of anaerobic corrosion in FEBEX II.

The heater displayed only a thin fairly uniform corrosion layer of $\sim 15 \mu\text{m}$, which is much thinner than observed for FEBEX II ($\sim 200 \mu\text{m}$). Besides the longer reaction time, this difference is related to the higher moisture content in FEBEX II.

The liner in FEBEX I exhibited a fairly uniform corrosion layer of $100 - 180 \mu\text{m}$ which compares to a layer of $200 - 350 \mu\text{m}$ observed in FEBEX II. The latter is thus roughly twice as thick as on the liner in FEBEX I. Under the assumption that conditions were similar around both heaters, this result suggests that corrosion of the liner in FEBEX II proceeded at a similar rate after the dismantling of FEBEX I.

The metal coupons in FEBEX I generally showed very little corrosion effects due their close location to the heater and hence very low humidity. This is in line with the observations in FEBEX II. The largest average corrosion rates ($0.7 \mu\text{m/a}$) were observed in the copper coupons which contained Cu_2O as main corrosion product. In FEBEX II, similar corrosion features were observed for the Cu coupons, but in case of the Cu-ETP coupons, small pits had formed. The average corrosion rate estimated for one sample was $0.5 \mu\text{m/a}$.

The analysed sensor samples made of carbon and stainless steel in FEBEX I exhibited extensive corrosion phenomena, including microbial and pitting corrosion as well as stress corrosion cracking in the stainless steel specimen. This could be explained by the larger humidity conditions experienced by these materials compared to the coupons. In FEBEX II, less sensors samples were studied. Corrosion effects observed are also fairly extensive, but were found to be limited to the carbon steel parts.

5.4 Implications for repository conditions

Generally speaking, the FEBEX experiment was not designed in an ideal way to study corrosion without inducing disturbances during dismantling and sampling. Nevertheless, useful information regarding conditions of the early stage in the near field after repository closure could be deduced. These conditions can be characterised by a variable moisture content and a predominately oxidizing environment. The slow water ingress from the "cold" host rock and the heat emanating from the central part induced a humidity gradient and salt (mainly NaCl) accumulation on the hot side, which lasted until the end of the experiment. Swelling of bentonite occurred concomitantly, preferably in areas of high relative humidity, leading to inhomogeneous density and porosity distributions. Movement of air and moisture likely occurred in an uneven and partly "channelled" manner. Besides the air initially present, air presumably entered the tunnel through the plug, gas pipes and/or the EDZ. These conditions left a strong imprint on corrosion phenomena. Thus, corrosion effects are more pronounced in areas of higher moisture content, but accumulation of chloride adversely influenced corrosion in the drier areas.

Averaged corrosion rates for carbon steel can be roughly estimated from corrosion layer thicknesses observed on surfaces of the liner and heater which are in the range of about $200 - 350 \mu\text{m}$ (Section 5.1.1). This yields for a time period of 18 years averaged corrosion rates of $6 - 11 \mu\text{m/a}$. Note that this estimation neglects the Fe transferred to the clay on the one hand and the ongoing corrosion in the period after dismantling and before analysis on the other hand. From the amount of transferred Fe the corresponding corrosion depth was estimated to be about $250 \mu\text{m}$ in one "extreme" sample, thus yielding an additional average corrosion rate of $14 \mu\text{m/a}$.

(Section 4.4). On the other hand, in another nearby sample the amount of transferred Fe to the clay was negligible. Assuming that these samples are bounding cases for the amount of Fe transferred to the clay, the averaged corrosion rates are in the range of 6 – 25 $\mu\text{m/a}$.

The upper averaged corrosion rates are in line with the corrosion rates for aerobic conditions proposed by Foct & Gras (2003). Using their semi-empirical relationship for saturated aerobic conditions and a temperature of 95 °C, a corrosion rate of 27 $\mu\text{m/a}$ is derived. The lower averaged corrosion rates noted for most samples likely reflect unsaturated oxidizing conditions and/or the influence of subsequent anaerobic conditions.

As indicated from the mass balance estimate in Section 5.2.1, the amount of O_2 present in the package at the time of emplacement can only explain a small part of the total corroded Fe(III). This suggests the presence of an external source of air which may have entered the system through the cement plug, which was presumably not air-tight (NAB 14-55), through the gas pipes, the cable conducts or the EDZ as is also supported from gas monitoring data (Fernández & Giroud 2017). A further part of Fe(III), particularly in the case of the heater, may have been produced after excavation. Furthermore, most repository concepts contain a lower amount of carbon steel surfaces. Hence, the FEBEX experiment reflects accentuated conditions with regard to aerobic corrosion effects.

The data further point to anaerobic corrosion following the aerobic stage, leading to reduction of Fe(III) species and diffusion of Fe(II) further into the clay. This effect is expected to have continued in the experiment inducing a gradual depletion of the Fe(III) oxide layer and a slow dispersion of the Fe front. Note, that longterm anaerobic corrosion rates in bentonite are thought to decrease to less than 1 $\mu\text{m/a}$ (King 2008), thus further slowing down the Fe front in the clay.

The corrosion process in FEBEX II induced very little alteration of the clay. There are some indications of the formation of trioctahedral Mg smectite close to the heater contact, but this effect appears to be mainly related to temperature alone. Moreover, trioctahedral smectite is also a swelling clay with favourable sealing properties (Pusch 1999). The results obtained on the clay contacting the hot Fe source are in line with data from other in-situ tests, such as, for example, the ABM and TBT experiments.

5.5 Open questions/recommendations for future projects

In general, the main objectives regarding corrosion-related aspects were accomplished within FEBEX-DP. However, some findings raised further questions and highlighted uncertainties which were not clear at the beginning of the experiment 20 years ago.

The findings deduced from the corrosion of metal coupons are difficult to set in context because of the special conditions they were exposed to. Observations suggest that they were exposed to conditions of lower humidity throughout the experiment. Comparison with the same type of coupons in the wetter parts (i.e. outer parts) of the experiment would have helped in the interpretation. Moreover, the emplaced coupons were affected by the dismantling of FEBEX I, in particular by the further addition of gas/water sampling pipes. Finally, in retrospect it would have been better if the surface of the coupons had been analysed before their emplacement.

This last remark is also true for the other steel materials, such as the liner and heater. The analysis of the initial conditions (e.g. surface layer thickness) would have helped in the analysis of corrosion phenomena and specifically, to obtain more precise data on corrosion depths and corrosion rates.

The air space, in particular between the heater and perforated liner was large and contributed in prolonging the oxic phase. In a future experiment this design can be easily adapted to reduce the initial air space.

Several measures were taken to avoid contact with air during sampling, storage and preparation of subsamples. These should be further improved by elaborating well-defined protocols that are adopted by all involved teams.

6 Conclusions

Corrosion-related processes have been studied in the FEBEX-DP project, both by observations during dismantling as well as by in-depth analysis of metal and metal-clay interface samples. The majority of the studied samples included carbon-steel-based materials, such as the heater, the liner and, to a lesser extent, some sensors. In addition, metal coupons consisting of stainless steel, copper and titanium materials were analysed. In general, the findings yield a consistent picture. In particular, they have helped to improve the understanding regarding carbon-steel corrosion and its impact on the bentonite buffer in a repository-type setting.

Macroscopic observations

Observations made during dismantling were very useful and enabled a macroscopic view of the corrosion phenomena. They underlined the highly heterogeneous nature of the corrosion processes, which is primarily related to the differences in moisture content. Water saturation of the buffer blocks and air movement occurred unevenly, leaving strong imprints on steel corrosion. The inner zones close to the heater remained unsaturated until the final state, whereas the outer and "colder" inner zones reached saturation. Thus, the latter zones generally displayed more extensive corrosion with corrosion layers and surrounding halos in the clay. This feature was observed around different types of carbon-steel-based sensors. The sections closest to the plug were affected by the dismantling of FEBEX I in 2002 and exhibited a more complex evolution. The inner zones generally exhibited less corrosion, thus thinner corrosion layers and less visible effects of Fe-bentonite interaction. The metal coupons, located in a dry zone close to the heater, showed very few signs of corrosion visually.

Metal coupons

Microscopic and XRD analysis confirmed that corrosion effects were fairly moderate. The analysis of one carbon-steel coupon exhibited the same type of corrosion products as observed on the heater and liner. Stainless steel coupons showed almost no general corrosion, but some localised corrosion (maximum penetration depth 300 μm) and stress corrosion cracking at one location, probably favoured by chloride accumulation. For the Ti coupons, essentially no corrosion features were noted, both for welded and unwelded samples. For the Cu and Cu-Ni coupons, general corrosion was found to be the main corrosion mode. Cuprite was identified as a corrosion product in all coupons. From the weight-loss measurements of one Cu coupon, the total corrosion depth was estimated to be about 9 μm . This yields an average corrosion rate of $\sim 0.5 \mu\text{m/a}$. For the Cu coupons, localised corrosion in some spots with maximum penetration lengths of 20 – 100 μm was observed. Cu-Ni alloys showed less corrosion than the unalloyed Cu samples. Corrosion features from Cu and stainless steel surfaces can be explained by aerobic conditions. No effects of anaerobic corrosion could be observed on these surfaces. In contrast, the adjacent carbon-steel coupon surface revealed signs of aerobic and anaerobic corrosion displaying the formation of hematite, goethite, magnetite and siderite.

Carbon steel materials and surrounding clay

Microscopic and spectroscopic analysis was mainly focussed on samples from the liner and heater, but one coupon sample and some samples from sensors, partly located in the external parts close to the rock were also analysed.

General corrosion was found to be the main corrosion mode. The observed maximum corrosion layer thicknesses on the surface of the liner and heater were about 180 – 350 μm . The observed corrosion layer thicknesses and the derived corrosion depths ($\sim 110 - 190 \mu\text{m}$) are in line with the measured decrease of the liner thickness of $300 \pm 150 \mu\text{m}$, thus yielding $150 \pm 75 \mu\text{m}$ of corrosion depth.

The predominant corrosion products are Fe(III) oxides, mainly goethite, but hematite, lepidocrocite, maghemite could be identified as well. A considerable fraction is suspected to be microcrystalline Fe oxyhydroxides, which are not detectable by conventional XRD analysis. Chloride accumulation at the heater led to the formation of Cl-bearing Fe(III) oxyhydroxide (akageneite could be identified). Besides Fe(III) oxides, newly formed magnetite and siderite were identified, highlighting that conditions were partly anaerobic.

The bentonite clay contacting iron surfaces is enriched in Fe, but the extent of the Fe front into the clay is variable, in the range of 0 – 40 mm. It correlates with the local corrosion rates, which are mainly influenced by the variable moisture content. The main fraction of enriched Fe in the clay consists of Fe(III) oxides (mainly goethite), manifested by the reddish halo contacting the corrosion layer. The clay adjacent to this Fe(III) enriched zone is still slightly enriched in Fe, displaying a higher Fe(II)/Fe(III) ratio. This zone, visible by the blueish-greenish colour, may extend to thicknesses of up to 200 mm. The observed pattern can be explained by the following phenomenological model:

- Phase 1: Aerobic corrosion under unsaturated conditions. Formation of Fe(III) oxides on the magnetite-bearing steel surface.
- Phase 2: Anaerobic corrosion of steel at the inside of the corrosion layer leading to magnetite and siderite and aerobic corrosion at the external surface leading to further formation of Fe(III) oxides.
- Phase 3: Anaerobic corrosion proceeds everywhere upon depletion of O_2 . Diffusion of Fe(II) into the bentonite, which probably reacts with the structural Fe(III) of the clay.

From roughly estimated corrosion depths of the liner and heater (109 – 191 μm , see above), the average corrosion rates covering a timespan of 18 years are 6 – 11 $\mu\text{m/a}$. This estimate neglects the Fe transfer into the clay, which may add 0 – 250 μm , based on preliminary analysis. Accounting for this additional mass of oxidized Fe leads to a larger range in averaged corrosion rates of about 6 – 25 $\mu\text{m/a}$. The overall data suggest that the lower range reflects the corrosion rates experienced by the largest fraction of the corroded steel surface. Since the dominant oxidation state of the corrosion products and Fe transferred into the clay is Fe(III), aerobic corrosion was the main driver. The aerobic corrosion rate under saturated conditions derived from semi-empirical relationships is about 27 $\mu\text{m/a}$, thus close to the upper range of estimated corrosion rates. The lower values reflect unsaturated conditions and/or the stronger impact of anaerobic conditions on corrosion. Mass balance considerations indicate that the initially present molecular oxygen cannot explain the amount of corroded Fe(III). This suggests ingress of O_2 during the experiment through the plug, such as via gas pipes or cable conducts.

Alterations in the clay

Generally speaking, alterations of the clay at the steel contact were minor. Increase of Mg towards the heater was noted, which was, however, not systematic and appeared not to be related to corrosion but rather to the effect of temperature. The dissolution of some SiO_2 and formation of minor Mg-rich smectite (saponite) close to the heater could be detected. The latter may be partly related to the increase in Mg.

A further feature was the accumulation of chloride at the heater due to evaporation, which affected, and somewhat enhanced corrosion of the steel surface. This chloride originated from the bentonite clay.

Relevance for repository conditions

The conditions in the FEBEX experiment reflect the early near-field stage of a repository. The surface areas of emplaced carbon steel materials and the amount of O_2 are larger than would be present in most repository concepts. Hence, the FEBEX experiment reflects accentuated conditions with regard to aerobic corrosion effects. Nevertheless, the findings from this experiment are consistent with those from other in-situ experiments and have contributed to a deepening of understanding of corrosion-induced effects. For example, the results show that a prolonged aerobic phase is unfavourable not only for corrosion, but also potentially for alteration of the clay because of the large reducible pool of generated Fe(III) oxides. The effects on the clay, on the other hand, were found to be small, with minor to negligible alteration of the swelling clay.

The corrosion features observed on Cu coupons reflect oxidizing conditions which, as outlined above, persisted over a long time within the experiment.

7 References

- Ackermann, F. (1980): A procedure for correcting the grain size effect in heavy metal analyses of estuarine and coastal sediments. *Environmental Technology Letters*, 1(11): 518-527.
- Åkesson, M. (2012): Temperature buffer test - Final report. SKB Technical Report TR-12-04.
- Ammann L, Bergaya F, Lagaly G. (2005): Determination of the cation exchange capacity of clays with copper complexes revisited. *Clay Minerals* 40, 441-453.
- Ayari, F., Srasra, E. & Trabelsi-Ayadi, M. (2007): Effect of exchangeable cations on the physicochemical properties of smectite. *Surface Engineering and Applied Electrochemistry*, 43(5): 369-378.
- Barahona, E. (1974): Bricked clays in the Province of Granada: Evaluation of some raw materials test. University of Granada (PhD thesis (in spanish). Granada, Spain.
- Bárcena, I. & García-Siñeriz, J.-L., (2015): FEBEX-DP (GTS) Full dismantling sampling plan (In-situ experiment). Nagra Arbeitsbericht NAB 15-14.
- Bárcena, I. & García-Siñeriz, J.-L., (2015): FEBEX-DP (GTS) Full dismantling sampling plan (In-situ experiment). Nagra Arbeitsbericht 15-15.
- Bárcena, I., Fuentes-Cantillana, J.L. & García-Siñeriz, J.L. (2003): Dismantling of the Heater 1 at the FEBEX "*in situ*" test. Description of operations. Enresa Technical Report 9/2003.
- Bengtsson, A., Blom, A., Taborowski, T., Schippers, A., Edlund, J., Kalinowski, B. & Pedersen, K. (2017): FEBEX-DP: Microbiological report (draft). Nagra Arbeitsbericht NAB 16-15.
- Cuadros, J. & Linares, J. (1995): Some evidence supporting the existence of polar layers in mixed-layer illite/smectite. *Clays Clay Miner.* 43, 467–473.
- Cuadros, J. & Linares, J. (1996): Experimental kinetic study of the smectite to illite transformation. *Geochim. Cosmochim. Acta*, 60, 439–453.
- Dohrmann, R. & Kaufhold, S. (2009): Three new, quick CEC methods for determining the amounts of exchangeable calcium cations in calcareous clays. *Clays and Clay Minerals*, 57(3), 338–352.
- Dohrmann, R., Olsson, S., Kaufhold & S., Sellin, P. (2013): Mineralogical investigations of the first package of the alternative buffer material test – II. Exchangeable cation population rearrangement. *Clay Minerals*, 48, 215–233.
- Enresa (1998): FEBEX: Full-scale engineered barriers experiment in crystalline host rock: Final design and installation of the 'in-situ' test at Grimsel. Publication Tecnica Num.12/98.
- Enresa (2006): Full Scale Engineered Barrier Experiment – Updated final report 1994 – 2004. Publication Tecnica 05-0/2006.
- Fernández, A.M. & Giroud, N. (2017): Gas and water sampling in different pipes from the FEBEX *in situ* test at the Grimsel Test Site. Nagra Arbeitsbericht NAB 16-13.

- Fernández, A.M., Baeyens, B., Bradbury, M. & Rivas, P. (2004): Analysis of the porewater chemical composition of a Spanish compacted bentonite used in an engineered barrier. *Physics and Chemistry of the Earth, Parts A/B/C*, 29(1): 105-118.
- Ferrage, E., Lanson, B., Sakharov, B.A. & Drits, V.A. (2005): Investigation of smectite hydration properties by modeling experimental X-ray diffraction patterns: Part I. Montmorillonite hydration properties. *American Mineralogist*, 90, 1358-1374.
- Foct, F. & Gras, J.-M. (2003): Semi-empirical model for carbon steel corrosion in long term geological nuclear waste disposal. Prediction of long term corrosion behaviour in Nuclear Wastes System. 2003. Cadarache, France: European Federation of Corrosion.
- Fuentes-Cantillana, J.L. & García-Siñeriz, J.L (1998): "FEBEX Full-scale Engineered Barriers Experiment in Crystalline Host Rock. Final Design and Installation of the "*In situ*" Test at Grimsel ". Enresa Technical Report 12/98, Enresa, Madrid.
- Fuentes-Cantillana, J.L., García-Siñeriz, J.L., Franco, J.J., Obis, J., Pérez, A.; Jullien, F.; Alberdi, J., Barcala, J.M., Campos, R., Cuevas, J., Fernández, A.M., Gamero, E., García, M., Gómez, P., Hernández, A., Illera, A., Martín, P.L., Melón, A.M., Missana, T., Ortuno, F., Pardillo, J., Rivas, P., Turrero, M.J., Villar, M.V., Mingarro, M., Pelayo, M.; Caballero, E., Cuadros, J., Huertas, F., Huertas, F.J., Jiménez de Cisneros, C., Linares, J.; Bazargan-Sabet, B., Ghoreychi, M.; Jockwer, N., Wieczorek, K.; Kickmaier, W., Marschall, P.; Martínez, M.A.; Carretero, P., Dai, Z., Delgado, J., Juncosa, R., Molinero, J., Ruiz, A., Samper, J., Vázquez, A.; Alonso, E., Carrera, J., Gens, A., García-Molina, A. J., Guimera, J., Guimaraes, L.do N., Lloret, A., Martínez, L., Olivella, S., Pintado, X., Sánchez, M.; Elorza, F.J., Borregón, J.L., Canamon, I., Rodriguez Pons-Esparver, R.; Fariña, P., Farias, J. & Huertas, F., 2000: FEBEX full-scale engineered barriers experiment for a deep geological repository for high level radioactive waste in crystalline host rock Final Report. Enresa, Technical Report 1/2000.
- Fuentes-Cantillana, J.L., García-Siñeriz, J.L., Obis, J., Pérez, A.; Alberdi, J., Barcala, J.M., Campos, R., Cuevas, J., Fernández, A.M., Gamero, E., García, M., Gómez, P., Hernández, A., Illera, A., Martín, P.L., Melón, A.M., Mingarro, M., Ortuno, F., Pardillo, J., Pelayo, M., Rivas, P., Rodríguez, V., Turrero, M.J., Villar, M.V.; Caballero, E., Jiménez de Cisneros, C., Linares, J.; Martínez, M.A.; Samper, J., Delgado, J., Juncosa, R., Molinero, J.; Alonso, E., Carrera, J., Gens, A., García-Molina, A.J., Guimera, J., Guimaraes, L.do N., Lloret, A., Martínez, L.; Elorza, F.J., Borregón, J.L.; Fariña, P. & Farias, J. (1998): "FEBEX Full-scale Engineered Barriers Experiment in Crystalline Host Rock. Pre-operational Stage Summary Report". Enresa Technical Report 1/98, Enresa, Madrid.
- García-Siñeriz, J.-L., Abós, H., Martínez, V., De la Rosa, C., Mäder, U. & Kober, F. (2015): FEBEX DP: Dismantling of Heater 2 at the FEBEX "*in situ*" test. Description of operations. *Nagra Arbeitsbericht NAB 16-11*.
- García-Siñeriz, J.L., Martínez, L.V., Rey, M. & Abós, H., (2016): Results of laboratory investigations in preparation of the dismantling of the FEBEX-e/FEBEX-DP in-situ test and on-site experiments during the dismantling. *Nagra Arbeitsbericht NAB 16-09*.
- Giroud, N. (2014): FEBEX - assessment of redox conditions in phase 2 before dismantling. *Nagra Arbeitsbericht NAB 14-55*.

- Gregg, S. J. & Sing, K.S.W. (1982): Adsorption, Surface area and Porosity. Academic Press. 303 pp.
- Grimsel Test Site. <http://www.grimsel.com/gts-phase-vi/FEBEX-dp/FEBEX-dp-introduction>.
- Hadi, J. (2016): Subsampling of FEBEX related to the halo zone around the extensometer. Switzerland: Internal subsampling document, University of Bern, Switzerland.
- Hadi, J., & Wersin, P. (2015): Retrieving metallic coupons (RACK A) in the FEBEX experiment at Grimsel. Internal document, University of Bern, Switzerland.
- Handler, R.M. et al. (2014): Fe(II)-Catalyzed recrystallization of goethite revisited. *Environmental Science & Technology*, 48: 11302-11311.
- Hitomi, Kajiwaru K., Sugiyama T., et al. (2013): 67th Cement technical conference pp.80-8 (In Japanese).
- Huertas, F.; Fariñas, P.; Farias, J. & García-Siñeriz, J.L. Villar, M.V., Fernández, A.M., Martín, P.L; Elorza, F.J; Gens, A., Sánchez, M., Lloret, A.; Samper, J. & Martínez, M.A. (2006): "Full-scale Engineered Barriers Experiment. Updated Final Report 1994 – 2004" December 2006. Enresa, Technical Report 05-0/2006.
- Kaufhold, S., Dohrmann, R., Sandén, T., Sellin, P. & Svensson, D. (2013): Mineralogical investigations of the alternative buffer material test – I. Alteration of bentonites. *Clay Minerals*, 48, 199–213.
- Kaufhold, S., Hassel, A.W., Sanders, D. & Dohrmann, R. (2015): Corrosion of high-level radioactive waste iron-canisters in contact with bentonite. *Journal of Hazardous Materials*, 285: 464-473.
- Kerisit, S., Zarzycki, P. & Rosso, K.M. (2015): Computational Molecular Simulation of the Oxidative Adsorption of Ferrous Iron at the Hematite (001)–Water Interface. *The Journal of Physical Chemistry C*, 119(17): 9242-9252.
- Kober, F. & Van Meir, N. (2017): FEBEX-DP – Dismantling related supplementary documents. Nagra Arbeitsbericht NAB 16-68.
- Kober, F. (2015): FEBEX-DP Sample Log Book. Switzerland: Nagra Aktennotiz.
- Kurosawa, S., Yui, M. & Yokoyama, H. (1997): Experimental study of colloid filtration by compacted bentonite, *Mat. Res. Soc. Symp. Proc*, 1997, pp. 963-970.
- Lafuente, B., Drowns, R.T., Yang, H. & Stone, N. (2015): The power of databases: the RRUFF project. In: T, A., M, D.R. (Eds.), *Highlights in Mineralogical Crystallography*. W. de Gruyter, Berlin, Germany, pp. 1-30.
- Lanyon, G.W. & Gaus I. (2013): Main outcomes and review of the FEBEX *In situ* Test (GTS) and Mock-Up after 15 years of operation. Nagra Arbeitsbericht NAB 13-96.
- Latta, D.E., Neumann, A., Premaratne, W. & Scherer, M.M. (2017): Fe (II)-Fe (III) electron transfer in a clay mineral with low Fe content. *ACS Earth and Space Chemistry*.

- Luoma, S.N., (1990): Processes affecting metal concentrations in estuarine and coastal marine sediments. *Heavy Metals in Marine Environment* 51-66.
- Madejová, J. (2003): Review: FTIR Techniques in clay mineral studies. *Vibrational Spectroscopy*, 31(1), 1-10.
- Mäder U., Detzner K., Kober F., Abplanalp H., Baer T. & Cloet V. (2016): FEBEX-DP – Plug Overcoring and Concrete-Bentonite Interface Sampling prior to Dismantling. Nagra Arbeitsbericht NAB 16-10.
- Madina, V. (2016): Corrosion study of FEBEX-DP Components. Arbeitsbericht Nagra, NAB 16-54, 107 pp. Wettingen.
- Madina, V., & Azkarate, I. (2004): FEBEX project post-mortem analysis: Corrosion Study. Enresa S.A. Madrid: Enresa S.A.
- Manceau, A., Lanson, B., Drits, V., Chateigner, D., Gates, W. & Wu, J., et al. (2000a): Oxidation-Reduction mechanism of iron in dioctahedral smectites, 1. Crystal chemistry of oxidized reference nontronites. *Am. Mineral* 85, 153-172.
- Martínez, V., Abós, H. & García-Siñeriz, J.L. (2016): FEBEX-e: Final sensor data report (FEBEX *in situ* Experiment). Nagra Arbeitsbericht NAB 16-19.
- McCafferty, E. (2010): Introduction to Corrosion Science, Chapter 1, Springer.
- Mehra, O.P. & Jackson M.L. (1960): Iron oxide removal from soils and clays by a dithionite-citrate system buffered with sodium bicarbonate, Seventh National Conference on Clays and Clay Minerals, 1960.
- Meier LP & Kahr G. (1999): Determination of the Cation Exchange Capacity (CEC) of clay minerals using the complexes of copper(II) ion with triethylenetetramine and tetraethylenepentamine. *Clays Clay. Miner.* 47(3): 386-388.
- Moore, D., & Reynolds, R. (1989): X-Ray diffraction and the identification and analysis of Clay Minerals. Oxford University Press, 332. .
- Moore, D., & Reynolds, R. (1997): X-Ray Diffraction and the identification and analysis of clay minerals. Oxford University Press, 378.
- NEA-OCDE. (2003): Engineered Barrier Systems and the Safety of Deep Geological Repositories. State-of-the art Report. OECD Publications. Paris.
- Pusch, R. (1994): Waste Disposal in Rock. New York: Elsevier.
- Pusch, R. (1999): Is montmorillonite-rich clay of MX-80 type the ideal buffer for isolation of HLW? Technical Report TR 99-33. Swedish Nuclear Fuel and Waste Management (SKB), Stockholm.
- Pusch, R., Börgesson, L. & Ramqvist, G., (1985): Final report of the Buffer Mass Test. Volume II: Test Results. Nagra Technical Report NTB 85-59.
- Rey, M., Sanz , F.-J. & García-Siñeriz, J.-L. (2015): FEBEX-DP Post-mortem analysis: Sensors. Nagra Arbeitsbericht NAB 16-20.

- Rosso, K.M., Yanina, S.V., Gorski, C.A., Larese-Casanova, P. & Scherer, M.M. (2010): Connecting observations of hematite (α -Fe₂O₃) growth catalyzed by Fe(II). *Environmental Science & Technology*, 44: 61-67.
- Sakaki, T. (2016): FEBEX-DP Post-mortem analysis: TDR. Nagra Arbeitsbericht NAB 16-21.
- Sawhney, B.L. (1970): Potassium and cesium ion selectivity in relation to clay mineral structure. *Clays Clay. Miner.* 18: 47-52.
- Schaefer, M.V., Gorski, C.A. & Scherer, M.M. (2011): Spectroscopic evidence for interfacial Fe(II)-Fe(III) electron transfer in a clay mineral. *Environmental Science & Technology*, 45: 540-545.
- Schlegel, M.L., Bataillon, C., Brucker, F., Blanc, C., Prêt, D., Foy, E. & Chorro, M. (2014): corrosion of metal iron in contact with anoxic clay at 90 degrees C: Characterization of the corrosion products after two years of interaction. *Applied Geochemistry*, 51: 1-14.
- Shaw, H.G. (1972) The preparation of orientated clay mineral specimens for X-ray diffraction analysis by a suction-onto-ceramic method. *Clay Minerals*, 9, 349-350.
- Soltermann, D. et al. (2013): Fe(II) sorption on a synthetic montmorillonite. A combined macroscopic and spectroscopic study. *Environmental Science & Technology*, 47(13): 6978-6986.
- Soltermann, D. et al. (2014): Fe(II) uptake on natural montmorillonites. I. Macroscopic and spectroscopic characterization. *Environmental Science & Technology*, 48(15): 8688-8697.
- Svensson, D. (2015a): Saponite formation in the ABM2 iron-bentonite field experiment at Äspö hard rock laboratory, Sweden. Pp. 168–169 in: *Clays in natural and engineered barriers for radioactive waste confinement, sixth International Meeting, program & abstracts*, Brussels, Belgium.
- Svensson, D. (2015b): The bentonite barrier – Swelling properties, redox chemistry and mineral evolution. Ph. D. thesis. ISBN 978-91-7422-385-9, Lund, 184 pp.
- Svensson, D. Dueck, A., Nilsson, U., Olsson, S., Sandén, T., Lydmark, S., Jägerwall, S., Pedersen, K. & Hansen, S. (2011): Alternative buffer material - Status of the ongoing laboratory investigation of reference materials and test package 1, SKB Technical Report 11-06, Stockholm, Sweden.
- Svensson, P.D., Hansen, S. (2013): Redox chemistry in two iron-bentonite field experiments at Äspö hard rock laboratory, Sweden: an XRD and Fe K-edge XANES study. *Clays and Clay Minerals*, 61, 566-579.
- US-DOE.(U.S. Department of Energy) (2014): Evaluation of Options for Permanent Geologic Disposal of Spent Nuclear Fuel and High-Level Radioactive Waste. Vol I. Sandia National Laboratories SAND2014-0187P.
- Uyama et al. (2016): Oxide scale analysis of the carbon steel exposed to bentonite after electrochemical test. ICC2016 Conference.

- Villar, M.V. (2002): Thermo-hydro-mechanical characterisation of a bentonite from Cabo de Gata. A study applied to the use of bentonite as sealing material in high level radioactive waste repositories. Publicación Técnica Enresa 01/2002. 258 pp. Madrid.
- Villar, M.V. et al. (2006): FEBEX Project Final Report - Post-mortem bentonite analysis, Enresa, Madrid - Spain.
- Villar, M.V. & Lloret, A. (2004): Influence of temperature on the hydro-mechanical behaviour of a compacted bentonite. *Appl. Clay Sci.* 26, 337– 350.
- Villar, M.V., Fernández, A.M., Romero, E., Dueck, A., Cuevas, J., Plötze, M., Kaufhold, S., Dohrmann, R., Iglesias, R.J., Sakaki, T., Zheng, L., Kawamoto, K. & Kober, F. (2017): FEBEX-DP postmortem THM/THC analysis report (draft). Nagra Arbeitsbericht NAB 16-17.
- Villar, M.V., Iglesias, R.J., Abós, H., Martínez, V., de la Rosa, C. & Manchón, M.A. (2016): FEBEX-DP on-site analyses report. Nagra Arbeitsbericht NAB 16-12.
- Wersin, P., Birgersson, M., Olsson, S., Karnland, O. & Snellman, M. (2007): Impact of corrosion-derived iron on the bentonite buffer within the KBS-3H disposal concept - the Olkiluoto site as case study. Posiva Report 2007-11, Olkiluoto, Finland.
- Wersin, P., Jenni, A. & Mäder, U.K. (2015): Interaction of corroding iron with bentonite in the ABM1 experiment at Äspö, Sweden: a microscopic approach. *Clays and Clay Minerals*, 63(1): 51-68.
- Wilson, J.C., Benbow, S., Sasamoto, H., Savage, D. & Watson, C. (2015): Thermodynamic and fully-coupled reactive transport models of a steel-bentonite interface. *Applied Geochemistry*, 61: 10-28.
- Xia, X. et al. (2005): Corrosion of carbon steel in compacted bentonite and its effect on neptunium diffusion under reducing condition. *Applied Clay Science*, 28(1-4): 89-100.
- Yanina, S.V. & Rosso, K.M. (2008): Linked reactivity at mineral-water interfaces through bulk crystal conduction. *Science*, 320: 218-222.

Appendix A

Summary of observations from dismantling (Nagra)

Section 36

Note: this section has a complex history: section 36 was a central part of Heater 2 during initial construction, section was opened and ventilated in 2002, the heater was replaced by a dummy and partially re-instrumented in 2002.

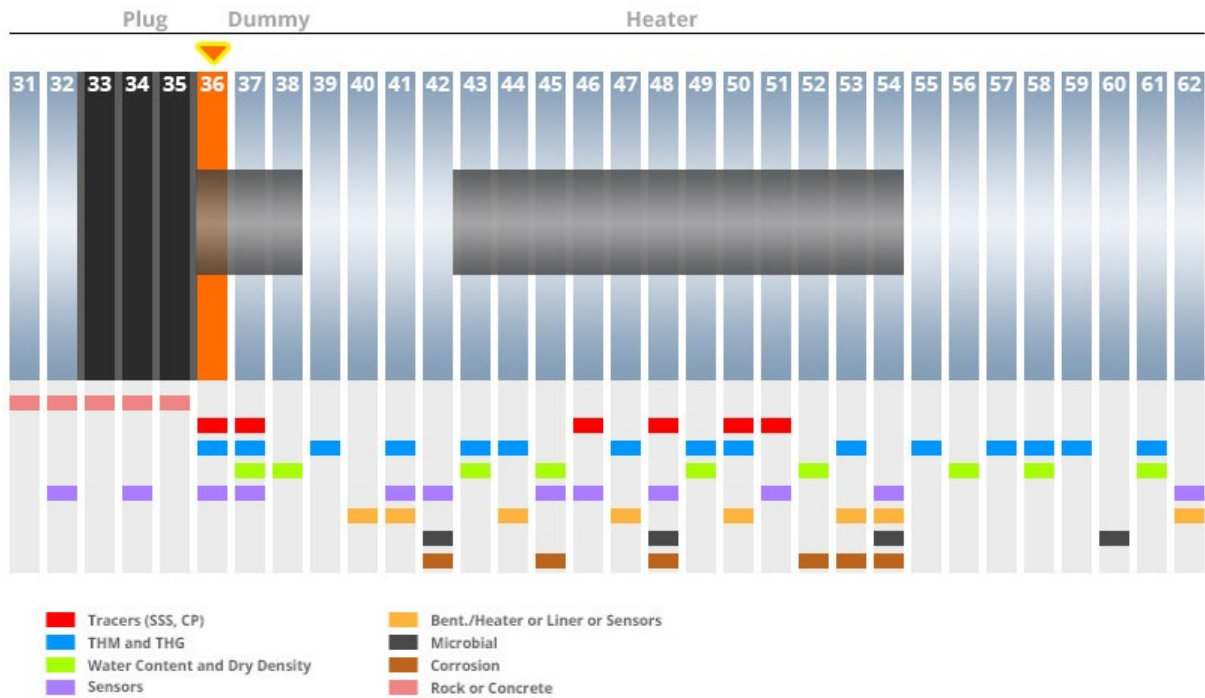


Fig. S-36-1: Location of dismantling Section 36.



Fig. S36-2: Side view of first section of the liner showing the perforated liner with holes filled by intruded bentonite.



Fig. S36-3: UPPER IMAGES: Cut liner lid showing frontal part of dummy and bentonite in between the liner and the dummy. LOWER IMAGES: Cut piece of perforated liner with bentonite that was squeezed through the liner holes (sample Obayashi BM-C-35-1).

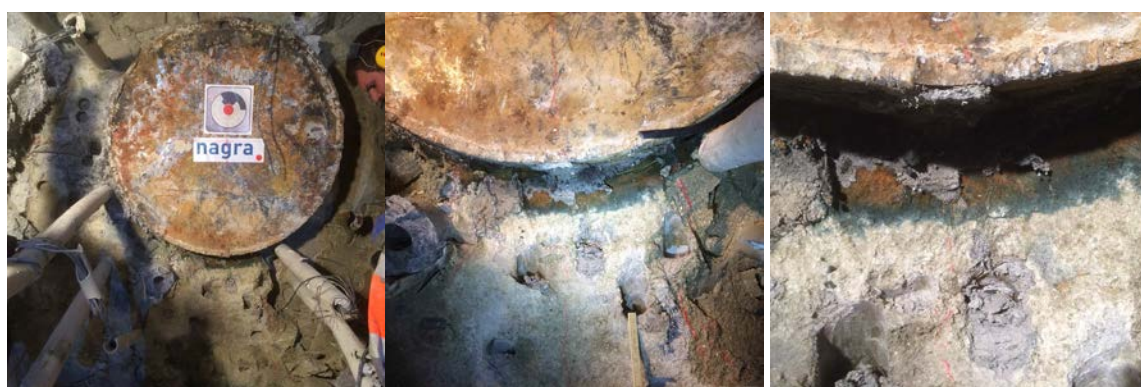


Fig. S36-4: Discoloration zones suggesting various redox conditions around the bottom part of the liner.



Fig. S36-5: Bentonite block B-B-36-3 showing negative marks of liner and oxidation margins.



Fig. S36-6: Corrosion halos above of cable duct to the right (3 o'clock).

Section 37

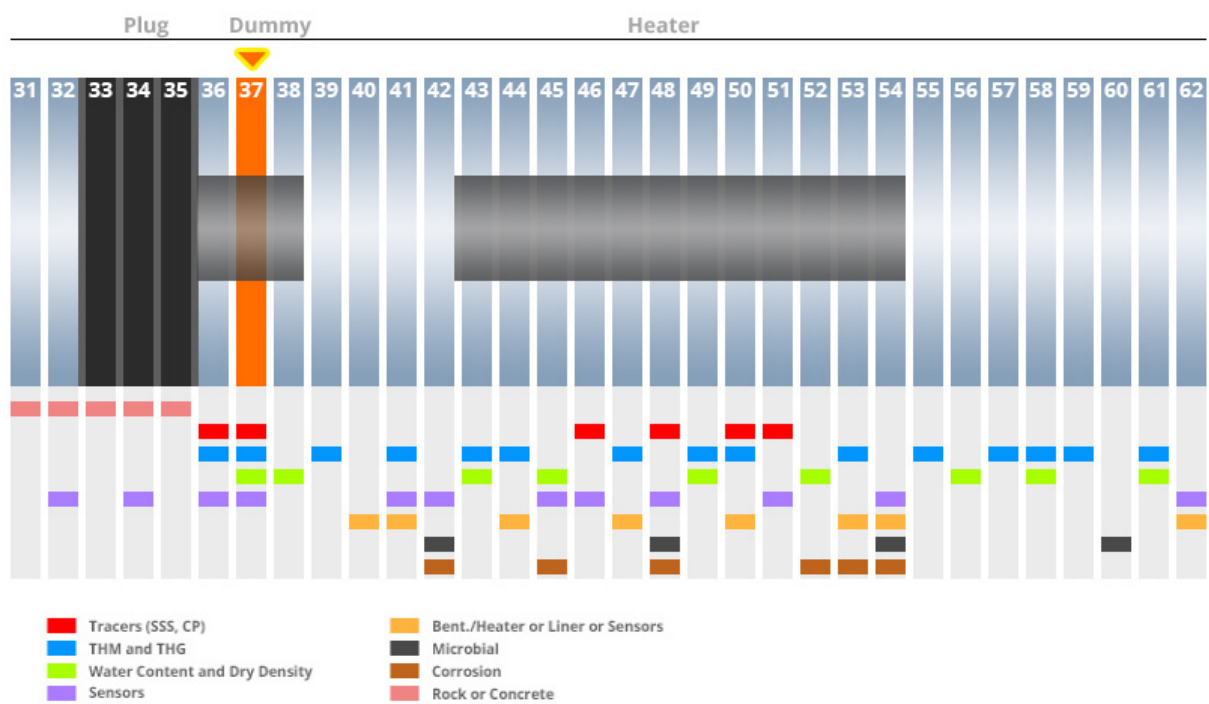


Fig. S37-1: Location of dismantling Section 37.



Fig. S37-2: LEFT: Cut of liner (more details of liner cutting see NAB 16-068). See also Fig 38-4; RIGHT: Corrosion feature at the bentonite-granite interface above the cable duct (12 o'clock position).

Section 38

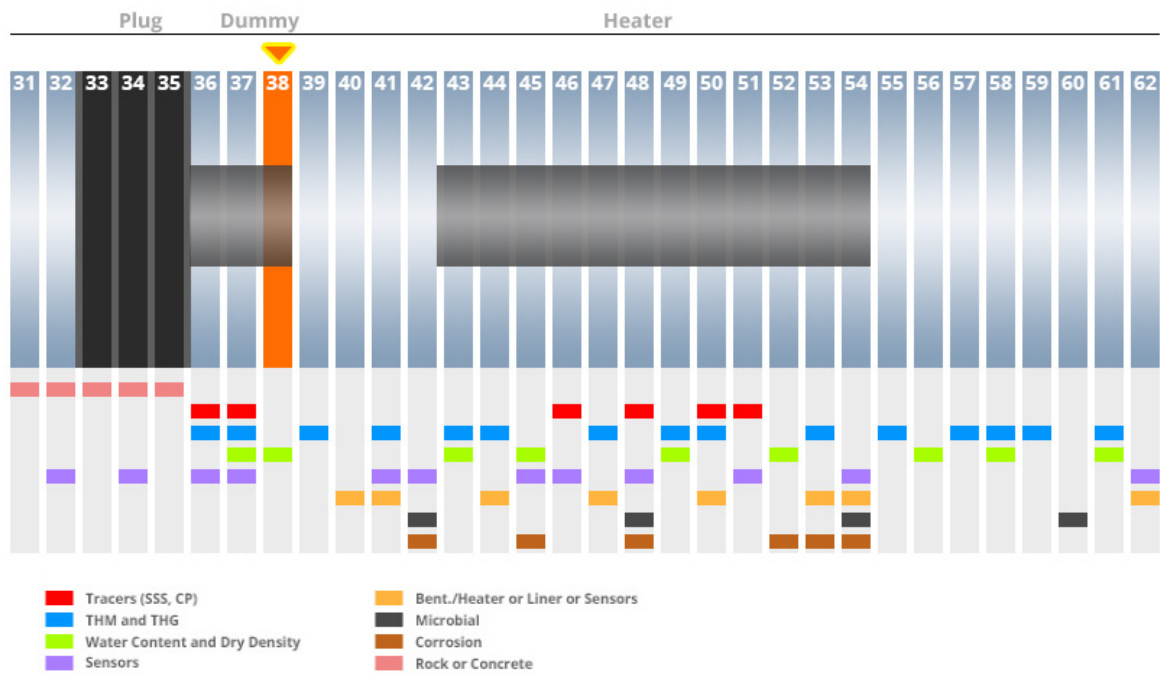


Fig. S38-1: Location of dismantling Section 38.



Fig. S38-2: Images of the liner-bentonite interface.

Section 38 – Dummy cutting

Fig. S38-4: Liner-dummy-bentonite interface.



Fig. S38-4: (cont.) Liner-dummy-bentonite interface.

Section 41

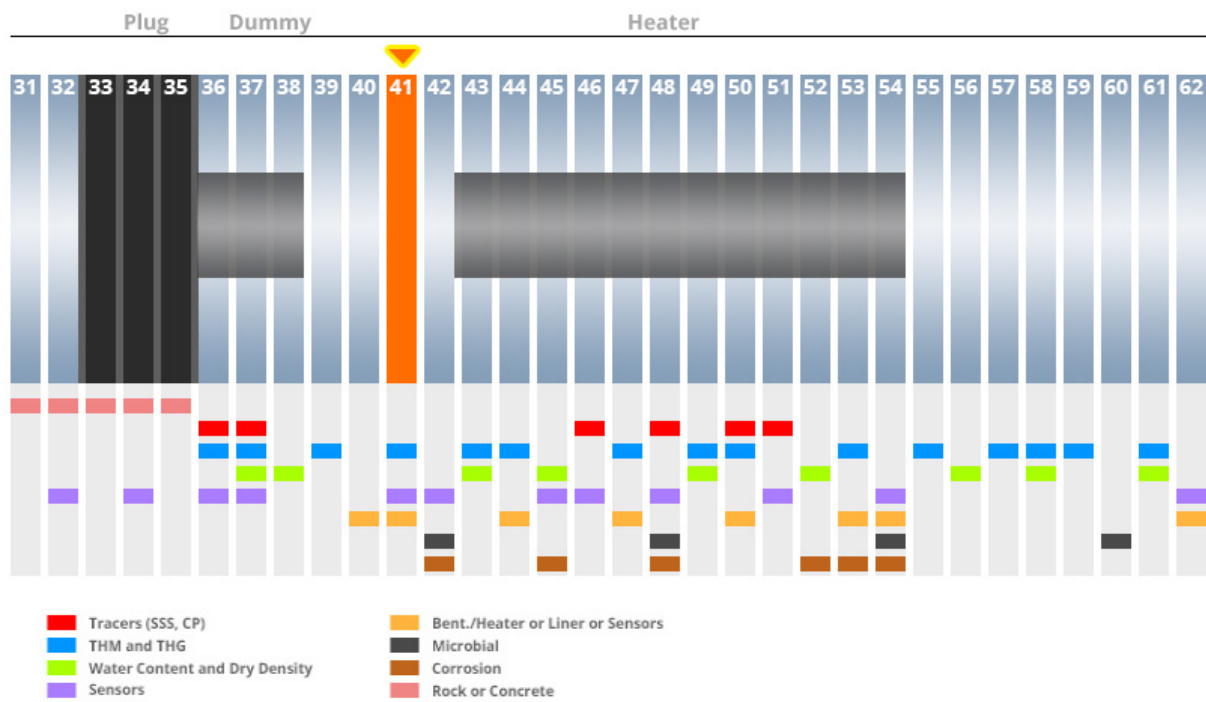


Fig. S-41-1: Location of dismantling section 41

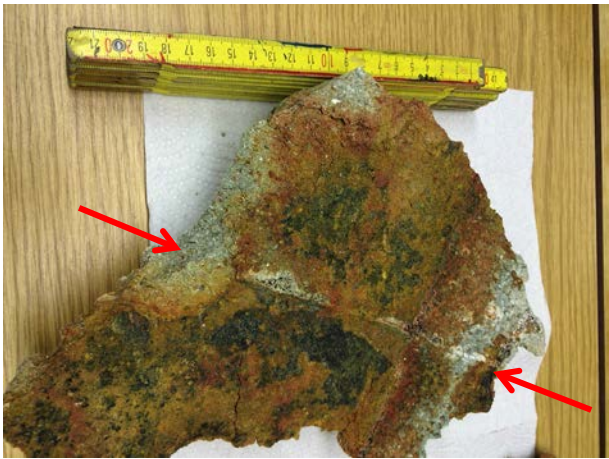


Fig. S41-2: Bentonite piece that was in contact with the liner, showing a oxidation features. Intact bentonite block boundary is clearly visible (red arrows).



Fig. S41-3: Bentonite discoloration (oxidation/reduction rings surrounding the upper part of the liner



Fig. S41-3: Cont.



Fig. S41-4: Bentonite block B-B-41 -1 displaying bentonite discolorations and the bentonite protrusion marks from the liner.



Fig. S41-5: Corrosion of pore pressure sensor S-S-41-10.



Fig. S41-6: Corrosion features inside the liner.

Section 42

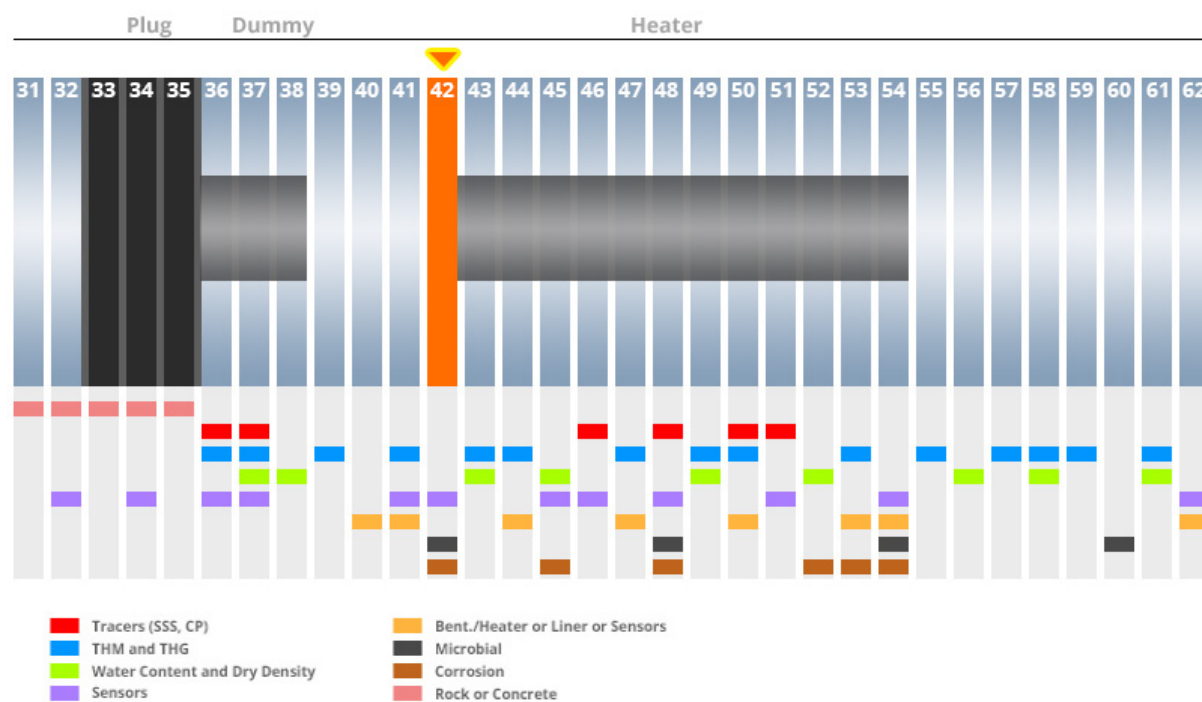


Fig. S42-1: Location of dismantling Section 42.



Fig. S42-2: Corrosion of a leftover metal anchor in the granite wall.



Fig. S42-4: Bentonite discoloration in front of the heater inside the liner.

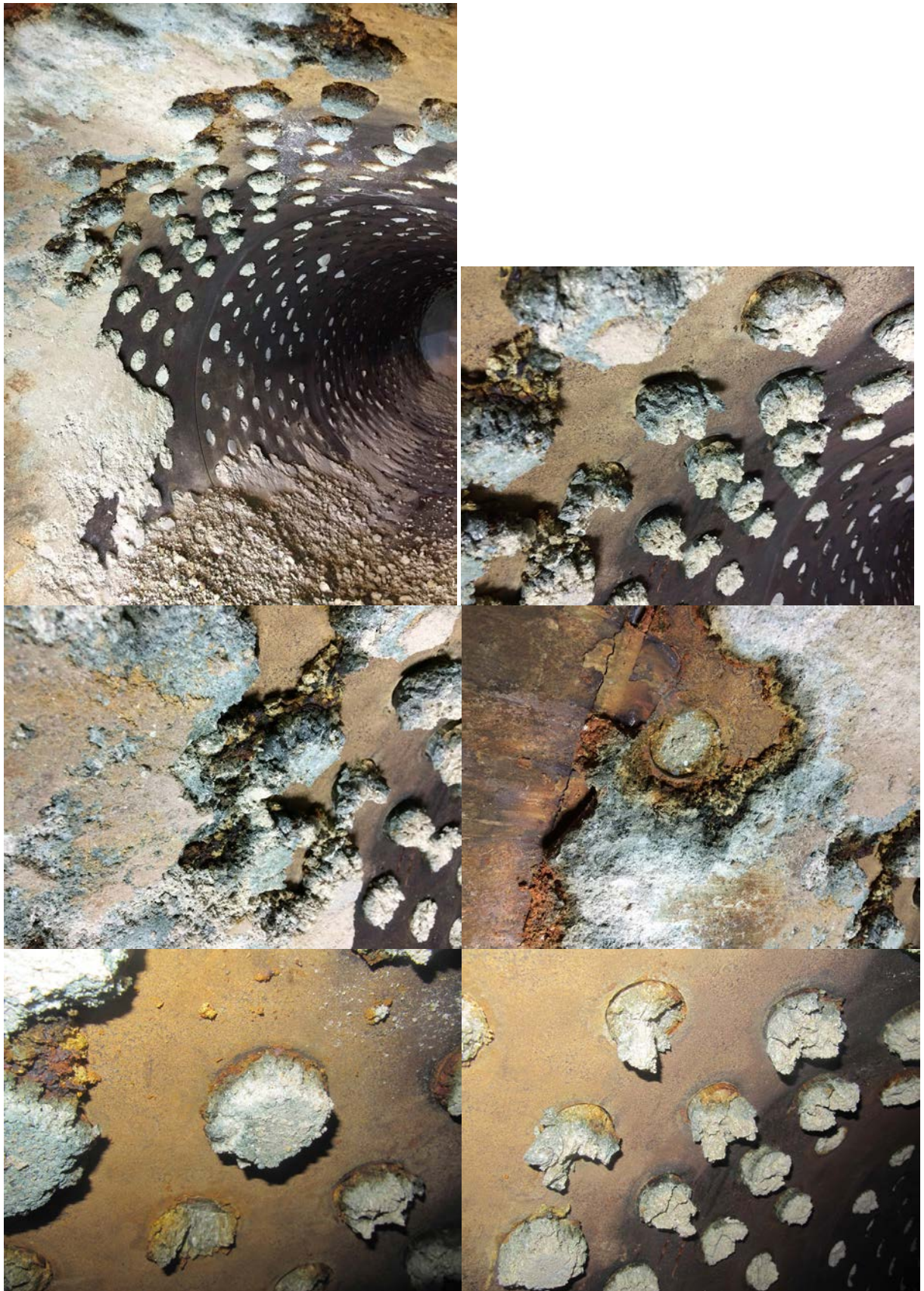


Fig. S42-5: Corrosion halos/features at bentonite protrusions inside the liner.



Fig. S42-6: Corrosion features at filters of gas pipes.



Fig. S42-6: Discolorations and the anchor positions of displacement sensors S-S42-1 (left) and S-S42-2 (right).



Fig. S42-7: Cont.



Fig. S42-8: Discolorations in front of an abandoned drill bit (see more details in Section 44).

Section 44

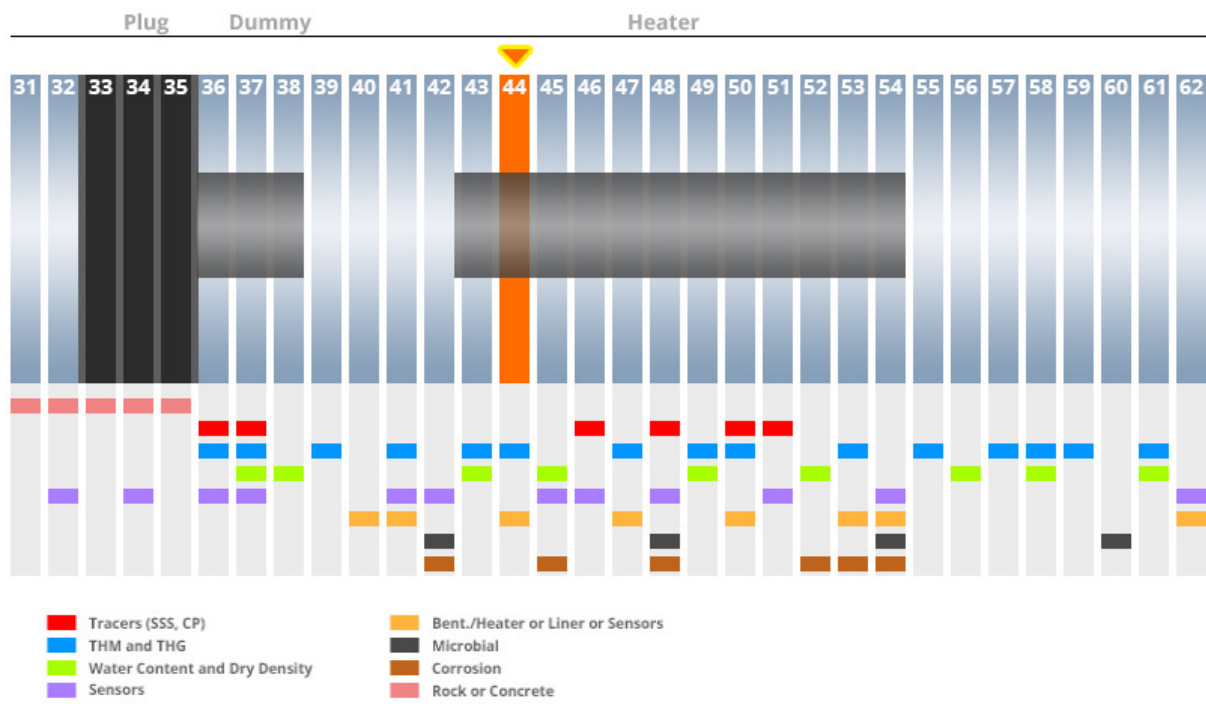


Fig. S44-1: Location of dismantling Section 44.



Fig. S44-2: Discolorations surrounding an abandoned drill bit. Drilling and bit were abandoned due to drilling problems during the partial dismantling in 2002 when further gas-water pipes were installed.

Section 46

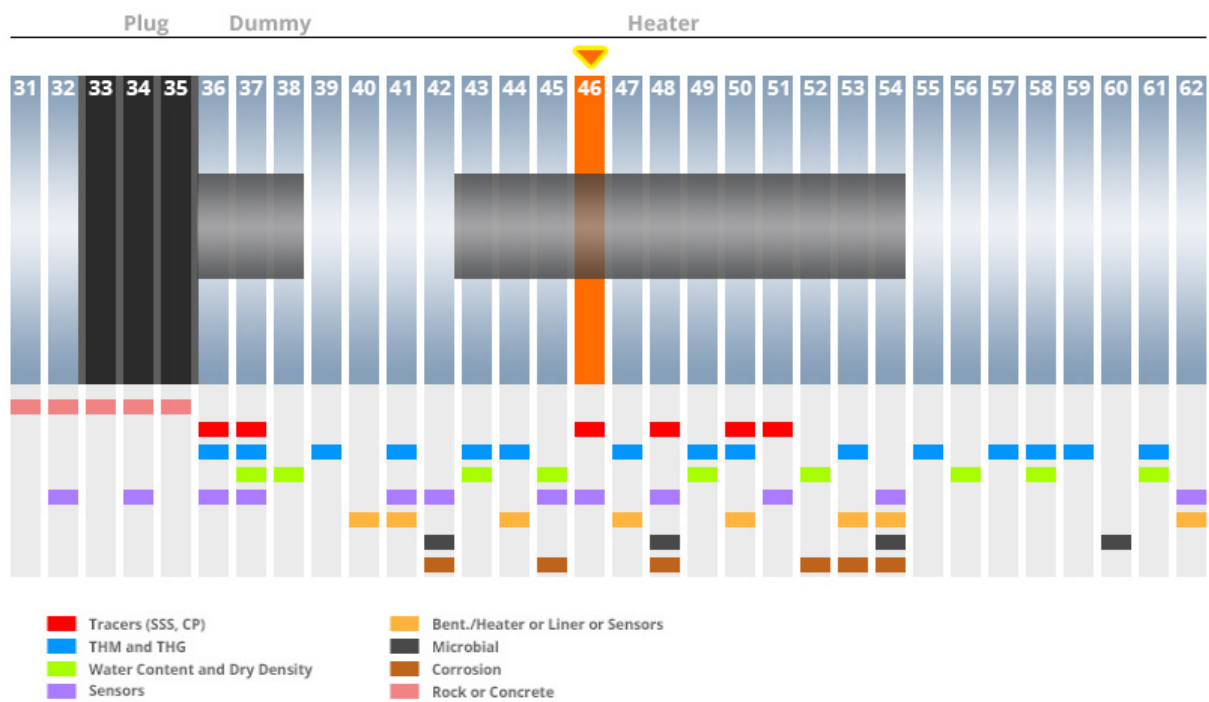


Fig. S46-1: Location of dismantling Section 46.



Fig. S46-2: Bentonite discoloration halos surrounding the roof cable duct and a piece thereof that was in contact with the bentonite.



Fig. S46-3: Bentonite discoloration related to the corroding fisurometer (see further details in Section 47).

Section 47

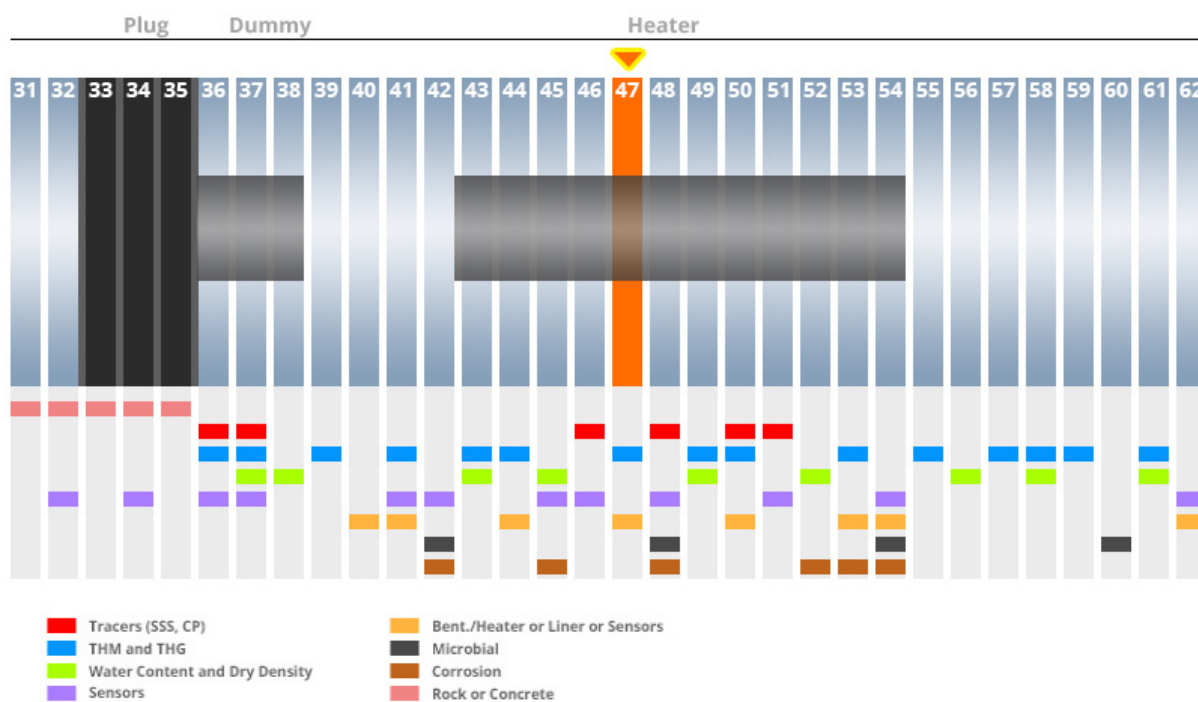


Fig. S47-1: Location of dismantling Section 47.



Fig. S47-2: Bentonite discoloration related to the corroding fissurometer (eventually filled with water) covering the outer and middle bentonite blocks.



Fig. S47-3: Dismantled fissurometer.

Section 48

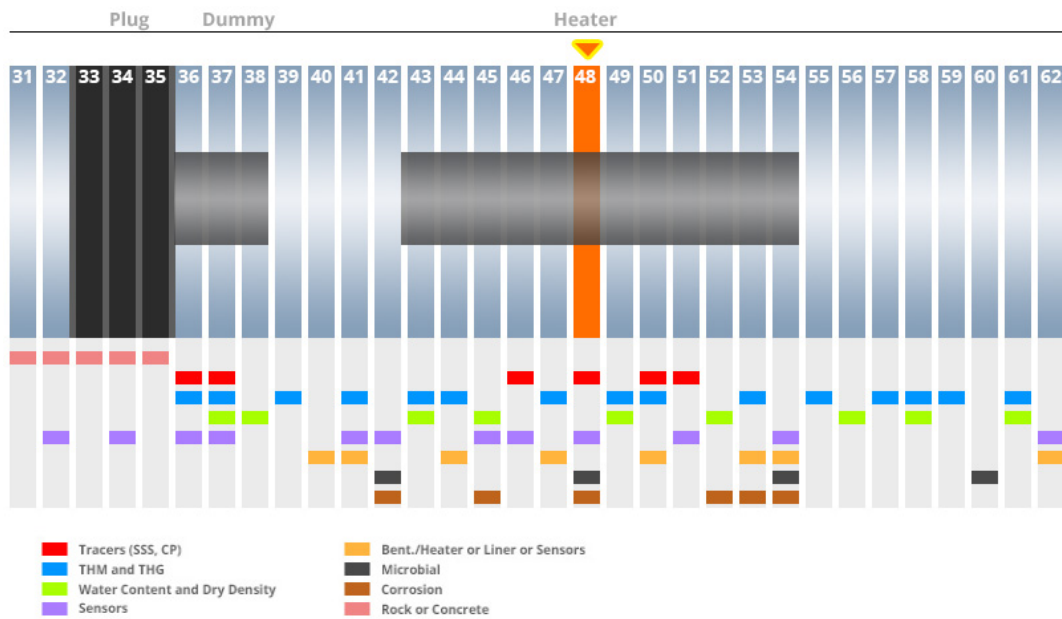


Fig. S48-1: Location of dismantling Section 48.



Fig. S48-2: Bentonite corrosion halos around the corroded displacement sensor S-S-48-30. The square at the granite gallery wall (centre left) and the blueish colour discolorations in the bentonite are related to the corrosion of the fissurometer (see also Fig. S-48-1 & Fig. S-48-3).



Fig. S48-3: Limited corrosion of extensometer in-between bentonite S-S-48-28/ SBF2-02.

Section 48 - heater

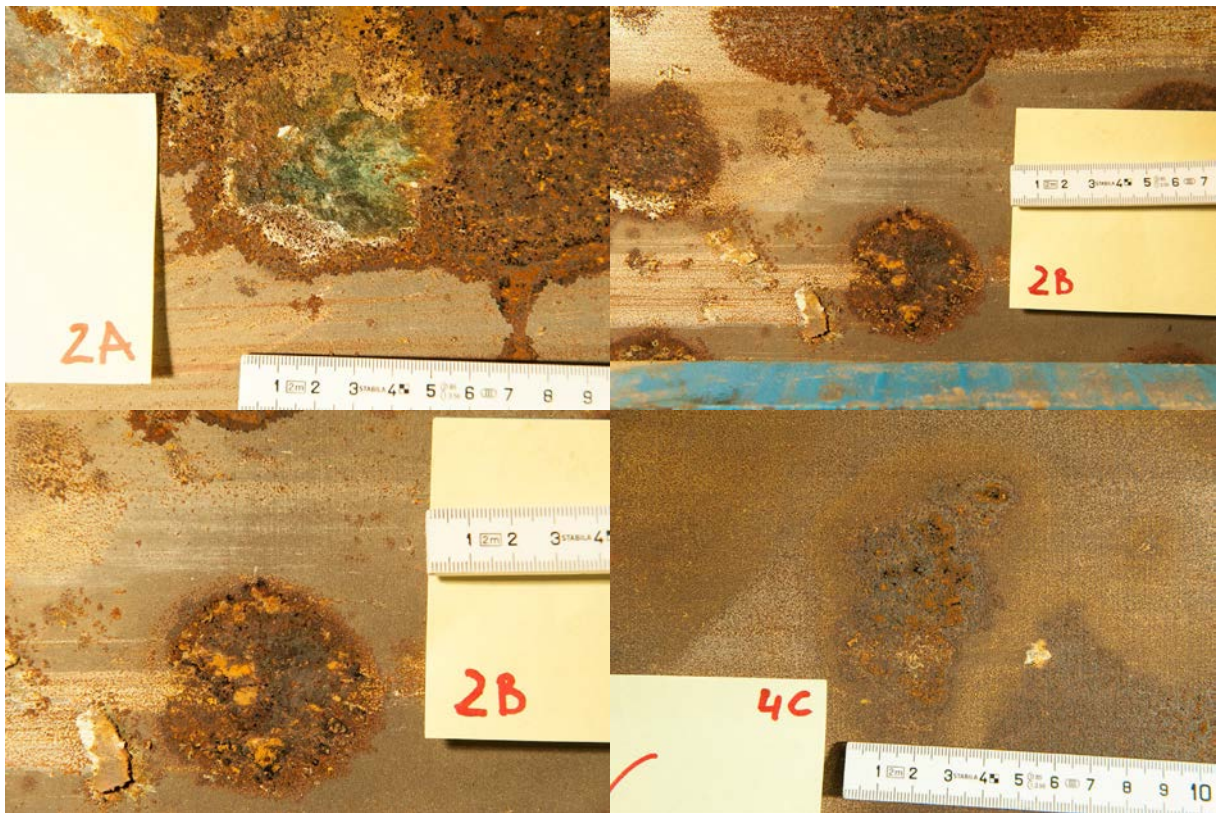


Fig. S48-4: Corrosion spots of the heater after dismantling (for numbering see auxiliary information on heater corrosion features, see NAB 16-054 and NAB 16-68).

Section 48 – coupons



Fig. S48-5: Coupon racks after dismantling showing weak enclosure of racks in the prefabricated emplacement hollows, where bentonite showed low moisture content due to proximity of the heater. LEFT PHOTO: carbon steel rack with partial covering (A1, left) and completely covered stainless steel rack (A2, right), RIGHT PHOTO: “cleaned” stainless steel rack A2 (see more information on coupon dismantling and investigations in NAB 16-054 and NAB 16-068).

Section 52

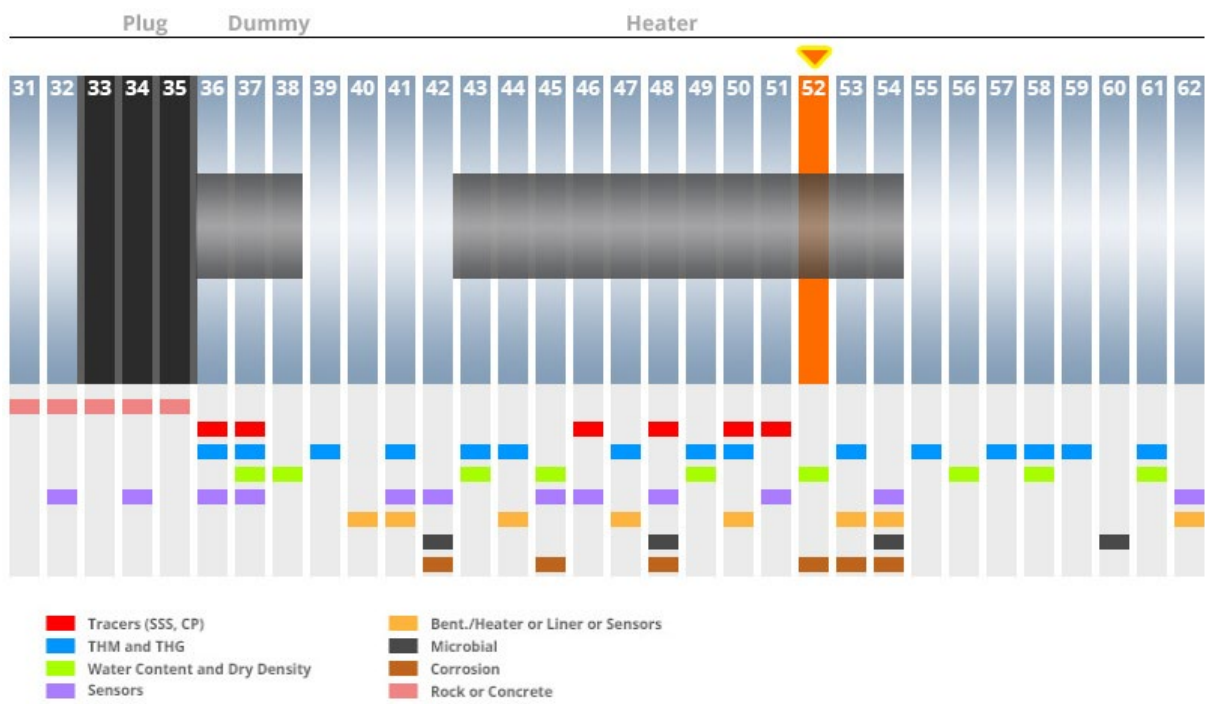


Fig. S52-1: Location of dismantling Section 52.



Fig. S52-1: Bentonite reduction zones at around 10 o'clock at the interface rock-iodine tracer-bentonite.

Section 54

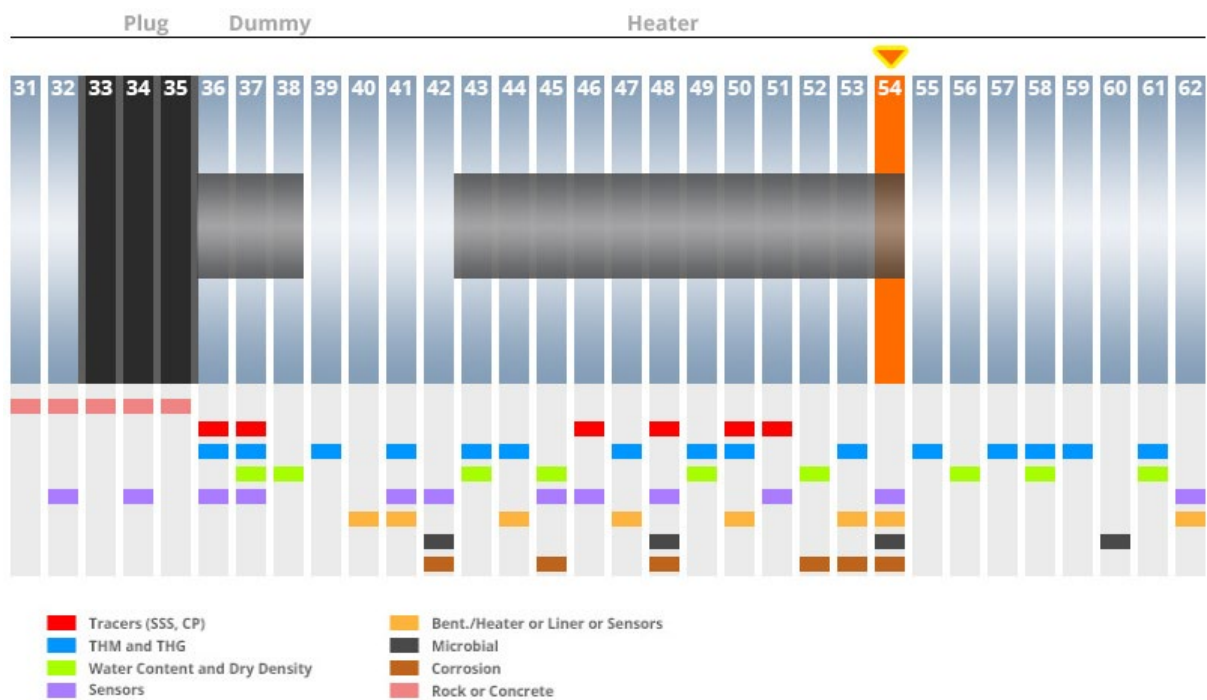


Fig. S54-1: Location of dismantling Section 54



Fig. S54-2: Corrosion halos when approaching and during dismantling of displacement sensor S-S-54-15 (see for more information in NAB 16-054).



Fig. S54-3: Corrosion feature around displacement sensor S-S-54-14 (see NAB 16-054 for more information).

Section 61

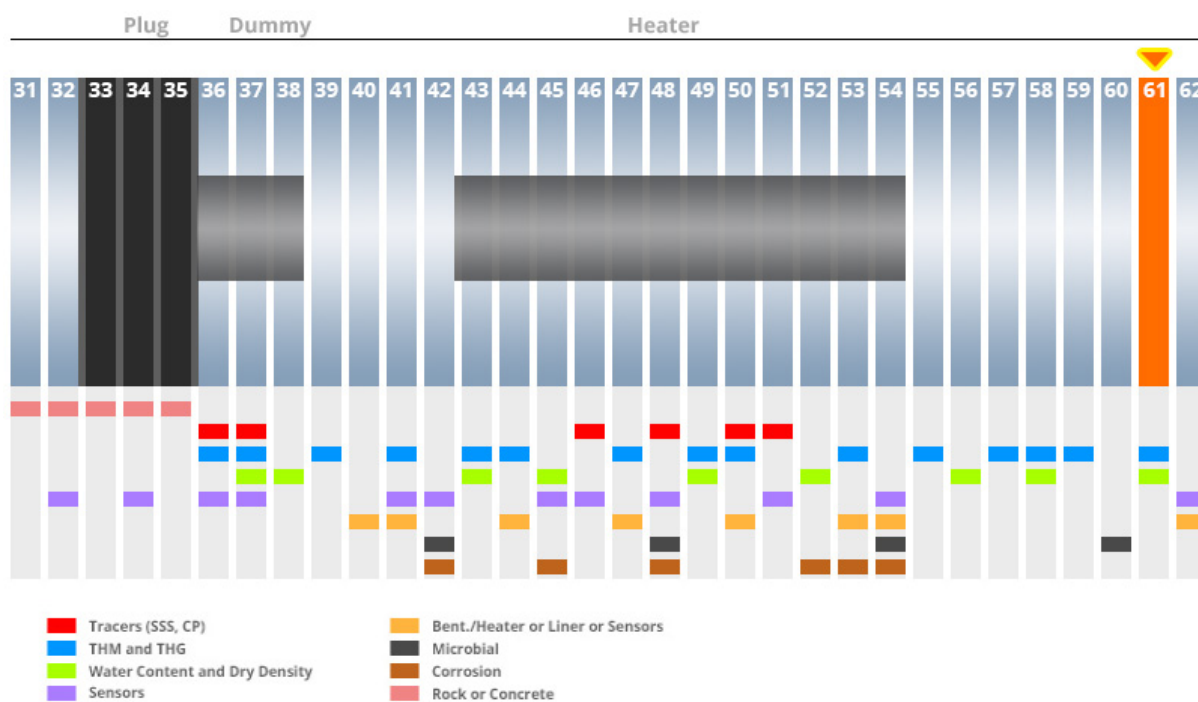


Fig. S61-1: Location of dismantling Section 61.



Fig. S61-2: Corrosion halos in bentonite below the center of the gallery at the interface to temperature sensor T-SB-02.

Appendix B

Additional Analyses on FEBEX-DP Copper Coupons (TECNALIA)

INDEX

- 1 STUDIES TO BE CARRIED OUT BY TECNALIA
- 2 PREVIOUS DATA
- 3 OPTICAL AND SEM/EDS ANALYSES ON METALLOGRAPHIC PROBE
REF.4A1
 - 3.1 0 mm depth
 - 3.2 5 mm depth

1 STUDIES CARRIED OUT BY TECNALIA

After discussions between the Swedish Nuclear Fuel and Waste Management Co (SKB), Nagra and Tecnalia, the following additional analyses were performed on the Febex DP copper ETP (99% Cu) coupons denoted 4A1 and 4A2:

1) Embedded metallographic sample reference 4A1

- Analysis of 3 pits, at present depth:
 - o These pits were selected from 3 areas previously designated by SKB.
 - o For each pit, Energy Dispersive Spectrometry (EDS) analysis were carry out to determine the spatial distribution of the elements in the corrosion products. One map of the different elements detected in the EDS analyses, was performed for one pit.
 - o For each of the three areas, a Scanning Electron Microscope (SEM) micrograph of the maximum pit depth was obtained. Micrographs were recorded
 - o The maximum pit depth was estimated with a micrometer microscope
- The metallographic sample was polished again, approximately 6 mm depth, in order to repeat the steps of the above procedure.

2) Uncut sample ref. 4A2

- Estimation of the average general corrosion rate according to the ASTM G1 standard.
- The mass losses resulting from the cleaning cycles were provided.
- Photographs of the descaled coupon were provided.

2 PREVIOUS DATA

Visual appearance of Cu-ETP coupons

The surface of the Copper ETP coupons references 4A1 and 4A2, show a brownish-red color, with greenish areas mixed with bentonite, Figures 1 and 2. Uniform general corrosion appears to be the predominant mechanism observed, with a quite adherent oxide layer. Only when the adhered bentonite in coupon ref. 4A2 is removed with a plastic brush, there are observed small areas of localized corrosion in one edge of the coupon, Figure 2.



Figure 1: Photographs showing coupon ref. 4A1 (one side and the other)

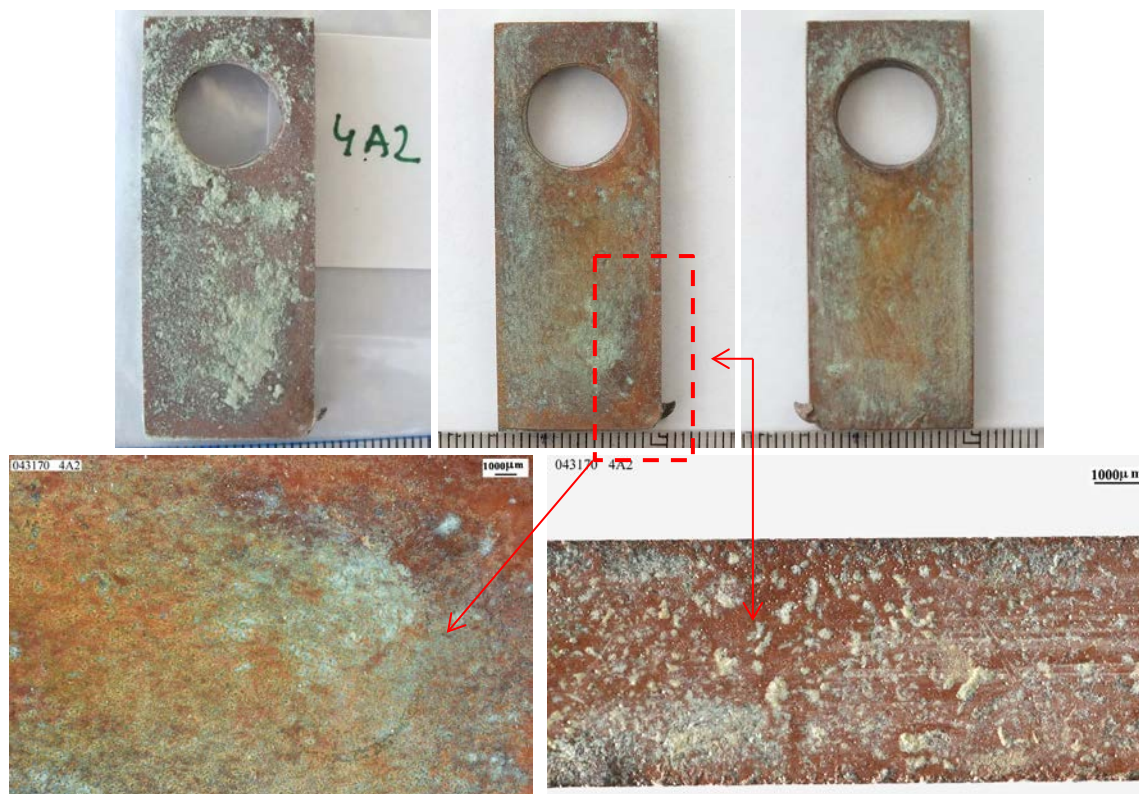


Figure 2: Photographs showing coupon ref. 4A2 (one side and the other), and details of the corroded surface

Corrosion products analysis: SEM/EDS and XRD

EDS spectra indicate that the surface of coupon ref. 4A1 is composed principally of copper and oxygen. Chloride was detected in all the corrosion products examined. The amount of chloride detected was higher for the blue greenish surface. Silicon, aluminum, magnesium and calcium proceeding from the adhered bentonite were also detected. The XRD spectrum of the surface of coupon ref. 4A1 reveals that the oxide layer generated could correspond to the molecular cuprite Cu_2O . The semi-quantitative results obtained in the EDS analyses carried out on copper alloy coupons are given in Table 1.

EDS analysis	Element (wt%)										
	C	O	Mg	Al	Si	Cl	K	Ca	Fe	Cu	Total
4A1 general corrosion surface	2.16	22.77	1.97	2.99	7.06	0.75		0.61	0.39	61.29	100.00
4A1 blue-greenish surface	4.89	38.78	2.68	4.58	12.20	5.65	0.31	1.20	0.91	28.80	100.00

Table 1: Semi-quantitative elemental chemical composition obtained in the EDS analyses carried out on copper coupon ref. 4A1

Metallographic study

A cross section extracted from coupon ref. 4A1 was prepared for metallographic study by embedding this cross section in resin and polishing. This metallographic probe was further studied by optical and SEM microscopy in order to study the morphology and extension of the corrosion damage.

Optical micrographs in Figure 3 show a slight localized corrosion on one side of the copper coupon ref. 4A1. This small localized corrosion area was also observed in the visual examination of copper coupon ref. 4A2 (Figure 2). The maximum penetration depth for this zone is about 100 microns. Apart from this, the copper coupon shows a generalized corrosion.

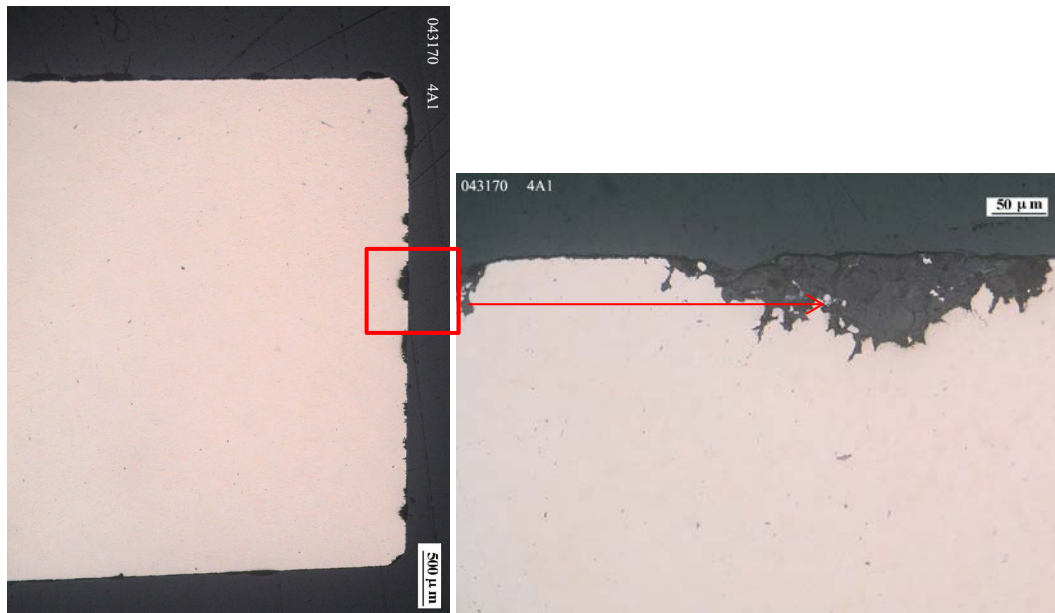


Figure 3: Optical micrographs of section of copper alloy ref. 4A1. Without metallographic etching

In order to obtain more information about the composition of the corrosion products inside copper pits, EDS analyses were conducted to determine the spatial distribution of the elements. Figure 4 shows the back-scattered electron micrograph obtained in a pit section from coupon ref. 4A1, together with the maps of the different elements. The obtained results indicate that the copper pit is filled with the elements making up the bentonite. Copper is not detected inside the pit.

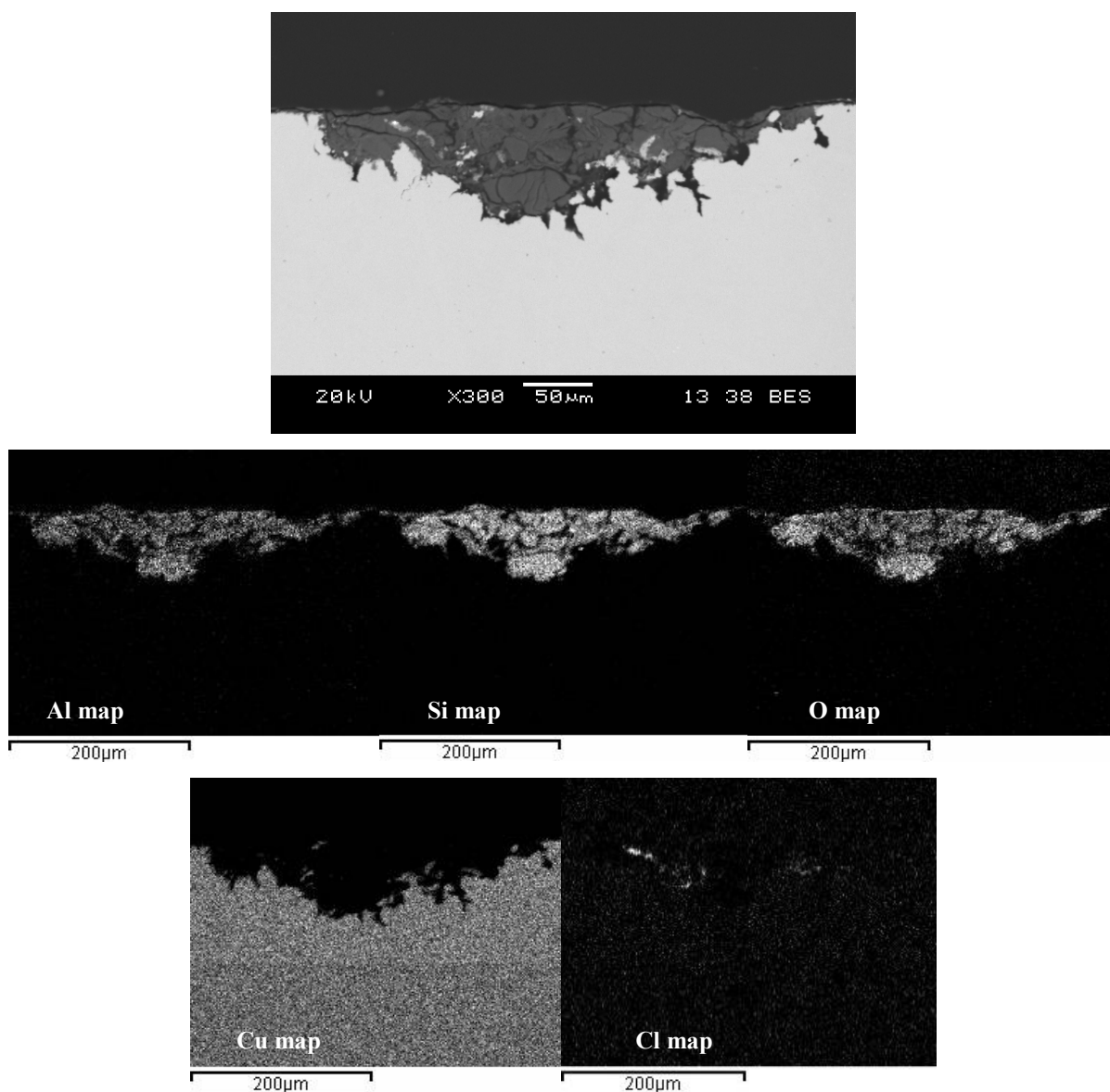


Figure 4: Back-scattered electron micrograph of pit section from coupon ref. 4A1 and associated element maps

3 OPTICAL AND SEM/EDS ANALYSES ON METALLOGRAPHIC PROBE REF.4A1

Following SKB indications, the metallographic probe ref. 4A1 was examined in zones 1, 2 and 3 suggested by SKB, at 0 and 5 mm depth, in order to study the extension of the corrosion damage (Figure 5).

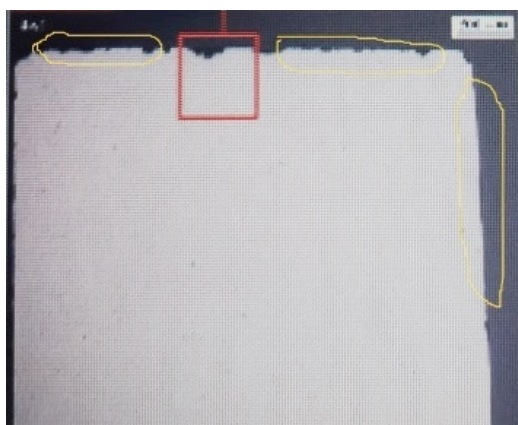


Figure 5: Image of the cross section of metallographic probe ref. 4A1, shown in Figure 4. The yellow lines indicate zones 1, 2 and 3 proposed by SKB for analysis

3.1 0 mm depth

The optical micrograph in Figure 6 shows a cross section of the metallographic embedded coupon ref. 4A1, at 0 mm depth. Zones 1, 2 and 3 are indicated in this micrograph. The section shown in this figure is not exactly the same as the one given in Figure 3. This is because the surface of the original metallographic sample was polished in order to remove some stains and maybe some kind of contamination, due to the elapsed time since the metallographic preparation. This very superficial polishing of the sample removes less than 100 microns of the metallic material.

The optical and SEM micrographs obtained in sections 1, 2 and 3, at 0 mm depth, are shown in Figures 7, 8 and 9, respectively. The EDS analyses carried out in these areas reveal a significant amount of silicon (Si), magnesium (Mg), aluminum (Al) and oxygen (O), which are the main elements making up the bentonite. Figure 10 shows the maps of the different elements for the maximum pit depth in zone 1a, at 0 mm depth. Copper (Cu) is not detected inside the pits, moreover, most of the pits are hollows and filled with the resin used in the metallographic coupon preparation, mainly constituted of carbon (C). It can be seen, that the morphology of pits in zones 1 and 2 -Figures 7 and 8-, is somewhat different from that observed in zone 3 (Figure 9), with more rounded edges. EDS analyses in zone 3, show again a majority presence of Mg, Al and O, but Cu is now detected in the corrosion products/deposits filling the pits. EDS analyses in zone 3 reveal also a significant chloride (Cl) peak.

3.2 5 mm depth

Figure 11 shows the appearance of the metallographic embedded coupon ref. 4A1, at 5 mm depth. Zones 1, 2 and 3 are indicated in this micrograph.

The optical and SEM micrographs obtained in sections 1, 2 and 3, at 5 mm depth, are shown in Figures 12, 14 and 15, respectively. Obtained results are quite similar to those found at 0 mm depth. Pits in zone 1 are quite similar to those observed in zones 1 and 2, for 0 mm depth. They are hollow, and filled with bentonite, see Figures 12 and 13. Pits in zone 2 and 3, with more rounded edges, are filled with the bentonite, but also with copper corrosion products. EDS analyses in zone 2 and 3

reveal also a significant chloride (Cl) peak. Results of the semi-quantitative EDS analysis carried out in coupon ref. 4A1, in zones 1, 2 and 3, at 0 and 5 mm depth are given in Table 2.

The maximum pit depth has been measured on SEM micrographs. Obtained results are given in Table 3. The accuracy of measurement with SEM micrographs is higher than obtained with the micrometer microscope.

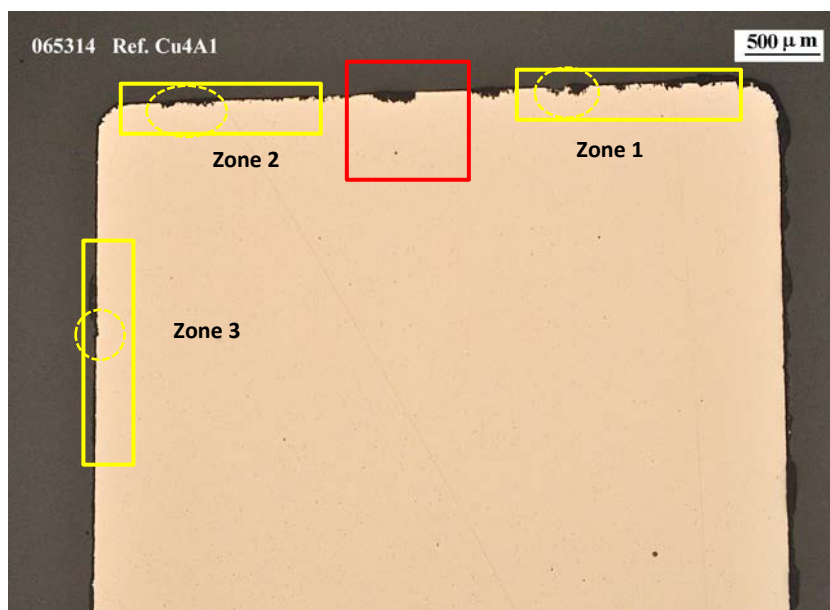


Figure 6: Optical micrograph of section of copper alloy ref. 4A1, at 0 mm depth. Without metallographic etching

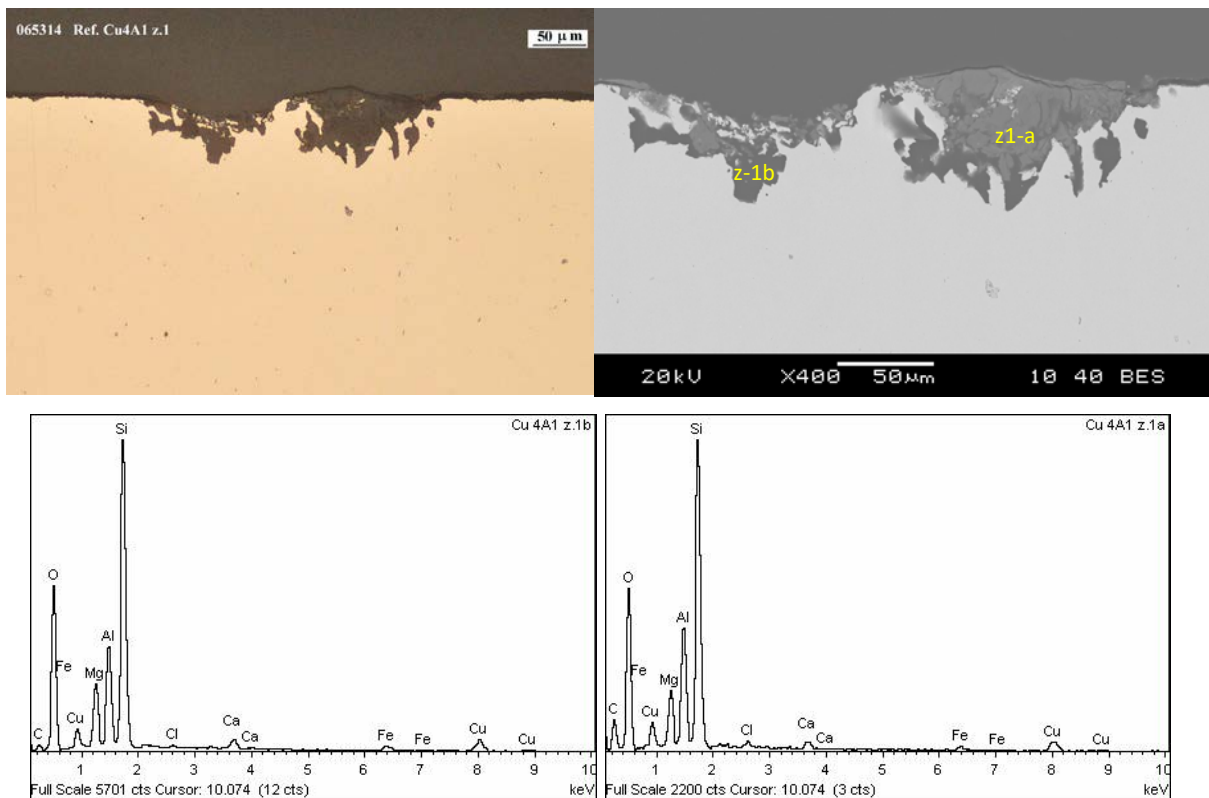


Figure 7: Optical and backscattered SEM micrographs of the maximum pit depth in zone 1, at 0 mm depth, and associated EDS spectra, from coupon ref. 4A1. Without metallographic etching

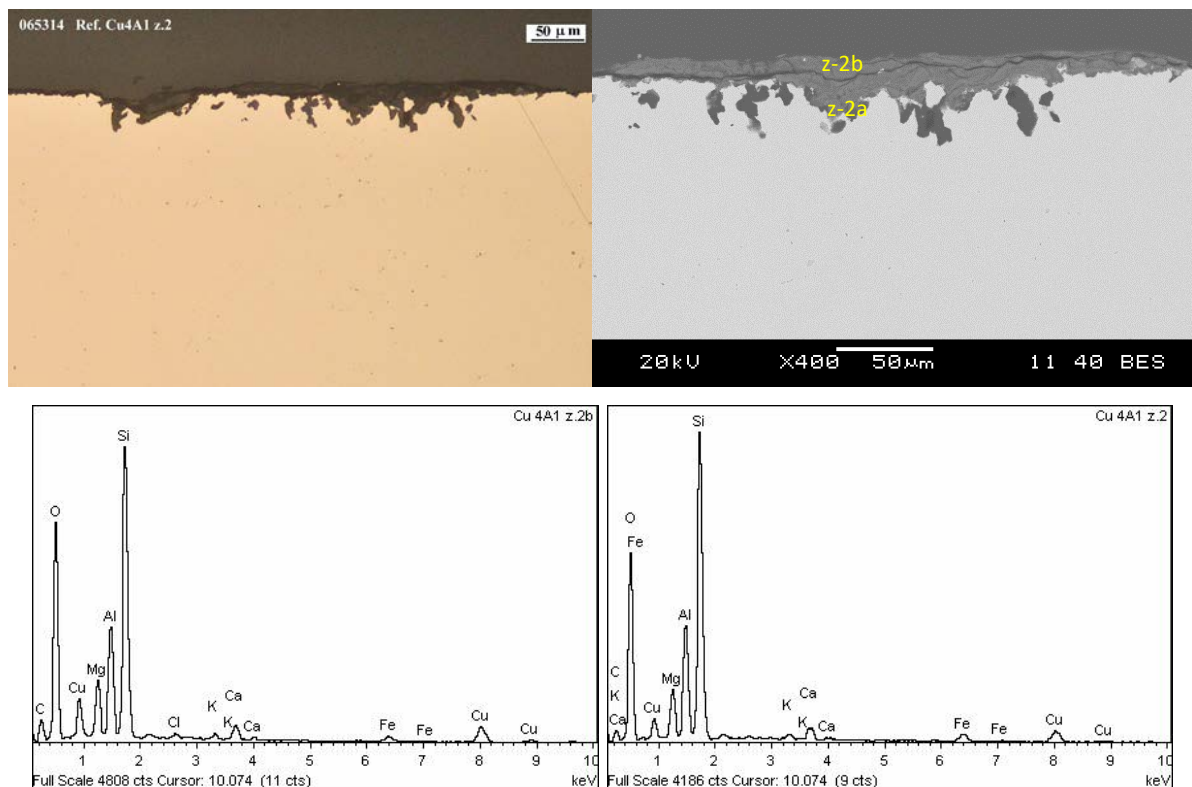


Figure 8: Optical and backscattered SEM micrographs of the maximum pit depth in zone 2, at 0 mm depth, and associated EDS spectra, from coupon ref. 4A1. Without metallographic etching

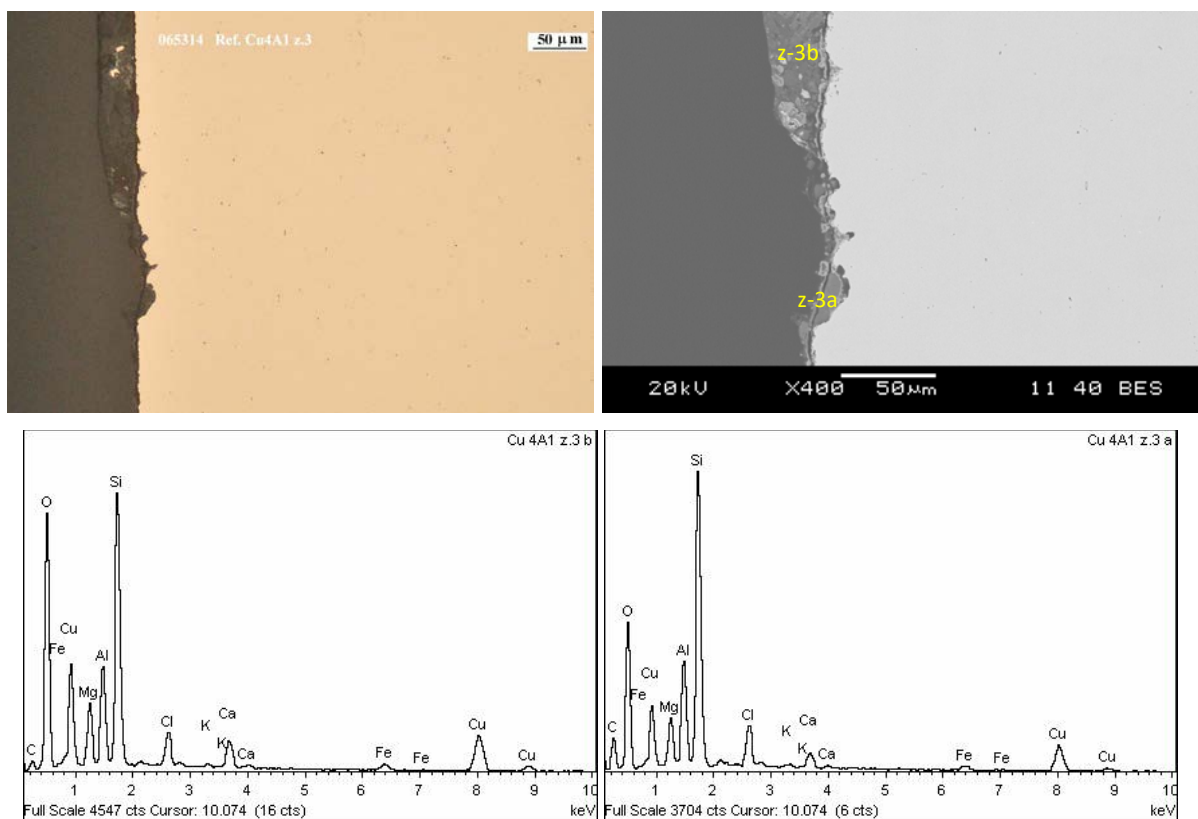


Figure 9: Optical and backscattered SEM micrographs of the maximum pit depth in zone 3, at 0 mm depth, and associated EDS spectrum, from coupon ref. 4A1. Without metallographic etching

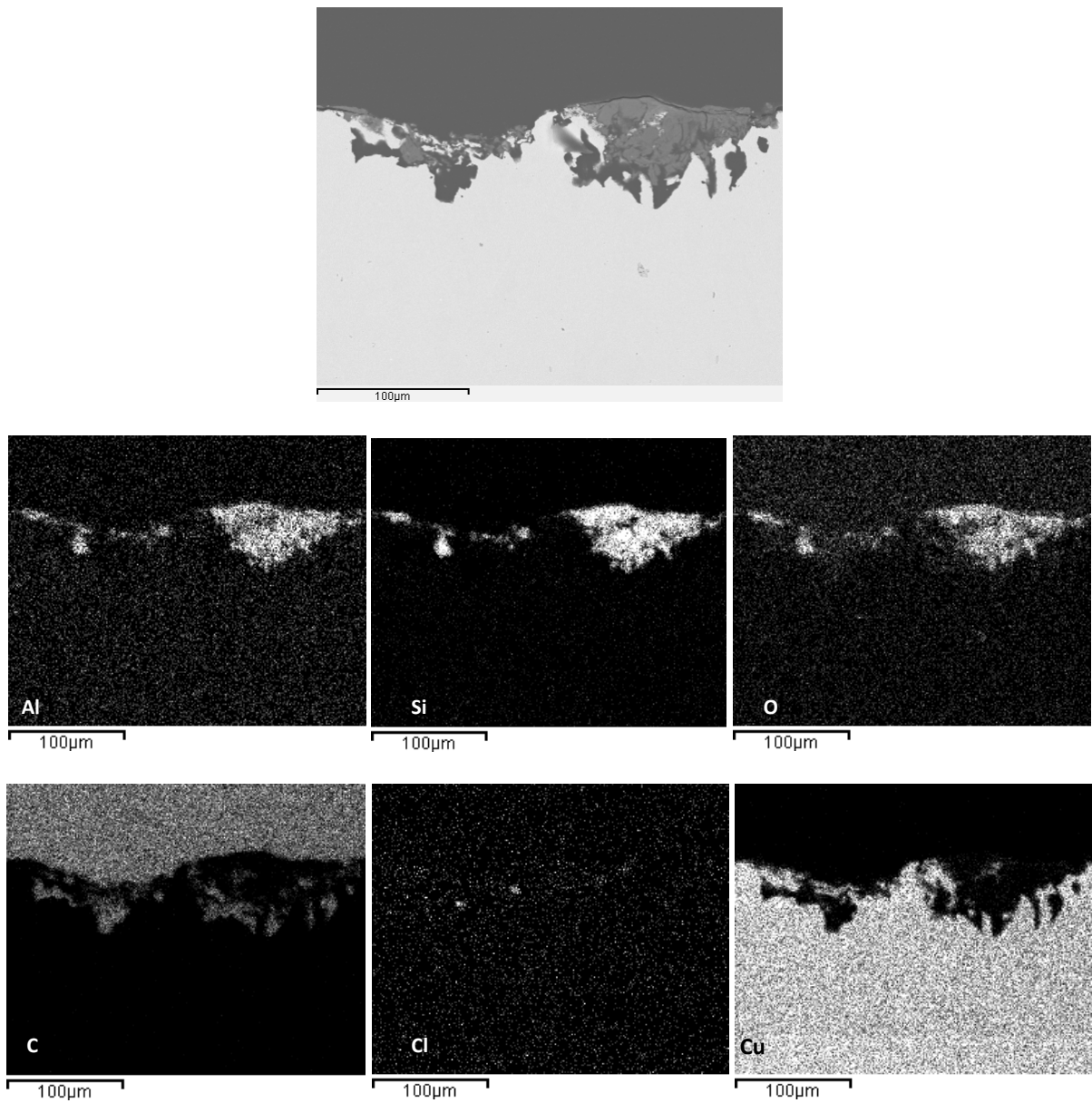


Figure 10: Backscattered SEM micrograph of maximum pit depth in zone 1a, at 0 mm depth, from coupon ref. 4A1, and associated element maps

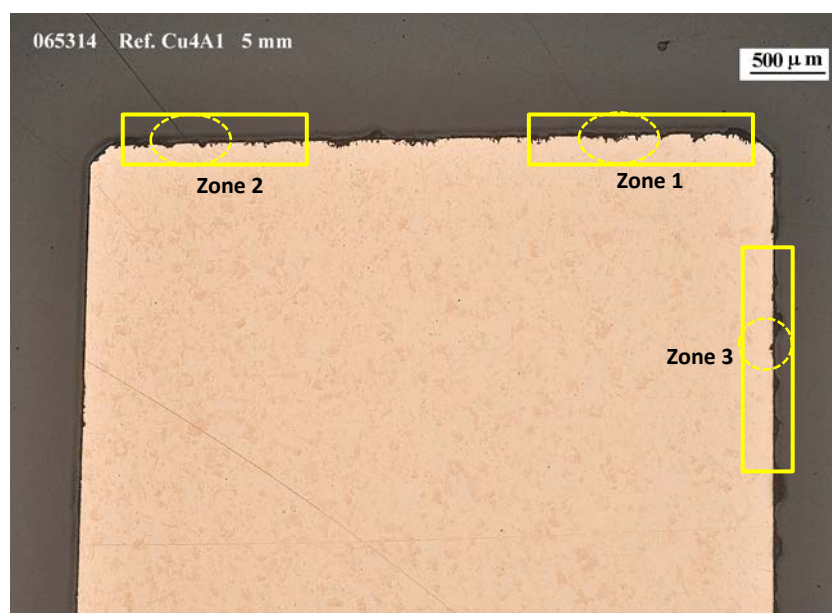


Figure 11: Optical micrograph of section of copper alloy ref. 4A1, at 5 mm depth, from coupon ref. 4A1. Without metallographic etching

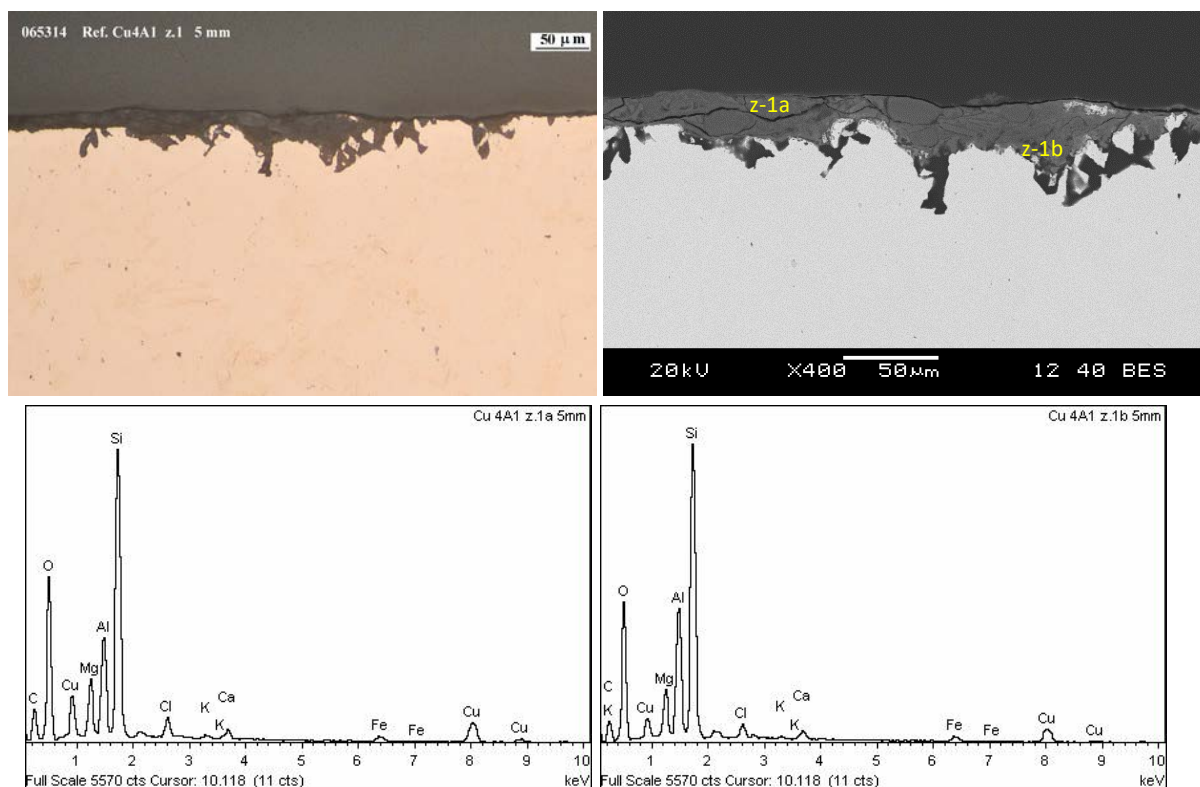


Figure 12: Optical and backscattered SEM micrographs of the maximum pit depth in zone 1, at 5 mm depth, and associated EDS spectra, from coupon ref. 4A1. Without metallographic etching

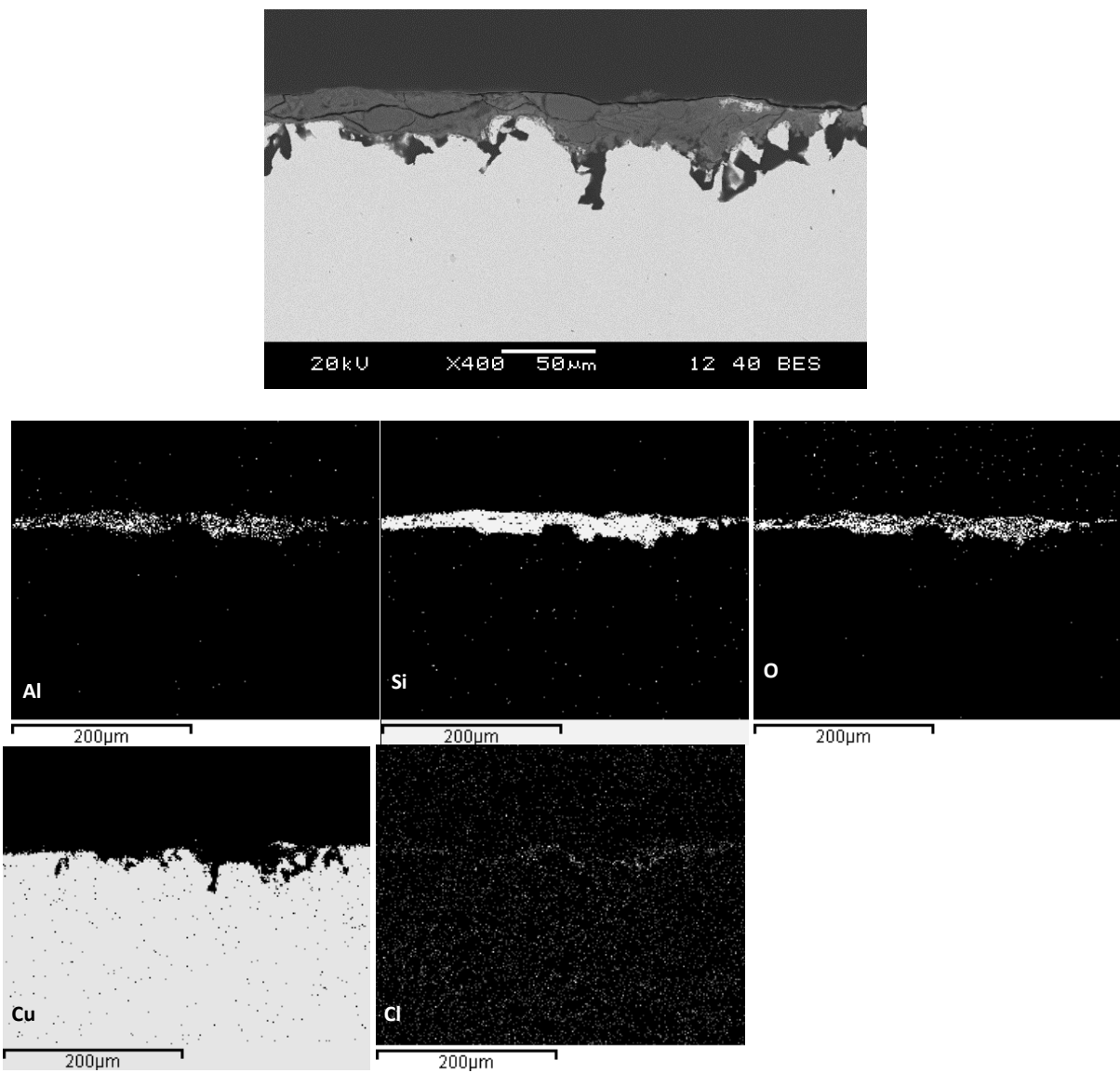


Figure 13: Backscattered SEM micrograph of maximum pit depth in zone 1, at 5 mm depth, from coupon ref. 4A1, and associated element maps

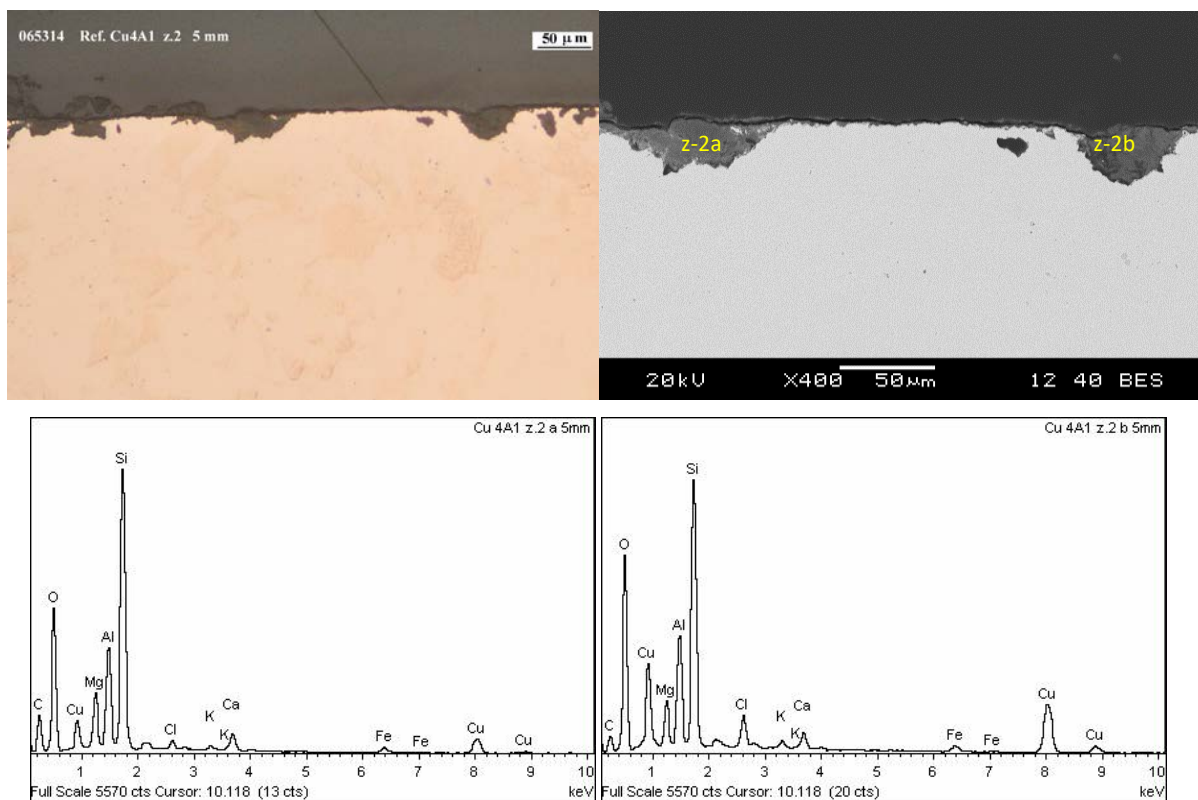


Figure 14: Optical and backscattered SEM micrographs of the maximum pit depth in zone 2, at 5 mm depth, and associated EDS spectra, from coupon ref. 4A1. Without metallographic etching

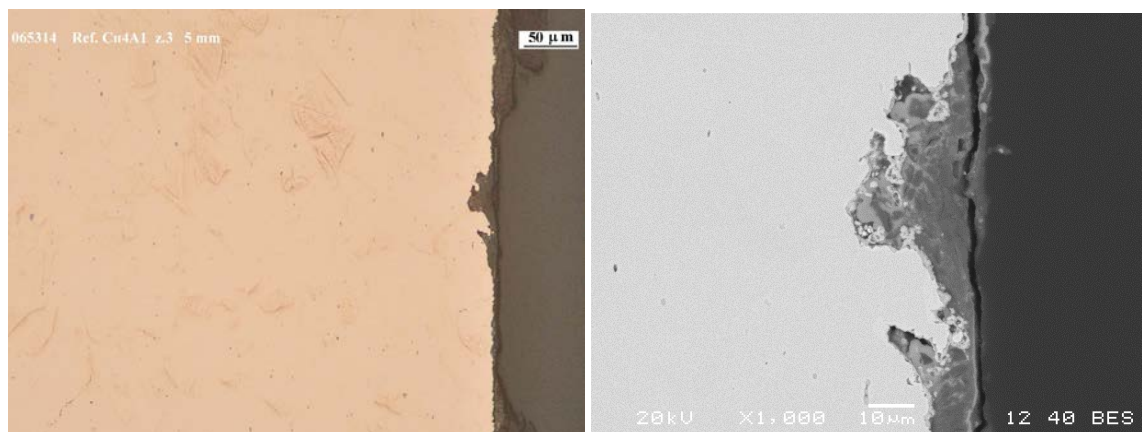


Figure 15: Optical and backscattered SEM micrographs of the maximum pit depth in zone 3, at 5 mm depth, from coupon ref. 4A1. Without metallographic etching

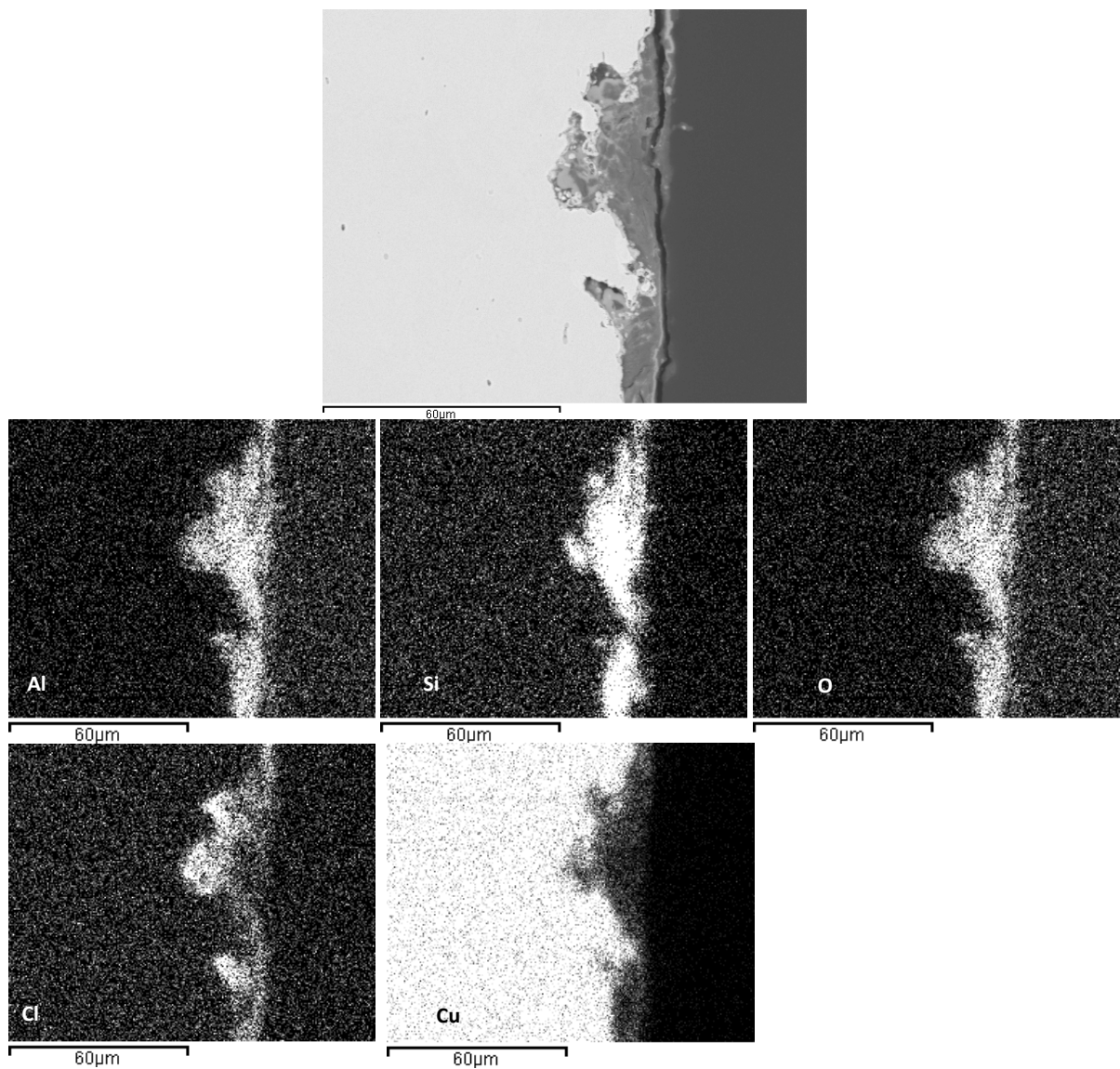


Figure 16: Backscattered SEM micrograph of maximum pit depth in zone 3, at 5 mm depth, from coupon ref. 4A1, and associated element maps

EDS analysis	Element (wt%)										
	C	O	Mg	Al	Si	Cl	K	Ca	Fe	Cu	Total
Cu 4A1 z.1a 0mm	18.33	44.90	3.76	6.76	19.30	0.46		0.68	1.03	4.78	100.00
Cu 4A1 z.1b 0mm	4.46	47.57	5.62	7.70	25.30	0.27		1.08	1.54	6.46	100.00
Cu 4A1 z.2 0mm	1.49	50.24	4.32	8.52	24.61		0.51	1.56	2.24	6.52	100.00
Cu 4A1 z.2b 0mm	12.48	49.67	3.83	6.37	17.67	0.35	0.40	1.21	1.14	6.88	100.00
Cu 4A1 z.3 a 0mm	19.13	39.33	3.02	5.63	16.61	3.16	0.26	1.20	0.99	10.66	100.00
Cu 4A1 z.3 b 0mm	7.11	48.36	4.11	5.41	15.16	2.37	0.20	2.04	1.19	14.04	100.00
Cu 4A1 z.1a 5mm	19.56	42.27	3.76	5.53	16.68	1.57	0.30	0.75	1.09	8.49	100.00
Cu 4A1 z.1b 5mm	17.27	41.53	3.36	7.92	19.67	1.31	0.18	0.91	1.23	6.62	100.00
Cu 4A1 z.2 a 5mm	20.37	41.91	3.83	5.89	17.32	0.77	0.29	1.57	1.18	6.87	100.00
Cu 4A1 z.2 b 5mm	10.89	40.36	3.34	6.31	15.26	2.26	0.46	1.22	1.14	18.76	100.00

Table 2: Semi-quantitative elemental chemical composition obtained in the EDS analyses carried out on metallographic sample ref. 4A1, at 0 and 5 mm depth

Metallographic coupon ref. 4A1	Maximum pit depth (microns)		
	Zone 1	Zone 2	Zone 3
0 mm depth	62	40	22
5 mm depth	52	30	27

Table 3: Maximum pit depth based on SEM micrographs

4 GENERAL CORROSION RATE ESTIMATION ON COPPER COUPON REF. 4A2

The average general corrosion rate of copper coupon reference 4A2 (see Figure 3) is estimated following the indications of ASTM G31 standard, *“Standard Practice for Preparing, Cleaning, and Evaluating Corrosion Test Specimens”*. According to this standard the “average” corrosion rate is calculated using the formula:

$$\text{corrosion rate} = (K \times \Delta p) / A \times t \times D$$

Where: K = Constant K in the corrosion rate equation is 8.76×10^7 , if the corrosion rate units are

expressed in microns per year ($\mu\text{m}/\text{year}$) and the total corrosion time is 18 years

Δp = Initial weight (before exposure) – weight of descaled test specimen (g)

t = Test duration (hours)

A = Test specimen area (cm^2)

D = Density of metal specimen (g/cm^3)

It is assumed that the loss of total weight undergone by tested samples is only due to generalized corrosion and not to local corrosion phenomena.

The removal of the corrosion products in the copper sample is carried out with the sulfuric acid solution reference C.2.3: H_2SO_4 10% weight, 1 to 3 min., 20-25 °C.

To assess the suitability of the cleaning procedure, the process was first tested on a pure copper sample, in order to verify that the descaling procedure does not remove any base metal. The descaling process was evaluated also in a section of one CuNi10 coupon. Table 4 shows the mass losses resulting from the descaling process on the copper coupons. These data indicate that:

- 1) The chemical descaling dissolution does not remove any metal from the “unattacked” Cu-ETP material
- 2) In contrast to that observed for the cupronickel alloy, the Cu-ETP coupon ref. 4A2, loses almost all the corrosion products and deposits in the first descaling cycle, with a duration of 0.5 minutes

The corrosion rate value obtained for copper coupon 4A2 is given in Table 5. Some considerations:

- It is assigned an initial weight (before exposure) of 36.0878 g
- Copper density is $8.92 \text{ g}/\text{cm}^3$ (density for copper ETP type C101)
- It is assumed that the total exposure time is 18 years, which gives 157680 hours.

- The initial total surface of the specimen is determined making corrections for the area associated with the mounting hole
- It is important to take into account that only one coupon has been used in the estimation of the average general corrosion rate.

Photographs of the descaled coupon ref. 4A2 are given in Figures 17 and 18.

Ref. Copper ETP (not exposed)	P1	P2	P3	P4	P5
Initial weight (g)					
23,1174	23,1173	23,1173	23,1172	23,1172	23,1172
Accumulated mass loss (g)	0,0001	0,0001	0,0002	0,0002	0,0002
Accumulated descaling time (min)	1	2	3	4	6

Ref. 4A3 (Cu10Ni)	P1	P2	P3	P4	P5	P6	P7	P8	P9
Weight of coupon before descaling (g)									
8,3189	8,3067	8,3045	8,2977	8,2975	8,2968	8,2967	8,2963	8,2959	8,2957
Accumulated mass loss (g)	0,0122	0,0144	0,0212	0,0214	0,0221	0,0222	0,0226	0,0230	0,0232
Accumulated Time (min)	1	2	3	4	5	6	9	12	15

Ref. 4A2 (Cu-ETP)	P1	P2	P3	P4	P5	P6	P7
Weight of coupon before descaling (g)							
35,9845	35,8918	35,8916	35,8915	35,8912	35,8911	35,8909	35,8909
Accumulated mass loss (g)	0,0927	0,0929	0,0930	0,0933	0,0934	0,0936	0,0936
Accumulated Time (min)	0,5	1	1,5	2	4	6	8

Table 4: Mass loss of copper samples coupons resulting from the descaling process

Ref.	Initial weight before exposure (g)	Final descaled weight (g)	Mass loss (g)	k (-)	Time of exposure (hours)	Density (g/cm3)	Specimen Area (cm2)	Corrosion depth (microns)	Average Corrosion rate (microns/year)
Cu4A2	36,0878	35,8908	0,1970	8.76E7	157680	8,92	26,09	8.51	0,47

Table 5: Corrosion depth and average general corrosion rate obtained for copper coupon reference 4A2

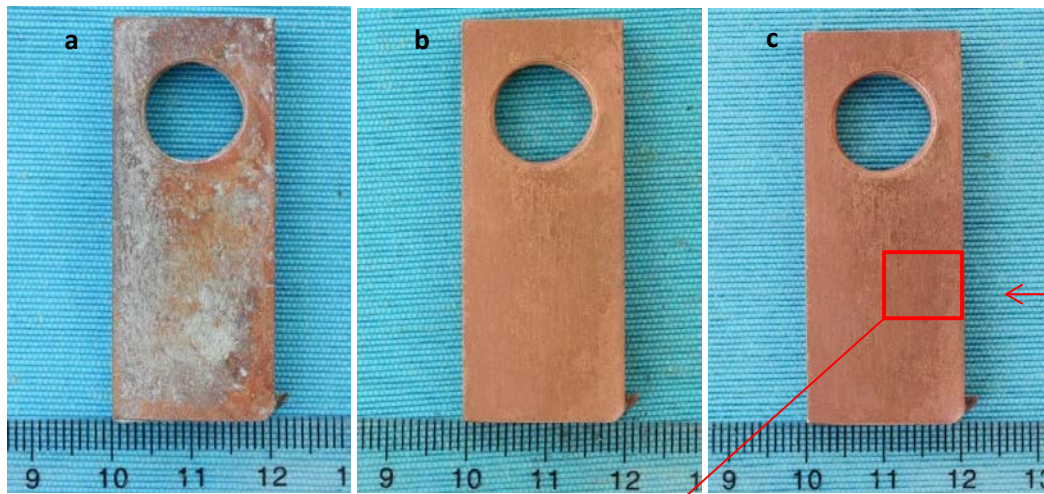


Figure 17: Photographs of copper coupon ref. 4A2, a) before removing corrosion products and deposits, b) after 0.5 minutes from the beginning of the descaling process and c) after 3.5 minutes from the beginning of the descaling process



Figure 18: Detail of the surface of the copper coupon ref. 4A2, after 3.5 minutes from the beginning of the descaling process

Chemical profiles in atomic%

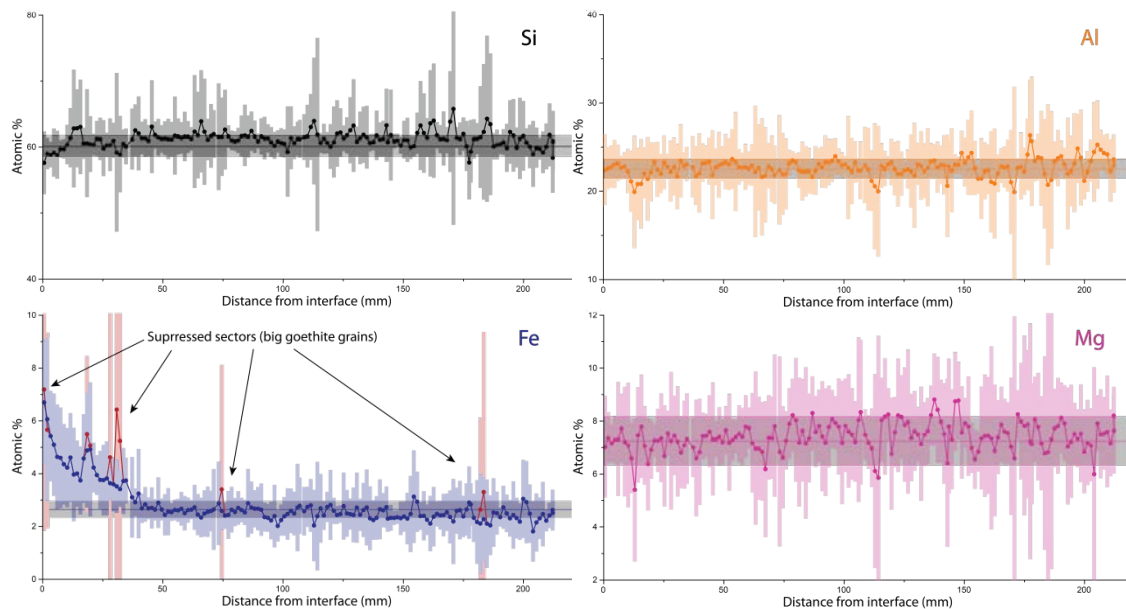


Figure 1: Chemical profiles of major elements Si, Al, Fe and Mg. Horizontal lines represent average reference value measured in raw material, grey area accounts for 2x the standard deviation on several measurements done in different laboratories (reference data in 16-068).

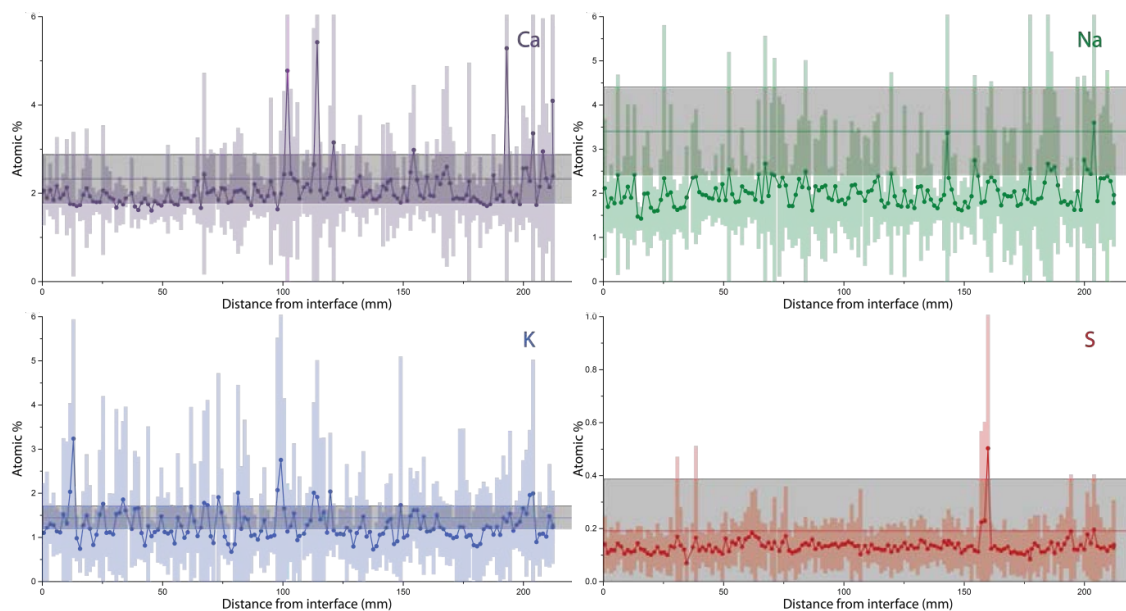


Figure 2: Chemical profiles of minor elements Ca, Na, K and S. Horizontal lines represent average reference value measured in raw material, grey area accounts for 2x the standard deviation on several measurements done in different laboratories (reference data in 16-068).

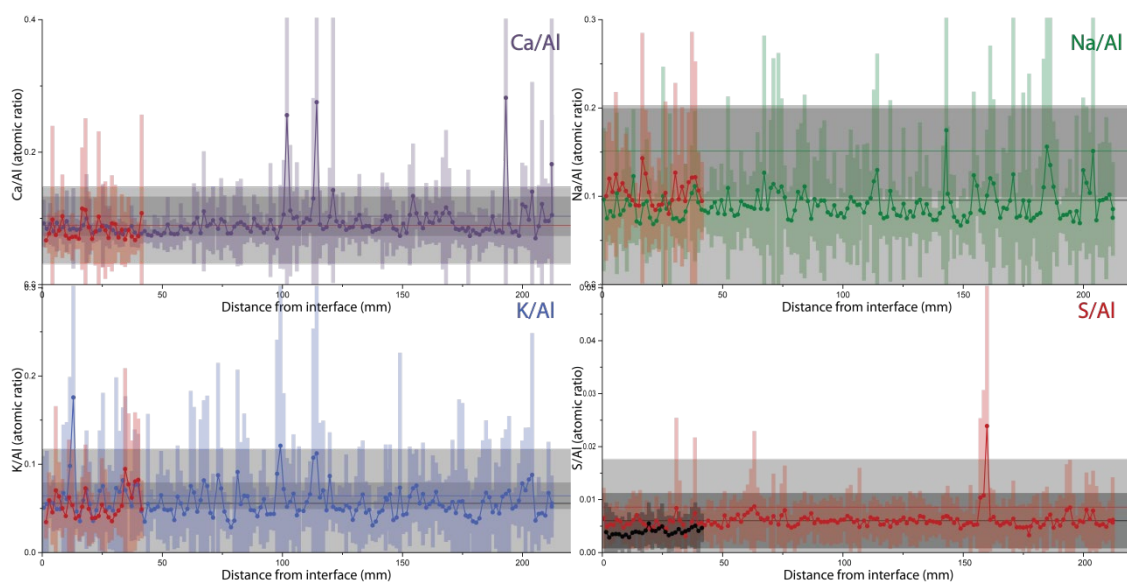


Figure 3: “Al-normalized” chemical profiles of major elements Ca, Na, K and S in block BM-B-41-1 and block BM-B-41-2 (red for Ca, Na, K and black for S) from section 62. Horizontal lines and grey areas represents same data as on Figure 65.

Additional Raman spectra

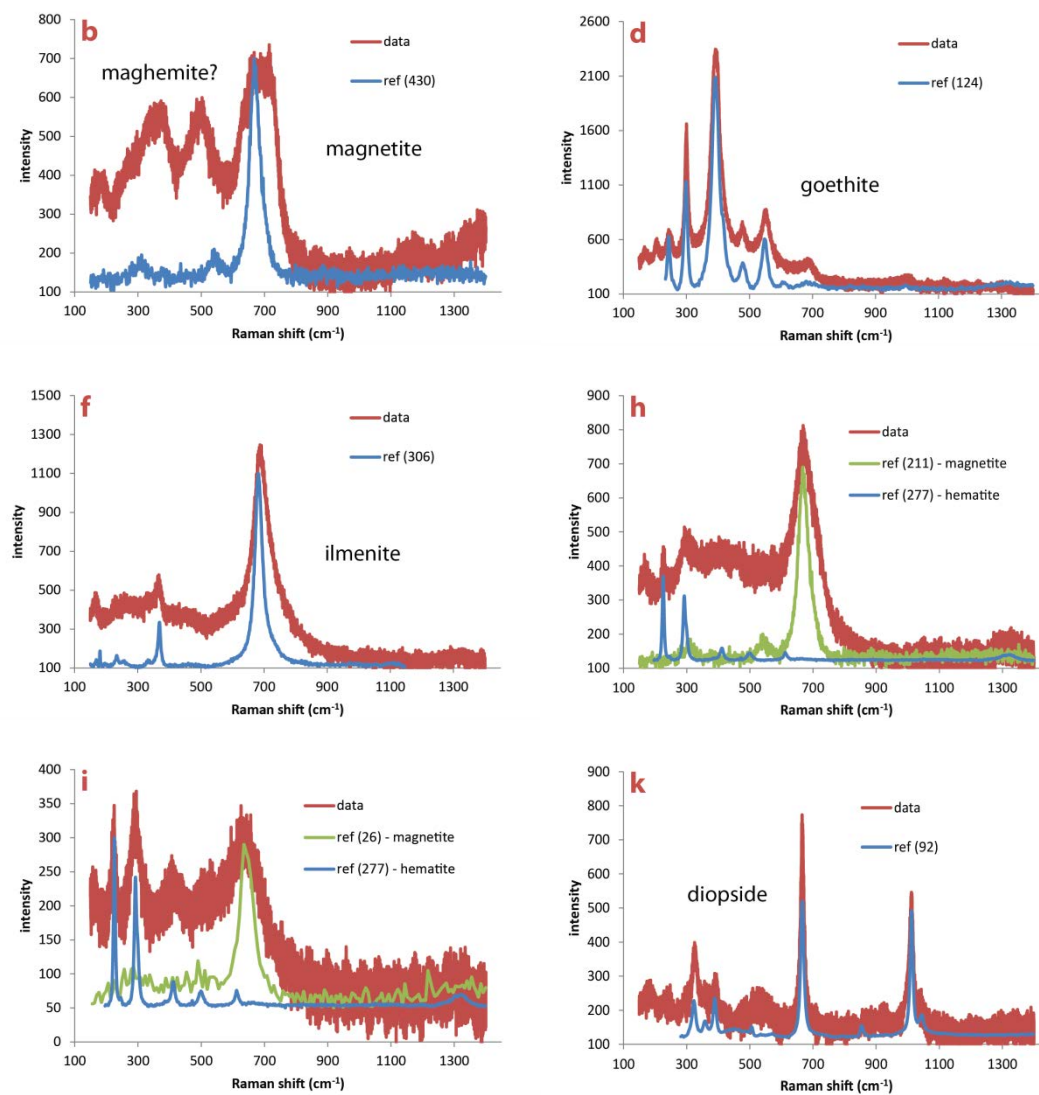


Figure 3: Raman spectra collected at spots indicated on Figure 66

Chemical composition inferred from XRF analysis

Table 1: Chemical composition of the powdered FEBEX-DP samples determined by XRF (and ATG).

Sample	R1	R2	R3	R4	R5	R6	O7	O8	O9	OB10	B11	B12	B13	B14	B15	B16	B17	B18
d. (mm)	2.5	8.2	13.9	19.6	25.3	31.0	36.6	42.3	48.0	53.7	59.4	65.1	70.8	76.5	82.2	87.9	93.5	99.2
%H ₂ O	5.1	4.2	4	3.1	3.7	4.7	3.7	4.7	4.1	4.9	4.1	3.9	3.8	4.4	4.1	4.8	3.2	5.3
LOI	8.1	7.9	8.1	8.1	8.1	8.2	8.2	8	8	8.1	8.1	8	8.2	8.3	8.3	8.2	8.2	8.2
Σ	99.17	99.37	98.60	99.06	99.26	99.35	99.09	99.02	98.66	98.76	99.07	99.68	99.04	99.03	99.19	99.06	98.16	98.46
Major elements (in oxide wt%)																		
SiO ₂	62.52	62.11	63.64	63.73	64.43	64.47	64.58	64.22	64.23	64.55	64.64	65.16	64.62	64.50	64.77	64.57	63.85	64.11
TiO ₂	19.41	19.35	19.47	19.95	19.70	20.02	20.11	20.16	19.75	20.14	20.21	20.35	20.13	20.19	20.12	20.15	19.91	19.90
Al ₂ O ₃	7.71	8.55	6.36	5.90	5.70	5.35	5.15	4.93	5.38	4.27	4.27	4.36	4.38	4.51	4.31	4.32	4.40	4.31
Fe ₂ O ₃	4.51	4.52	4.57	4.66	4.57	4.67	4.69	4.69	4.70	4.75	4.90	4.89	4.85	4.85	4.87	4.89	4.84	4.83
MnO	1.67	1.67	1.68	1.69	1.66	1.72	1.69	1.72	1.72	1.96	2.01	1.92	1.95	2.01	2.03	2.06	2.09	2.07
MgO	1.73	1.60	1.35	1.58	1.61	1.52	1.29	1.56	1.27	1.46	1.47	1.38	1.43	1.35	1.45	1.44	1.43	1.57
CaO	1.19	1.16	1.09	1.13	1.17	1.17	1.16	1.29	1.18	1.20	1.14	1.18	1.22	1.17	1.20	1.17	1.19	1.20
Na ₂ O	0.27	0.25	0.27	0.26	0.26	0.26	0.26	0.28	0.25	0.26	0.26	0.26	0.28	0.27	0.26	0.26	0.27	0.27
TiO ₂	0.05	0.04	0.05	0.04	0.05	0.05	0.05	0.05	0.05	0.05	0.05	0.04	0.05	0.05	0.05	0.05	0.05	0.05
P ₂ O ₅	0.04	0.04	0.03	0.03	0.04	0.03	0.03	0.04	0.04	0.04	0.04	0.04	0.04	0.04	0.04	0.05	0.04	0.04
MnO	62.52	62.11	63.64	63.73	64.43	64.47	64.58	64.22	64.23	64.55	64.64	65.16	64.62	64.50	64.77	64.57	63.85	64.11
Trace elements (in ppm)																		
Ba	130	182	188	146	117	178	123	309	113	172	133	244	145	167	178	228	177	130
Cr	10	18	17	15	14	8	14	17	12	20	13	9	17	10	10	10	13	14
Cu	6	6	8	7	6	8	7	7	8	8	9	12	9	10	11	10	9	9
Nb	12	15	12	15	13	13	13	13	14	14	13	14	14	14	13	15	15	14
Ni	19	25	22	21	22	22	20	21	23	22	33	49	36	34	35	32	25	28
Pb	30	30	26	28	30	31	32	33	36	36	38	40	40	39	39	38	36	39
Rb	47	47	45	46	49	47	46	50	50	49	48	50	47	48	49	48	47	49
Sr	180	183	184	188	187	191	189	199	191	202	199	208	199	204	204	211	213	212
V	23	18	16	13	77	76	71	24	45	11	13	35	12	21	10	28	9	28
Y	18	21	18	34	25	26	26	25	28	34	31	35	35	36	36	35	32	32
Zn	70	70	68	71	70	74	72	73	74	74	77	77	77	77	76	77	75	75
Zr	215	217	209	226	225	218	209	209	236	210	213	211	218	227	211	218	216	215

Sample identity: letters correspond to the color of the bentonite sampled area (R = red, O = orange, B = blue G = green, OB = transition from orange to blue, BG = transition from blue to green, out = outer layer of the block), and number to the order of sampling, (starting from the interface)

d: approximate distance between the sampled layer and the interface

LOI: Loss On Ignition

%H₂O: water content measured at 105°C

Σ: sum of elements (excludes LOI and %H₂O)

Table 2: Chemical composition of the powdered FEBEX-DP samples determined by XRF (and ATG).

Sample	B19	B20	B21	B22	BG23	BG24	BG25	BG26	BG27	G28	G29	G30	out	raw
d. (mm)	104.9	110.6	116.3	122.0	127.7	133.4	139.1	144.8	150.4	156.1	161.8	167.5	217.5	-
%H ₂ O	4.8	3.2	4	3.1	3.2	4.2	4.7	4.4	4.3	7.6	5.3	3	3.3	11
LOI	8.4	8.1	8.2	8.6	8.2	8.5	8.4	8.5	8.2	8.5	8.4	8.3	8.5	8.8
Σ	98.67	98.75	99.35	98.49	99.28	98.61	98.74	99.15	99.25	99.20	99.82	101.29	98.93	98.67
Major elements (in oxide wt%)														
SiO ₂	64.38	64.47	64.78	63.64	64.42	64.24	64.62	64.81	64.89	64.99	65.42	66.06	64.61	64.38
TiO ₂	20.04	20.04	20.13	19.66	19.73	19.71	19.85	20.15	20.17	20.01	20.17	20.80	20.04	20.04
Al ₂ O ₃	4.23	4.22	4.19	4.13	4.09	3.97	3.98	3.82	3.87	3.86	3.87	3.93	3.91	4.23
Fe ₂ O ₃	4.85	4.84	4.87	4.80	4.84	4.77	4.84	4.93	4.94	4.87	5.00	5.01	4.98	4.85
MnO	2.13	2.12	2.17	3.18	2.22	2.71	2.42	2.47	2.32	2.33	2.35	2.38	2.32	2.13
MgO	1.40	1.35	1.51	1.40	2.34	1.54	1.36	1.34	1.44	1.48	1.37	1.42	1.39	1.40
CaO	1.21	1.25	1.24	1.21	1.18	1.21	1.22	1.18	1.16	1.21	1.18	1.24	1.22	1.21
Na ₂ O	0.26	0.27	0.27	0.26	0.27	0.26	0.26	0.27	0.27	0.26	0.26	0.27	0.26	0.26
TiO ₂	0.05	0.05	0.05	0.07	0.05	0.04	0.05	0.05	0.05	0.05	0.05	0.05	0.05	0.05
P ₂ O ₅	0.04	0.04	0.04	0.06	0.05	0.05	0.05	0.05	0.05	0.05	0.05	0.06	0.05	0.04
MnO	64.38	64.47	64.78	63.64	64.42	64.24	64.62	64.81	64.89	64.99	65.42	66.06	64.61	64.38
Trace elements (in ppm)														
Ba	179	195	217	188	179	188	190	193	141	174	254	155	179	195
Cr	15	16	13	18	15	12	16	14	10	19	18	6	15	16
Cu	7	9	8	8	10	9	11	11	9	9	10	11	7	9
Nb	13	14	12	13	13	12	14	15	13	13	13	14	13	14
Ni	25	25	24	22	24	21	22	21	23	21	22	22	25	25
Pb	34	32	37	35	38	34	35	39	33	35	37	36	34	32
Rb	50	51	50	50	48	49	48	47	48	48	48	47	50	51
Sr	218	223	228	237	229	235	238	236	239	239	238	239	218	223
V	26	34	29	16	16	16	19	29	25	32	28	31	26	34
Y	32	31	30	33	31	35	31	31	28	32	32	29	32	31
Zn	75	73	74	74	75	73	75	74	75	76	75	75	75	73
Zr	212	209	216	213	221	212	213	214	221	211	220	215	212	209

Sample identity: letters corresponds to the color of the bentonite sampled area (R = red, O = orange, B = blue G = green, OB = transition from orange to blue, BG = transition from blue to green, out = outer layer of the block), and number to the order of sampling, (starting from the from the interface)

d: average distance between the sampled layer and the interface

LOI: Loss On Ignition

%H₂O: water content measured at 105°C

Σ: sum of elements (excludes LOI and %H₂O)

Appendix C

Additional Data from the Study by Uni Bern

Mössbauer hyperfine parameters

Table 3: refined values of Mössbauer parameters and doublet structural attributions for the three contact samples collected in block BM-B-41-1 (spectra shown in Figure 72).

Hyperfine parameters				Area(%)	Attribution
I.S.	F.W.H.M.	Q.S./2ε	B _{hf}		
raw					
300K					
0.35	0.67	0.54	28.8	83%	HS-oct-Fe(III)
1.2	0.5	2.35		4%	HS-oct-Fe(II)
0.45	0.9	-0.2		13%	goethite
77K					
0.46	0.71	0.56	55.0	75%	HS-oct-Fe(III)
1.35	0.5	2.54		5%	HS-oct-Fe(II)
0.53	0.69	0.06		9%	hematite
0.47	1.07	-0.25		11%	goethite
G180					
300K					
0.34	0.67	0.55	47.7	80%	HS-oct-Fe(III)
1.26	0.56	2.37		8%	HS-oct-Fe(II)
0.34	0.56	-0.2		5%	hematite
0.32	0.7	-0.2		7%	goethite
77K					
0.46	0.73	0.57	53.7	81%	HS-oct-Fe(III)
1.29	0.72	2.71		9%	HS-oct-Fe(II)
0.44	0.46	0		6%	hematite
0.47	0.46	-0.2		4%	goethite
B100					
300K					
0.32	0.62	0.59		86%	HS-oct-Fe(III)
1.32	0.5	2.27		14%	HS-oct-Fe(II)
77K					
0.46	0.64	0.56	55.6	75%	HS-oct-Fe(III)
1.26	0.6	2.92		15%	HS-oct-Fe(II)
0.57	0.46	0.25		4%	hematite
0.47	0.46	-0.23		6%	goethite

I.S. = Isomer shift value relative to that of the α -Fe at 300 K. ($\text{mm}\cdot\text{s}^{-1}$)

F.W.H.M = Full width of line at half of its maximum intensity. ($\text{mm}\cdot\text{s}^{-1}$)

Q.S./2ε = Quadrupolar splitting

B_{hf} = Magnetic hyperfine field (T)

Table 4: refined values of Mössbauer parameters and doublet structural attributions for the three contact samples collected in block BM-B-41-1

Hyperfine parameters					Attribution
I.S.	F.W.H.M.	Q.S./2ε	B_{hf}	Area(%)	
B75					
300K					
0.34	0.62	0.53		84%	HS-oct-Fe(III)
1.17	0.67	2.57		16%	HS-oct-Fe(II)
77K					
0.47	0.66	0.56		74%	HS-oct-Fe(III)
1.28	0.66	2.88		16%	HS-oct-Fe(II)
0.41	0.56	0.22	53.5	6%	hematite
0.53	0.7	-0.2	48.0	4%	goethite
R20					
300K					
0.34	0.66	0.56		53%	HS-oct-Fe(III)
1.25	0.5	2.32		2%	HS-oct-Fe(II)
0.38	0.59	-0.2	49.3	14%	goethite
<0.43>		<-0.25>	<31.6>	31%	goethite
77K					
0.47	0.7	0.54		55%	HS-oct-Fe(III)
1.32	0.5	2.76		4%	HS-oct-Fe(II)
0.51	0.49	-0.11	52.9	12%	goethite
0.48	0.65	-0.23	49.1	29%	goethite
crust					
300K					
0.36	0.58	0.63		41%	HS-oct-Fe(III)
1.17	0.5	2.57		5%	HS-oct-Fe(II)
0.44	0.89	-0.2--	49.1	9%	goethite
<0.46>		<-0.30>	<30.2>	45%	goethite
77K					
0.46	0.56	0.63		37%	HS-oct-Fe(III)
1.24	0.71	2.74		8%	HS-oct-Fe(II)
0.5	0.42	-0.22	49.8	37%	hematite
0.5	0.64	-0.23	48.1	18%	goethite

I.S. = Isomer shift value relative to that of the α -Fe at 300 K ($\text{mm}\cdot\text{s}^{-1}$)F.W.H.M = Full width of line at half of its maximum intensity ($\text{mm}\cdot\text{s}^{-1}$)

Q.S./2ε = Quadrupolar splitting

 B_{hf} = Magnetic hyperfine field (T)

Appendix D

Laboratory Sampling Logs of Samples for interface Studies (CIEMAT)

**Ciemat****MUESTREO DE BLOQUES EN LABORATORIO**

Referencia	BM-C-42-1	Sección	42	Tipo de muestra	Core
Fecha muestreo	03/06/2015	Fecha llegada		Fecha apertura	21/10/2015
Lugar almacenamiento	Cámara húmeda Estante 1	Tipo empaquetado	Bolsa de plástico sin vacío + bolsa de aluminio sin vacío + bolsa de aluminio al vacío + film transparente		
Análisis previstos	Interfase hierro/bentonita				
Medida conductividad térmica (W/m·K)					
Medida HR (%)					

Diagram showing the fragmentation of a core sample BM-C-42-1 into three cylindrical pieces. The pieces have diameters of 5 cm and lengths of 3 cm, 4 cm, and 4.5 cm respectively. A cross-section diagram shows the sample divided into concentric rings.

Posición

Foto 1. Aspecto del testigo fragmentado en 3 trozos.

Fotos 2 y 3. Fragmento en contacto con la mitad superior del "cable cap"

Observaciones: **testigo extraído del bloque B-B-42-5 que está en contacto con la mitad superior del "cable cap"**





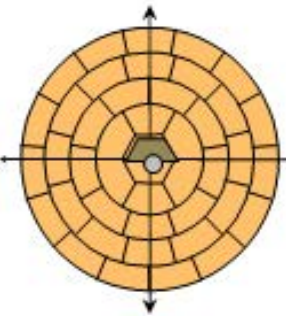



Re-embalaje y almacenamiento	Se re-embala la muestra en 2 paquetes, ambos con film transparente + bolsa de aluminio al vacío 1. Uno de los paquetes contiene el fragmento de core directamente en contacto con el "cable cap" (fotos 2 y 3) y el otro el resto. Almacenamiento en nevera edificio 19.
------------------------------	--



Ciemot

MUESTREO DE BLOQUES EN LABORATORIO

Referencia	B-B-42-5	Sección	42	Tipo de muestra	Bloque
Fecha muestreo	03/06/2015	Fecha llegada	21/08/15	Fecha apertura	22/10/2015
Lugar almacenamiento	Cámara húmeda Estante 2	Tipo empaquetado	Bolsa de plástico sin vacío + bolsa de aluminio sin vacío + bolsa de aluminio sin vacío + film transparente		
Análisis previstos	Estudios interfase interfase hierro/bentonita (sales, intercambio, FTIR, DRX, SEM, porosidad, BET)				
Medida HR (%) y densidad	Fragmento a) HR(%) = 25.1, ρ_c = 1.55 g/cm ³ Fragmento b) HR(%) = 25.6, ρ_c = 1.49 g/cm ³				

<p>Desmuestre del bloque a (izquierda)</p>  	<p>Desmuestre del bloque b (derecha)</p>  	<p>Posición</p> 
		
<p>Foto 1. Aspecto de la muestra embalada en bolsa de aluminio.</p>	<p>Foto 2. Cara de bentonita en contacto con el "cable cap" en el bloque a</p>	<p>Foto 3. Cara de bentonita en contacto con el "cable cap" en el bloque b</p>

Observaciones: Del bloque, que está en contacto con la mitad superior del "cable cap", se han extraído las muestras BM-C-42-1 y BM-C-42-2

Re-embalaje y almacenamiento	Se re-embala la muestra restante con film transparente + bolsa de aluminio al vacío 1 + bolsa de aluminio al vacío 2. Almacenamiento en cámara húmeda.
------------------------------	--

**Ciemat****MUESTREO DE BLOQUES EN LABORATORIO**

Referencia	BM-D-45-2	Sección	45	Tipo de muestra	Fragmento
Fecha muestreo	23/06/2015	Fecha llegada	7/08/2015	Fecha apertura	17/10/2015
Lugar almacenamiento	Cámara húmeda Estante 6	Tipo empaquetado	Bolsa de plástico sin vacío + bolsa de aluminio al vacío + bolsa de aluminio sin vacío + film transparente		

Análisis previstos	Interfase hierro/bentonita
--------------------	----------------------------

Medida conductividad térmica (W/m.k)	
Medida HR (%)	

Foto 1. Aspecto de la muestra fragmentada en 2 trozos.

Foto 2. Fragmento más grande del cual se toma una muestra que se denomina BM-D-45-2a.

Observaciones: **contigua a la M-L-45-2 que enviaron a Tecnalia (cuarto de liner de ese cuadrante)**

Re-embalaje y almacenamiento	Se re-embala la muestra sobrante con film transparente + bolsa de aluminio al vacío 1 + bolsa de aluminio al vacío 2. Almacenamiento en cámara húmeda, estante 6.
------------------------------	---

**Ciemat****MUESTREO DE BLOQUES EN LABORATORIO**

Referencia	B-C-47-10	Sección	47	Tipo de muestra	Core
------------	------------------	---------	-----------	-----------------	-------------


Fecha muestreo	26/06/2015	Fecha llegada		Fecha apertura	21/10/2015
----------------	-------------------	---------------	--	----------------	-------------------

Lugar almacenamiento	Cámara húmeda Estante	Tipo empaquetado	Bolsa de plástico sin vacío + bolsa de aluminio al vacío + bolsa de aluminio al vacío + carcasa acero con tapones de plástico en los extremos
----------------------	--------------------------	------------------	---

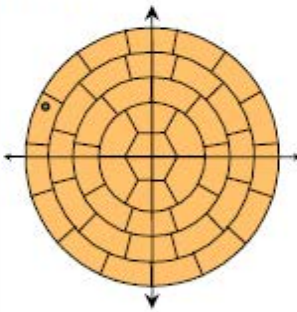
Análisis previstos	Interfase hierro/bentonita
--------------------	----------------------------

Medida conductividad térmica (W/m·K)	
Medida HR (%)	

Cara en contacto con el fisurómetro



Posición






Foto 2. Cara del testigo opuesta al fisurómetro.




Foto 3. Cara del testigo en contacto con el fisurómetro.

Observaciones: testigo de bentonita alrededor del fisurómetro

Re-embalaje y almacenamiento	Se re-embala la muestra con parafilmfilm + bolsa de aluminio al vacío. Almacenamiento en nevera edificio 19.
------------------------------	--